Magnetic Gear Electric Continuously Variable Speed Transmission (ECVT) for Helicopter Application

A Dissertation Presented for the
Doctor of Philosophy
Degree
The University of Tennessee, Knoxville

Zhisheng Ai
August 2025

ACKNOWLEDGEMENTS

I would like to express my deepest gratitude to my advisor, Dr. Hans DeSmidt and all participants in VLRCOE, for their invaluable guidance, encouragement, and patience throughout the course of this research. Their expertise in Aerospace & Mechanical engineering and Helicopter drivetrain systems greatly shaped the direction and quality of this thesis.

I am also sincerely thankful to the members of my committee, Dr. David K. Hall, Dr. Zhenbo Wang and Dr. Seddik M. Djouadi, for their thoughtful feedback and support. Their perspectives helped refine both the technical depth and clarity of this work.

Special thanks go to my colleagues and friends at the University of Tennessee, whose collaboration and discussions made this research process both productive and enjoyable. I would also like to thank the institutions and collaborators who provided access to simulation tools and reference data, including NASA, PSU and VLRCOE.

Finally, I extend my heartfelt appreciation to my fiancée Ms. Connie Ku and family for their unwavering encouragement and belief in me throughout my academic journey. Without their support, this work would not have been possible.

PREFACE

The idea for this thesis emerged during my doctoral research on advanced electromechanical transmission systems, particularly in the context of lightweight and efficient solutions for aerospace and electric mobility applications. Motivated by the limitations of conventional gear systems and inspired by the potential of magnetic technologies, I focused on developing a theoretical and simulation-based design framework for motor-integrated magnetic transmissions.

This work reflects both my academic interest in hybrid powertrain systems and my aspiration to contribute to the future of electric propulsion design. The process has involved extensive modeling, simulation, and critical evaluation of trade-offs between mass, torque, and efficiency. I hope that the methods and insights presented here can be useful to both researchers and engineers working in this field.

ABSTRACT

This thesis presents the modeling, design, and evaluation of Motor/Generator Integrated Permanent Magnet Gear (MIPMG) systems, with a focus on coaxial magnetic gear (CMG) architectures and their integration into Magnetic Electric Continuously Variable Transmission (MECVT) systems. A theoretical torque model is developed to characterize the magnetic coupling between inner and outer rotors through a ferromagnetic modulator. This model captures the sinusoidal torque–angle relationship based on pole pair configurations and material properties.

A key contribution is the derivation of a maximum torque line, allowing early estimation of torque limits without relying on repeated finite element analysis. Parametric studies show that increasing the outer pole pair number and optimizing magnet dimensions significantly improves torque density in space-constrained applications. Dynamic simulations validate the model under both partial and steady-state engagements, demonstrating consistent torque behavior under realistic loads.

Loss analysis reveals that eddy current loss dominates at high speeds, contributing to a notable drop in efficiency. Despite this, CMG-based systems show up to 17% total mass savings compared to multi-stage planetary gear transmissions at high gear ratios, due to shared magnetic components and compact design.

A system-level comparison between CMG and planetary gear-based MECVTs indicates that CMG systems are more suitable for high-ratio, mass-sensitive scenarios, while planetary systems remain advantageous in low-to-moderate ratios where efficiency is critical. This work provides a comprehensive framework for developing high-torque, lightweight magnetic transmission systems suitable for electric vehicles, aerospace propulsion, and robotics.

TABLE OF CONTENTS

LIST OF TABLES

LIST OF FIGURES

CHAPTER ONE

INTRODUCTION AND BACKGROUND

1.1 Overview of conventional helicopter transmission systems

In this decade, vertical lift aircraft, particularly helicopters, have gradually become an indispensable component of modern aviation due to their unique operational capabilities. Their defining characteristic—vertical take-off and landing—enables them to operate effectively in diverse environments, which makes them particularly vital in emergency situations. The unparalleled agility of helicopters in hovering and maneuvering within confined spaces offers a tactical advantage not achievable by other types of aircraft. This versatility, combined with advances in technology, has also opened the possibility of helicopters serving as a convenient mode of daily transportation in crowded urban environments.

In emergency services, helicopters have proven to be invaluable assets in a variety of life-saving missions. Their ability to perform vertical take-offs and landings in confined or otherwise challenging environments enables rapid and efficient responses in critical situations. During search and rescue operations, helicopters can access remote and rugged terrains that ground vehicles or fixed-wing aircraft cannot reach, making them indispensable in mountainous regions, dense forests, and flood-stricken areas. The medical sector also relies heavily on helicopters for emergency medical evacuations, allowing patients to receive urgent care and transport to medical facilities much faster than traditional means. Additionally, helicopters are essential tools in firefighting operations, especially in areas with difficult access. They can drop water or fire retardant in precise locations to contain wildfires, safeguarding lives, property, and critical infrastructure.

In recent years, the significance of helicopters has become even more evident during large-scale natural and man-made disasters. When earthquakes, floods, hurricanes, or large industrial accidents occur, helicopters are often the first to arrive at the scene, delivering aid, transporting relief personnel, and evacuating those in need. Their ability to navigate harsh weather conditions and land in tight spots makes them an irreplaceable asset in these scenarios.

Helicopters also play a pivotal role in military operations, where their flexibility and adaptability provide a range of strategic advantages. They are crucial for troop transport, allowing for the rapid deployment and extraction of personnel in combat zones. Reconnaissance missions benefit from the helicopter’s ability to fly at lower altitudes and hover for extended periods, enabling ground support and real-time intelligence gathering. Furthermore, helicopters are frequently used for supply drops in forward operating bases or isolated regions where ground transport would be risky or impractical. Combat helicopters also provide close air support to ground troops, increasing their effectiveness and safety during missions. Their mobility, speed, and agility make them essential assets for armed forces across the globe.

Beyond emergency and military applications, helicopters have established themselves as key players in numerous industrial and commercial roles. In law enforcement, helicopters are integral for aerial surveillance, assisting police forces in tracking suspects, monitoring large crowds during events, and patrolling expansive urban areas. In the energy sector, helicopters are employed to inspect and maintain infrastructure such as power lines, pipelines, and offshore oil rigs. They provide a fast and safe means of transporting personnel and equipment to remote or hard-to-reach sites, facilitating regular maintenance and emergency repairs.

In commercial aviation, helicopters serve as vital links between urban centers, offshore oil platforms, remote locations, and other areas without traditional airports. In cities with significant traffic congestion, helicopters offer an efficient alternative for transporting VIPs, business executives, and news crews, saving valuable time. Moreover, helicopters have become popular for tourism purposes, enabling visitors to experience scenic landscapes and explore remote or isolated regions that would otherwise be inaccessible.

The unique engineering of helicopters enables them to excel in such a wide range of applications. Their design integrates sophisticated aerodynamic principles with advanced powertrain systems to achieve vertical lift and precise control. The ability to hover, change directions swiftly, and operate at low altitudes requires a delicate balance of rotors, engines, and control systems. Over the years, continuous innovations in rotorcraft technology have enhanced their safety, efficiency, and capabilities. Modern helicopters are equipped with advanced avionics, autopilot systems, and improved noise-reduction technologies, making them more reliable, versatile, and environmentally friendly.

With the advent of urban air mobility (UAM) and electric vertical take-off and landing (eVTOL) aircraft, the future of vertical lift aviation seems poised for further expansion. These innovations promise to revolutionize daily transportation in congested urban environments, offering quieter, more sustainable, and efficient alternatives to conventional helicopters.

In summary, helicopters remain indispensable due to their versatility, adaptability, and unique vertical lift capabilities. From emergency services and military applications to industrial roles and commercial aviation, helicopters contribute significantly to a wide range of industries and missions. Their ability to perform tasks and reach locations that other vehicles and aircraft cannot, combined with continuous technological advancements, ensures that helicopters will continue to play a crucial role in aviation for decades to come.

1.2 Background of variable speed helicopter design

The numerous advantages of helicopters are closely tied to their complex structural design and sophisticated propulsion systems. Unlike fixed-wing aircraft and ground vehicles, helicopters' unique rotor systems, based on complex aerodynamic models, enable separate efforts for vertical lift and forward thrust. The helicopter propulsion system strikes a delicate balance, considering the trade-off between blade size, vertical lift force, forward thrust force, and rotor blade tip vortices.

According to the principle of force balance in helicopter flight scenarios, helicopter flight modes are typically divided into different phases:

Hovering and Lifting Phases

During hovering, the helicopter needs to generate a lift from the main rotor to maintain a stable hovering attitude or achieve continuous lift. In this situation, the rotors generally rotate in a horizontal plane but still experience some flapping due to the difference in speed between the two sides of the helicopter. This speed difference leads to an imbalance in lift between the left and right sides. To address this, modern helicopter designs include a blade pitch variation mechanism that allows the rotor to compensate for changes in lift by adjusting the blade angle during rotation. This mechanism automatically tilts the blades so that the retreating blades have a larger angle of attack, compensating for the reduced lift.

Forward Flight Phases

When moving forward, the helicopter is no longer stationary but travels at a certain speed. The balance of forces becomes more complex in this phase, involving:

- **Lift:** The rotor still generates lift, but the aerodynamic environment changes as the helicopter moves forward, affecting the direction and distribution of lift.
- **Gravity:** As in hovering, gravity acts vertically downward and remains equal to the total weight of the helicopter.
- **Thrust:** Forward motion requires horizontal thrust to overcome air resistance. This thrust is created by tilting the rotor, converting a portion of the lift force into forward thrust.
- **Drag:** During forward flight, the helicopter encounters air resistance, primarily consisting of the induced drag from the rotor and frictional resistance from the fuselage surface. Drag increases as forward speed increases.

In forward flight, lift is no longer solely equal to the helicopter's weight but must be balanced with thrust and drag. The differences in rotor control and flight operations between forward flight and hovering have inspired the design of variable-speed rotors. According to [2], helicopters with variable-speed transmissions have a significant advantage over conventional ones, not only in multiple flight modes (such as cruising, climbing, hovering, etc.) but also in fuel efficiency and performance, with 10–20% fuel savings. Additionally, they offer noise and vibration reduction during different flight conditions. All these advantages contribute to improved overall helicopter performance.

1.3 Conventional helicopter design challenges and solutions

Addressing the challenges of high energy and torque in helicopter transmission systems requires a comprehensive approach, blending advanced engineering techniques, innovative designs, and the use of specialized materials. Critical components such as gears, shafts, and clutches are typically crafted from high-strength alloys like titanium and steel, providing the durability to handle extreme torque loads while minimizing overall system weight. Meanwhile, non-critical components, such as casings and structural supports, often incorporate lightweight composite materials to further reduce weight and enhance system durability without compromising structural integrity.

Beyond material selection, optimizing thermal and lubrication management plays a pivotal role in maintaining stability under heavy operational loads. High-performance lubricants minimize friction between moving parts, while advanced oil or air-cooled heat exchangers efficiently dissipate heat generated during operation. This prevents overheating, reduces the risk of wear, and ensures the long-term reliability of the system.

Split transmission designs, particularly those involving dual-turbine configurations, provide a robust solution to managing high energy and torque. These systems distribute loads across multiple power sources, alleviating stress on individual turbines, gearboxes, and shafts. By balancing energy dissipation, dual-turbine setups not only enhance redundancy and safety but also often achieve reduced overall system weight and size due to the optimized energy flow. When integrated with multi-stage gear designs, such as involute and planetary systems, these configurations further refine torque distribution, minimize power losses, and mitigate mechanical stress. Compact and efficient, these systems ensure that every component operates within its optimal performance range.

Managing vibrations and sudden torque fluctuations is equally critical for the resilience of helicopter transmission systems. Torsional dampers are strategically placed near drive shafts or main gears to absorb and mitigate vibrations that could propagate through the system, causing long-term damage. Similarly, sliding bearings and flexible couplings effectively cushion torque spikes, reducing mechanical stress and enhancing the longevity of the system.

A vital component of modern helicopter transmissions is the use of multi-disc clutches. Constructed from high-temperature-resistant materials like carbon-fiber-reinforced composites or ceramics, these clutches are designed to handle immense energy loads during operation. Their oil-cooling systems prevent overheating, while precise control systems ensure smooth engagement and disengagement of the clutch, reducing the risk of sudden torque shocks that could damage the system. This combination of durability, efficient cooling, and precision control significantly enhances system performance and reliability.

By integrating advanced materials, optimized thermal management, dual-turbine power distribution, multi-stage gear designs, vibration-damping mechanisms, and innovative clutch systems, modern helicopter transmission systems achieve the resilience, efficiency, and reliability required to operate under high-energy, high-torque conditions. These solutions collectively address the technical challenges associated with helicopter transmission design, ensuring safe and efficient operation in even the most demanding environments.

1.4 Motivation for Magnetic ECVT design

In the past four years, our research has focused on designing various variable-speed transmission systems for single main rotor helicopters. During the first two years, we developed an Offset Compound Gear (OCG) transmission system with two disk clutches connected by an OCG transmission. By shifting between a high-speed clutch and a lower-speed clutch, we created a two-speed transmission that could adapt to different helicopter flight scenarios, such as hovering, cruising, and forward flight.

Throughout the design process, we approached the system from multiple angles. We developed a minimum-size model for the OCG transmission gearbox and disk clutch system, performed system-level design, and optimized a two-speed OCG helicopter model. This work culminated in a comprehensive study of flight range performance and scaling.

However, the OCG transmission system faced several constraints. It was limited by various geometric factors, such as maximum shaft radius, clutch baseplate size, and the

axial length of the two clutches. To achieve maximum torque transmission without being compromised by frictional heat during the clutch engagement phase, we incorporated a wet disk clutch to minimize heat generation during shifts. Despite this, the main powertrain shaft temperature still increased, and analysis indicated that the disk clutch would wear quickly under multiple shifts, even at relatively low cruising speeds.
Another challenge arose from adding an extra transmission gearbox to the powertrain. The increased maximum torque required balancing the overall helicopter size and weight. To avoid a significant weight penalty—estimated at nearly triple the weight of a single-turbine engine powertrain with an OCG—we divided the power across two turbine engines.

The OCG transmission system, however, does not offer continuous speed variation. When shifting from high to low speed, the disk clutch disconnects from both clutches momentarily, causing a pulse torque adjustment that temporarily varies rotor speed. This rotor speed fluctuation could be unsafe during certain flight scenarios, and the drivetrain block experiences temperature increases due to clutch slipping. Nonetheless, the OCG transmission system demonstrated a substantial advantage. Our flight range performance results showed that variable-speed operation allowed the helicopter to achieve around 20% more nautical miles when operating at reduced main rotor RPM compared to a conventional single-speed main rotor helicopter.

Based on the discussion about both the advantages and disadvantages of the Offset Compound Gear (OCG) transmission system with two disk clutches, we conclude that implementing the OCG transmission system to achieve variable speed transmission in helicopter drivetrains significantly contributes to improved performance across different flight scenarios. This is particularly evident in the extended flight range and fuel economy savings during forward flight conditions. However, there remains room for improvement based on the performance simulation phase of the OCG transmission. For example, during the variable speed shifting phase, additional heat generation occurs due to disk clutch engagement. Additionally, sudden torque adjustments between power sources result in rapid speed changes in the downstream drivetrain. This phenomenon tests the material stability of the gearbox and shaft transmission system, potentially affecting their service life.

Given the known analysis and design results, the goal is to retain the advantages of variable speed transmission while mitigating its drawbacks. Specifically, efforts should focus on reducing thermal generation and minimizing the effects of sudden torque shifts. Meanwhile, the weight and size of additional components required for variable speed transmission remain critical factors for helicopter performance. Oversized or overly heavy components may improve forward flight performance but compromise performance during hovering or cruising scenarios. Exaggerating the weight or size penalty of additional gearbox components could affect the original design of the entire helicopter transmission system and potentially necessitate upgrades to the helicopter's turbine engines. Regardless of production difficulty or economic costs, designers often prioritize relatively simple component additions or structural optimizations to maintain balance in the original design. Furthermore, achieving a larger speed variation range is an essential goal for improving helicopter power transmission performance.

With electric transmission systems becoming increasingly powerful and controllable, a promising direction is to design a hybrid electric-mechanical transmission system for variable speed performance in helicopters. The key concept involves integrating a multiple-connection gearbox system with an electric motor/generator pair and an alternative control system for variable speed shifting. This approach introduces a power recirculation mechanism within the helicopter powertrain, offering a novel pathway to address the challenges associated with traditional variable speed transmission systems. In other words, this is a kind of hybrid electric transmission method which is used in hybrid electric vehicles (HEVs) to enable efficient energy conversion and management. However, the differences between hybrid electric vehicles (HEVs) and helicopter hybrid transmission system are high energy level and higher speed/torque integration method applications.

Theoretically, the hybrid electric vehicles (HEVs) applications for motor/generator operation are dependent on the working conditions, with motor mode driving or acceleration will convert the electrical energy stored in battery into mechanical energy to provide the energy for wheels acceleration and deliver higher torque for startup and efficiency for cruising. During generator mode (energy recovery), the motor/generator will operate as a generator convert the mechanical energy back to electrical energy (e.g., from deceleration or braking) and charge the battery through regenerative braking. To switch the hybrid electric vehicles (HEVs) motor/generator operating mode to helicopter transmission, the driving mode represents the lifting and hovering flight mode which mean the higher torque and speed transmit from engine and motor to make the propellers provide higher thrust force to lifting the helicopter. And for the generator mode the helicopter could keep the forward flight speed performance but reduce the propeller rotating speed which is like the deceleration and regenerative braking mode in hybrid electric vehicles (HEVs). Due to the higher torque demand in helicopter propellers this hybrid transmission is restricted to rotating at the higher torque level but lower speed to keep the steady flight performance after shifting to forward flight mode. And it's benefit we have known in hybrid electric vehicles (HEVs) attracted and drive us to implement those hybrid transmission technologies to helicopter transmission because of those similarities.

1.5 Problem Statement & Expected Contribution

The design of helicopter transmission systems requires special attention to their unique operational demands. Unlike transmission systems in cars, airplanes, or ships, helicopter transmissions must not only incorporate the advantages of these systems but also address the specific challenges of rotary-wing aircraft. Helicopters operate in dynamic and ever-changing environments, demanding transmission systems capable of handling significant variations in torque, speed, and load under harsh conditions. As a result, the design process involves not only applying advanced engineering principles but also developing complex and innovative transmission mechanisms. These systems are designed to ensure exceptional performance, reliability, and efficiency in scenarios where precision and adaptability are critical.

Compared to car transmission systems, one of the most apparent differences lies in engine power levels. According to [10]– [15], helicopter transmission systems handle engine power levels ranging from 300 hp to 5000 hp nearly ten times that of commonly used vehicles, whether powered by electric motors or turbine engines. This disparity leads to significant differences in the design and functionality of their respective transmission systems.

In variable-speed transmission systems for vehicles, conventional gasoline cars utilize manual or automatic clutch systems to achieve continuously variable speed transmission. In contrast, electric vehicles (EVs) rely on motors with a wide and efficient operating range. These motors deliver high torque at low speeds while maintaining stability at high speeds, enabling EVs to adjust speed directly by modulating the motor's operation rather than relying on multi-gear transmissions.

For helicopters, the high torque levels required for lifting and maneuvering make transmission torque optimization critical. The final speed of the propeller and the management of engine power play key roles in achieving optimal performance. Unlike cars, helicopter transmission systems must accommodate extremely high torque levels and operate under challenging conditions, such as heavy loads and vibrations generated by the rotors. Additionally, the complexity of helicopter operation and the emphasis on safety further distinguish their transmission systems from those in vehicles.

According to comparison of helicopter transmission systems to vehicles transmission systems in power level and torque transmission. The helicopter transmission always has multiple fix-speed transmission gearboxes to eliminate the vibration and noise that may be caused during the transmission process ensure the transmission stability. However, such a fixed-speed transmission often lacks the ability to provide variable rotor speeds. This constraint reduces operational flexibility and efficiency during different flight modes like hovering, cruising and forward flight. And those fixed transmission systems in helicopters will result in a limitation of optimizations for helicopters performances which lead to reduced flight range and fuel consumption.

As a result, the exceptionally high engine power, averaging around 2000 horsepower, and the high torque density of the transmission system impose substantial demands on maintaining precise transmission speed ratios in a fixed configuration. The immense heat generated during operation requires an advanced heat dissipation system to prevent material degradation and ensure component durability. Without effective thermal management, critical parts like gears and bearings can wear out rapidly, leading to mechanical failures, reduced energy efficiency, and potential safety risks. Addressing these challenges demands innovative cooling strategies and high-performance materials to balance reliability and safety under such extreme conditions.

1.5.1 Magnetic ECVT contributions

Over the past four years, our research has focused on the design and development of various variable-speed transmission systems for single main rotor helicopters. This exploration has been driven by the rapid advancements in continuous transmission technologies across diverse fields. The adoption of these technologies in industries such as electric and hybrid vehicles, wind energy generation, robotics, aerospace propulsion systems, and marine propulsion systems has provided us with a wealth of inspiration and technical insights. Magnetic transmission systems have emerged as a highly promising technology due to their unique operational principles and extensive advantages. These systems employ a contactless mechanism, which significantly reduces mechanical wear during operation. Unlike traditional mechanical systems that rely on direct contact, magnetic transmissions minimize frictional losses, leading to higher overall efficiency in variable-speed transmissions. This efficiency not only optimizes energy conversion processes but also contributes to more sustainable and cost-effective system performance. The lightweight nature of magnetic transmissions is another critical advantage, especially in aerospace applications. By replacing bulky mechanical components with compact magnetic systems, it becomes possible to enhance the performance and efficiency of propulsion systems. In helicopter transmission systems, where weight optimization is paramount, such advancements could lead to transformative improvements in overall design and functionality. Furthermore, magnetic transmissions inherently incorporate overload protection mechanisms. These mechanisms are essential for safeguarding components against damage caused by excessive torque or force, a common risk in demanding operational conditions.

Understanding these advantages and applying them to the theoretical and practical requirements of helicopter transmission systems has led us to explore the integration of magnetic transmission technology in this context. The insights gained from similar applications in other industries underscore the feasibility and potential of this approach. For instance, magnetic transmissions have demonstrated remarkable success in electric vehicles and hybrid systems, where they enable seamless energy conversion and contribute to prolonged system lifespans. Similarly, their application in wind turbines enhances energy generation efficiency by minimizing wear and maintenance requirements, while robotic machinery benefits from their precise and reliable torque transmission capabilities.

In the context of helicopter drivetrain systems, magnetic transmission technology offers several critical benefits. First, the contactless transmission mechanism not only enhances energy efficiency but also reduces wear and tear, leading to lower maintenance requirements and increased durability. This is particularly valuable in scenarios involving severe operational conditions, where traditional mechanical systems are prone to failure or degradation. Second, the lightweight design enabled by magnetic transmissions aligns with the industry's growing emphasis on weight reduction to improve flight performance and fuel efficiency. Finally, the built-in overload protection feature provides an additional layer of safety, preventing potential damage caused by sudden propeller malfunctions or other unexpected stresses.

Moreover, the advantages of magnetic transmissions extend beyond technical performance. Reduced wear results in lower noise and vibration levels, which not only enhances the operational environment but also contributes to the comfort and safety of the crew and passengers. These factors are crucial in the design and development of next-generation helicopter systems, where performance, reliability, and user experience are interdependent considerations. By integrating the principles of magnetic transmission technology into helicopter drivetrain systems, we aim to achieve a comprehensive performance enhancement that addresses the limitations of traditional mechanical transmissions. This approach not only opens new avenues for design innovation but also aligns with broader industry trends toward sustainable, efficient, and high-performing aerospace systems.

In conclusion, magnetic transmission technology represents a paradigm shift in the design of variable-speed transmission systems for helicopters. Its unique combination of contactless operation, high efficiency, lightweight construction, and overload protection offers a compelling solution to the challenges of modern helicopter systems. By leveraging these advantages, we envision a future where helicopters achieve unprecedented levels of performance, reliability, and operational efficiency.

Magnetic electric variable speed transmission is an innovative transmission concept that combines magnetic and electric principle to achieve variable-speed operation. It is designed to provide efficient and seamless torque transmission while reducing mechanical wear and improving the reliability in helicopter transmission system. The core concept of magnetic transmission is to use magnetic gear transmission to replace mechanical gearbox systems and integrate those magnetic transmission components with motor/generator system and implement all to helicopter drivetrain system. In mechanical gear transmission, its operation principle is simple to understand the teeth in gear contact and engage with other gear teeth and then when you rotate any of gears connect by shafts or other rotate components the mechanical power transmits from one gear teeth to the other teeth. Basically, because of the contact between teeth of gears their transmission capacity is limited by the teeth material properties like tensile strength, yield strength, hardness and elastic modulus. If applied force or torque is larger than the capacity of the gear teeth will result in wear and fatigue resistance through surface modifications. And there are two typical gear teeth that fail through primary modes: bending fatigue at the tooth root and contact fatigue at the tooth flank. Bending fatigue occurs due to cyclic stresses concentrated at the root, leading to crack initiation and eventual tooth fracture after repeated load cycles. Contact fatigue arises from stresses at the contact area between teeth flanks, causing surface or subsurface crack nucleation. Over time, these cracks propagate, resulting in material removal through pitting (small cavities) or spalling (deeper flaking). Both failure modes are influenced by material properties, stress concentrations, lubrication, and load conditions, highlighting the importance of proper design, materials, and maintenance to prevent gear failure [16]. Back to the physical principle of gear transmission, it's a force or torque transmission, mechanical gears are transmitting the force by teeth contact then the resistance of material obtain force or motion energy from one side of gear teeth and then transmitted to the teeth on the other side through contact. Compared to mechanical gear transmissions the magnetic gear transmissions are slightly different, the teeth in mechanical gears are replaced by permanent magnets or other components which could generate magnetic field (e.g., electric magnets), and the magnet will generate a permanent magnetic field, the term magnetic field denotes a property of space, so that the field quantity has a numerical value at each point of space. These values may also vary with time. The value of the electric or magnetic field is a vector—i.e., a quantity having both magnitude and direction. The value of the electric field at a point in space, for example, equals the force that would be exerted on a unit charge at that position in space [17]. Then the input magnetic gear rotor generates a rotating magnetic field as its turns and the rotating field will interact with modulation layers creating a time varying magnetic field that align with magnetic pattern of output rotors or other magnetic field generate from output side of magnets. And the torque can be transferred magnetically vis the interaction of attractive and repulsive forces between the aligned poles of input and output rotors [90],[91]. So, the most of the mechanical gear types can be replicated as magnetic gear by simply replacing the metal gear teeth by alternating magnetic poles of permanent magnets (PMs) or electric magnets. When a magnetic gear rotates, its magnetic poles exert a force on the poles present in the other rotor transmitting a magnetic torque via the air gap, causing this rotor to rotate simultaneously. Hence, power is transmitted without physical contact through a magnetic flux in the air gap [92],[93].

CHAPTER TWO
LITERATURE REVIEW

Rotorcraft propulsion plays a crucial role in overall aircraft performance. Unlike fixed-wing aircraft, where propulsion primarily generates thrust, rotorcraft rely on their rotor and propulsion systems for lift, control, and forward thrust. Consequently, rotorcraft engines and gearbox systems must be highly reliable and efficient. As future rotorcraft designs demand greater versatility, efficiency, and power, advancements in propulsion system technologies become increasingly necessary.

Variable-speed rotors have been recognized as a key factor in addressing critical rotorcraft challenges. Currently, rotor speed adjustments are limited to a small range: typically, around 15% due to constraints in engine efficiency and stall margins. The recent NASA Heavy Lift Study [18] identified variable-speed propulsion as essential across all studied aircraft concepts. Maintaining efficiency and torque while varying rotor speed is crucial for enabling high-speed operation with reduced noise.

Previous NASA studies on variable-speed transmissions focused on 15% speed variations [19][20]. However, the NASA Heavy Lift Study [18] suggests that expanding this range to 50% could significantly enhance rotorcraft performance while reducing external noise. Achieving such a wide speed variation requires the development of advanced variable or multispeed drive system concepts. This report explores potential configurations for both two-speed and variable-speed drive transmissions to meet these evolving demands.

2.1 Diversity variable speed transmission and limitations in helicopter

To achieve variable speed at the rotor stage, a comprehensive approach is required, focusing on both external maneuver control and the internal design of the powertrain system. This involves optimizing control inputs to dynamically adjust rotor speed based on flight conditions while simultaneously refining the mechanical and aerodynamic properties of the drivetrain to ensure efficient power transmission. These methods can be broadly categorized into the following approaches:

1. Blade Pitch Control (Fig.2.2 Collective, Cyclic & Differential Collective)

- **Collective Pitch Control:** Controls the lift of the rotor by changing the overall angle of attack (pitch) of the rotor blades (**Fig.2.1**), thereby affecting the overall flight altitude and speed. Increasing the pitch increases lift, causing the helicopter to rise; reducing the pitch decreases lift, causing the helicopter to descend.
- **Cyclic Pitch Control:** Adjusts the angle of attack of each rotor blade during its rotation cycle, thereby controlling forward, backward, left, and right movement of the helicopter. Cyclic pitch control affects the asymmetric lift of the blades as they rotate, thus changing the flight direction and speed of the helicopter.
- **Differential Collective Pitch:** Varies collective pitch asymmetrically across the rotor system, primarily in multi-rotor helicopters (e.g., coaxial, tandem, or intermeshing designs). It aids in controlling yaw, roll, and differential thrust between rotor systems while optimizing lift and thrust distribution, enhancing acceleration and forward flight efficiency.

However, all above blade-control methods have limitations in controlling helicopter speed stem from aerodynamic constraints, power availability, and mechanical complexity. Collective pitch, while essential for vertical movement, increases induced drag as pitch angle rises, limiting forward speed and placing higher power demands on the engine. Excessive collective input can also lead to retreating blade stalls and vortex ring state, affecting stability. Cyclic pitch controls forward motion by tilting the rotor disk, but at high speeds, it introduces dissymmetry of lift, requiring blade flapping to compensate. However, excessive flapping reduces control effectiveness, causes vibrations, and contributes to retreating blade stalls, which ultimately limits speed. Meanwhile, differential collective pitches, used in multi-rotor configurations like coaxial or tandem helicopters, allows for efficient lift distribution but comes with added mechanical complexity, increased power management challenges, and potential yaw instability at high speeds. Even with optimized pitch control, helicopters face inherent speed limitations due to retreating blade stalls, compressibility effects on advancing blades, and finite engine power. These constraints prevent helicopters from

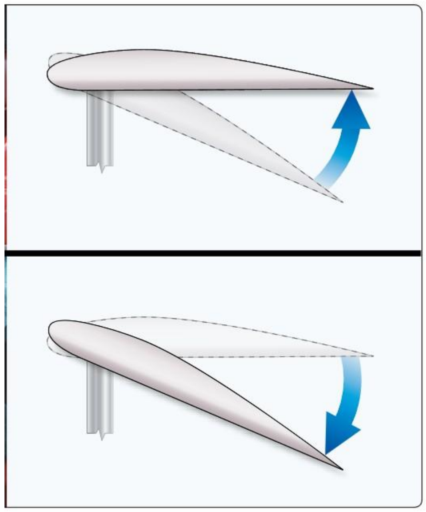

Fig. 2.1. Pitch angle control.

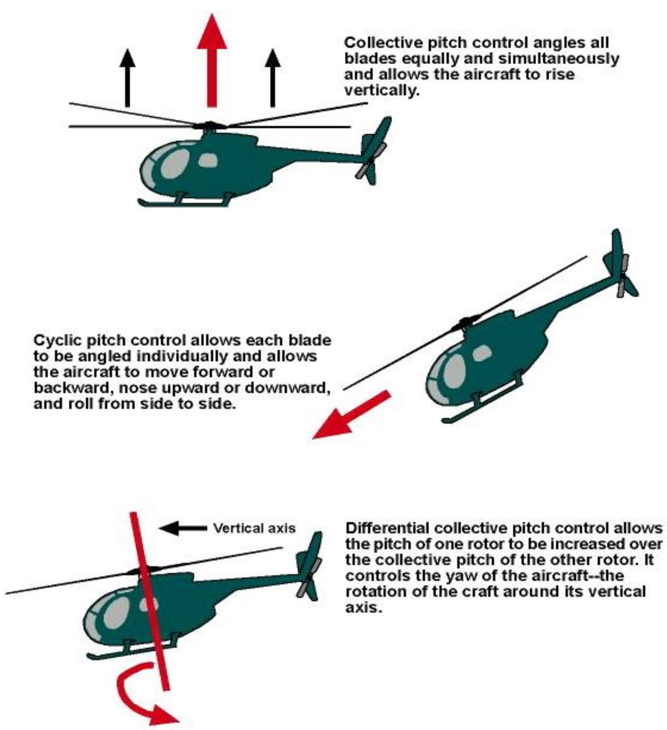

Fig. 2.2. Three different types of Pitch Control: collective pitch, cyclic pitch, and differential pitch control.

reaching fixed-wing aircraft speeds, requiring alternative designs such as compound helicopters and tiltrotors to push speed boundaries.

2. Engine Power Regulation

The rotor speed is adjusted by regulating the engine's output power. Increasing engine power increases rotor speed, which in turn enhances lift and forward speed. Conversely, reducing engine power decreases rotor speed and flight speed. However, there are some limitations shown in [21], the engine power output always has lag due to the power-matching relationship between engine and rotor, because if you want to have a more power engine the rotor will increase simultaneously. Therefore, when the helicopter requires a sudden increase in power the turboshaft engine cannot instantly deliver the needed torque which will result in a torque response time increase leading to a reduced maneuverability. Meanwhile, the longer response time will affect the altitude stability for rotor thrust adjustment.

Also, the turboshaft engine in a helicopter experiences significant heat buildup in the gas turbine, power turbine, and compressor due to continuous power demands, leading to thermal stress on critical components.

3. Variable Speed Gearbox Clutch System

A variable-speed clutch system can provide different rotor speeds by shifting the gearbox ratio. This method allows the helicopter rotor to maintain 100% power flow from the main engine. In different flight scenarios, the clutch system will synchronize to the required gear ratio gear set. During hovering and lifting phase, helicopters need as much as possible power flow from turbo engines, the clutch will connect with a one-to-one gearbox transmission line to deliver full power to final rotor blade. For the cruising phase, rotor speed can be reduced by shifting the output shaft to a lower-ratio gearbox. From the turbo engine energy aspect, the power still full transmit to the next stage which just changes the speed and torque by gearbox ratio simultaneously. Therefore, the final rotor will generate more torque than high speed mode which is not necessarily for helicopter flight performance.

Additionally, wet disk clutches, commonly used in transmission systems, generate excess heat due to slipping, particularly during shifts between flight modes. This accumulation of heat can result in torque fluctuations, degrading flight stability and making precise control more challenging. Elevated temperatures also affect material properties, accelerating wear and reducing the lifespan of key engine and transmission components. If not properly managed, excessive heat can decrease rotor efficiency, forcing the engine to supply additional power to compensate for losses, which in turn exacerbates thermal stress and reduces overall system reliability.

4. Tail Rotor Control

The tail rotor provides lateral thrust to counteract the torque generated by the main rotor. Additionally, the variable pitch control of the tail rotor can affect the turning speed and stability of the helicopter. Different maneuvering controls can be achieved by adjusting the angle and speed of the tail rotor.

However, by maneuvering the blade to achieve rotor angle control, the speed variation can still be limited to a small range of approximately -10% to 10% under different flight speed mode conditions, which increases the potential for a margin stall phenomenon. Additionally, blade pitch control requires an additional engine power control system to compensate for blade angle variation, as changes in blade angles lead to a rebalance of thrust, lift, and drag forces. Therefore, a variable output power turbine engine is necessary to maintain the rotor speed within the desired operational range. Thus, blade pitch control could only serve as an auxiliary maneuvering system for variable-speed rotors, working in conjunction with other methods capable of altering powertrain rotation speed.

2.2 Gearbox-Based Transmission Systems

A gearbox transmission is a mechanical system designed to regulate power transmission from an engine or motor to the driven machinery, enabling precise control over speed and torque. It accomplishes this by utilizing a series of gears with different ratios that adjust the rotational speed and force applied to the output shaft. By engaging specific gear combinations, the transmission allows for efficient adaptation to varying load conditions, optimizing performance, fuel efficiency, and mechanical durability. The design of a gearbox can range from simple manual gear systems to complex automated or continuously variable transmissions (CVTs), each tailored to specific operational needs. Key factors influencing gearbox performance include gear material, lubrication, thermal management, and overall mechanical design to minimize energy losses and wear.

2.2.1 Two-speed and multi-speed clutch transmission

1. Dynamics and Operation of Two-Speed Transmission Concepts

A two-speed clutch transmission is a system that enables a vehicle or machinery to switch between two distinct speed ratios using clutches. It is commonly used in applications where variable speeds are required to optimize efficiency, performance, and fuel consumption. With one or two input power resources from turbo engines, motors, output to the next stage drivetrain or load, two sets of gearboxes provide different gear ratios and two clutches by engage or disengage to connect the specific gear set to achieve two speed variations.

The Glenn Research Center (GRC) designed and fabricated a gearbox for use on the NASA Chariot vehicle shown in [29], the power and drivetrain system is assembled by couple of motor/gearboxes, then pass speed and torque through a steering gearbox and different gearbox and final to each wheel. The concept figure of GRC Chariot gearbox is shown in **Fig. 2.3**. To achieve a two-speed variation this gearbox is designed to be a two-stage, two speed gearbox. The input power resource is two brushless electric servo motors connected by pinion (Gear 1 **Fig. 2.3**). There is a reduction stage including the pinion gear drives a bull gear (Gear 2) to get a 3.94:1 speed reduction. Gear 2 then

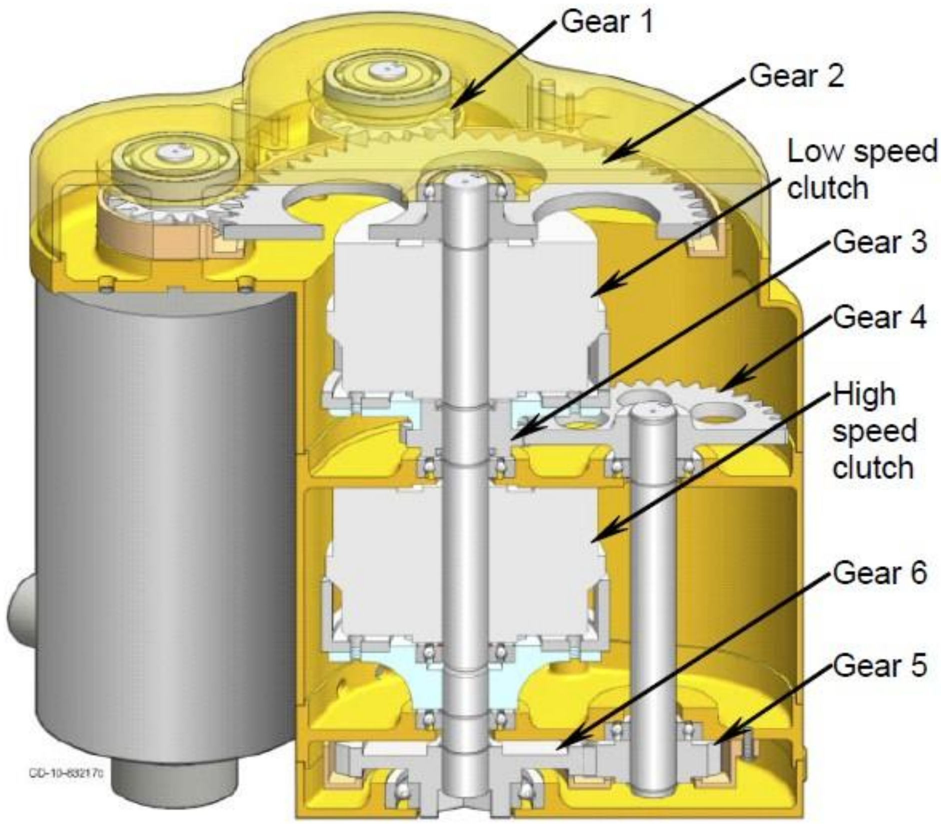

Fig. 2.3. NASA Glenn Research Center Chariot gearbox design.

transfers power to two concentric, electromagnetically actuated (EMA) multi-disk clutches.

For low-speed operation, the top clutch (low-speed clutch) is engaged while the bottom clutch (high-speed clutch) remains disengaged. The output from the low-speed clutch is transmitted through two sets of spur gears (Gears 3, 4, 5, and 6), further reducing the speed by 16.14:1.

For high-speed operation, the bottom clutch (high-speed clutch) is engaged, and the top clutch (low-speed clutch) is disengaged. In this configuration, the output from the bull gear (Gear 2) bypasses the additional spur gears and exits the gearbox directly, maintaining a 3.94:1 speed reduction [29]. During high-speed engagement, Gears 3 through 6 freewheels without transmitting any load. A disk clutch is a conventional transmission system that operates based on the principle of friction [28]. Among various clutch types, the friction disk clutch has been the most widely used for an extended period. It primarily consists of four components: the driving part, the driving part, the pressing mechanism, and the operating mechanism. The driving and driven parts, along with the pressing mechanism, form the core structure that ensures the clutch remains engaged and effectively transmits power. Meanwhile, the operating mechanism is responsible for disengaging the clutch when necessary.

The system functions by utilizing mechanical friction between contact surfaces to transfer torque from the driving shaft to the driven shaft shown in **Fig.2.4**, enabling the engagement or disengagement of the driven shaft based on operational requirements [22]. Due to its structurally stable design and the high strength of its materials, a disk clutch system can achieve a highly efficient transmission ratio when sufficient pressure is applied to the friction surface. This results in a high-power density, allowing it to transmit substantial energy by efficiently transferring torque [23-27].

As a result, disk clutch systems are widely used in single-engine and parallel transmission units equipped with high-power, medium-speed diesel engines. These characteristics make disk clutches particularly well-suited for helicopter transmission systems, where they serve as a reliable solution for clutching mechanisms.

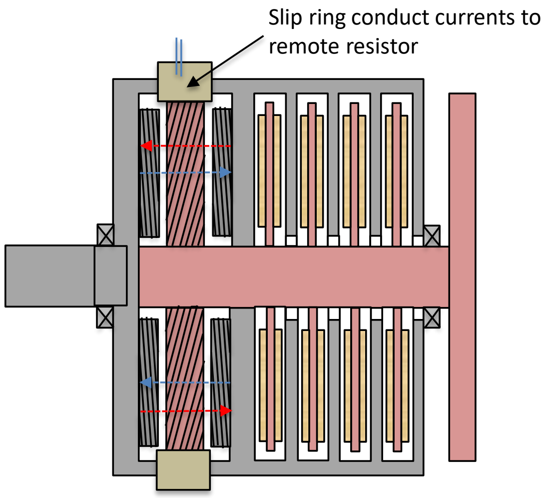

Fig. 2.4. Schematic of a multi-disc clutch.

2.2.2 Dynamics and Operation of Variable-Speed Transmission Concepts

Continuously Variable Transmissions (CVTs) are a type of automatic transmission that provides a seamless range of gear ratios rather than fixed gear steps like traditional manual or automatic transmissions. CVTs are commonly used in scooters, motorcycles, and some cars due to their ability to optimize engine performance and fuel efficiency. In [2], They mentioned and discussed the existing Continuously Variable-Speed Transmission (CVT) gear design and the future development direction of CVT. They primary discuss the Belt Continuously Variable-Speed Transmission (CVT) and Planetary Continuously Variable-Speed Transmission.

A Belt Continuously Variable Transmission (CVT) is a type of automatic transmission that provides seamless and infinite gear ratio adjustments by using a controllable variable-diameter pulley system with flexible belts or chains shown in **Fig. 2.5.a**). Unlike traditional transmissions with fixed gears, a belt CVT consists of two pulleys—one connected to the engine and the other to the drivetrain (driven pulley). Each pulley is made of two conical halves that can move closer together or farther apart, changing the belt's position and effectively altering the transmission ratio. When the drive pulley-

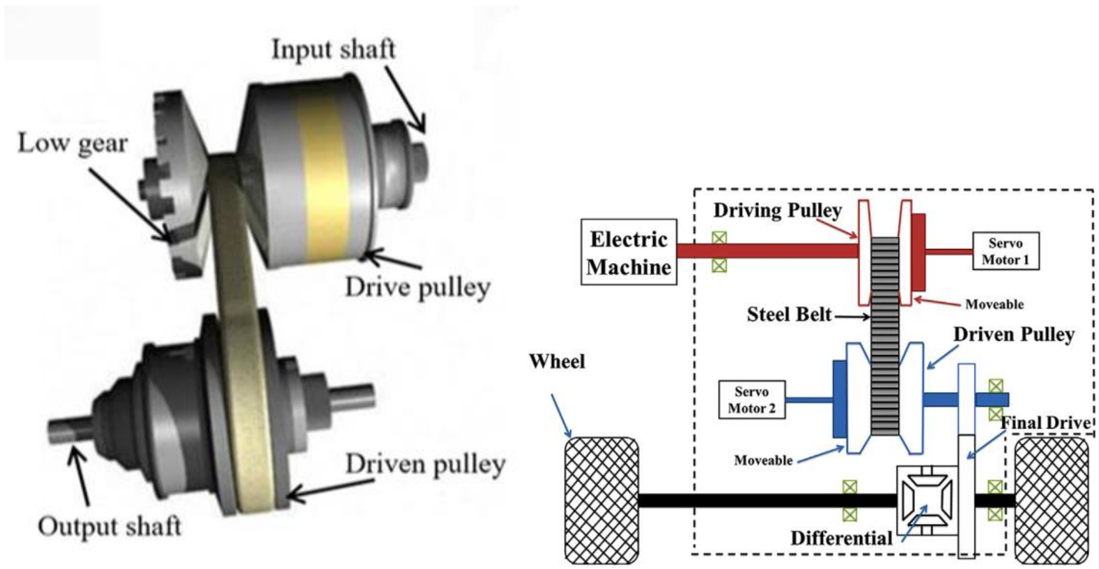

Fig. 2.5 a) Belt Continuously Variable Transmission & b) Schematic of motor-assisted CVT

narrows, the belt moves outward, increasing its effective diameter and creating a higher gear ratio. Conversely, when the drive pulley widens, the belt moves inward, reducing the ratio for lower speed operation.

The Planetary Continuously Variable-Speed Transmission (PCVT) is a type of CVT that integrates a planetary gear system with a continuously variable mechanism, offering a unique combination of efficiency, durability, and smooth power delivery. Unlike conventional belt-driven CVTs, the PCVT utilizes a planetary gear train to distribute torque between different paths, allowing for stepless speed variation while maintaining mechanical robustness. The system shown in **Fig. 2.6** typically consists of a sun gear, planet gears, and a ring gear, with a variable-speed control mechanism, such as a hydraulic pump or an electric motor, adjusting the relative speeds of these components. By dynamically controlling the power split, a PCVT can optimize engine performance across a wide range of operating conditions, providing improved fuel efficiency and better load adaptability. This design is commonly found in hybrid vehicles, heavy-duty machinery, and certain advanced automotive applications, where it enhances power management and extends transmission longevity compared to traditional CVTs.

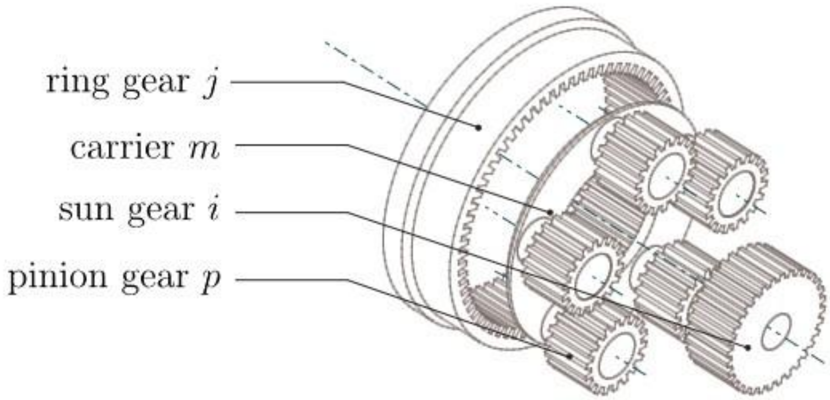

Fig. 2.6. planetary gearbox with ring, sun, pinion gear and carrier

Additionally, the planetary structure reduces the stress on individual components, improving overall reliability and allowing for higher torque transmission without excessive wear.

2.2.3 Variable Speed Transmission Summary

Engine power regulation is a good alternative method for variable speed transmission, as it addresses the problem at its source. The variable speed engine of a helicopter optimizes performance and efficiency by adjusting engine speed, but there are some limitations and drawbacks in practical applications. First, the variable speed engine has a slow response time during flight, making it difficult to immediately adapt to the pilot's inputs, which affects the precision and overall stability of the control. Second, the complex mechanical and control systems increase potential failure points, resulting in higher maintenance costs and longer downtime.

Although the variable speed engine can improve fuel efficiency under specific operating conditions, frequent speed changes lead to increased transmission losses, where traditional fixed-speed engines may offer more advantages during critical flight phases, such as takeoff and hovering. Additionally, the extra components of a variable speed engine increase the system's weight and space requirements, impacting on the helicopter's payload and fuel capacity. The introduction of a variable speed engine also necessitates that pilots learn and adapt to new control strategies, raising the demands on pilot skills and training. Moreover, the design, manufacturing, and maintenance of variable speed engines are more complex and expensive, requiring high-precision components and intricate software controls. This complexity leads to higher manufacturing and maintenance costs. Although variable speed engines offer potential improvements in efficiency and flexibility, their limitations include slow response times, increased complexity, reduced efficiency stability, additional weight, higher control difficulty, and elevated costs.

According to NASA's report [1], due to limitations in engine efficiency and stall margin, engine speed variation is limited to a maximum of approximately 15 percent. However, the NASA Heavy Lift Study [3] indicates that increasing the speed variation from 15 percent to 50 percent could significantly reduce external noise while enhancing rotorcraft performance.

Based on the discussion above, we consider that a continuously variable speed gearbox system is a more effective method for achieving a continuously variable speed rotor.

Over the past decade, there have been numerous investigations into variable ratio gear transmissions for rotorcraft and other applications, such as wind turbines and automotive drivetrains [4]-[8].

For helicopter transmission systems, both two-speed transmissions and traction-drive Continuously Variable Transmissions (CVT) concepts, based on Split Torque Differential Planetary arrangements, have been explored in studies [4]-[6]. Additionally, NASA has initiated a research project focused on the Pericyclic CVT (P-CVT), which has shown very promising results [9]. The P-CVT is a new type of non-friction, positive meshing transmission system that achieves stepless speed changes through rollers and cams. It offers higher torque density and power transmission efficiency compared to other known continuously variable mechanical transmission systems. While this CVT has been proposed for use in helicopter transmission systems, further research is needed due to the requirement of dual power input to achieve speed changes.

Some studies have suggested using a multi-speed gearbox instead of a CVT to achieve speed changes through controlled clutching and shifting mechanisms. For example, NASA's research mentions a sequential shift control algorithm that smoothly adjusts the main rotor speed by coordinating the disengagement and engagement of dual engines. Although this system is not a traditional CVT, it provides a certain degree of speed control. One example is the dual-speed clutch system featuring an Offset Compound Gear (OCG) Inline Two-Speed Drive Transmission System [94],[96]. This two-speed transmission, which includes an input shaft and an output shaft, is capable of transitioning between fixed ratios, with the high-range ratio being a direct 1:1 and the low-range ratio approximately 2:1. The transmission is a simple, lightweight, yet robust configuration utilizing only two gear meshes, consisting of an input gear, a cluster gear, and an output gear [93],[95]. The transmission is controlled through a clutch and a sprag, with the input and output shafts rotating in the same direction.

There are also newer and less well-researched Magnetic Gear Transmission systems and Hybrid Electric Continuously Variable Speed Transmissions (ECVT). Magnetic gears transmit torque through a magnetic field rather than physical contact, making them suitable for applications with high requirements for weight, vibration, and reliability, such as helicopters. They reduce friction and wear, extend gear life, and minimize the need for lubrication. Magnetic gears also provide high torque density in a small volume, making them ideal for reducing helicopter transmission weight. Additionally, they significantly reduce vibration and noise since there are no meshing gears, enhancing passenger comfort and reducing environmental noise. Magnetic gears also have an inherent "slip" feature that prevents damage in case of overload, enhancing system safety. However, they face challenges such as manufacturing complexity, high magnet costs, and operating temperature limits.

Electric Continuously Variable Transmission (E-CVT) is a hybrid transmission system that combines electric motors with traditional mechanical transmissions to improve power flexibility and fuel efficiency. In helicopters, E-CVT uses electric motors and generators to enable seamless power switching and adjust transmission ratios electronically rather than mechanically. This allows continuous speed control by converting part of the engine power to electricity, which provides additional torque when needed. E-CVT can reduce fuel consumption, with studies indicating up to an 18% reduction, particularly during cruise phases. It also provides flexible speed control for switching between different flight modes and helps optimize system weight by reducing the complexity of traditional transmissions. Despite its potential, E-CVT is complex to integrate and presents power management challenges, especially during different flight phases. Currently, E-CVT systems are still in the experimental stage but have promising potential for making helicopter systems more efficient and environmentally friendly.

2.3 Magnetic Gear Transmission

Magnetic gears (MGs) use magnetic forces to transmit torque, eliminating the need for physical contact between gear teeth. This contactless power transmission method relies on permanent magnets or electromagnets arranged in specific configurations to ensure smooth, silent, and maintenance-free operation. Unlike conventional mechanical gears, which rely on direct meshing of teeth, magnetic gears achieve motion transfer through controlled magnetic interactions.

The concept of magnetic gears dates back to 1901 when Armstrong designed an electromagnetic spur gear [29]. Early developments primarily focused on spur-type [29-32] and worm-type [32-33] topologies. Initially, these gears were designed as direct replacements for conventional mechanical gears but were gradually improved with structural modifications, as shown in **Fig. 2.7.** In recent years, advancements in high-energy-density permanent magnets and the emergence of new gear topologies have significantly enhanced the performance of MGs, allowing them to compete with traditional mechanical gears in torque density. Among the most notable modern MG topologies are concentric, harmonic, and planetary magnetic gears, as illustrated in **Fig. 2.8.**

The fundamental principle of magnetic gear transmission is based on magnetic field modulation, where ferromagnetic pole pieces act as intermediaries to convert input torque into amplified output torque. Unlike mechanical gears that transmit force through

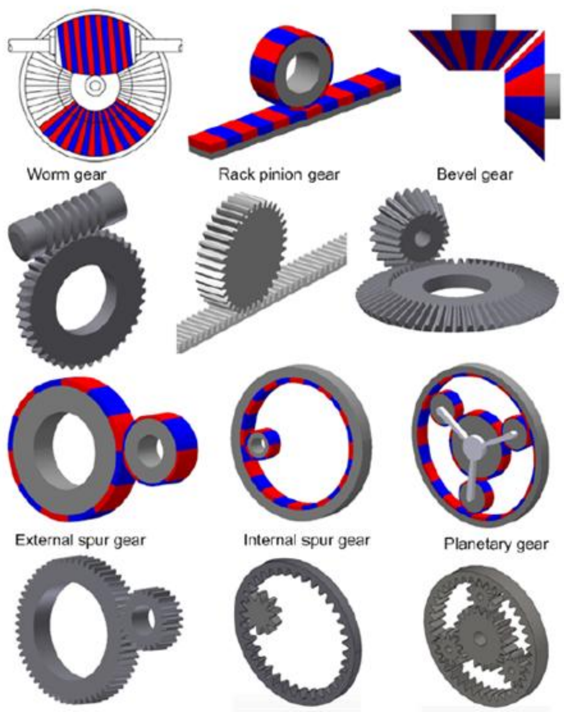

Fig. 2.7. Early mechanical and magnetic gear comparison.

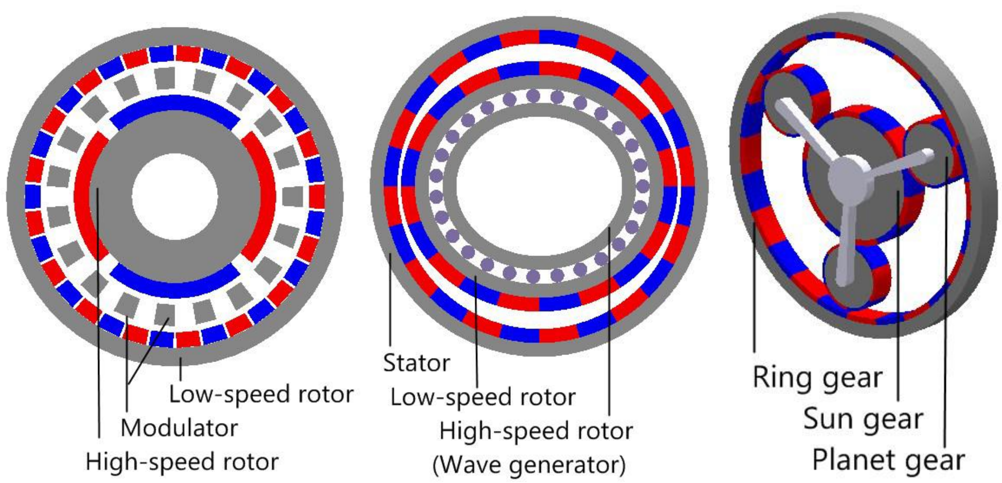

Fig. 2.8. a) Concentric, b) harmonic, and c) planetary magnetic gears

physical meshing, magnetic gears operate by leveraging controlled magnetic attraction and repulsion. This allows for efficient torque conversion while minimizing mechanical losses and wear. Magnetic gears offer several advantages over their mechanical counterparts. Since there is no physical contact between components, they require little to no maintenance, eliminating the need for lubrication or frequent replacements. Additionally, they provide built-in overload protection, as excessive torque simply results in slip rather than mechanical damage.

The absence of direct contact also enables hermetically sealed designs, making MGs ideal for applications in industries such as chemical processing, food production, and aerospace, where contamination must be avoided. Furthermore, modern magnetic gear designs achieve torque densities comparable to, and sometimes even exceeding, those of mechanical gears.

The key advantages of magnetic gears over traditional mechanical gears transmission include:

- **Reduced Maintenance**: No physical wear means no need for lubrication or frequent replacements.
- **Overload Protection**: If excessive torque is applied, the magnetic coupling can slip without damaging the system.
- **Isolation of Components**: Magnetic gears allow for hermetically sealed designs, making them ideal for applications in chemical, food, and aerospace industries where contamination must be avoided.
- **High Torque Density**: Modern magnetic gear designs achieve torque densities comparable to, and sometimes exceeding, mechanical gears.

Magnetic gear transmission presents an innovative solution for torque and speed conversion, addressing many of the limitations associated with conventional mechanical gears. By eliminating friction, wear, and lubrication requirements, MGs offer a reliable and efficient alternative, particularly in variable-speed transmission systems where precision and durability are essential.

2.3.1 Different Types of Magnetic Gears Structure

Magnetic gear systems are modeled after conventional gear transmissions and have been developed in various configurations to meet specific gear ratio requirements, accommodate spatial constraints, and handle varying load capacities. Based on the structure shown in **Fig. 2.7** [35] and the principles of force transmission, magnetic gears can be categorized into two main types: analogous mechanical transmission magnetic gears, which directly replace mechanical gear teeth with permanent magnets, and mechanical derived magnetic gears,
which employ alternative gear structures while maintaining similar transmission principles. Additionally, magnetic gears can be classified by the method of magnetic force generation into two types: permanent magnet gears, which rely on fixed permanent magnets, and electromagnetic gears, which use electrically energized coils to generate magnetic fields.

When evaluating various magnetic and mechanical gear types, torque density serves as a key performance metric for transmission systems. As shown in **Table 2.1** [36], and considering the demands of practical gearbox applications, certain magnetic gear configurations exhibit torque densities that are comparable to or exceed those of conventional mechanical gears. Specifically, magnetic harmonic gears, magnetic planetary gears, and concentric magnetic gears demonstrate relatively high torque density and are used in a variety of operating conditions.

According to our future research and design combine magnetic gear with variable speed transmission driveline. There is another way to distinguish different type of high torque densities mechanical derived magnetic gears:

1. Radial-Flux Magnetic Gear

Radial-flux magnetic gears typically use a radial magnetic flux path to transmit torque between the input and output shafts without physical contact, relying solely on magnetic fields. Their basic structure typically consisted of inner rotor, outer rotor and modulators. The inner rotor is equipped with an array of permanent magnets arranged either in an alternating polarity configuration (i.e., sequential north and south poles) or with

Table 2.1. Torque density of different gears [36].

Gear Type	Torque density (kNm/m^3)
Mechanical spur gear [30]	100-200
Mechanical helical gear(3G)	50-150
Magnetic worm gear [9]	<2
Magnetic bevel gear	<5
Magnetic spur gear	10-20
Magnetic harmonic gear(1G)	140-180
Magnetic harmonic gear(2G)	75
Magnetic planetary gear [26]	≈ 100
Concentric magnetic gear	70-150

unidirectional magnetization distributed circumferentially. Correspondingly, the outer rotor contains permanent magnets arranged in either a matching alternating polarity or in a unidirectional configuration with magnetization opposite to that of the inner rotor. In most implementations, the outer rotor counter-rotates relative to the inner rotor to achieve effective torque transmission.

In radial-flux magnetic gears employing alternating polarity magnet arrays, a modulator is typically integrated between the rotors. This modulator is composed of ferromagnetic segments or soft magnetic materials, which function to spatially modulate the air-gap magnetic field. This modulation introduces spatial harmonics that facilitate non-contact magnetic coupling between the inner and outer rotors, enabling efficient torque transmission without mechanical contact.

Based on their internal configurations, radial-flux magnetic gears can be broadly classified into two categories: those with modulators and those without modulators, as illustrated in **Fig. 2.8**, which shows typical examples such as concentric and harmonic magnetic gears. The presence of modulators usually composed of ferromagnetic or soft magnetic segments plays a crucial role in shaping the air-gap magnetic field distribution between the inner and outer permanent magnet (PM) rotors. This modulation enables the interaction of spatial magnetic harmonics, allowing for non-contact torque transmission. Due to the field modulation mechanism, the transmission ratio between the inner and outer PM rotors can be tailored by selecting appropriate numbers of pole pairs and modulator segments. In certain configurations, multiple modulators may be introduced to achieve alternative or adjustable gear ratios, offering design flexibility for specific torque and speed requirements.

2. Axial-Flux Magnetic Gear

An Axial Flux Magnetic Gear (AFMG) is a state-of-the-art, contactless power transmission system that utilizes modulated magnetic fields to enable torque conversion between two axially aligned rotors—one high-speed and one low-speed. Unlike conventional mechanical gears, the AFMG transmits torque without any physical contact, relying entirely on magnetic coupling. This results in a highly efficient, low-noise, and virtually maintenance-free operation, ideal for advanced applications where reliability and performance are critical.

The system is composed of three key components: a high-speed rotor, a low-speed rotor, and a modulation ring. Both rotors are embedded with high-performance permanent magnets arranged in alternating polarities. The modulation ring, positioned between the two rotors, consists of ferromagnetic segments that spatially distort and harmonize the magnetic fields [38]. This modulation enables the magnetic fields of the two rotors to couple in a synchronized fashion, thus transferring torque across different rotational speeds. The gear ratio is defined by the number of magnetic pole pairs on each rotor and follows the relationship $G = -\frac{p_{high}}{p_{low}}$, where p refers to the number of pole pairs. As demonstrated in [37], an Axial Flux Magnetic Gear (AFMG) was designed and tested with a gear ratio of 30:1, specifically for application in wind turbine generator systems. This configuration achieved a notably high torque density of approximately 91 $N \cdot M/L$. The combination of such a high gear ratio and substantial torque density makes this type of AFMG particularly attractive—not only for renewable energy systems but also for aerospace applications where compactness, weight efficiency, and high torque performance are critical.

One of the key advantages of axial flux magnetic gears is their non-contact nature, which eliminates friction, reduces mechanical wear, and significantly lowers maintenance requirements. In overload conditions, the system naturally slips due to magnetic saturation, providing inherent torque protection without damaging components. Additionally, the axial topology offers a flat, compact form factor, making it highly suitable for applications with tight axial space constraints. The magnetic coupling is also completely backlash-free, allowing for precise and smooth motion control.

AFMGs are increasingly used in next-generation systems across various industries. In aerospace and unmanned aerial vehicles, they offer high torque density and lightweight performance [37]. In electric mobility, especially in-wheel motors for electric vehicles, they allow for compact and efficient powertrains. Wind turbines benefit from their ability to handle variable-speed inputs with minimal maintenance, and robotics take advantage of the precise, responsive torque transmission for delicate and accurate motion control.

3. linear magnetic gear

Linear magnetic gears (LMGs) present an innovative solution for linear motion applications, offering a contactless alternative to traditional mechanical gears. By coupling magnetic fields instead of physical components, LMGs enable high efficiency, reliability, and inherent overload protection, making them especially attractive for safety-critical applications [39]. As shown in **Fig. 2.9** Linear magnetic gear consists of three magnetic coaxial armatures: Inner rotor with high speed, out rotor with low-speed high torque stick with permanent magnet inside and field-modulation ferromagnetic rings. And its gear ratio is defined by the number of pole-pairs on the high-speed and low-speed armatures and the number of pole-pieces. Importantly, the configuration enables torque (or thrust, in the linear case) transmission without mechanical contact, and any overload leads to a harmless slip. A study in [40] introduced an innovative solution for wave energy harvesting by integrating Linear Magnetic Gears (LMGs) into a Permanent Direct Drive (PDD) system. Traditional generators struggle with the slow and irregular reciprocating motion of ocean waves, but this design overcomes that limitation by cascading an LMG with a linear permanent magnet (PM) generator. The system shares a high-speed mover between the gear and the generator through a common shaft, enabling efficient mechanical coupling. Additionally, a tubular structure is used to improve thrust force, enhance space efficiency, and minimize magnetic flux leakage [41].

Linear magnetic gears are maturing from theoretical concepts to practical innovations. When integrated into pseudo-direct-drive systems, they offer a unique bridge between low-speed natural energy sources and high-speed electrical generation needs. Future work should continue optimizing manufacturing precision, enhancing model accuracy under nonlinear conditions, and exploring other applications beyond wave energy, such as electric vehicles, robotics, or biomedical devices.

2.4 Motor/Generator integrated Permanent Magnet Gear

A Motor-Integrated Permanent Magnet Gear (MIPMG), as the name suggests shown in **Fig. 2.10**, combines a motor and a magnetic gear into a single unit to achieve higher torque transmission than conventional electric motors without mechanical gears. Based-on the structural prototypes of permanent magnet motors and magnetic gears, MIPMGs can adopt either axial or coaxial magnetic flux configurations. These configurations enable the integration of the motor and magnetic gear, aiming to deliver higher torque, smooth motion, and contactless direct transmission from the motor to the output shaft.

In [42], an early attempt was made to integrate a permanent magnet (PM) motor with a magnetic gear to create a novel electric actuator. This actuator was capable of directly operating a robot arm with low speed, high torque, smooth motion, and intrinsic braking ability required for typical space applications [97],[98]. In their designed actuator consists of a Permanent Magnet Brushless Motor (PMBM) and a high efficiency magnetic gearbox built into the motor airgap. However, the permanent magnet gear was based on a complex reluctance structure, which included magnets on only one of the rotating shafts.

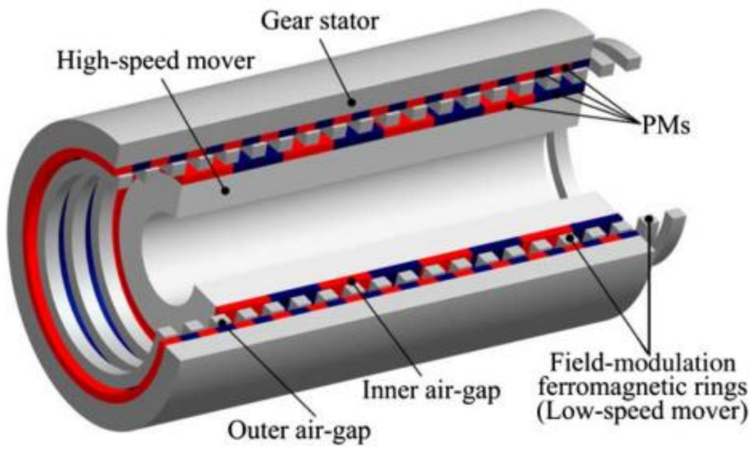

Fig. 2.9. Linear magnetic gears [40]

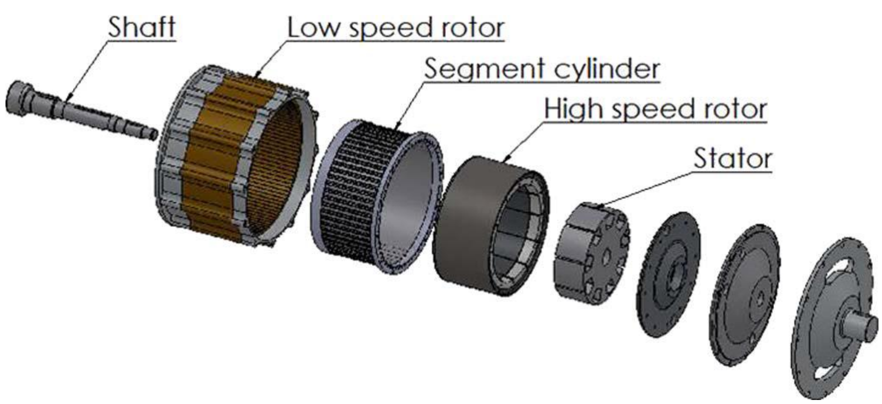

Fig. 2.10. View of a Motor-integrated Permanent Magnetic Gear [41]

This design required an impractically small air gap of 0.3 mm to achieve both a reasonably high torque density and a high gear ratio of 50. In addition to the tight air-gap constraint, the axial topology introduced problematic unbalanced axial forces, making the overall construction less practical. A unique aspect of the design was the use of a single, common four-pole magnetic disk shared by both the PM motor and the magnetic gear.

In [43] the topology proposed was integrated with an electrical machine, a coaxial magnetic flux magnetic gear and motor was combined and evaluated. This design is rare because the structure of MIPMG was inverted with the electric motor outside and the magnetic gear parts inside. This prototype of combination would result in a smaller dimension for magnetic gearbox limit the maximum torque could be generate by magnetic field flux between the inner and outer PM rotors [44]. From the perspective of utilization of motor power density, the motor was designed to be thinner than usual to keep the space of motor be fully utilized or the total volume of the MIPMG would be too large to lose their advantages of simple structure and higher torque density. In [43], it stated that the magnetic
transmission capability was reached before the thermal limit of the non-cooled machine. Specifically, the current density was only 2 A/mm^2 when the gear stalled, whereas a common rule of thumb for Totally Enclosed Non-Ventilated (TENV) machines is to use a current density of 5 A/mm^2 to achieve good thermal utilization [44].

In [45] and [46], planetary-type magnetic gear combinations were proposed—one integrated with a brushless generator and the other with a permanent-magnet (PM) brushless DC motor. Both machines share a common PM rotor as the rotating element. In [45], a new PM brushless machine was developed specifically for wind power generation. This machine features an outer-rotor topology, designed to capture wind energy directly. To achieve high power density, a high-speed PM brushless generator is integrated with a coaxial magnetic gear. The design addresses the specific constraints of wind power applications, and its performance—under both no-load and on-load conditions—was simulated using the time-stepping finite element method. In [46], a novel in-wheel motor is presented, which integrates a magnetic gear into a PM brushless DC motor by sharing a common PM rotor. This integration achieves both high efficiency and high-power density, while simultaneously satisfying the low-speed requirement for direct drive and the high-speed requirement for compact motor design. Based on their research, the torque density for device is 87 kNM/m^3.

With the optimization of magnetic gear structure and development of motor transmission efficiency, the Motor/Generator Integrated Magnetic Gear technology is developed faster than except. From the previous review about the magnetic gear torque density can reach higher as 239 kNM/m^3. And in [47], a motor-integrated permanent magnet gear unit for traction applications is proposed. Based on the specifications of a commercial HEV traction motor (Toyota Camry), the unit integrates a permanent magnetic gear with a ratio of 8.67 and an outer-rotor PM motor. The motor has a base speed of 4000 rpm and delivers 35 kW of constant power up to 14,000 rpm under flux weakening. This design features high magnetic decoupling between motor and gear, enabling effective flux weakening and a shorter motor stack length. The torque density of the unit reaches 130 Nm/l, outperforming values reported in [46] (87 Nm/l) and [45] (60 Nm/l). While four such units are needed to match the Camry's peak torque, they can eliminate the need for oil cooling, reduction gears, and differentials. Compact size and simplified system architecture make the unit especially promising for pure EVs and in-wheel motor applications.

2.5 Chapter Two Summary

The advancement of Motor/Generator Integrated Permanent Magnet Gear (MIPMG) technology represents a significant step forward in meeting the growing demands for efficiency, compactness, and torque density in modern propulsion systems. By integrating high-performance permanent magnet motors with magnetic gear transmissions—especially in axial and coaxial configurations—these systems offer smooth, contactless power delivery with reduced maintenance requirements and enhanced overload protection. Studies have demonstrated promising results across diverse applications, from wind energy and space robotics to traction drives and electric vehicles, achieving torque densities that rival or exceed those of traditional mechanical gear systems. Despite challenges such as thermal limitations, manufacturing complexity, and size constraints, continuous innovation in gear topology, magnetic field modulation, and motor-gear integration continue to push the boundaries of performance. As variable-speed and multi-speed rotorcraft designs evolve, MIPMGs hold strong potential as a lightweight, efficient, and scalable solution for next-generation aerospace and electric mobility platforms.

CHAPTER THREE

THEORETICAL MODELING AND DESIGN

A Magnetic Electric Continuously Variable Transmission (ECVT) system is typically a hybrid transmission that integrates a conventional powertrain with an electric powertrain. In the case of a single main rotor helicopter drivetrain, where we specifically apply the Magnetic ECVT, the system is traditionally equipped with a turbine engine, a series of speed reduction stages, and a combining stage that merges the power output from a pair of turbine engines. Following that, an additional speed reduction geartrain is used to maintain appropriate rotor speed and torque, ensuring stable and efficient blade operation. Therefore, the ECVT system is designed to serve as a parallel addition to the conventional helicopter drivetrain, enabling stable speed variability with minimal changes to the overall powertrain architecture.

From this perspective, it is further clarified that the objective is to achieve a stable continuously variable-speed transmission under high specific energy conditions. Given that the primary propulsion source of the helicopter remains a pair of turbine engines, the hybrid electric component is incorporated via the integration of an electric motor. A significant engineering challenge lies in the design of a combining stage capable of efficiently merging the mechanical output from the conventional powertrain with the parallel electric drive system, while maintaining drivetrain integrity stability and continuous.

It is well known that different types of transmission mechanisms are widely used across various industrial fields, including gear transmissions, belt drives, chain drives, friction drives, and various types of linkage and rod joint connections. These diverse transmission modes enable a wide range of power transmission architectures. For instance, belt drives are commonly used in conventional automotive engines to transfer mechanical power between subsystems, while chain drives, which operate similarly to belts but offer higher strength and durability, are often employed in motorsports applications to transmit power across different stages. Among these systems, gear transmissions are the most prevalent in mechanical applications, as they can achieve high power density by adjusting the number of teeth and gear sizes across multiple stages.

In addition to conventional transmission systems, another major focus of our discussion is variable speed transmission. In mechanical systems powered by a single energy source, variable speeds are typically achieved using a clutch system, which shifts the transmission ratio between different stages. Essentially, the clutch system operates as a coordinated mechanism involving multiple gear pairs, where speed variation is realized by engaging gear stages with different ratios.

With the evolution of vehicle technology, clutch systems have undergone significant advancements. Initially, vehicles relied on manual clutch systems, where drivers manually disengaged and shifted gears using a lever. Over time, clutch systems transitioned into automated solutions, leading to the development of automatic transmissions, dual-clutch transmissions (DCTs), and continuously variable transmissions (CVTs). These systems shifted from purely mechanical disengagement to more sophisticated methods—such as utilizing planetary gear sets and gear ratio changes—allowing for smoother and more efficient speed transitions during shifting phases.

In high-performance vehicles, dual-clutch transmission (DCT) systems have been designed to maximize efficiency and eliminate torque interruption during gear shifts. This is achieved by integrating two separate clutch subsystems that alternate engagement, enabling seamless transitions between gears without disconnecting the transmission from the power source.

Alongside clutch-based systems, alternative methods have also been developed for variable speed transmission. One example is the conical gear continuously variable speed transmission (CVTs) system, where multiple gear stages are combined into a conical gearbox. A chain mechanism is employed to link different stages, allowing for speed variation by shifting the chain connection across the conical gears.

Building upon the design principles of variable speed transmissions in high-performance vehicles, we drew significant inspiration for helicopter drivetrain innovation. By carefully evaluating and comparing the powertrain architectures of helicopters and high-performance vehicles, we developed an advanced dual-clutch transmission system specifically for helicopters. This system enables two-speed operation to support both vertical lift mode and forward flight endurance mode.

The design integrates a Dual-Clutch Transmission (DCT) system with an Offset Compound Gearbox (OCG), providing variable speed reduction and efficient torque transmission within the helicopter drivetrain. In forward flight endurance mode, the OCG Dual-Clutch system achieves a 30% reduction in rotor speed without compromising the helicopter's forward velocity. This rotor speed reduction directly translates into significant operational benefits, enabling up to 18% fuel savings during forward flight.

By introducing the OCG Dual-Clutch variable speed transmission into single-main-rotor helicopters, we demonstrated the potential for substantial improvements in fuel efficiency and drivetrain performance through advanced variable speed drivetrain design. Based on the performance analysis of helicopter equipped with OCG Dual-Clutch to achieve two speed variation flight mode, we can identify the benefit and advantages of variable speed transmission system in helicopters performance.

However, the Dual-Clutch system is fundamentally a discontinuous transmission method, consisting of two multi-disk clutch subsystems. During the shifting phase when transitioning from one speed ratio to another an unstable interval is introduced into the drivetrain, affecting the power transmission components during helicopter flight mode changes.

For instance, during a shift, the turbine engine experiences torque and power fluctuations along the shaft transmission path, creating potential instability. A major concern is the engine compressor's surge margin, which becomes especially critical during these transient events. From the perspective of engine response, it is necessary to design a gradual shifting strategy to prevent the compressor pressure from approaching or exceeding the surge margin boundary, which could jeopardize engine stability.

However, the nature of a multi-disk clutch system presents a conflicting challenge. Clutch engagement relies on pressure-induced friction before full torque transfer is achieved. Therefore, prolonging the shifting duration—intended to smooth the engine response—results in increased frictional heat between the clutch disks. This creates a fundamental conflict in system requirements: while the engine compressor demands a slower, smoother speed transition to maintain surge margin stability, the Dual-Clutch system requires rapid engagement to minimize thermal buildup within the clutch packs. Helicopter performance evaluations highlight this contradiction, emphasizing the difficulty of simultaneously optimizing both engine compressor stability and Dual-Clutch thermal management.

Nonetheless, despite these challenges, the advantages offered by a dual-speed clutch system—particularly in terms of operational flexibility and fuel efficiency—remain highly attractive. This motivated us to explore newer and more advanced continuously variable transmission (CVT) architectures as a potential solution for achieving superior drivetrain performance in helicopters.

3.1 Mechanical CVT System Design and Analysis

A Continuously Variable Speed Transmission (CVT) enables smooth and seamless adjustments of speed and torque without the need for stepped gear shifts. Traditional drivetrains use fixed gear ratios, while CVTs allow for an infinite range of gear ratios within a specified range, optimizing power delivery and efficiency.

In this design, a hybrid electric approach is adopted, integrating an electric motor with mechanical or magnetic gear coupling. This setup achieves continuous variability in output speed and torque, enhancing overall drivetrain performance. Power transfer relies on the interaction of toothed wheels or magnetic flux, allowing for smooth transitions and improved energy efficiency.

The gearboxes transmission is a mechanical system designed to transfer power from driving source turbine engines to driven component (blade rotor in helicopter drivetrains), specifical alternating the torque and speed. The mechanical gearboxes transmission is combined of couple of gear pairs, and gear transmit is dependent on the gear teeth interaction of toothed wheels to transmit mechanical power between the rotating components. In the simplest gear transmission, when gear teeth mesh each other the rotated of drive gear cause the driven gear to rotate in the opposite direction. This transfer of gear motion allows for change in the torque by the force in gear teeth and rotating speed depending on the gear sizes.

The gear transmission ratios are defined by the number of teeth on the drive gear and driven gear:

$$Gear\ Ratio = \frac{Teeth\ of\ Driven\ Gear}{Teeth\ of\ Drive\ Gear}$$

When the driven gear teeth number is larger than the drive gear, the output torque increases and the speed decreases, if the driven gear has reversed less gear teeth number, the output speed increases and torque decreases.

In practice, there is another way to define gear transmission ratios when the gear teeth are properly meshed. In this approach, the transmission is simplified by representing the gears as pairs of meshing pitch circle, this is known as the pitch circle calculation method. Using this method, the gear ratio can be expressed as:

$$Gear\ Ratio = \frac{Pitch\ Circle\ Diameter\ of\ Driven\ Gear}{Pitch\ Circle\ Diameter\ of\ Drive\ Gear}$$

Because both gear pairs share the same modules and are proper meshed, the relation between the gear teeth, pitch diameter and pitch circle are:

$$Pitch\ Diameter = \frac{Number\ of\ Teeth\ in\ Gear}{Module}$$

$$Total\ center\ distance = \frac{D_{in} + D_{out}}{2}$$

Where D_{in} is the pitch diameter of input drive gear,

D_{out} is the pitch diameter of output driven gear.

From the fundamental principles of rotational mechanics, gear transmissions exhibit an inverse relationship between angular velocity and torque: as speed increases, torque decreases proportionally, and vice versa. This relationship underpins the core function of gearbox systems in helicopter drivetrains, where the high-speed, low-torque output of turbine engines must be efficiently converted into the low-speed, high-torque input required by the main rotor system. Gear trains achieve this by manipulating gear ratios to maintain constant mechanical power transfer. The efficiency of gear transmission systems, however, is inevitably impacted by practical considerations such as frictional forces, mechanical wear, lubrication effectiveness, and thermal management. These factors must be carefully addressed in the design and operation of helicopter CVT systems to minimize energy losses and optimize performance and reliability.

3.1.1 Planetary Gear Transmission

After understanding the fundamental gear transmission theory described above, gear transmission systems in practical applications typically utilize multi-stage configurations assembled into gearboxes. To enhance torque-loading capabilities, the most commonly employed solution is the planetary gearbox (**Fig. 3.1**), which incorporates several basic spur gears arranged as sun gears, planetary gears, and an inner ring gear with distinct geometry. Additionally, a carrier structure is designed to interconnect all planetary gears, forming an integrated gearset assembly.

The structure of planetary gears is typical consist of main components and acting as different role in maintaining the transmission.

1. Sun Gear:

   Positioned centrally within the gear arrangement, it can serve as the input, output, or remain stationary depending on the configuration.

2. Planet Gears:

   These are multiple small gears (typically 3–6) that surround and mesh with the sun gear. They are mounted on a common component called the *carrier* and rotate around their own axes while simultaneously orbiting the sun gear.

3. Carrier:

   This component connects and supports the planet’s gears. It can function as an input, output, or remain stationary, depending on the power flow configuration.

4. Ring Gear:

   The outermost gear with internal teeth that encases the planet gears. It can serve as the input, output, or remain stationary as well.

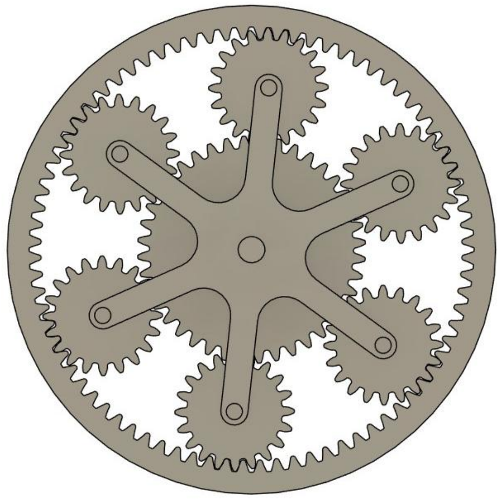

Fig. 3.1. Planetary gear.

Due to the multi-component combined be a planetary gear. There are different connection ways for drive and driven components and will result of different connectivity transmission ratios depending on the teeth number of each gear for energy transmission. and its ratios will always follow the basic concept of gearbox transmission:

$$Gear\ Ratio = \frac{N_{output}}{N_{input}}$$

Type I. Sun gear driven, ring gear fixed, the carrier becomes the output

The input power is applied to the sun gear while the ring gear remains fixed, causing power modulation within the planetary gear set. Power flows from the input sun gear to the output carrier through the planet gears. Specifically, the sun gear delivers a high-speed, low-torque input, which is transformed by the planet gears rotating around the stationary ring gear, resulting in a low-speed, high-torque output at the carrier. The gear ratio for this configuration is given by:

$$Gear\ Ratio = \frac{\omega_{output}}{\omega_{input}} = \frac{z_{sun}}{z_{sun} + z_{ring}}$$

Where the ω_{output} is carrier's output speed, ω_{input} is sun gear's input speed from preceding stage, and the z_{sun} and z_{ring} is the teeth number in sun and ring gear, respectively.

Type II. Sun gear fixed, carrier input, the ring gear becomes the output

In this configuration, the sun gear is held stationary while the carrier acts as the input. Power is transferred from the input carrier through the planet gears, causing them to rotate around the fixed sun gear and subsequently driving the ring gear. The carrier provides a lower-speed, higher-torque input, which is converted into a higher-speed, lower-torque output at the ring gear. The gear ratio for this arrangement is expressed as:

$$Gear\ Ratio = \frac{\omega_{output}}{\omega_{input}} = \frac{z_{sun} + z_{ring}}{z_{ring}}$$

Where the ω_{output} is output speed of the ring gear, ω_{input} is the carrier's input speed from preceding stage, and the z_{sun} and z_{ring} denote the number of teeth on sun and ring gear.

Type III. Sun gear input, carrier fixed, the ring gear becomes the output

In this arrangement, the carrier is held stationary, and the sun gear serves as the input. The input power from the sun gear drives the planet gears, which rotate about their own axes but remain stationary relative to the fixed carrier. This motion transfers power to the ring gear, causing it to rotate in the opposite direction of the sun gear. The sun gear provides a high-speed, low-torque input, which is converted into a lower-speed, higher-torque output at the ring gear. The gear ratio for this configuration is defined as:

$$Gear\ Ratio = \frac{\omega_{output}}{\omega_{input}} = -\frac{z_{sun}}{z_{ring}}$$

Where the ω_{output} is output speed of the ring gear, ω_{input} is the sun gear's input speed from preceding stage, and the z_{sun} and z_{ring} denote the number of teeth on sun and ring gear, respectively.

These three configurations illustrate the versatility and efficiency of planetary gear systems, allowing for different torque and speed outputs by merely adjusting the fixed, input, and output components. This makes planetary gears ideal for applications requiring compactness, high load capacity, and flexible speed variations.

3.1.2 Planetary Gear Drivetrain Size model

In designing the planetary gear size model, we consider the geometric relationships and load distribution among the sun gear, planetary gears, and the ring gear. The primary design objectives include optimizing torque capacity, minimizing weight, and ensuring mechanical integrity under varying load conditions.

To facilitate the design process, a computational model of the planetary gear system is developed. This model serves as a reference for conducting parametric dimensional optimization analysis. The key physical parameters and material properties used in the model are detailed in **Table 3.1**.

Firstly, determine the Planetary Gear around the sun gear by the gear transmission ratio from sun to ring gear. A calculation equation are inplement following:

$$NP_{max} = floor(\frac{\pi}{\arcsin(\frac{1+n}{1-n})}) \qquad \text{(Equ. 3.1.1)}$$

Where this equation is to estimate the conceptual maximum number of planetary gear could be arranged in the free space without interaction with each others. This formula estimates the *maximum number of planet gears* NP_{max} that can be placed around the sun gear without causing interference. The constraint arises from geometric considerations: each planet gear must fit within the annular space between the sun and ring gears and be evenly spaced around the circumference without colliding with its neighbors.

The term inside the $\arcsin$ () function captures the angular spacing required between adjacent planet gears. Dividing π (half the circular angle) by this angle gives the theoretical maximum number of evenly spaced gears that can fit in the available space. Then, a correction factor γ is applied to ensure practical feasibility in the gear design. While NP_{max} provides a theoretical limit, in real-world applications, additional factors must be considered: Manufacturing tolerances, Thermal expansion, Lubrication clearance and Dynamic loading and gear vibration. Choosing $\gamma = 0.9$ means that only 90% of the theoretical capacity is utilized to provide sufficient design margin for reliability and robustness.

$$NP_{max} = round(NP_{max} * \gamma) \qquad \text{(Equ. 3.1.2)}$$

Table 3.1. Planetary gear size model inputs values.

Planetary Gear Transmission Ratio	n
Torque at input Gear	Tq
Safety Factor	SF
Pressure Angle	α
Young's Modulus	E
Poisson's Ratio	ν
Material Density	ρ
Tensile Strength	Str

Finalize the planetary gear number NP is computed by Equ. 3.1.2 scaling down the theoretical maximum by the correction factor and rounding to the nearest integer using the $round()$ function. This ensures the final value is both geometrically viable and practically robust.

To estimate the volume of each gear in the planetary gear set, an empirical filling factor (**Table 3.2**) is applied in the size model to account for the actual material usage within the gear geometry. The filling factors for the ring gear and carrier are determined based on the sizes of the sun and planet gears, once the number of planet gears required for the transmission has been specified.

Due to the different connection types and gear ratios between the sun gear and ring gear, the size model varies depending on the specific configuration of the planetary gear transmission, as discussed in Section 1: Planetary Gear Transmission.

The final volume formula for the sun gear is derived based on Hertzian contact stress theory, which estimates the material volume required to safely transmit torque without exceeding the allowable contact stress [99]. It incorporates the material's elastic properties (Young's modulus and Poisson's ratio), the gear ratio effect on stress distribution, the applied torque shared across multiple planet gears, and the influence of the pressure angle on contact force direction [100]. A safety factor is included to ensure the contact stress remains within permissible limits.

Table 3.2. Planetary gear size model filling factor.

Name	Parameter	Number
Sun Gear Filling Factor	ffs	1
Planet Gear Filling Factor	ffp	1
Ring Gear Filling Factor	ffr	1.15^2-1^2
Carrier Gear Filling Factor	ffc	1^2-0.5^2

Overall, the formula captures the relationship between mechanical load, material strength, geometry, and stress tolerance, allowing for a stress-constrained estimation of the sun gear's envelope volume.The volume model and volume to weight model is following:

Type I:

$$V_s = \frac{E}{1-\nu^2} * \frac{1-n}{1+n} * \frac{|Tq|}{NP \cdot \sin(2\alpha)} * (\frac{SF}{str})^2 \quad \text{(Equ. 3.1.3)}$$

$$m_s = \rho \cdot V_s \cdot ffs \quad \text{(Equ. 3.1.4)}$$

$$m_p = \rho \cdot (\frac{n+1}{2n})^2 \cdot V_s \cdot ffp \quad \text{(Equ. 3.1.5)}$$

$$m_R = \rho \cdot (\frac{1}{n})^2 \cdot V_s \cdot ffr \quad \text{(Equ. 3.1.6)}$$

$$m_C = \rho \cdot (\frac{n-1}{2n})^2 \cdot V_s \cdot ffc \quad \text{(Equ. 3.1.7)}$$

Type II:

$$V_s = \frac{E}{1-\nu^2} * \frac{1}{1-2n} * \frac{|Tq|}{NP \cdot \sin(2\alpha)} * (\frac{SF}{str})^2 \quad \text{(Equ. 3.1.8)}$$

$$m_s = \rho \cdot V_s \cdot ffs \quad \text{(Equ. 3.1.9)}$$

$$m_p = \rho \cdot (\frac{1}{2n} - 1)^2 \cdot V_s \cdot ffp \quad \text{(Equ. 3.1.10)}$$

$$m_R = \rho \cdot (\frac{1}{n} - 1)^2 \cdot V_s \cdot ffr \quad \text{(Equ. 3.1.11)}$$

$$m_C = \rho \cdot (\frac{1}{2n})^2 \cdot V_s \cdot ffc \quad \text{(Equ. 3.1.12)}$$

Type III:

$$V_s = \frac{E}{1-\nu^2} * \frac{n-1}{2n-1} * \frac{|Tq|}{NP \cdot \sin(2\alpha)} * (\frac{SF}{str})^2 \quad \text{(Equ. 3.1.13)}$$

$$m_s = \rho \cdot V_s \cdot ffs \quad \text{(Equ. 3.1.14)}$$

$$m_p = \rho \cdot (\frac{2-n}{2n-2})^2 \cdot V_s \cdot ffp \quad \text{(Equ. 3.1.15)}$$

$$m_R = \rho \cdot (\frac{1}{n-1})^2 \cdot V_s \cdot ffr \quad \text{(Equ. 3.1.16)}$$

$$m_C = \rho \cdot (\frac{n}{2n-2})^2 \cdot V_s \cdot ffc \quad \text{(Equ. 3.1.17)}$$

Total Weight of Planetary Gear:

$$m_{pgt} = m_s + NP * m_p + m_R + m_C \quad \text{(Equ. 3.1.18)}$$

Since the size model estimates the mass of a single planet gear, the total contribution from the planet gears is obtained by multiplying this value by the number of planet gears (NP). The total weight of the planetary gear set is then calculated by summing the masses of the sun gear, all planet gears, the ring gear, and the carrier, as shown in Equation (3.1.18).

3.2 Magnetic Gear Design Method and Simulation

This chapter presents the methodologies employed in the design and analysis of magnetic gears. A systematic approach is taken to optimize torque transmission, minimize size, and enhance efficiency. Key design principles and optimization strategies are introduced to overcome performance limitations and achieve high power density and energy efficiency. The design process is further validated through simulation techniques, providing insights into magnetic flux distribution, torque output, and mechanical integrity under various operating conditions.

Magnetic gear systems are modeled after conventional gear transmissions and have been developed in various configurations to meet specific gear ratio requirements, accommodate spatial constraints, and handle varying load capacities. Based on the structure shown in **Fig. 3.2** [35] and the principles of force transmission, magnetic gears can be categorized into two main types: analogous mechanical transmission magnetic gears, which directly replace mechanical gear teeth with permanent magnets, and mechanical derived magnetic gears, which employ alternative gear structures while

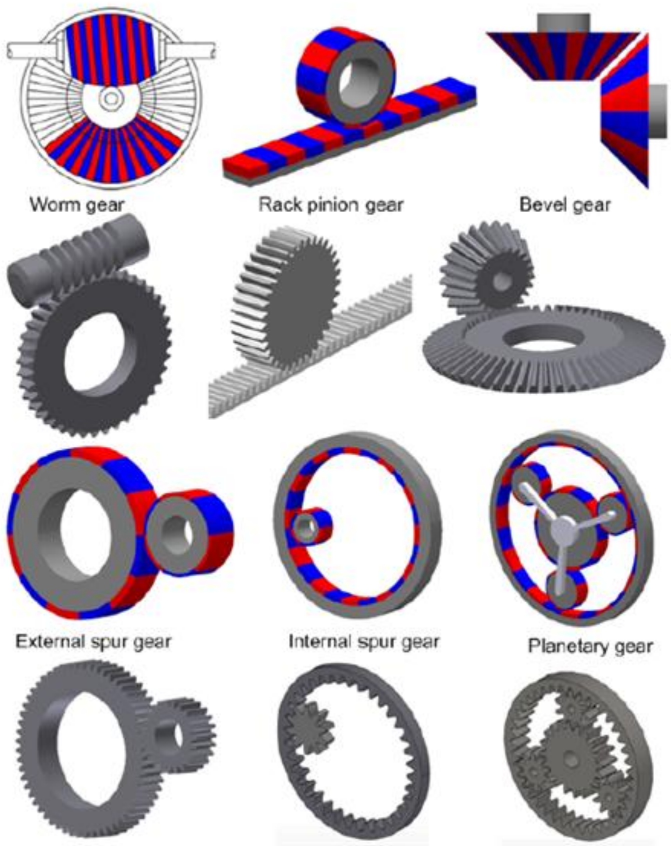

Fig. 3.2. Early mechanical and magnetic gear comparison.

maintaining similar transmission principles. Additionally, magnetic gears can be classified by the method of magnetic force generation into two types: permanent magnet gears, which rely on fixed permanent magnets, and electromagnetic gears, which use electrically energized coils to generate magnetic fields.

When evaluating various magnetic and mechanical gear types, torque density serves as a key performance metric for transmission systems. As shown in **Fig. 3.3** and **Table 3.3** [36], consider the demands of practical gearbox applications, certain magnetic gear configurations exhibit torque densities that are comparable to or exceed those of conventional mechanical gears. Specifically, magnetic harmonic gears, magnetic planetary gears, and concentric magnetic gears demonstrate relatively high torque density and are used in a variety of operating conditions.

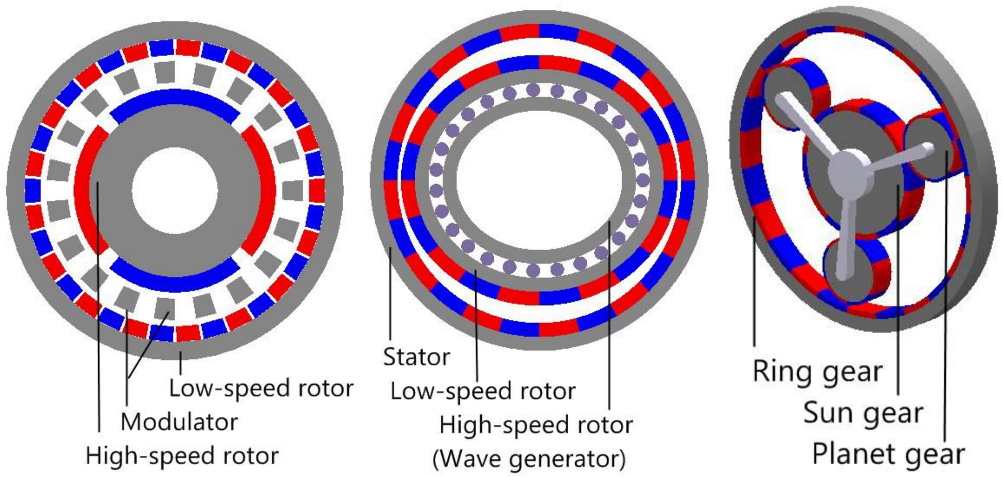

Fig. 3.3. a) Concentric, b) harmonic, and c) planetary magnetic gears.

Table 3.3. Magnetic and mechanical gear torque density list.

Gear Type	Torque density (kNm/m^3)
Mechanical spur gear [30]	100-200
Mechanical helical gear(3G)	50-150
Magnetic worm gear [9]	$<$2
Magnetic bevel gear	$<$5
Magnetic spur gear	10-20
Magnetic harmonic gear(1G)	140-180
Magnetic harmonic gear(2G)	75
Magnetic planetary gear [26]	$\approx$100
Concentric magnetic gear	70-150

3.2.1 Concentric Magnetic Gear (CMG) Principle of Operation

The Concentric Magnetic Gear (CMG) operates similarly to a mechanical planetary gear set. It consists of two permanent magnetic rotors with differing numbers of poles, functioning analogously to the ring and sun gears in a planetary system. Positioned between these magnetic rotors is a flux modulator, which serves the role of planet gears. This modulator is composed of alternating sections of ferromagnetic and non-magnetic materials. Through a process called flux modulation, it enables magnetic poles on the sun and ring rotors to fully engage with each other, achieving a specific gear ratio [101]. This complete magnetic pole engagement allows CMGs to achieve higher torque densities compared to other types of magnetic gears.

The working principle of a Concentric Magnetic Gear (CMG) is based on magnetic flux modulation and synchronized magnetic coupling between the inner rotor, outer rotor, and the flux modulator. The inner rotor and outer rotor are equipped with permanent magnets arranged in pole pairs, while the flux modulator, positioned between them, consists of alternating ferromagnetic and non-magnetic segments. As the inner rotor rotates, its magnetic field interacts with the flux modulator, which modulates the flux path, enabling synchronized magnetic coupling with the outer rotor. This interaction allows torque to be transmitted efficiently and at a fixed gear ratio without physical contact. Yokes made of high-permeability materials surround the inner and outer rotors, providing a closed magnetic path, minimizing flux leakage, and enhancing transmission efficiency. As a result, CMG achieves high torque density, smooth operation, and reduced mechanical wear compared to traditional mechanical gear systems.

Fig.3.4 illustrates a 1:3 gear ratio Concentric Magnetic Gear (CMG) configuration. It consists of an inner rotor permanent magnet (PM) with a pole pair number of $p_{in} = 2$, an outer rotor permanent magnet (PM) with a pole pair number of $p_{out} = 6$, and a flux modulator containing $N_m = 8$ ferromagnetic poles. The relationship between the inner and outer pole pairs and the number of modulator poles is defined by:

$$N_m = p_{in} + p_{out} \qquad \text{(Equ. 3.2.1)}$$

This arrangement is designed to optimize torque stability and speed transmission efficiency within the CMG.

As illustrated in **Fig. 3.4**, the Concentric Magnetic Gear (CMG) can be viewed as a two-degree-of-freedom (2 DOF) system when its components are grouped accordingly: the inner yoke and inner rotor form a single integrated component, the outer yoke and outer rotor constitute another, and the flux modulators, though physically disconnected, act as a unified component. This 2 DOF configuration requires two independent inputs to achieve one controlled output. The three primary components—inner rotor with yoke (sun gear equivalent), outer rotor with yoke (ring gear equivalent), and flux modulator (planetary gear equivalent)—are capable of independent rotation. This independent movement enables flexible control of torque and speed, mirroring the functional principles of mechanical planetary gear sets.

In its natural state, to determine the speed and torque of any one component, the speeds or torques of the other two must be known or controlled. However, when one of the three components is fixed (e.g., the flux modulator is held stationary), the system's DOF is reduced to 1 DOF, allowing the rotational speed and torque of the remaining two components to be directly linked by a fixed gear ratio. This reduction simplifies the control and operation of the PMG, making it behave similarly to a traditional single-degree-of-freedom gear mechanism.

Operational Gear Ratios in Concentric Magnetic Gear Systems

As the transmission principle has been discussed in perivous, the most common transmit situation of Concentric Magnetic Gear (CMG) systems is a 1DOF allowing the rotational speed and torque transmited by remaining two components be the flexiable and given a constant speed and torque ratio.

1. Modulator rotor fixed

As the example shown in **Fig. 3.4** the Concentric Magnetic Gear (CMG) have $N_m = 8$, and $p_{in} = 2$; $p_{out} = 6$ inner/outer pole pairs in high speed and low speed rotor. Therefore, the combination gear ratio from inner rotor to outer is:

$$G_r = \frac{p_{out}}{p_{in}} \qquad \text{(Equ. 3.2.2)}$$

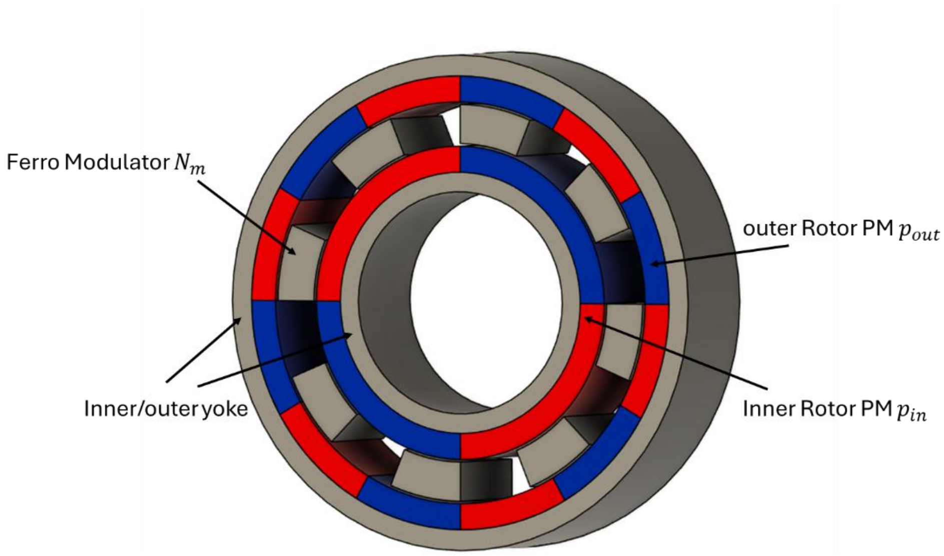

Fig. 3.4. Concentric Magnetic Gear (CMG) inner rotor to outer rotor 1:3 gear ratio.

This gear ratio just express the relatoinship between two rotors which does not show the rotate direction like mechancial gear expressions. Accordingly, the conceptual angular velocity can be calculate by this gear ratios relationship:

$$\omega_{out} = -\frac{1}{G_r} * \omega_{in} = -\frac{1}{3} \quad \text{(Equ. 3.2.3)}$$

Where the ω_{out} is the lower angular velocity on the lower speed rotor outer rotor in the example and ω_{in} is angular velocity on the high speed rotor (inne rotor in **Fig. 3.4**). The rotational direction shift is expressed by the negative sign means the inner and outer rotor is rotate in opposite direction.

With the gear and speed ratio relationship in Concentric Magnetic Gear (CMG), the torque transmission ratio can be calculated by the energy balance law with the assumption that the gear rotors operating in a stable condition with a constanst angular velocity and no power loss between the inner and outer rotor. The total mechanical power outside the CMGs system must be zero and normal angular velocities is define by the Equ. 3.2.4. When the angular velocity of ferro modulator rotor is zero the torque ratio will be:

$$P_{in} + P_m + P_{out} = 0 \quad \text{(Equ. 3.2.4)}$$

$$T_{in} * \omega_{in} + T_m * \omega_m + T_{out} * \omega_{out} = 0$$

$$T_{in} * \omega_{in} + 0 + T_{out} * -\frac{1}{G_r} * \omega_{in} = 0$$

$$T_{out} = G_r * T_{in} \qquad \text{(Equ. 3.2.5)}$$

2. Outer rotor fixed

Similar to the scenario where the modulator rotor is fixed, the gear ratio for the Concentric Magnetic Gears (CMGs) when the outer rotor is fixed is represented as follows:

$$G_r = \frac{N_m}{p_{in}} \qquad \text{(Equ. 3.2.6)}$$

The gear configuration shown in **Fig. 3.4** example result in a gear ratio of $G_r = 4$. conceptual angular velocity relationship between the inner rotor and the modulator rotor can be formulated as follows:

$$\omega_m = \frac{1}{G_r} * \omega_{in} = \frac{1}{4} \qquad \text{(Equ. 3.2.7)}$$

At this point, the rotational directions of the input and output will be the same. The mechanical power assumption from outside the system remains consistent with the scenario where the modulator is fixed. The calculated torque ratios are as follows:

$$P_{in} + P_m + P_{out} = 0 \qquad \text{(Equ. 3.2.8)}$$

$$T_{in} * \omega_{in} + T_m * \omega_m + T_{out} * \omega_{out} = 0$$

$$T_{in} * \omega_{in} + T_m * \frac{1}{G_r} * \omega_{in} + 0 = 0$$

$$T_m = -G_r * T_{in} \qquad \text{(Equ. 3.2.9)}$$

3. Inner rotor fixed

When the Inner Rotor is fixed, the gear ratio for the Concentric Magnetic Gears (CMGs) is represented as follows:

$$G_r = \frac{N_m}{p_{out}} \qquad \text{(Equ. 3.2.10)}$$

The gear configuration shown in **Fig. 3.4** example result in a gear ratio of $G_r = \frac{4}{3}$. The conceptual angular velocity relationship between the outer rotor and the modulator rotor can be formulated as follows:

$$\omega_m = \frac{1}{G_r} * \omega_{out} = \frac{3}{4} \qquad \text{(Equ. 3.2.11)}$$

At this point, the rotational directions of the input and output will be the same. The mechanical power assumption from outside the system remains consistent with the scenario where the modulator is fixed. The calculated torque ratios are as follows:

$$P_{in} + P_m + P_{out} = 0 \qquad \text{(Equ. 3.2.12)}$$

$$T_{in} * \omega_{in} + T_m * \omega_m + T_{out} * \omega_{out} = 0$$

$$0 + T_m * \frac{1}{G_r} * \omega_{out} + T_{out} * \omega_{out} = 0$$

$$T_m = -G_r * T_{out} \qquad \text{(Equ. 3.2.13)}$$

3.2.2 Concentric Magnetic Gear Systems Torque Calculation

The previous discussion on Concentric Magnetic Gears (CMGs) focused only on the basic conceptual operation of internal transmission. The analysis primarily highlighted the synchronized magnetic coupling facilitated by the flux modulator, enabling torque transfer between the inner and outer rotors. However, it did not delve into the critical aspects of torque calculation, efficiency optimization, and the impact of flux modulation on power density. A deeper exploration of these factors is necessary to understand the practical performance of CMGs, including their torque capabilities, loss mechanisms, and potential design optimizations for high-efficiency power transmission in advanced mechanical systems. The following sections will expand on these elements, providing a comprehensive analysis of torque dynamics, flux path interactions, and magnetic field distribution within CMG structures.

The torque and speed transmission mechanism of Concentric Magnetic Gears (CMGs) is fundamentally driven by the magnetic interaction between the permanent magnets (PMs) on the inner and outer rotors, facilitated through a ferro-based flux modulator. Due to the significantly higher magnetic permeability of the flux modulator compared to air, magnetic flux is preferentially channeled through the ferromagnetic segments rather than air gaps during transmission [102]. This principle of magnetic flux concentration allows CMGs to achieve efficient flux modulation, enabling seamless torque transfer and controlled rotational speed differentials between the two rotors. The flux modulator's role in synchronizing magnetic field interactions is critical for maintaining the desired gear ratio, serving as the core mechanism for power transmission and precise speed regulation within CMG architectures.

1. Magnetic Field and flux calculations

Therefore, the key aspect of calculating magnetic gear transmission lies in accurately modeling the magnetic field distribution and flux propagation, as the transmission efficiency and torque capacity are heavily influenced by the material properties and magnetic permeability variations across different regions of the gear assembly.

1.1. Mathematic Magnetic Field Flux Calculations

In a Concentric Magnetic Gears (CMGs), the magnetic fields are generated by the inner and outer rotor PMs. To simplify torque analysis, do not include the stationary steel teeth' magnetic saturation, assuming a linear magnetic path. This enables torque calculation using superposition, without affecting the magnetic field harmonics that ensure stable torque transmission at different rotor speeds. First, insolate the inner rotor PMs and yokes, assuming that the PMs is oriented in a ideal positive and negative magnetization and the permability of yokes are infinite, the magnetic field in the air gap region can be described using the scalar magnetic potential approach, which follows the Laplace and quasi-Poisson equations. The radial and tangential components of the magnetic flux density at a radial location r, generated individually by the inner rotor and the outer rotor, can be derived analytically with:

$$B_{rin}(r,\theta) = \sum_{n=1,3,5,\dots}^{\infty} b_{rin}(r)\cos\left[n * p_{in} * (\theta - \omega_{in} * t) + np_{in}\theta_{in0} + (n+1)p_{out}\theta_{out0} - nN_m\theta_{m0}\right] \quad \text{(Equ. 3.2.14)}$$

$$B_{\theta in}(r,\theta) = \sum_{n=1,3,5,\dots}^{\infty} b_{\theta in}(r)\sin\left[n * p_{in} * (\theta - \omega_{in} * t) + np_{in}\theta_{in0} + (n+1)p_{out}\theta_{out0} - nN_m\theta_{m0}\right] \quad \text{(Equ. 3.2.15)}$$

$B_{rout}(r,\theta) = \sum_{n=2,4,6,\ldots}^{\infty} b_{rout}(r) \cos[n * p_{out} * (\theta - \omega_{out} * t) + (n-1)p_{in}\theta_{in0} + np_{out}\theta_{out0} - nN_m\theta_{m0}]$ (Equ. 3.2.16)

$B_{\theta out}(r,\theta) = \sum_{n=2,4,6,\ldots}^{\infty} b_{\theta out}(r) \sin[n * p_{out} * (\theta - \omega_{out} * t) + (n-1)p_{in}\theta_{in0} + np_{out}\theta_{out0} - nN_m\theta_{m0}]$ (Equ. 3.2.17)

Where the$b_{rin}(r)$, $b_{\theta in}(r)$, $b_{rout}(r)$, $b_{\theta out}(r)$ are Fourier coefficients, p_{in}, p_{out} , N_m are inner outer PMs pole pairs number and the Ferro modulators poles number respectively. And the θ_{in0}, θ_{out0}, θ_{m0} are the initial rotor position of inner/outer PMs and ferro modulators.

After determining the magnetic flux generated by the inner and outer PMs, the Ferro modulators are considered. Assuming no magnetic saturation and infinite permeability of the ferromagnetic materials, the ferro modulators' distortion effect on the magnetic field is analogous to the slotting effect in PM motors. This distortion is approximated using a modulating function applied to the original field distribution. Due to its two-dimensional nature, a 2-D complex permeance function is utilized to analyze average torque and torque ripples, emphasizing behavior analysis over precise calculations. Thus, the magnetic flux density of the ferro modulators is given by:

$$B_m = B_{in/out} * \lambda_{air} \quad \text{(Equ. 3.2.18)}$$

Then the permeance fucntion of the Ferro modulators is presents as follow:

$$\lambda_{Fm\_r}(r,\theta) = \lambda_{air\_r}(r) + \sum_{m=1,2,3,\ldots}^{\infty} \lambda_{fm\_r}(r) \cos[m * N_m * (\theta - \omega_m * t)]$$

(Equ. 3.2.19)

$$\lambda_{Fm\_\theta}(r,\theta) = \lambda_{air\_\theta}(r) + \sum_{m=1,2,3,\ldots}^{\infty} \lambda_{fm\_\theta}(r) \cos[m * N_m * (\theta - \omega_m * t)]$$

(Equ. 3.2.20)

Where the $\lambda_{air\_r}(r)$, $\lambda_{fm\_r}(r)$, $\lambda_{air\_\theta}(r)$, $\lambda_{fm\_\theta}(r)$ are Fourier coefficients of air and Ferro modulators. The resultant radial and tangential field of B_{m_rin}, $B_{m\_\theta in}$, B_{m_rout}, $B_{m\_\theta out}$ mean the magntic flux desnity in the Ferro modulators excited by the inner/outer rotor.

$$B_{m\_rin} = B_{rin}(r,\theta) * \lambda_{Fm\_r}(r,\theta)$$
$$B_{m\_\theta in} = B_{\theta in}(r,\theta) * \lambda_{Fm\_\theta}(r,\theta)$$
$$B_{m\_rout} = B_{rout}(r,\theta) * \lambda_{Fm\_r}(r,\theta)$$
$$B_{m\_\theta out} = B_{\theta out}(r,\theta) * \lambda_{Fm\_\theta}(r,\theta) \qquad \text{(Equ. 3.2.21)}$$

Eventually, the magnetic field flux density can be calculated in the polar coordinates because of the interaction of radial and tangential flux between inner/outer rotor PMs and Ferro modulators.

1.2 Numerical Method (Finite Element Method) Magnetic Field Flux Calculations

The Finite Element Method (FEM) is widely used for calculating the magnetic field and flux desnity in the electromagnetic devices. The main steps are as follow:

1. Geometry Modeling:
   - Create a 2D or 3D geometric model of the magnetic gear, motor, or electromagnetic component.
2. Meshing:
   - Discretize the model into finite elements (triangles or quadrilaterals for 2D, tetrahedrons for 3D) to enhance calculation accuracy.
3. Material Property Definition:
   - Assign material properties like magnetic permeability for permanent magnets, ferromagnetic regions, and air.
4. Boundary Conditions Setup:
   - Define boundary conditions, such as external magnetic field boundaries, zero-field boundaries, or periodic boundaries.
5. Current or Magnetization Conditions:

- Apply current density for electromagnetic excitation or specify magnetization direction and strength for permanent magnets.

6. Solve Maxwell's Equations:

- FEM solves Maxwell's equations to compute the magnetic vector potential A.

The magnetic flux density B is derived as:

$$\nabla \times \mathbf{H} = \mathbf{J} \quad \text{(Equ. 3.2.22)}$$

Where the J is the current density which will be 0 in the permanent magnets, the equation can be simplified and the magentic flux density (**B**) is expressed as:

$$\mathbf{B} = \mu_0(\mathbf{H} + \mathbf{M}) \quad \text{(Equ. 3.2.23)}$$

Where the **B** is magnetic flux density (T), **H** is magnetic field intensity (A/m) and **M** is magnetization (A/m), the μ_0 is the permeability of the vacuum ($4\pi * 10^{-7}$ H/m).

Gauss's Law for Magnetism (Equation 2.2.3) states that magnetic flux lines are continuous and have no starting or ending points, implying the non-existence of magnetic monopoles. In FEM calculations, this guarantees that magnetic flux lines always form closed loops, passing through materials or surrounding air, ensuring flux conservation and accurate simulation of magnetic fields.

$$\nabla \cdot \mathbf{B} = \mathbf{0} \quad \text{(Equ. 3.2.24)}$$

Let **A** denote the magnetic vector potentia, **B** is the curl of **A,** express as $\mathbf{B} = \nabla \times \mathbf{A}$. For non-ferromagnetic materials, **B** = μ**H**, where μ is the magnetic permeability of the medium. Consequently,

$$\mathbf{H} = \frac{1}{\mu} \nabla \times \mathbf{A} \quad \text{(Equ. 3.2.25)}$$

$$\mathbf{J} = \nabla \times (\frac{1}{\mu} \nabla \times \mathbf{A}) \quad \text{(Equ. 3.2.26)}$$

Using the identity,

$$\nabla \times (\nabla \times \mathbf{A}) = \nabla \cdot (\nabla \cdot \mathbf{A}) - \nabla^2 \mathbf{A} \quad \text{(Equ. 3.2.27)}$$

In magnetostatic problems involving permanent magnets, the constitutive relationship between the magnetic flux density **B** and **H** within the magnetized region incorporates with magnetization **M**, relation as:

$$\mathbf{B} = \mu \mathbf{H} + \mu_0 \mathbf{M} \quad \text{(Equ. 3.2.28)}$$

Here, the $\mu = \mu_0 \mu_r$, where the μ_r is the relative magnetic permeability of the materials, and μ_0 is the vacuum permeability as a constant ($4\pi * 10^{-7}$ H$/m$). Because ∇·**B**=0, there exists a magnetic vector potential **A**, such that **B**=∇×**A**. Therefore,

$$\mathbf{H} = \frac{1}{\mu_0\mu_r}\mathbf{B} - \frac{1}{\mu_r}\mathbf{M} \qquad \text{(Equ. 3.2.29)}$$

$$\nabla \times \mathbf{H} = \nabla \times \left(\frac{1}{\mu_0\mu_r} \times \mathbf{A} - \frac{1}{\mu_r}\mathbf{M}\right) = \mathbf{J} \qquad \text{(Equ. 3.2.30)}$$

The magnetic vector potential **A** can be formulated based on the current density **J** and magnetization **M**, the governing equation is given by:

$$\nabla \times \left(\frac{1}{\mu_0\mu_r} \times \mathbf{A}\right) = \mathbf{J} + \nabla \times \frac{1}{\mu_r}\mathbf{M} \qquad \text{(Equ. 3.2.31)}$$

2. 2D FEM Concentric Magnetic Gear Magnetic Flux Calculation

By apply the FEM in Matlab Parital Different Equation (PDE) toolbox specially for the Electromagnetics analysis. Still using the struture shown in **Fig. 3.4** a Concentric Magnetic Gears (CMGs) as an example, a sketch of 1:3 gear ratio CMG's dimension and physical data are listed in **Table 3.4**.

A two-dimensional nonlinear model of the Concentric Magnetic Gear is developed in MATLAB using the Partial Differential Equation (PDE) Toolbox. By solving Maxwell's equations, the model computes the magnetic vector potential, magnetic field intensity, and magnetic flux density at the nodes and elements, capturing the static magnetic interactions among the internal components of the gear system.

2.1 FEM Simulation Steps and Results:

1. Geometry Modeling: Develop a 2D geometric model of the magnetic gear component, including the Permanent Magnets, inner and outer yokes, and Ferro Modulators. Each component should be represented as distinct, numbered regions as outlined in **Fig. 3.5**.

2. Meshing: Discretize the model into finite elements (triangles for 2D) to enhance calculation accuracy. For saving computational resources and optimizing calculation performance, local mesh refinement is applied to distinguish different regions across various components in CMGs. The finite element model of the CMG primarily emphasizes the magnetic interaction between the permanent magnets and the ferromagnetic modulators.

This interaction plays a critical role in producing the spatially varying magnetic field within the air gap that separates the inner and outer rotors. As illustrated in **Fig. 3.5**, material definitions are assigned as follows:

- Inner PMs: F14 – F17
- Outer PMs: F1 – F12
- Ferro Modulators: F20 – F27
- Inner/Outer Yokes: F18 for the inner yoke and F28 for the outer yoke

Additionally, regions F13, F19, and F29 are designated as Air. To optimize the mesh distribution:

- The air regions inside the inner rotor (F19) and outside the outer rotor (F29) are meshed with a coarser grid to save computational resources.
- The air gap between the inner and outer rotors, particularly surrounding the Ferro Modulators, is refined with a denser mesh to accurately capture magnetic flux interactions and field variations.

This strategy balances computational efficiency with accuracy, ensuring critical magnetic interactions are precisely represented. **Fig. 3.6** provides a visual representation of the mesh distribution and its optimization across different regions.

3. Material Property Definition: Assign material properties like magnetic permeability for permanent magnets, ferromagnetic regions, and air. In our CMG FEM model, the primary focus is on the interaction between the Permanent Magnets (PMs) and the Ferro Modulators, which is crucial for generating a multi-variation magnetic field within the air gap between the inner and outer rotors.

As illustrated in **Fig. 3.5**, material definitions are assigned as follows:

- Inner PMs: F14 – F17
- Outer PMs: F1 – F12
- Ferro Modulators: F20 – F27
- Inner/Outer Yokes: F18 for the inner yoke and F28 for the outer yoke

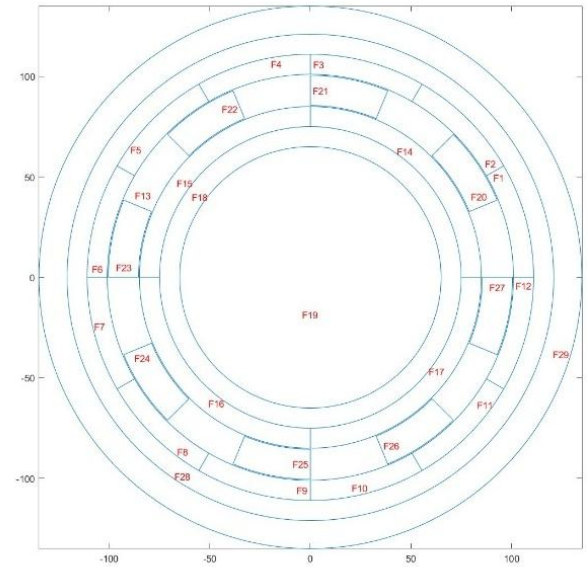

Fig. 3.5. CMG 1:3 Gear ratio geo model with number of region define.

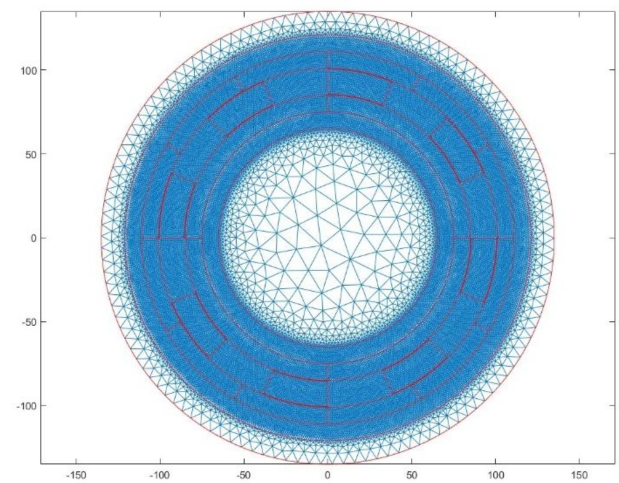

Fig. 3.6. Refined mesh geometry of CMG 1:3 gear ratio model.

Additionally, regions F13, F19, and F29 are designated as Air. To optimize the mesh distribution:

- The air regions inside the inner rotor (F19) and outside the outer rotor (F29) are meshed with a coarser grid to save computational resources.
- The air gap between the inner and outer rotors, particularly surrounding the Ferro Modulators, is refined with a denser mesh to accurately capture magnetic flux interactions and field variations.

4. Boundary Conditions Setup: Define boundary conditions, such as external magnetic field boundaries, zero-field boundaries, or periodic boundaries.
5. Solve Maxwell's Equations: FEM solves Maxwell's equations to compute the magnetic vector potential A and the magnetic flux density B is shown in the **Fig. 3.7.**

Fig. 3.7 presents the magnetic flux distribution within the concentric magnetic gear (CMG) model configured with a gear ratio of 1:3. The visualization includes the following key elements:

1. Color Gradient Representation

The color gradient (from blue to red) represents the magnitude of the magnetic potential (measured in Webers per meter, Wb/m). The color bar on the right illustrates the range of magnetic potential, showing both positive and negative values that indicate directional changes in the magnetic flux path.

- The blue-shaded regions correspond to areas of negative magnetic scalar potential, indicating the orientation of the magnetic field in one direction.
- In contrast, the red-shaded regions represent zones of positive potential, associated with the opposing direction of the magnetic field lines.

2. Magnetic Flux Lines

The contour lines depict the magnetic flux paths and their directional flow within the CMG. Flux lines are:

- Densely packed in regions where magnetic flux is concentrated.
- Widely spaced in regions with weaker flux pathways.

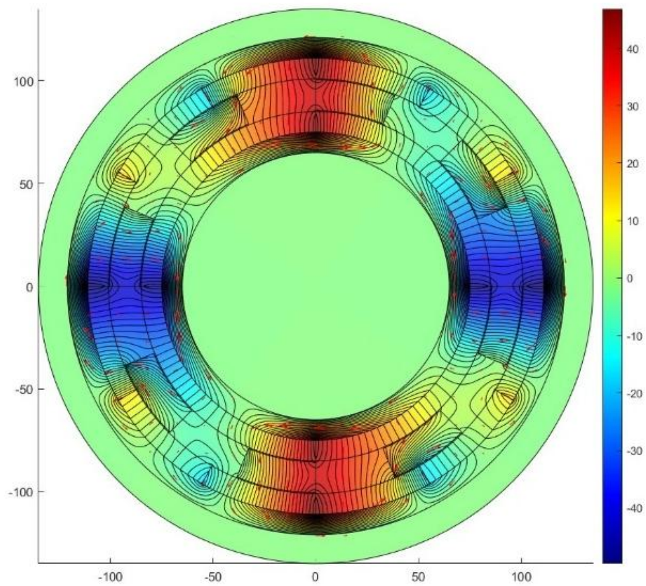

Fig. 3.7. Magnetic flux density distribution of the 1:3 CMG geometric model.

These flux lines curve through the ferro modulator regions and around the permanent magnets, illustrating the magnetic coupling mechanism essential for torque transmission.

3. Magnetic Field Interaction

The variation in magnetic potential across the geometry drives flux modulation. Strong potential differences near the modulator regions confirm effective flux path manipulation, critical for the 1:3 gear ratio. This interaction enables the CMG to achieve speed reduction or multiplication with high efficiency and minimal mechanical loss.

The numerical results are stored in the MATLAB workspace, with the scale illustrated in **Table 3.5**:

Once the magnetic flux density distribution is obtained through the solution of Maxwell's equations, the subsequent key task is to evaluate the electromagnetic torque produced within the concentric magnetic gear. This torque arises from the magnetic coupling between the permanent magnets and the ferromagnetic modulators, and is influenced by the relative rotational movement between the inner and outer rotors.

Table 3.4. Concentric Magnetic Gear (CMG) FEM simulation results.

MagneticPotential:	[155165×1 double]
MagneticField:	[1×1 FEStruct]
MagneticFluxDensity:	[1×1 FEStruct]
Mesh:	[1×1 FEMesh]

3.2.3 Magnetic Torque Transmission Calculation Method

In concentric magnetic gears (CMGs), the calculation of magnetic torque is primarily governed by the interaction between the magnetic fields generated by the permanent magnets on both the inner and outer rotors. This interaction is further shaped by the flux modulation effect introduced by the ferromagnetic modulator positioned between them. Unlike conventional mechanical gears, where torque is transferred through physical contact, CMGs leverage magnetic coupling to achieve non-contact torque transmission, enhancing durability and reducing maintenance requirements. This section presents the analytical and numerical methods for determining magnetic torque, including the application of the Maxwell Stress Tensor method and Finite Element Method (FEM) simulations. These approaches allow for precise estimation of the torque generated under varying operating conditions, providing critical insights for optimizing CMG designs.

1. Maxwell Stress Tensor Torque Calculation Method

The Maxwell Stress Tensor is a mathematical tool used to describe the electromagnetic forces and stresses exerted by electric and magnetic fields on materials. It is particularly useful in determining the mechanical forces and torques in electromechanical devices such as motors, magnetic gears (CMGs), and transformers.

1. Definition of Maxwell Stress Tensor

In the context of electromagnetics, the Maxwell stress tensor describes the mechanical stress exerted by the electromagnetic field, expressd in following:

$$\sigma_{ij} = \epsilon_0 E_i E_j + \frac{1}{\mu_0} B_i B_j - \frac{1}{2}\left(\epsilon_0 E^2 + \frac{1}{\mu_0} B^2\right)\delta_{ij} \qquad \text{(Equ. 3.2.32)}$$

where ϵ_0 is the electric constant and μ_0 is the magnetic constant, E is the electric field, B is the magnetic field and δ_{ij} is Kronecker's delta. The tensor represents the electromagnetic stress on a surface. Each component of the tensor describes the force per unit area in the respective direction.

2. Tensor Matrix Representation

In the normal coordinate for calclution of Maxswell Tensor, we could use a Matrix to represent the values and elements:

$$\sigma_{ij} = \begin{bmatrix} \sigma_{xx} & \sigma_{xy} & \sigma_{xz} \\ \sigma_{yx} & \sigma_{yy} & \sigma_{yz} \\ \sigma_{zx} & \sigma_{zy} & \sigma_{zz} \end{bmatrix} \quad \text{(Equ. 3.2.33)}$$

Since σ_{xx}, σ_{yy}, σ_{zz} represent the normal stress;

σ_{xy}, σ_{yz}, σ_{zc} represent the shear stress.

In our model, regardless of the chosen computational or numerical method for calculating and simulating the Concentric Magnetic Gears (CMGs), the force and stress components along the Z-axis are considered negligible and therefore ignored. This assumption simplifies the analysis by reducing the three-dimensional (3x3) stress tensor matrix to a two-dimensional (2x2) matrix. Consequently, the torque calculation is focused solely on the X-Y plane, where the primary magnetic interactions occur. This reduction not only optimizes computational efficiency but also aligns with the inherent planar magnetic flux distribution characteristic of CMGs.

3. Electromagnetic Force and Torque Calculation

Electromagnetic Force Calculation

According to the discussion above about the Maxwell Stress Tensor, the Electromagnetic Force **F** is easy to be calculated by the integrating the 2D Maxwell Stress Tensor over a closed path (contour) in the 2D plane:

$$\mathbf{F} = \oint \sigma_{ij} \, dl \quad \text{(Equ. 3.2.34)}$$

The integration is carried out along a closed contour, which is typically selected to coincide with the boundaries of the air gap region between the inner and outer rotors. Here, dl represents the differential element along this contour. By substituting the simplified 2D stress tensor matrix from Equation (2.2.11) into Equation (2.2.12), the expression for magnetic torque expands as follows:

$$\mathbf{F} = \oint \begin{bmatrix} \sigma_{xx} & \sigma_{xy} \\ \sigma_{yx} & \sigma_{yy} \end{bmatrix} dl \qquad \text{(Equ. 3.2.35)}$$

Physical Meaning the line integral sums up the differential forces along the boundary path, yielding the net electromagnetic force in the 2D plane.

Electromagnetic Torque Calculation

Torque quantifies the rotational influence of a force applied at a certain distance from the axis, and is computed as the product of the force and its perpendicular offset from the rotational axis. Mathematically, it could be derived into:

$$\mathbf{T} = \oint (\mathbf{r} \times \sigma_{ij})\, dl \qquad \text{(Equ. 3.2.36)}$$

Where the **r** is the position vector relative to the axis of rotation and cross production to the force means the rotate torque in the close loop path. By substituting the simplified 2D stress tensor matrix from Equation (2.2.11) into Equation (2.2.14), the expression for magnetic torque expands as follows:

$$\mathbf{T} = \oint (x(\sigma_{xx} + \sigma_{xy}) - y(\sigma_{yx} + \sigma_{yy})\, dl \qquad \text{(Equ. 3.2.37)}$$

Finally, the torque equation can be derived from the Maxwell Stress Tensor equations. Additionally, there exists a relationship between the Stress Tensor and **B** is the Magnetic Flux Density. By substituting the simplified 2D stress tensor matrix from Equation (2.2.10) into Equation (2.2.15), we can obtain an expression that relates Magnetic Flux Density to Electromagnetic Torque:

$$\mathbf{T} = \frac{r^2}{\mu_0} \int_0^{2\pi} B_r B_\theta \, d\theta \qquad \text{(Equ. 3.2.38)}$$

Where the B_r and B_θ is conversion values from Cartesian coordinates (x, y) to polar coordinates (r, θ). Recalling **Sections 2.1.1 and 2.1.2**, we have introduced in detail the methods for calculating the magnetic flux density using two different approaches: the Mathematical Method and the Numerical Method (FEM).

In the Mathematical Method, analytical equations were derived based on the magnetic field distribution within the defined geometric boundaries, allowing for an exact representation of B_r and B_θ in polar coordinates. This method is particularly efficient for idealized geometries where the boundary conditions are well-defined and the material properties are uniform. Since the magnetic flux density in CMGs is computed on a 2D polar plane, obtaining the actual torque requires multiplying the result by L which represents the effective axial length of the gear.

2. Mathematical Method

In the Mathematical Method, analytical equations were derived based on the magnetic field distribution within the defined geometric boundaries, allowing for an exact representation of B_r and B_θ in polar coordinates. This method is particularly efficient for idealized geometries where the boundary conditions are well-defined, and the material properties are uniform.

As the magnetic flux density in the CMG is computed only on the two-dimensional polar plane, the derived torque expression represents the torque per unit length along the axial direction. To compute the real torque of the actual CMG, it is necessary to account for its effective axial length. Thus, the total electromagnetic torque can be obtained by multiplying the derived 2D torque expression by the effective axial length L of the CMG:

$$T_{total} = T_{2D} * L \qquad \text{(Equ. 3.2.39)}$$

This multiplication extends the 2D torque calculation into the real three-dimensional space, providing an accurate estimation of the torque generated by the entire CMG structure.

$$\mathrm{T_m}(r) = L * \frac{r^2}{\mu_0} \int_0^{2\pi} B_r B_\theta \, d\theta \qquad \text{(Equ. 3.2.40)}$$

The choice of the radius *r* is crucial, as it reflects the region where the torque is being evaluated:

- In the case of the inner rotor, *r* represents the effective radius within the magnetic region where field interaction occurs.
- For the outer rotor, *r* denotes the radial position along the outer magnetic path that significantly contributes to torque production through magnetic flux interaction.

The expression remains valid for both configurations, provided the correct radius is selected during integration. This flexibility allows for targeted torque calculations in different regions of the CMG, enhancing design optimization and performance analysis.

3. Numerical Method (FEM)

On the other hand, the Numerical Method (FEM) enables the computation of magnetic flux density in more complex and irregular geometries. By discretizing the region into finite elements, FEM solves Maxwell's equations locally at each element, accounting for non-linear material properties, complex boundary conditions, and the interactions between magnetic components. Through this method, we obtained the Cartesian components B_x and B_y, which were then converted to their polar counterparts using the transformations:

$$B_r = B_x \cos(\theta) + B_y \sin(\theta) \quad \text{(Equ. 3.2.41)}$$

$$B_\theta = -B_x \sin(\theta) + B_y \cos(\theta) \quad \text{(Equ. 3.2.42)}$$

These two approaches complement each other by providing both theoretical insight and practical accuracy, forming the foundation for further torque calculations in electromagnetic systems.

In the Numerical Method (FEM) we have discuss the model setup steps and show the FEM simulation results in the **Table. 3.6**.

Due to the coordinate system setup in the MATLAB PDE Toolbox, which is inherently defined by Cartesian coordinates, the final expression for the electromagnetic torque within the CMG's ring must be transformed accordingly. To achieve this, Equations (2.2.19) and (2.2.20), representing the electromagnetic torque in polar coordinates, are substituted into Equation (2.2.18). This substitution facilitates the conversion of the electromagnetic torque expression from polar coordinates back to Cartesian coordinates, aligning with MATLAB's computational framework. This step ensures that the torque calculations are compatible with the finite element analysis and post-processing operations within the MATLAB environment.

Table 3.5. Concentric Magnetic Gear (CMG) FEM simulation results.

MagneticPotential:	[155165×1 double]
MagneticField:	[1×1 FEStruct]
MagneticFluxDensity:	[1×1 FEStruct]
Mesh:	[1×1 FEMesh]

Beyond the transformation from Cartesian to polar coordinates, the fundamental concept of the Finite Element Method (FEM) involves discretizing a complex domain into smaller, manageable elements connected through defined nodal points. Instead of attempting to solve the entire complex problem simultaneously, FEM approaches the problem locally within each finite element. By applying the governing physical equations (such as Maxwell's equations for magnetic fields) to these smaller regions, FEM computes local solutions. The individual element-level solutions are integrated to construct a comprehensive global approximation, which reflects the physical response of the complete structure.

The integration of magnetic flux density equations used to calculate electromagnetic torque is fundamentally a process of summing the effects of magnetic flux components across the defined spatial region. For numerical computation, this continuous integration is approximated by a summation of discrete elements:

$$\mathrm{T_m}(r) = L * \frac{r^2}{\mu_0}\int_0^{2\pi} B_r B_\theta \, d\theta = L * \frac{r^2}{\mu_0}\sum_{n=1,2,3,\ldots}^{\infty} B_r(r,\theta) B_\theta(r,\theta) \quad \text{(Equ. 3.2.43)}$$

$$\mathrm{T_m}(r,x,y) = L * \frac{r^2}{\mu_0}\int_0^{2\pi} B_r B_\theta \, d\theta = L * \frac{r^2}{\mu_0}\sum_{n=1,2,3,\ldots}^{\infty} B_x(x,y) B_y(x,y) \quad \text{(Equ. 3.2.44)}$$

Regardless of the coordinate system used, the fundamental principle holds that electromagnetic torque results from the integrated effect of magnetic field interactions along the spatial domain, represented as a series of discrete elements when implemented in computational methods.

4. Torque FEM Simulation Steps and Results:

Continued from the procedures established in Section 2.1.4 for the FEM simulation of magnetic field and flux density in Concentric Magnetic Gears (CMGs), the next crucial step is the simulation of electromagnetic torque. This process involves the careful definition of a ring or closed-loop path within the magnetic structure, which serves as the region of interest for torque calculation.

The torque simulation relies on selecting a specific closed-loop path that encapsulates the region where the magnetic interaction primarily contributes to torque generation. In our simulation, we employ the Cartesian coordinate system *(x,y)* to accurately define the nodes along this closed path. The selection of this loop is critical, as it represents the boundary along which the magnetic stress tensor components are integrated to determine the torque output.

By defining the closed-loop path through these *(x,y)* coordinates (**Fig. 3.8**), we can accurately represent the integration path across the CMGs' regions, particularly around the air gaps and flux modulators. This transformation allows us to sum the electromagnetic interactions at each node, reflecting the local contributions to torque.

In the FEM model, this integration of Equ 2.2.22 is discretized into a summation over the nodes located along the closed-loop path:

$$\mathrm{T_m}(r,x,y) = L * \frac{r^2}{\mu_0}\int_0^{2\pi} B_r B_\theta \, d\theta = L * \frac{r^2}{\mu_0} * \frac{2\pi r}{N}\sum_{n=1}^{N} B_x(x_n, y_n) B_y(x_n, y_n)$$

(Equ. 3.2.45)

The FEM simulation outputs the magnetic flux densities at each node along the path. These results are then processed to compute the torque by summing the contributions as outlined above. This method provides an accurate estimation of the electromagnetic torque generated by the CMG, accounting for all local variations in magnetic flux interactions.

5. Torque FEM Simulation Results and Summary:

Figure 3.9 displays the torque results obtained through both the analytical computational approach and the finite element method (FEM), highlighting the torque characteristics of a concentric magnetic gear (CMG) operating at a gear ratio of 1:3. The torque values are determined by the static geometric configuration of the CMG, meaning that once the physical design parameters are fixed, the torque output remains constant. However, the angular position θ is introduced as a variable to represent the relative positioning of the Inner Rotor, Outer Rotor, and Ferro Modulators. By varying θ, we can observe the torque ripple and performance under different alignment conditions. **Fig. 3.9 a) & b)** presents the comparative analysis of torque values generated by the Computational Method and FEM Method can get the value in the inner/outer rotor.

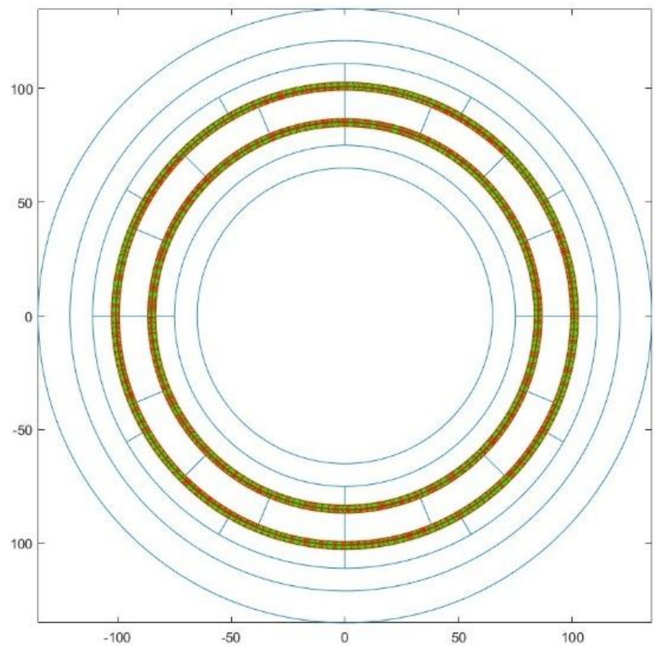

Fig. 3.8. Concentric Magnetic Gear (CMG) geometric layout and flux path visualization.

The angular variation of θ is mapped against the calculated torque, highlighting any discrepancies or phase shifts in torque output between the two methods. The FEM method typically captures localized magnetic saturation and flux leakage effects that are often idealized in the Computational Method, resulting in a more detailed representation of torque ripples.

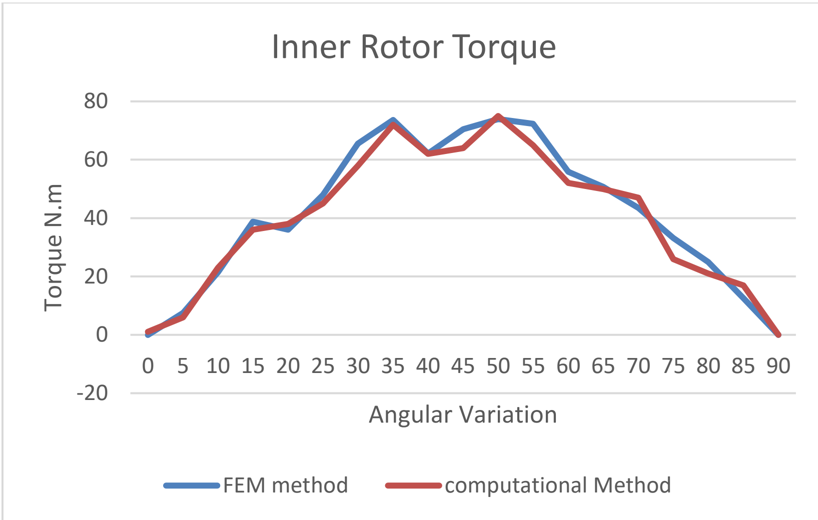

Fig. 3.9. a) Inner torque comparasion vs angular variation.

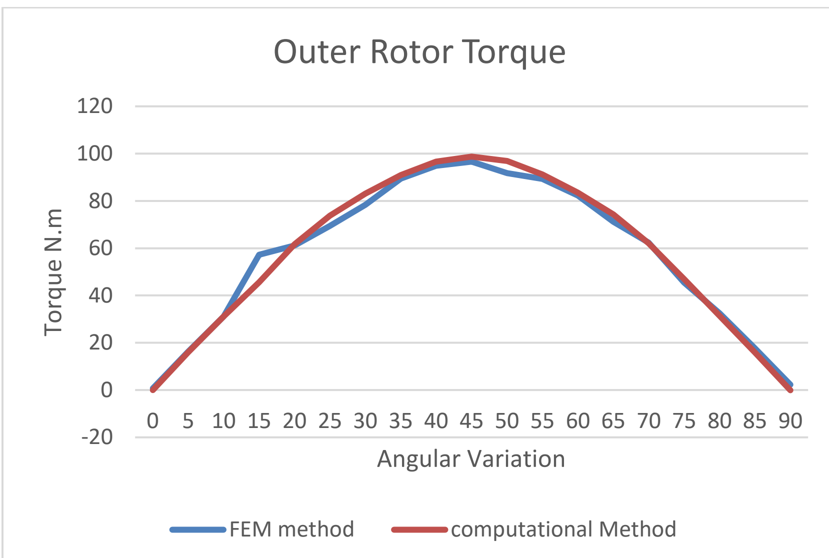

Fig. 3.10. b) Outer torque comparasion vs angular variation.

3.3 Magnetic and Mechanical Dynamic Simulation Model Establish

This section presents a comprehensive simulation model aimed at analyzing the intrinsic dynamic characteristics of magnetic gears. Building upon the static torque transmission model developed in the previous sections, this dynamic model captures the coupled interactions between electromagnetic torque generation and the mechanical response of the system under various operating conditions. Through both transient and steady-state simulations, the model provides critical insights into phenomena such as torque ripple, dynamic stiffness, and vibration modes. Such dynamic analysis is essential for assessing the stability, responsiveness, and overall performance of magnetic gears, especially in drivetrain applications that demand high torque density and smooth, reliable operation.

3.3.1 Static Torque Variation of Coaxial Magneitc Gear Transmission

In the preceding discussion, two approaches for estimating the torque output of a magnetic gear were introduced: an analytical formulation and a finite element method (FEM)-based numerical simulation. Once the geometric configuration is established, the magnetic contributions from the permanent magnets and ferromagnetic yokes are incorporated into the total torque estimation. The gear ratio can be tuned by modifying the number of pole pairs on the inner and outer rotor assemblies [103]. Each rotor produces a spatially distributed magnetic flux that interacts with the ferromagnetic pole pieces. The ferromagnetic modulator alters these flux distributions within both air gaps, facilitating the coupling of spatial harmonics shared between the two rotors [104]. This coupling gives rise to a sustained magnetic torque characterized by a non-zero mean value over a mechanical rotation cycle.

To extend the static magnetic torque calculation into a dynamic torque response for the inner and outer rotors, it is necessary to revisit the magnetic flux equations (Equations 3.2.14 - 3.2.17) describing the interaction between the inner and outer permanent magnets. These equations allow magnetic flux to be calculated at specific regions or discrete points by assigning fixed values to the radial and angular coordinates r and θ. However, in a dynamic magnetic gear system, the magnetic field distribution evolves over time, and the magnetic flux varies accordingly. As a result, several constants in the static formulation become time-dependent variables. For instance, θ_{in0}, θ_{m0} and θ_{out0} now represent the initial angular positions of the inner rotor, the ferromagnetic modulators, and the outer rotor, respectively, and their values evolve with rotor motion during dynamic operation.

$$B_{rin}(r,\theta) = \sum_{n=1,3,5,\ldots}^{\infty} b_{rin}(r)\cos\left[n * p_{in} * (\theta - \omega_{in} * t) + np_{in}\theta_{in0} + (n+1)p_{out}\theta_{out0} - nN_m\theta_{m0}\right] \quad \text{(Equ. 3.2.14)}$$

$$B_{\theta in}(r,\theta) = \sum_{n=1,3,5,\ldots}^{\infty} b_{\theta in}(r)\sin\left[n * p_{in} * (\theta - \omega_{in} * t) + np_{in}\theta_{in0} + (n+1)p_{out}\theta_{out0} - nN_m\theta_{m0}\right] \quad \text{(Equ. 3.2.15)}$$

$$B_{rout}(r,\theta) = \sum_{n=2,4,6,\ldots}^{\infty} b_{rout}(r)\cos\left[n * p_{out} * (\theta - \omega_{out} * t) + (n-1)p_{in}\theta_{in0} + np_{out}\theta_{out0} - nN_m\theta_{m0}\right] \quad \text{(Equ. 3.2.16)}$$

$$B_{\theta out}(r,\theta) = \sum_{n=2,4,6,\ldots}^{\infty} b_{\theta out}(r)\sin\left[n * p_{out} * (\theta - \omega_{out} * t) + (n-1)p_{in}\theta_{in0} + np_{out}\theta_{out0} - nN_m\theta_{m0}\right] \quad \text{(Equ. 3.2.17)}$$

In the geometry illustrated in **Fig. 3.11**, the angular positions of the inner rotor, outer rotor, and ferromagnetic modulators are denoted as θ_{in0}, θ_{m0} and θ_{out0} respectively, within the static FEM CAD model. Variations in these angular positions influence the spatial alignment between magnetic components, which in turn affects the distribution of magnetic flux and field intensity. Consequently, the magnetic torque generated in each component will vary with their relative positions. Based on this principle, a torque–angle relationship can be established, allowing the derivation of a torque profile as a function of angular displacement between the rotors and modulators.

Under normal operating conditions, a magnetic gear typically consists of a fixed ferromagnetic modulator, while the inner and outer rotors are both allowed to rotate. One of the rotors functions as the input and the other as the output. To investigate the torque transmission mechanism based on the relative angular position between magnetic components, we conducted a phase-based analysis. In this analysis, the ferromagnetic modulator and the outer rotor with permanent magnets were kept stationary, while the angular position of the inner rotor was systematically varied. This approach enabled us to observe how the transmitted torque changes in response to the angular misalignment

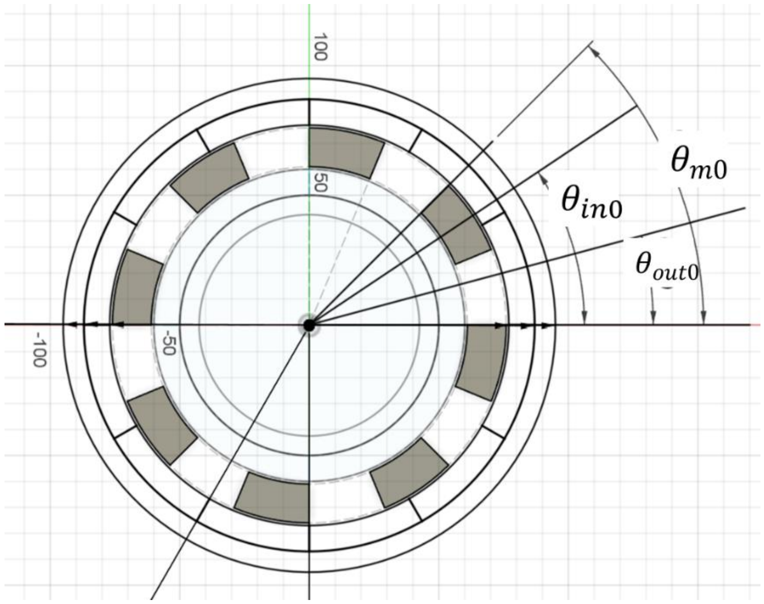

Fig. 3.11. Concentric Magnetic Gear angular position.

between the inner and outer rotor magnets. The torque variation was calculated using our MATLAB-based finite element method (FEM), by continuously adjusting the position of the inner rotor within the defined geometry.

As illustrated in **Fig. 3.12** (1) through (18), the inner rotor is rotated incrementally in 5-degree steps, as specified in **Table 3.7**, while both the outer rotor and the ferromagnetic modulator are held stationary. Using the torque data computed via the MATLAB-based finite element method (FEM), a torque-angle profile is generated to reveal how the torques acting on the inner and outer rotors vary with their relative angular displacement. The modeled system corresponds to a coaxial magnetic gear (CMG) configuration with a transmission ratio of 2:3. In this setup, the inner rotor comprises two pole pairs, the outer rotor has three pole pairs, and five ferromagnetic segments serve as the modulation elements. **Fig. 3.13** displays the torque fluctuations on both rotors as functions of the angular position of the inner rotor. By defining the initial angular positions of all components, the inner rotor's position can be converted into the relative angle between the two rotors, which is essential for analyzing torque transmission behavior.

Table 3.6. Inner rotor angular position variation vs. inner/outer rotor torque.

inner angular position	inner torque	outer torque	inner angular position	inner torque	outer torque
0	-0.8318	2.2908	95	5.976	-21.2607
5	-22.6429	18.0496	100	46.0209	-36.9229
10	-9.7641	33.3142	105	27.1746	-52.3917
15	-41.8124	49.1155	110	43.6685	-68.2816
20	-40.2495	64.8725	115	42.1171	-81.0306
25	-42.9139	77.6146	120	42.7537	-89.9717
30	-58.3336	85.9685	125	36.0112	-98.6818
35	-15.9392	95.5274	130	64.8575	-105.2776
40	-54.1522	98.1755	135	62.4305	-106.7863
45	-50.9619	100.5239	140	46.939	-104.6471
50	-63.7675	97.8958	145	67.9273	-98.2399
55	-50.9594	90.5565	150	63.3241	-89.3453
60	-44.0992	81.5832	155	46.803	-78.0923
65	-43.1207	73.2371	160	35.64	-65.0093
70	-41.1401	58.0781	165	34.0327	-47.6258
75	-26.1437	42.4422	170	11.827	-30.2722
80	-35.8673	26.6915	175	11.7988	-14.0751
85	-11.3918	11.1045	180	-0.8318	2.2908
90	-0.7489	-3.2262			

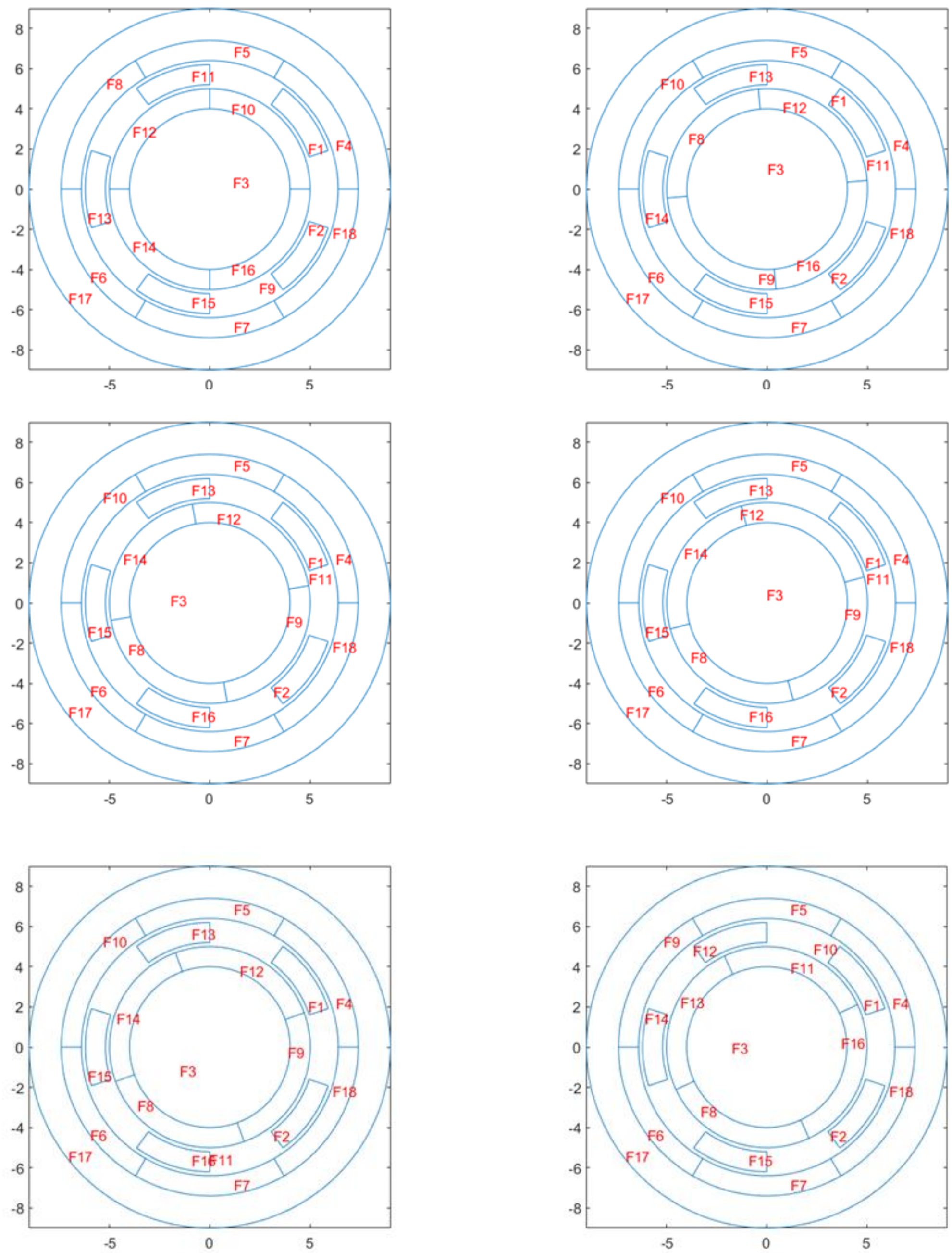

Fig. 3.12. (1) – (18) The angular position variation of inner rotor.

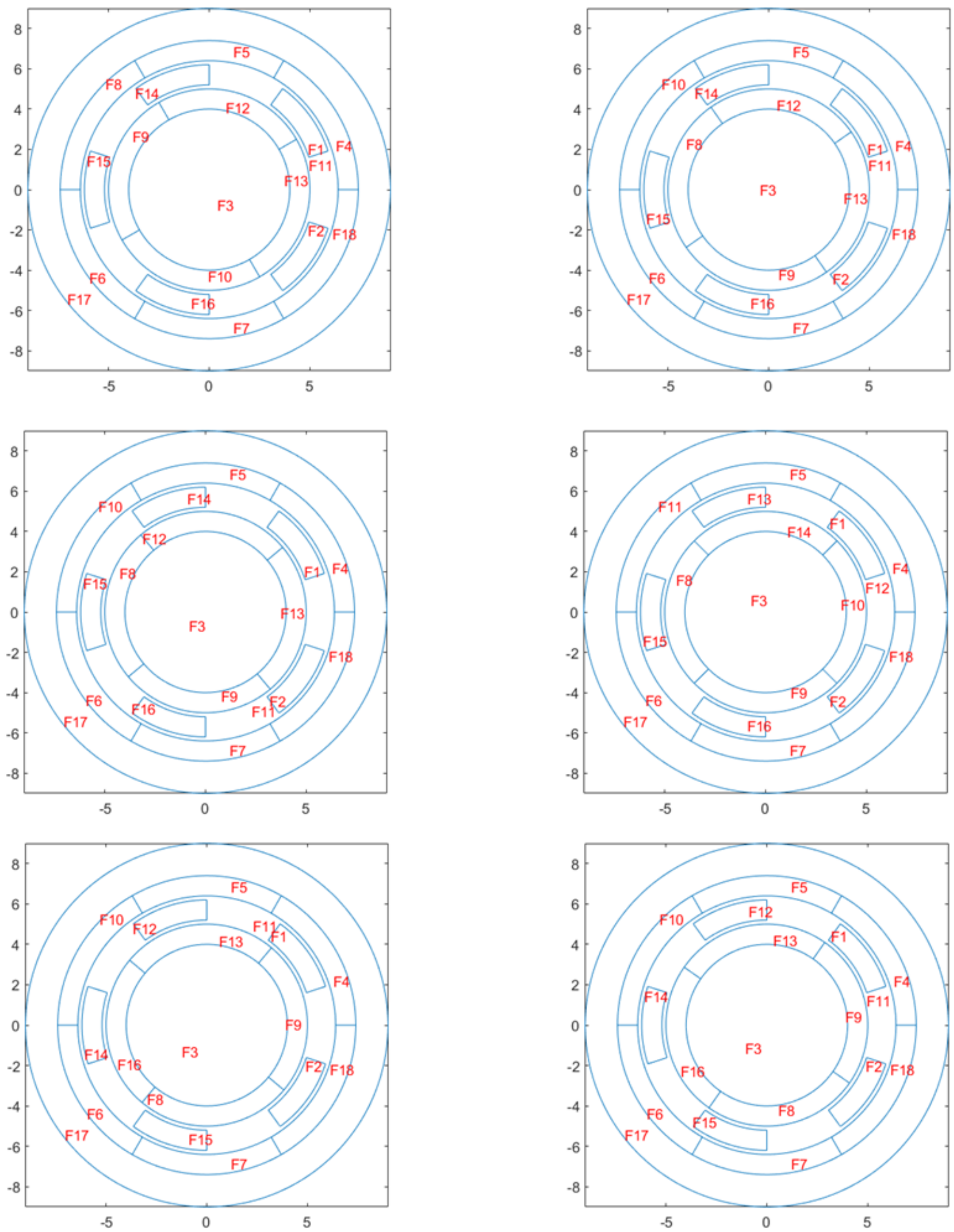

Fig. 3.13. (Continued) The angular position variation of inner rotor.

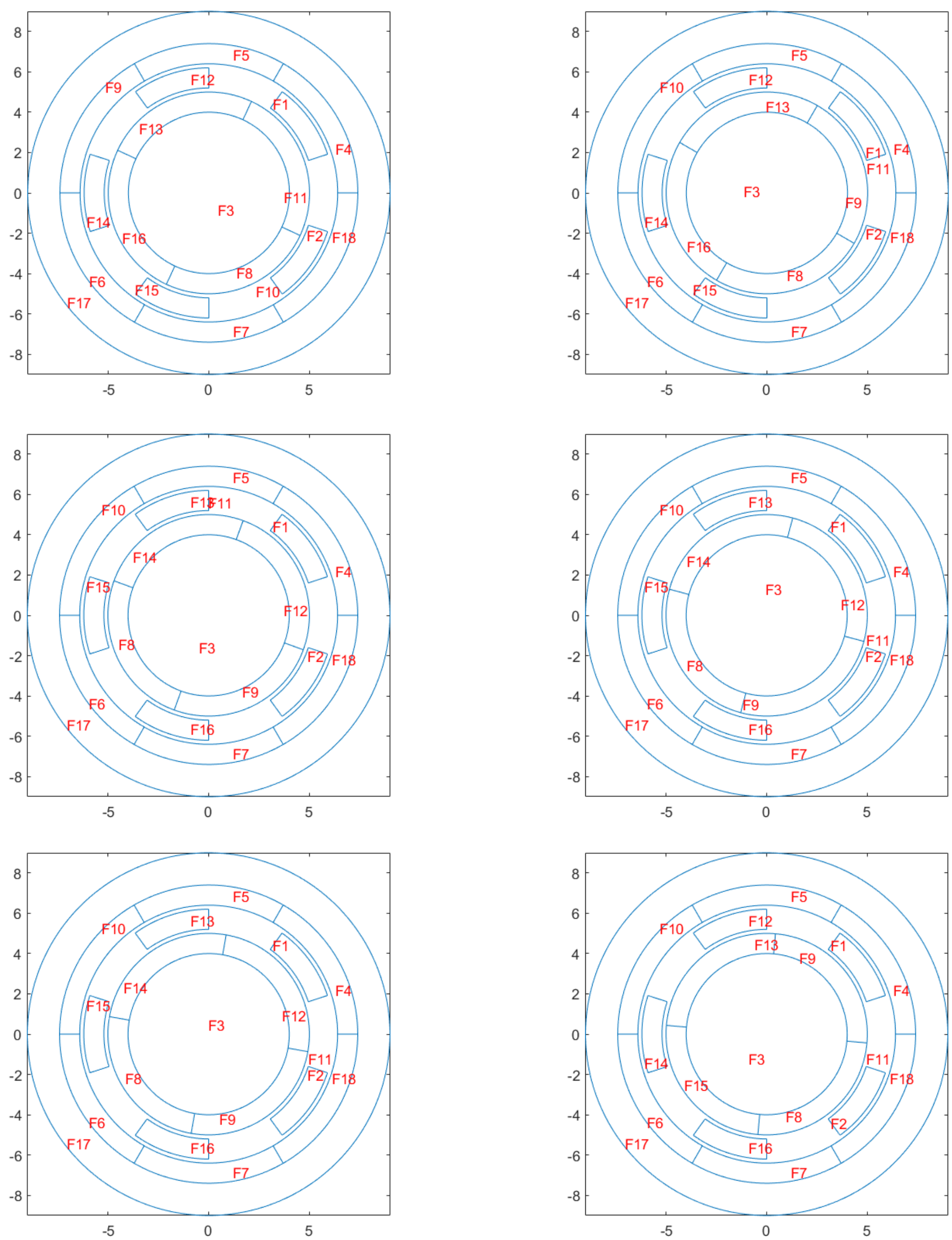

Fig. 3.14. (Continued) The angular position variation of inner rotor.

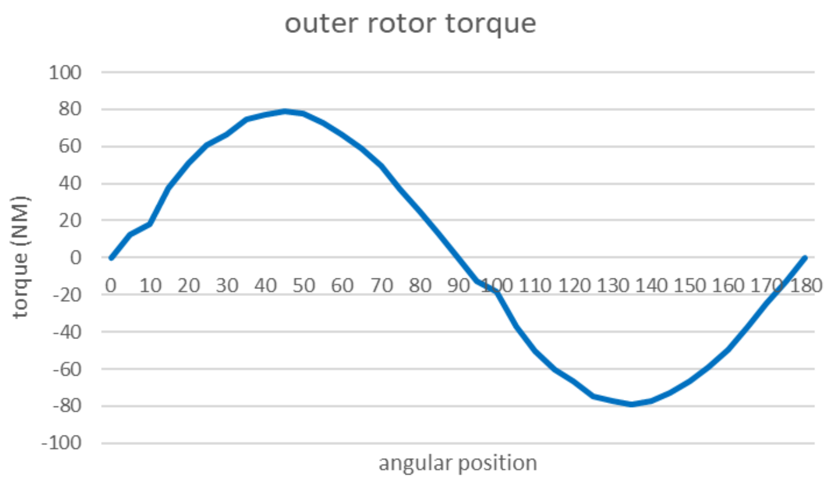

Fig. 3.15. a) Outer rotor torque by FEM method.

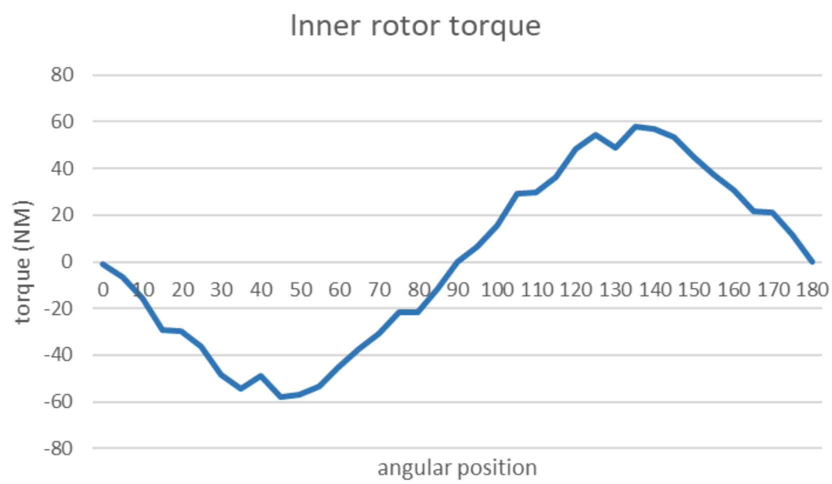

Fig. 3.16. b) Inner rotor torque by FEM method.

Based on the structure of the 2:3 gear ratio coaxial magnetic gear (CMG), the size of a single magnetic pole on the inner rotor is determined by its radius and spans an angular range of 90 degrees. As a result, the torque response of the system exhibits periodicity with respect to the inner rotor, where one full period corresponds to a 90-degree rotation. Rotating the inner rotor from 90 to 180 degrees merely reverses the sequence of the magnetic poles, effectively producing a mirrored torque response. Therefore, the torque analysis in the previous figure is limited to the range of 0 to 90 degrees, which sufficiently captures the fundamental variation within one complete period. The torque profiles of the inner and outer rotors are presented in **Fig. 3.13**. The outer rotor torque exhibits a nearly ideal sinusoidal pattern, reaching a peak amplitude of approximately 78 Nm. Additionally, a clear transition from positive to negative torque occurs during the second half of the inner rotor's rotational phase, consistent with the periodic behavior expected from the relative pole alignment.

In contrast, the inner rotor torque exhibits an irregular pattern with significant fluctuations over the 0-to-180-degree range. The torque varies between a minimum of -57 Nm and a maximum of 55 Nm, which are nearly equal in magnitude but opposite in direction. Although the overall trend resembles a reversed sinusoidal waveform, it is superimposed with considerable noise and disturbances. The torque irregularities may result from variations in the magnetic field distribution, imperfections or non-uniform spacing within the air gap between the inner rotor and the ferromagnetic modulator, as well as minor asymmetries in the magnetic coupling process. Furthermore, the small number of pole pairs on the inner rotor could also lead to a less smooth torque profile. According to theoretical principles of magnetic gear operation, the torque ratio between the inner and outer rotors is expected to be the inverse of the corresponding speed ratio:

$$\frac{p_i}{p_o} = \frac{\omega_o}{\omega_i} = \frac{T_i}{T_o} = \frac{2}{3}$$

Firstly, comparing the maximum and minimum torque values of the inner and outer rotors yields ratios of approximately $-\frac{55}{78}$ and $-\frac{54}{78}$, respectively. The negative signs indicate the opposite rotational direction between the input and output rotors, as expected in torque transmission. When compared to the theoretical or conceptual torque ratio of 0.66 (based on the 2:3 pole pair ratio), the observed values show only a 0.5% to 1% deviation, indicating good agreement with the expected transmission behavior.

In addition to the torque ratio, the critical points at which the torque cycle transitions (such as the zero-crossings or phase shifts and the maximum/minimum peak point) serve as important indicators for validating the accuracy and periodicity of the magnetic gear's operation. These transition points help confirm whether the torque behavior aligns with the theoretical expectations based on the gear's pole configuration and relative motion. As shown in **Table 3.7**, the outer rotor torque reaches its maximum at 45 degrees and its minimum at 135 degrees. In contrast, the inner rotor torque reaches its minimum at 45 degrees and its maximum at 135 degrees, indicating a phase shift between the two. The zero-crossing point for both inner and outer rotor torques consistently occurs around 90 degrees, further supporting the symmetry align with the size and angular design of the inner rotor poles and periodicity predicted by the CMG gear's design.

3.3.2 Dynamic Torque Variation of Coaxial Magnetic Gear Transmission

The dynamic torque behavior of the coaxial magnetic gear (CMG) is evaluated by extending the static angular position analysis into a representation of continuous rotational motion. Through the static torque response, the peak and trough values corresponding to specific angular alignments of the inner and outer rotors are identified. These torque variations, dependent on the inner rotor's position, reveal the influence of relative rotor alignment on magnetic coupling. By interpolating the discrete torque data points obtained from static simulations, a continuous torque profile can be synthesized to approximate the dynamic performance of the CMG during real-time operation.

In order to achieve such a dynamic transmission simulation performance, we should have such an assumption that to convert static torque response analysis into a dynamic torque estimation model for CMGs:

1. Rigid Geometry and Magnetic Structure

It is assumed that the geometry, material property (permeability of permanent magnets and ferro material, the maximum magnetization of PMs), and the airgap remain constant throughout the dynamic rotation

2. Constant Loading Condition

Similar to the static torque variation analysis, we fix the ferro modulator and the outer rotor as static, immovable components that only interact with the rotating inner rotor through magnetic flux. In the dynamic case, torque is generated by the relative motion between two rotating components—the inner and outer rotors. Both rotors operate under constant loading during rotation, meaning there is no fluctuation in applied load over time.

3. Constant Angular Rotational speed

The inner and outer rotor is assumed to rotate at a uniform angular speed, to have a linear relationship between relative angular position over time.

4. No Heating Effect in Magnetization

The effects of temperature on the permeability and magnetization of permanent magnets and ferro modulators are ignored in this analysis.

With such assumptions in the CMG, we could establish a torque calculation analysis by making couple of figures illustrate the geometry rotation. Based on the result of static inner rotational rotor analysis, we could find that the torque transmit in the inner and outer rotor is variate depending on the relative angular position of the inner and outer rotor.

Therefore, it is necessary to establish appropriate timing for applying loads to both the inner and outer rotors. One way to conceptualize this is to assume a high load applied to the outer rotor (not exceeding the maximum torque determined from static analysis). Initially, the inner rotor begins to rotate while the relative angular position between the rotors is insufficient to generate enough torque/force to overcome the outer rotor's load. As rotation continues and the relative alignment progresses, the torque transmission increases. Once it reaches a threshold where the generated torque exceeds the resistance on the outer rotor, the outer rotor begins to rotate. From that point on, it can achieve a steady rotational speed, as assumed in the dynamic model setup.

Based on the magnitude of the applied load and the initial relative angular position between the inner and outer rotors, different operating conditions can be defined for the CMG system. Specifically:

Condition I: No Outer Rotor Movement

When the initial relative angular position is small and the generated torque is insufficient to overcome the external load on the outer rotor, the system remains in a static state with only the inner rotor rotating. No motion is transferred to the outer rotor. Same as static analysis.

Condition II: Early Engagement (Intermediate Steady-State Operation)

If the load on the outer rotor is high but still within the static torque transmission capability, and the inner rotor continues rotating, the system will eventually reach a relative angular alignment where the generated torque becomes sufficient to overcome the load. However, this engagement does not necessarily occur at the point of maximum torque transmission. Instead, the outer rotor begins to move once the transmitted torque exceeds the load threshold, which may happen before the relative alignment reaches its peak torque condition. This scenario reflects a phase transition from static coupling to dynamic motion, where the system shifts from a locked state to active torque transfer between the rotors.

Condition III: Fully Engagement (Full Steady-State Operation)

When the initial relative angle and applied load allow for immediate torque transfer, both rotors can rotate in a synchronized, steady-state manner. The outer rotor begins moving shortly after the inner rotor initiates motion, consistent with the assumed torque ratio and velocity ratio derived from the gear's pole configuration.

Since Condition I corresponds directly to the static torque variation analysis already presented, we will focus on illustrating Condition II and Condition III, which represent approximately 70% steady-state engagement and full steady-state operation, respectively. In the context of the 2:3 gear ratio CMG, this configuration implies that the inner rotor contains two pole pairs, the outer rotor contains three pole pairs, and the system includes five ferromagnetic pole pieces. These conditions highlight how torque builds and transitions under dynamic loading as the system moves from partial engagement to full transmission.

Condition II: 70% steady-state operation

As described in **Table 3.8** and illustrated in **Fig. 3.19**, the inner rotor functions as a steady-state input, maintaining a constant torque and angular velocity. During the initial phase—corresponding to the inner rotor's rotation from 0 to 20 degrees—the generated torque is insufficient to overcome the applied 50 Nm load on the outer rotor, resulting in no movement of the output shaft. Once the inner rotor advances beyond approximately 20 degrees, the relative angular alignment allows the magnetic coupling to produce torque exceeding the load threshold, initiating rotation of the outer rotor. Following this point, both rotors achieve synchronized motion governed by the gear ratio. The inner rotor continues rotating at 9 degrees per second, while the outer rotor follows at 6 degrees per second, consistent with the expected 2:3 speed-to-torque transmission relationship.

Under this condition, the resulting torque behavior is shown in **Fig. 3.20** & **21**. As expected from the design phase, the inner rotor begins rotating from 0 to 20 degrees with an increasing torque magnitude (ignoring the negative sign that indicates direction). During this interval, the outer rotor remains stationary due to the applied load of 50 Nm, which exceeds the torque transmitted from the inner rotor (**Fig. 3.20**). However, as the relative angular position progresses, the transmitted torque continues to rise. At approximately 20 degrees, the inner rotor generates a torque of 51 Nm at the interface with the ferromagnetic modulator, surpassing the load threshold. This initiates engagement, and the outer rotor begins to rotate (**Fig. 3.21**).

After engagement, the torque values of both the inner and outer rotors begin to stabilize. However, a small amount of torque ripple remains, with the inner rotor showing approximately 6.3% fluctuation and the outer rotor only 0.33%. This reflects a reasonably stable transmission at the outer rotor, consistent with the expected behavior under a 70% steady-state CMG operation.

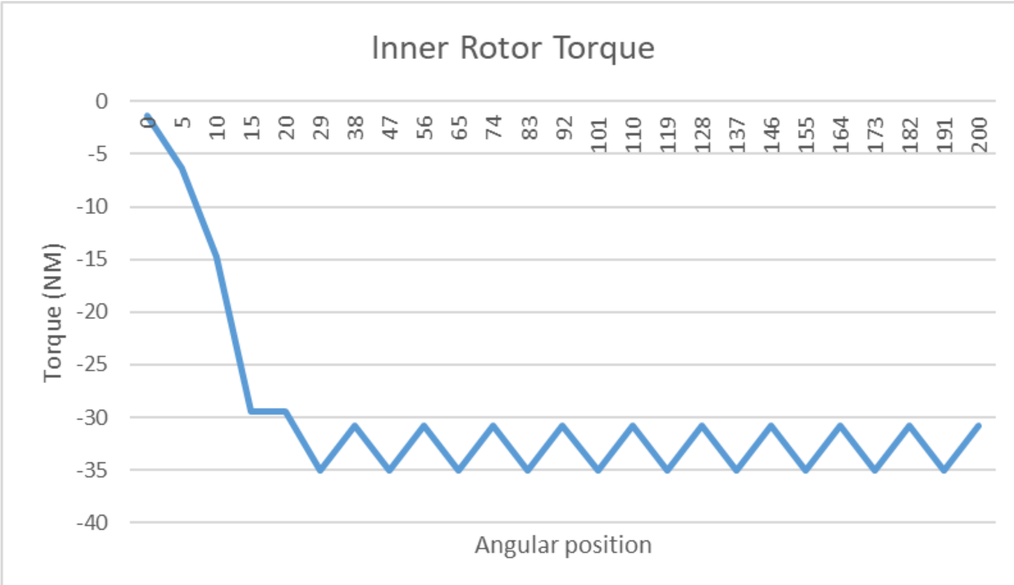

Fig. 3.20. a) Inner rotor torque transmission in Condition II.

The observed torque ripple may result from several factors, including magnetic field harmonics due to the discrete number of poles, minor geometric asymmetries, variations in air gap distribution, and localized magnetic saturation. These effects can cause fluctuations in magnetic coupling, leading to periodic torque variations even under steady-state operation.

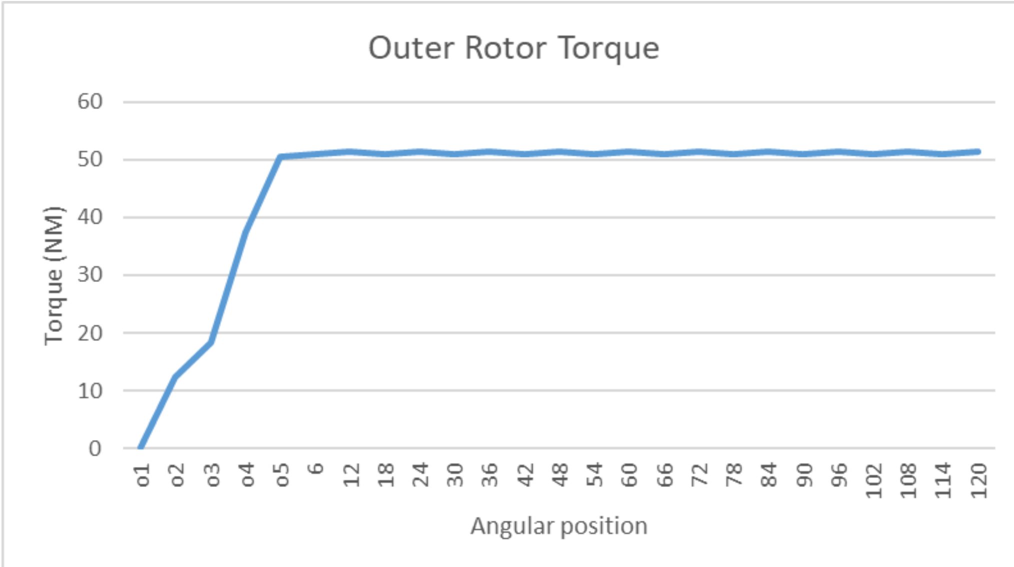

Fig. 3.21. b) Outer rotor torque transmission in Condition II.

Condition III: Fully Engagement (Full Steady-State Operation)

Similar to Condition II, this condition is shown in **Table 3.9** and **Fig. 3.23**. It skips the engagement phase in which the inner rotor must rotate to reach the torque threshold required to drive the outer rotor. Instead, the system enters full steady-state operation from the beginning. The inner rotor functions as a constant-speed input, rotating at 9 degrees per second with a steady torque output. From the initial position at 0 degrees, the relative angular alignment between the inner and outer rotors is already sufficient to generate torque greater than the 78 Nm load applied to the outer rotor. As a result, both rotors begin rotating simultaneously without delay. The outer rotor rotates at a synchronized lower speed of 6 degrees per second, consistent with the 2:3 gear ratio, and delivers the required output torque. This condition represents continuous and stable torque transmission, with both rotors fully engaged from the start of operation.

In Condition III, the torque responses of both rotors are presented in **Fig. 3.23**. As expected, the inner rotor begins rotation from the maximum torque position at 45 degrees and immediately transmits high torque to the outer rotor, overcoming the applied load

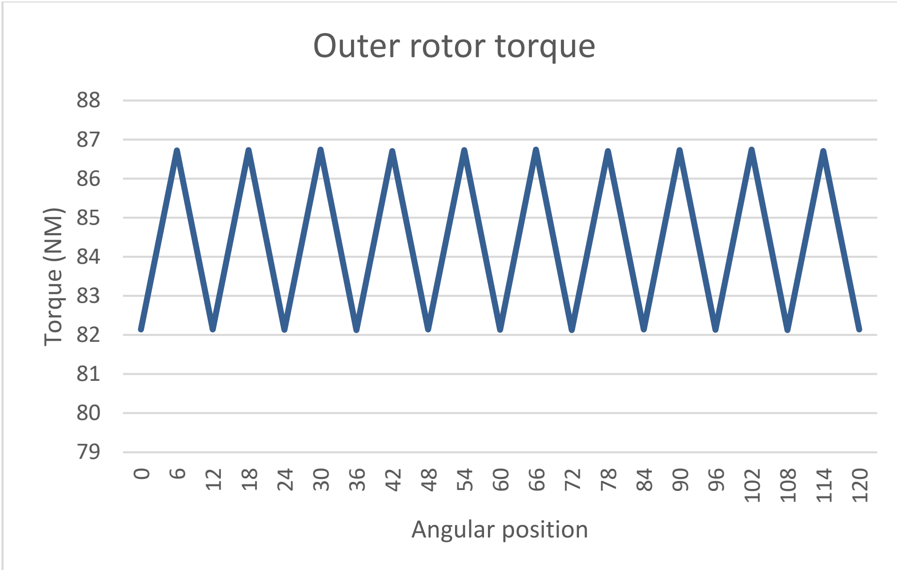

Fig. 3.25. b) Outer rotor torque transmission in Condition III.

and achieving synchronous rotation between the two rotors. Both rotors display periodic torque waveforms.

The inner rotor exhibits a repeating sawtooth pattern, fluctuating between –55 Nm and –47 Nm, corresponding to a torque ripple of approximately 7.8 percent (**Fig. 3.24 a**). In contrast, the outer rotor shows milder torque oscillations ranging from 82 Nm to 86 Nm, resulting in a fluctuation of about 3 percent (**Fig. 3.25 b**). This behavior reflects consistent torque output, in agreement with the anticipated performance of the coaxial magnetic gear (CMG) during full steady-state operation.

The observed torque ripple may be attributed to magnetic field harmonics caused by the discrete pole configuration, minor geometric asymmetries, variations in air gap spacing, and localized magnetic saturation. These factors contribute to periodic fluctuations in magnetic coupling, even under otherwise steady-state conditions.

Comparison of Condition II and Condition III

Conditions II and III represent two distinct dynamic behaviors of the coaxial magnetic gear (CMG) system during torque transmission. In Condition II, the system undergoes an initial engagement phase, where the inner rotor must first rotate through approximately 20 degrees before generating sufficient torque to overcome the outer rotor load. This results in a delayed start for the outer rotor and characterizes a transitional phase toward steady-state operation. In contrast, Condition III begins with full steady-state operation from the initial angular position. The torque generated by the inner rotor at 0 degrees is already sufficient to immediately engage and drive the outer rotor.

Both conditions demonstrate periodic torque waveforms in the inner and outer rotors, but with different levels of ripple. Condition II exhibits slightly higher ripple in the inner rotor (6.3%) and minimal ripple in the outer rotor (0.33%), indicating a smooth output after engagement. Condition III shows a slightly higher ripple in both rotors (7.8% inner, 3% outer), likely due to the more immediate load coupling.

Overall, Condition III reflects more efficient and stable transmission from the onset, whereas Condition II provides insight into the dynamic engagement process and torque buildup. Together, these two conditions help illustrate the torque transmission characteristics of CMGs under different loading and initialization scenarios.

3.3.3 General dynamic equation of coaxial magnetic gear transmission

In the section on magnetic flux and torque analysis modeling, both mathematical and numerical methods were employed to calculate and compare the results for coaxial magnetic gear (CMG) transmission. The analysis concludes that the magnetic flux and torque transmission in a CMG is primarily governed by the relative angular position between the inner and outer rotors. This relationship is governed by the spatial harmonic interactions between the magnetic fields produced by the permanent magnets and those shaped by the ferromagnetic modulator, as illustrated in **Fig. 3.26** [48].

Based on the flux calculations and the corresponding representation (**Fig. 3.21**) , it is evident that the resulting torque follows a similar pattern, typically resembling a sinusoidal function that describes the relationship between angular position and transmitted torque.

The general torque–angular position relationship can be approximated by a sinusoidal expression as:

$$T_r = (\pm)T_{max} * \sin\left(N_k * \Delta\theta_k + \varphi\right) \qquad \text{(Equ. 3.3.1)}$$

Where:

- The T_r is the rotor magnetic coupling torque,

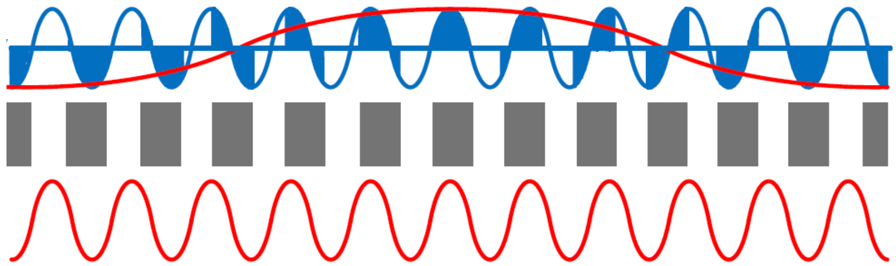

Fig. 3.26. Magnetic flux in coaxial magnetic gear transmission [48]

- The positive and negative sign mean the rotating direction of the components,
- The T_{max} is the maximum transmitted torque depending on the rotating components (determined by the magnetic loading, geometry and materials),
- The $\Delta\theta_k$ is the relative angular position of the inner and outer rotor and ferromagnetic modulator,
- The N_k is the pole pair or piece number of the inner and outer rotor and ferromagnetic modulator.
- The φ represent the initial relative angular position of the inner and outer rotor and ferromagnetic modulator.

The detailed torque expressions for each rotating component are provided in Equation (3.4.2 – 3.4.4).

$$T_{in} = (\pm)T_{m_{in}} * \sin\left(p_{in} * \theta_{in} + p_{out} * \theta_{out} - N_m * \theta_m + \varphi\right) \quad \text{(Equ. 3.3.2)}$$

$$T_m = (\pm)T_{m_m} * \sin\left(p_{in} * \theta_{in} + p_{out} * \theta_{out} - N_m * \theta_m + \varphi\right) \quad \text{(Equ. 3.3.3)}$$

$$T_{out} = (\pm)T_{m_{out}} * \sin\left(p_{in} * \theta_{in} + p_{out} * \theta_{out} - N_m * \theta_m + \varphi\right) \quad \text{(Equ. 3.3.4)}$$

And the relationship between $T_{m_{in}}$, T_{m_m} and $T_{m_{out}}$ is follow the relation of the poles number of inner and outer pole and piece number of ferromagnetic modulators.

$$\left|\frac{T_{out}}{p_{out}}\right| = \left|\frac{T_{in}}{p_{in}}\right| = \left|\frac{T_m}{N_m}\right|$$

Which is reverse of the speed and poles numbers relationship. Based on the generalized torque expression, the torque transmission behavior in a coaxial magnetic gear (CMG) can be effectively described using a limited set of parameters, including the number of pole pairs on the inner and outer rotors, the quantity of ferromagnetic modulation segments, and the peak torque transmitted by either rotor. This compact formulation offers a practical tool for predicting torque behavior under varying angular positions.

To verify the accuracy and applicability of the general equation in modeling CMG torque transmission, both static and dynamic torque conditions are compared against the results derived from the general sinusoidal expressions. Static torque analysis typically involves finite element method (FEM) simulations or bench tests under fixed rotor positions, while dynamic torque assessments evaluate real-time FEM performance during rotational operation. Agreement between the predicted torque values from the general model and those obtained through numerical simulation or experimental measurement serves as validation of the model's fidelity in capturing the fundamental behavior of torque transmission in CMGs.

Comparison of General Equation with FEM result

Keeping on using the same dimensions of coaxial magnetic gear with 2 to 3 gear ratio which is used in this chapter shown in **Table 3.10**.

With such a dimension and material determination of CMG, we could know the maximum transmission torque in the inner and outer rotor.

1. Static Torque Comparison

In this condition, both the outer rotor align with ferromagnetic modulator remain static, and the only rotating component is the inner rotor. Based on the CMG operating principle and finite element method (FEM) calculation of the maximum transmitted torque, system parameters are defined as follows: the inner rotor's permanent magnet pole pair number $p_{in} = 2$, the outer rotor's pole pair number $p_{out} = 3$, and the number of ferromagnetic modulation pieces N_m=5, in accordance with the harmonic relationship:

$$N_m = p_{in} + p_{out}$$

The initial phase offset between the inner rotor, outer rotor, and the modulator is denoted by φ. Under these conditions, since both θ_{in} and θ_m are constant (zero in this static configuration), the equation reduces further to:

Table 3.10. Dimension for 2:3 Gear Ratio CMG.

Symbol	Dimensions for models		
	Description	Size	Units
Ryi	Inner yoke inner Radius	65	mm
Rii	Inner Rotor inner Radius	75	mm
Rio	Inner Rotor outer Radius	85	mm
g_air	Air gap thickness	1	mm
Rfi	Ferro Modulator inner Radius	86	mm
Rfo	Ferro Modulator outer Radius	101	mm
Roi	Outer Rotor inner Radius	102	mm
Roo	Outer Rotor outer Radius	112	mm
Ryo	Outer yoke outer Radius	122	mm
Robc	Outer Boundary Condition	135	mm
L	Length/height of CMG	50	mm
p_in	Inner PMs Pole pairs number	2	/
p_out	Outer PMs Pole pairs number	6	/
N_m	Ferro Modulator poles number	8	/
Br	Remanence flux density	1.2	T
μ_0	Permeability of Vacuum	1.24E-06	H/m
μ	Absolut Permeability of Magnets	1.32E-07	H/m
μ_r	Relative Permeability of Magnets	1.05	/

$$T_{in} = (\pm)T_{m_{in}} * \sin(2 * \theta_{in} + \varphi) \quad \text{(Equ. 3.3.5)}$$

$$T_m = (\pm)T_{m_m} * \sin(2 * \theta_{in} + \varphi) \quad \text{(Equ. 3.3.6)}$$

$$T_{out} = (\pm)T_{m_{out}} * \sin(2 * \theta_{in} + \varphi) \quad \text{(Equ. 3.3.7)}$$

This expression describes the sinusoidal variation of transmitted torque as a function of the inner rotor's angular position θ_{in}, modulated by the system's initial phase φ. The sinusoidal nature reflects the spatial harmonic interaction between the inner rotor magnets and the fixed magnetic field configuration set by the static outer rotor and modulator.

The comparison is illustrated in Fig. 3.27 – 3.32, which presents the effects of initial angular position φ and pole number configuration on the variation of transmitted torque. These figures validate the accuracy of the simplified general equation by comparing its predicted torque profile with results obtained from finite element method (FEM) simulations.

Fig. 3.27 & 28 presents the torque comparison at an initial angular position $\varphi = 0°$ .The torque waveform predicted by the general equation closely matches the FEM results in both amplitude and phase, indicating that the simplified sinusoidal model accurately captures the core transmission behavior.

Fig. 3.29 & 30 shows the torque variation when the initial phase offset is $\varphi = 5°$. Although a slight phase shift is introduced, the analytical model still aligns well with the FEM results, demonstrating robustness to changes in initial alignment.

Fig. 3.31 & 32 illustrates the torque behavior when the outer rotor is rotated by $\varphi = 20°$, showing the effect of cumulative pole pair interaction. While minor deviations near the peaks are observed—likely due to magnetic saturation or higher-order harmonics—the general model still effectively predicts the overall waveform and torque magnitude.

Fig. 3.27 – 3.32 present a comparative analysis between the FEM-simulated torque and the general analytical equation for both the inner and outer rotors under an $\varphi = 0°\sim5°\sim20°$ inner rotor rotation. For the inner rotor torque, the general equation demonstrates strong phase alignment with the FEM result, correctly predicting the periodicity and peak positions despite visible discrepancies in local waveform sharpness.

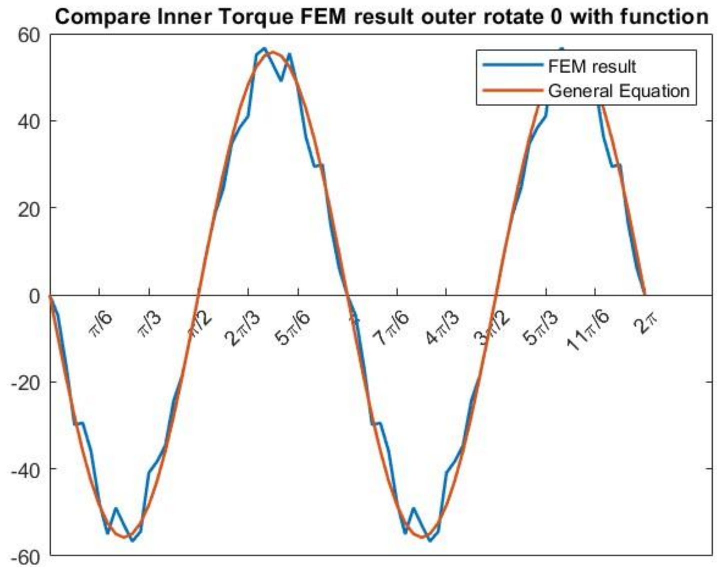

Fig. 3.17. Comparison of inner rotor torque at $\varphi = 0°$.

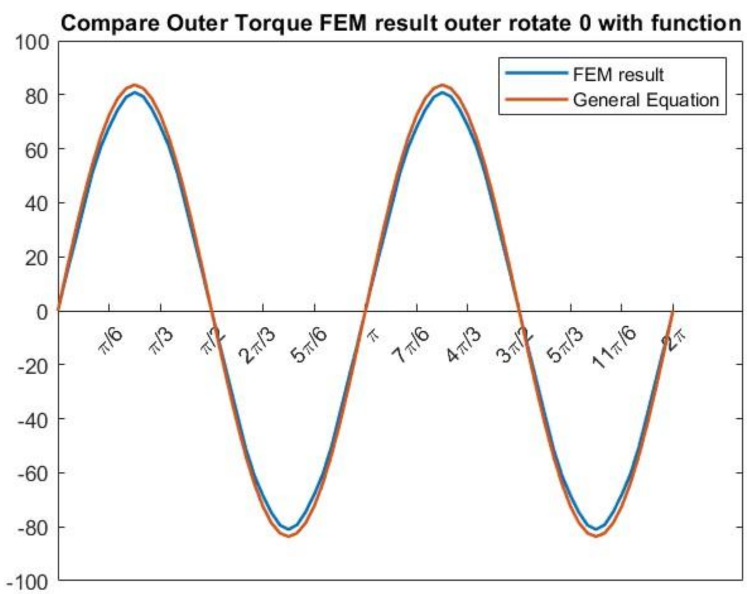

Fig. 3.28. Comparison of outer rotor torque at $\varphi = 0°$.

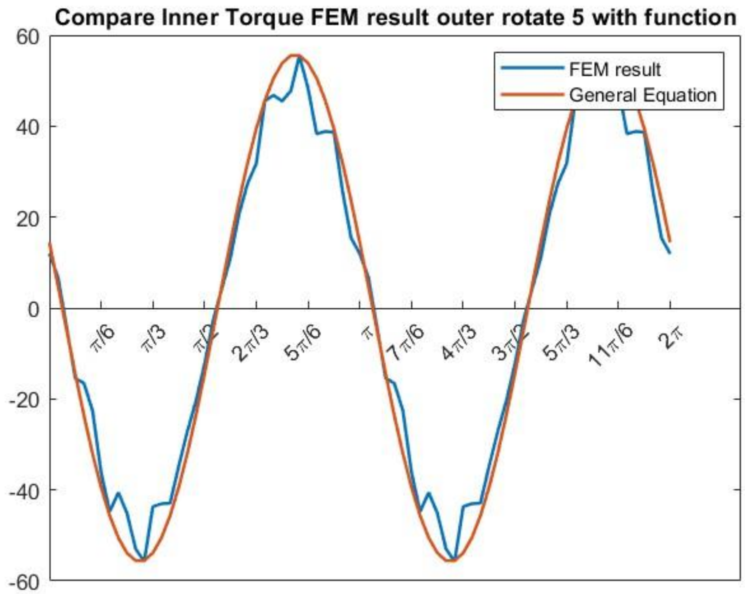

Fig. 3.29. Comparison of inner rotor torque at $\varphi = 5°$.

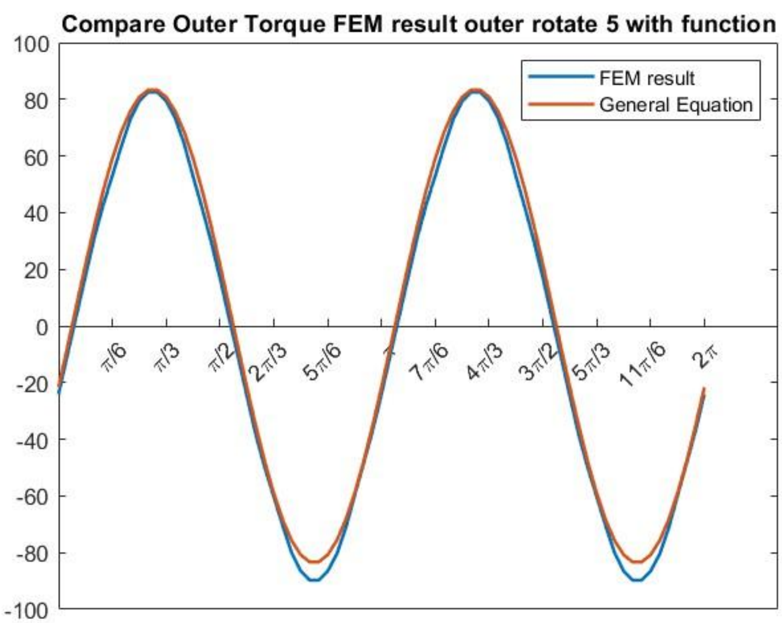

Fig. 3.30. Comparison of outer rotor torque at $\varphi = 5°$.

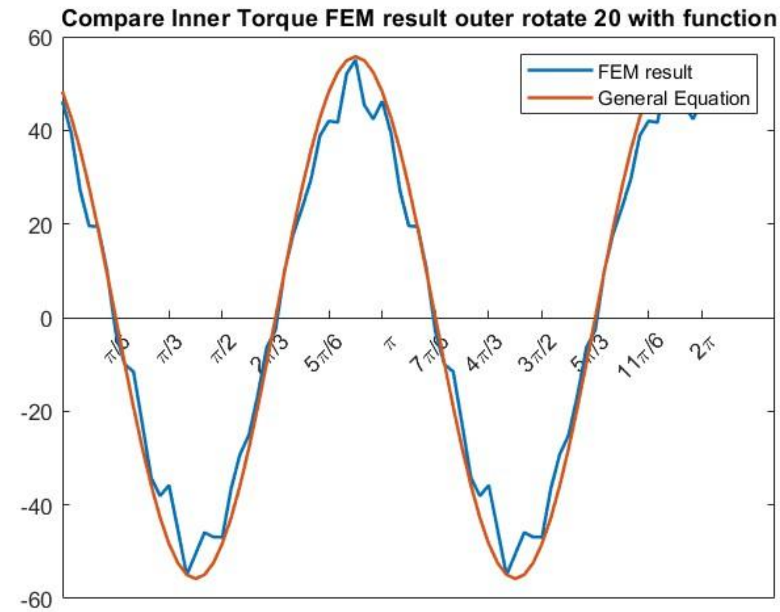

Fig. 3.31. Comparison of inner rotor torque at $\varphi = 20°$.

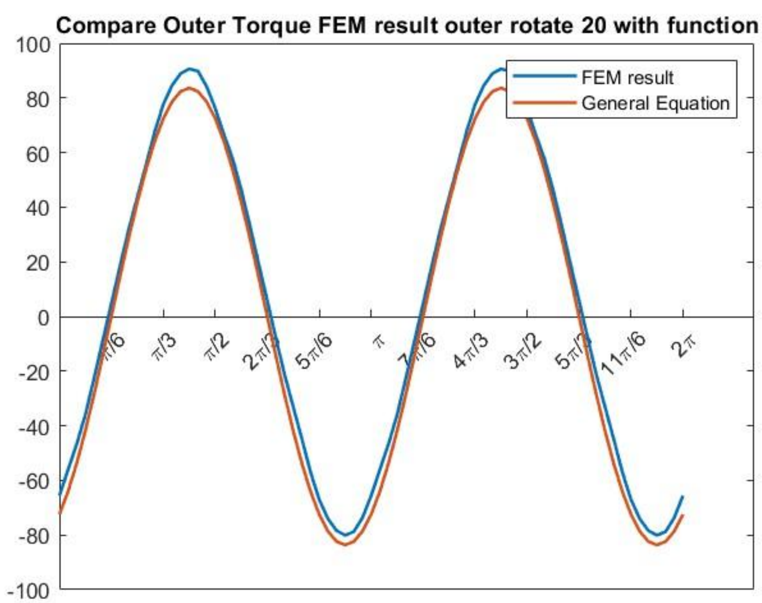

Fig. 3.32 Comparison of outer rotor torque at $\varphi = 20°$.

These differences, primarily near extrema, can be attributed to magnetic harmonics and nonlinear field interactions captured by FEM but absent in the idealized sinusoidal model.

Nonetheless, the close agreement in phase confirms that the general equation accurately reflects the underlying coupling mechanism driven by the relative angular position of magnetic components.

In contrast, the outer rotor torque shows near-perfect agreement with the general model in both amplitude and phase, with the FEM and analytical curves almost overlapping throughout the full rotation cycle. This indicates that the output torque is less sensitive to local field distortions and validates the general equation's suitability for system-level modeling.

Overall, the comparison results highlight that while FEM reveals fine-grained effects like torque ripple and higher-order harmonics, the general equation remains a reliable and accurate tool for capturing the primary torque transmission characteristics and the effect of phase shift in CMG systems—especially for understanding torque development and guiding early-stage design.

2. Dynamic Torque Comparison

A further analysis is about the dynamic torque evaluation for the applicability of the general transmit torque equation under the dynamic conditions, a scenario in which both the inner and outer rotors a rotating simultaneously was examined. In this case, the relative angular position between the two rotors and the ferromagnetic modulator varies continuously, introducing a compound angular velocity that affects the torque generation on both sides. This relative motion alters the torque phase evolution and enables continuous torque transfer, mimicking real operational states of coaxial magnetic gears under load. Despite the increased dynamic complexity, the general torque expression:

$$T_{in} = (\pm)T_{m_{in}} * \sin\left(p_{in} * \theta_{in} + p_{out} * \theta_{out} + \varphi\right) \quad \text{(Equ. 3.3.8)}$$

$$T_{m} = (\pm)T_{m_{m}} * \sin\left(p_{in} * \theta_{in} + p_{out} * \theta_{out} + \varphi\right) \quad \text{(Equ. 3.3.9)}$$

$$T_{out} = (\pm)T_{m_{out}} * \sin\left(p_{in} * \theta_{in} + p_{out} * \theta_{out} + \varphi\right) \quad \text{(Equ. 3.3.10)}$$

Here, p_{in} represents the number of pole pairs on the inner rotor, and θ_{in} denotes the angular position of the inner rotor. Similarly, p_{out} represents the number of pole pairs on the outer rotor, and θ_{out} denotes the angular position of the outer rotor. Since the ferromagnetic modulator remains stationary in this scenario, the torque equation can be simplified by eliminating the angular variation associated with the modulator, effectively setting $\theta_m = 0$.

In **Fig. 3.33 – 3.34**, two operation conditions are shown like last section the 70% steady-state operation and 100% fully engage steady-state operation which depend on the loading torque in the output side.

Fig. 3.33 presents the system under 70% steady-state operation, where the required output torque is lower than the system's maximum transmission capability. The system still operates in a synchronized and stable manner, but the magnetic gear transmits only a portion of its rated torque to match the load demand. Under this condition, both the FEM simulation and the dynamic torque function show consistent torque waveforms, with the outer rotor torque maintaining a nearly constant level and the inner rotor torque exhibiting small periodic fluctuations. These minor ripples in the inner rotor torque may arise from magnetic field harmonics or local transient effects, but the general trend is accurately captured by the analytical model.

Fig. 3.34 illustrates the 100% fully engaged steady-state operation, where the output load matches the maximum torque capacity of the magnetic gear. In this case, both inner and outer torques are fully engaged, and the dynamic function aligns extremely well with the FEM results in both amplitude and phase. The torque curves are smooth, symmetrical, and free of significant deviations, confirming that the magnetic coupling is fully developed and operating at peak efficiency.

The comparison between the two figures highlights how load demand influences the torque profile in coaxial magnetic gear operation. Although both scenarios represent steady-state conditions, the 70% case illustrates a reduced torque output corresponding to lower load requirements, rather than incomplete magnetic engagement.

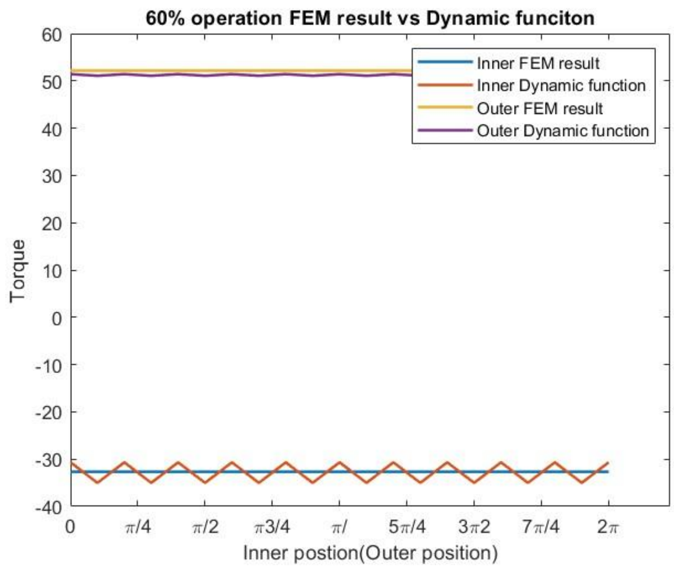

Fig. 3.33. Dynamic torque comparison under partial (60%) steady-state engagement.

In this lower-load condition, the FEM results adapt to the actual torque demand by showing reduced amplitude and slight waveform fluctuations—reflecting the physical field response under light loading. Meanwhile, the analytical torque function remains unchanged, as it represents the maximum theoretical torque capacity of the gear system, independent of external loading. This distinction reveals that the general equation defines an idealized torque envelope, while FEM simulations capture the realized torque shaped by loading conditions and magnetic field interactions.

In the 70% case, the inner rotor torque shows slightly greater sensitivity to local dynamic effects, such as magnetic harmonics or transient field distortion. However, the overall waveform and phase progression remain consistent with the analytical model. In both scenarios, the outer rotor torque maintains excellent agreement between FEM and the dynamic function, underscoring the output side's mechanical and magnetic stability.

These results demonstrate that the general dynamic torque equation is robust across a range of operating conditions, from partial to full load. Although it does not automatically reflect torque amplitude scaling with load, its ability to maintain accurate phase alignment and waveform structure makes it highly useful for predicting system-

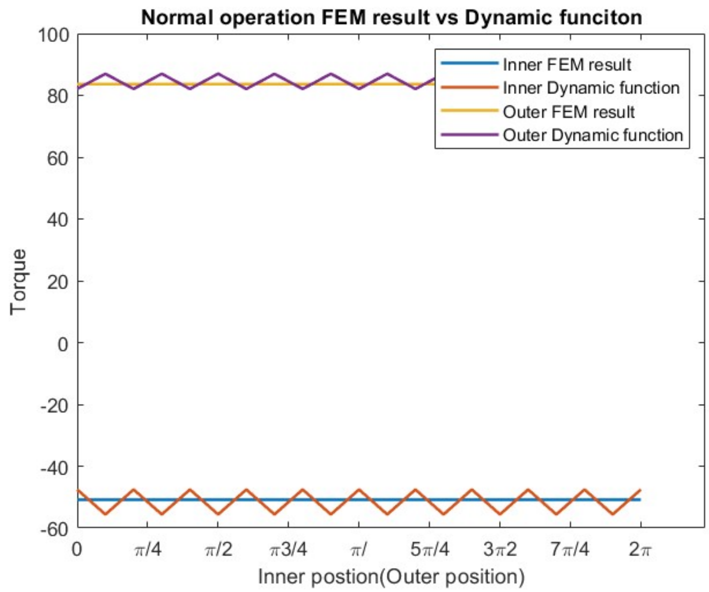

Fig. 3.34. Dynamic torque comparison under full steady-state engagement.

level torque behavior. Therefore, the equation serves as a valuable tool for real-time control, performance estimation, and design optimization in CMG systems, especially when supplemented with FEM-based calibration for specific load cases.

3. Surface Visualization of Torque-Angle Dynamic Response in CMG

Building on the previous analyses of static and dynamic torque transmission in the inner and outer rotors of the Coaxial Magnetic Gear (CMG), this section presents a surface visualization of the torque-angle dynamic response. In earlier sections, the general torque equation was validated under static conditions, including the impact of initial angular position on torque transmission. Subsequently, the dynamic torque equation—formulated as a time-varying extension of the general model—was introduced to further evaluate the torque behavior under steady-state transmission scenarios.

To assess the dynamic model's accuracy, two different loading conditions were simulated and compared against finite element method (FEM) results. While FEM simulations revealed detailed behaviors such as torque ripple and higher-order harmonics, the dynamic torque equation proved to be a reliable approximation for capturing the essential characteristics of torque transmission and phase alignment in CMG systems. These results underscore the robustness of both the general and dynamic torque equations across a wide range of operating conditions, from partial to full load engagement.

Fig. 3.35 and **3.36** present 3D surface plots of the inner rotor torque and outer rotor torque, respectively, as functions of the angular positions of both rotors. These visualizations illustrate the sinusoidal nature of torque generation within the magnetic gear system and demonstrate the influence of angular alignment on torque magnitude and polarity.

Fig. 3.35 displays the inner rotor dynamic torque, computed from the general torque expression:

$$T_{in} = (\pm)T_{m_{in}} * \sin\left(2 * \theta_{in} + 3 * \theta_{out} + \varphi\right) \qquad \text{(Equ. 3.3.11)}$$

This surface reveals a high-frequency sinusoidal waveform along both rotor axes, capturing how torque varies with angular misalignment between the input and output shafts. The pattern shows clearly periodic characteristics, with peaks and valleys corresponding to specific angular alignments where magnetic coupling is either maximized or reversed. The negative sign reflects the relative direction of torque transfer under standard operating polarity. As the input rotor progresses through one full cycle, the torque oscillates periodically based on harmonic alignment, consistent with the theoretical torque envelope.

Fig. 3.36 shows the outer rotor torque, described by the function:

$$T_{out} = (\pm)T_{m_{out}} * \sin\left(2 * \theta_{in} + 3 * \theta_{out} + \varphi\right) \qquad \text{(Equ. 3.3.12)}$$

This plot displays a similar periodic torque pattern, though the amplitude and frequency differ due to the change in torque scaling and pole pair ratios. Notably, the surface appears more “stretched” along the outer rotor axis, reflecting the slower rotation and larger torque output at the output side, consistent with the gear ratio and conservation of power in the system. The outer torque waveform remains smooth and symmetric, validating the phase consistency of the analytical model.

Together, these two surface plots demonstrate the general torque equation’s ability to characterize torque response not just over time but across full rotational states of both rotors. They also emphasize how the torque waveform maintains its structure across angular variations, reinforcing the earlier finding that the equation is phase-accurate under both light and full loading conditions. This level of predictive consistency highlights the analytical model’s utility for system-level design, especially in scenarios requiring real-time torque estimation across a continuous rotational cycle.

These two surface plots not only visualize the torque behavior across the full angular state space of the CMG but also underscore the practicality of using the general torque equation in real-time modeling. Rather than relying on computationally expensive multi-frame FEM simulations to estimate torque at every angular configuration, the analytical expression enables fast, continuous evaluation of torque based on rotor positions and system parameters. This makes it highly suitable for integration into dynamic system models, control algorithms, and onboard estimators for real-time torque prediction, feedback regulation, or performance monitoring. Its closed-form structure ensures rapid computation while preserving phase accuracy and torque waveform fidelity, offering a highly efficient alternative for real-time CMG response analysis.

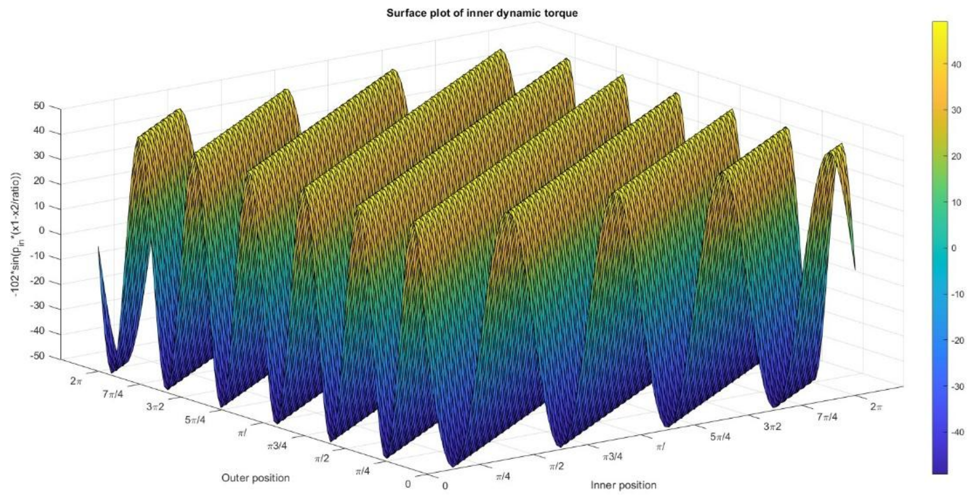

Fig. 3.35. Inner rotor dynamic torque surface based on relative angular position (inner and outer variation asynchronously).

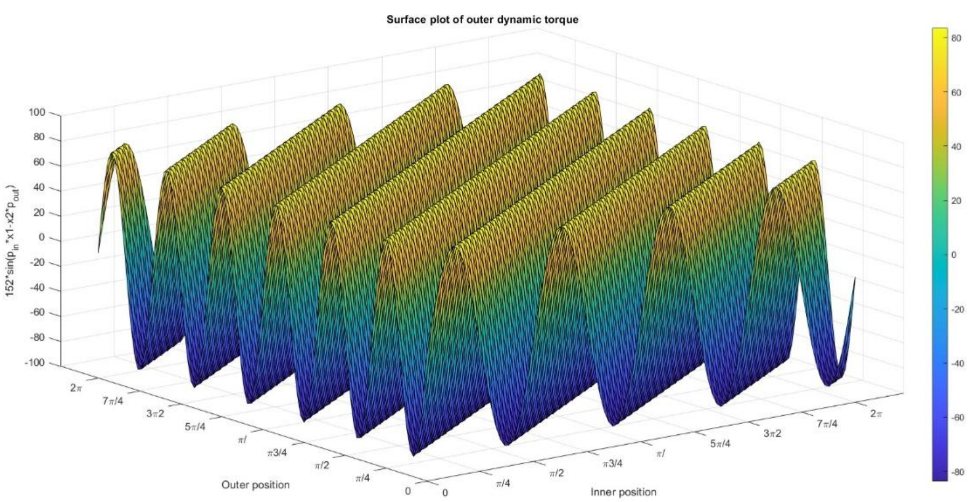

Fig. 3.36. Outer rotor dynamic torque surface based on relative angular position (inner and outer variation asynchronously).

3.3.4 General dynamic simulation model of coaxial magnetic gear transmission

To generate a dynamic simulation of coaxial magnetic gear (CMG) transmission, it is essential to begin from the fundamentals of its physical structure. The CMG system architecture consists of an inner rotor, a ferromagnetic modulator (which may be stationary or rotating), and an outer rotor. These components interact magnetically to enable contactless torque transmission, where the transmitted torque depends on the relative angular positions among the inner rotor, outer rotor, and the ferro modulator. Unlike conventional mechanical gears, which transmit torque through direct, linear contact, CMG systems rely on nonlinear magnetic coupling. The key to simulating this nonlinear interaction lies in accurately capturing the torque-angular position relationship. This relationship forms the basis of the general dynamic equation for CMG transmission. By establishing this equation, the magnetic gear system can be abstracted into a simplified rotating-component model, as presented in **Fig. 3.37**.

In this schematic, **Fig. 3.37** illustrates the generalized architecture of a coaxial magnetic gear (CMG) system, comprising an inner rotor, a stationary or modulated ferromagnetic core (ferro modulator), and an outer rotor. The green line represents the inner rotor power transmission path, where T_{in} denotes the input torque applied to the inner rotor and J_{in} is the corresponding rotational inertia.

Along the magnetic power transmission path, the inner rotor couples with the ferromagnetic modulator (indicated by the blue path), which alters the spatial harmonic content of the magnetic field between the inner and outer rotors. If the ferro modulator is stationary, it serves purely as a passive magnetic coupling interface. However, in dynamic models where it also rotates, it is associated with its own torque input T_m and rotational inertia J_m, as shown in the blue segment.

The outer rotor, illustrated by the red path, receives transmitted magnetic torque from the ferro modulator. This output rotor drives the load, characterized by the output torque T_{out} and rotational inertia J_{out} . The arrows indicate the direction of mechanical power flow and rotational motion of each component. This configuration enables contactless torque transfer and speed conversion between the inner and outer rotors,

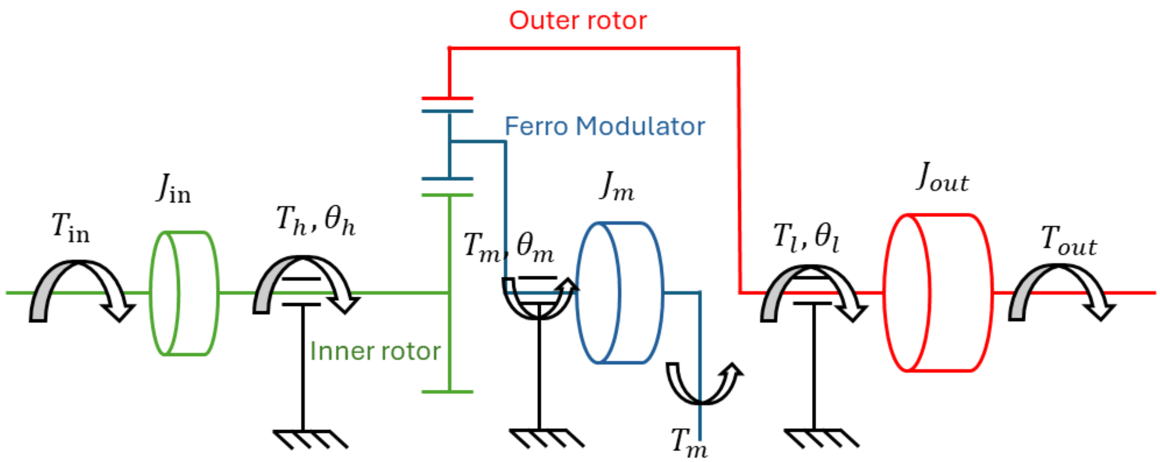

Fig. 3.37. Dynamic modeling framework of CMG system to three rotating bodies system.

with the ferro modulator acting as the intermediary magnetic coupler. Such a system enables high torque density, low maintenance, and is particularly suitable for applications requiring sealed or non-contact transmissions.

With the knowledge of the Newton's Second Law for Rotational systems, the rotating component's function is:

$$J \cdot \ddot{\theta} = T_{input} - T_{load}$$

Where:

- J is the rotational inertia
- $\ddot{\theta}$ is the angular acceleration
- T_{input} is the applied torque (in this case, the **magnetic torque** from the CMG interaction)
- T_{load} is the external torque or resistive load

This equation can be applied separately to both inner/outer rotor and ferro modulators. Then these dynamic equations are deduced to three rotating components as shown in Equ. 3.4.1-3.4.3.

$$J_{in} \cdot \frac{d^2\theta_{in}}{dt^2} = T_{input} - T_{in} \quad \text{(Equ. 3.3.13)}$$

$$J_m \cdot \frac{d^2\theta_m}{dt^2} = T_{in} - T_{out} + T_{input,m} \qquad \text{(Equ. 3.3.14)}$$

$$J_{out} \cdot \frac{d^2\theta_{out}}{dt^2} = T_{output} - T_{out} \qquad \text{(Equ. 3.3.15)}$$

In this model, θ_{in} and θ_{out} represent the angular positions of the inner and outer rotors, respectively. These correspond to the θ_h and θ_l in **Fig. 3.25**, where the subscripts denote high-speed (inner rotor) and low-speed (outer rotor) components, consistent with the typical speed relationship in CMG systems. The terms J_{in}, J_m and J_{out} denote the rotational inertias of the inner rotor, the ferromagnetic modulator, and the outer rotor, respectively. T_{in} and T_{out} represent the torques transmitted within the CMG system from the inner rotor and to the outer rotor during operation. For the T_{input}, $T_{input,m}$ and T_{output} is the input torque and output or loading torque respectively.

As previously established in Equations 3.3.2 to 3.3.4, the general torque expressions are functions of the angular positions of the inner rotor, outer rotor, and ferromagnetic modulator. By substituting these torque expressions into the dynamic equations presented in Equations 3.4.1 to 3.4.3, we can derive the complete and detailed dynamic equations governing each component of the CMG system.

$$J_{in} \cdot \frac{d^2\theta_{in}}{dt^2} = (\pm)T_{m_{in}} * \sin\left(p_{in} * \theta_{in} + p_{out} * \theta_{out} - N_m * \theta_m + \varphi\right)$$

(Equ. 3.3.16)

$$J_m \cdot \frac{d^2\theta_m}{dt^2} = (\pm)T_{m_{in}} * \sin(p_{in} * \theta_{in} + p_{out} * \theta_{out} - N_m * \theta_m + \varphi) - T_{m_{out}} * \sin\left(p_{in} * \theta_{in} + p_{out} * \theta_{out} - N_m * \theta_m + \varphi\right) + T_{input,m}$$

(Equ. 3.3.17)

$$J_{out} \cdot \frac{d^2\theta_{out}}{dt^2} = T_{output} - T_{m_{out}} * \sin\left(p_{in} * \theta_{in} + p_{out} * \theta_{out} - N_m * \theta_m + \varphi\right)$$

(Equ. 3.3.18)

To simulate CMG transmission, we will use the Matlab/Simulink to generate the dynamic response of CMG torque and speed reaction. With the angular position of inner/outer rotor θ_{in}, the $\dot{\theta}_{in}$ is the speed of the rotating components and $\ddot{\theta}_{in}$.

To simulate the CMG transmission, we employ MATLAB/Simulink to generate the dynamic response of torque and speed within the system. The simulation tracks the angular positions of the inner and outer rotors, denoted as θ_{in} and θ_{out}. The first derivatives, $\dot{\theta}_{in}$ and $\dot{\theta}_{out}$, represent the angular velocities of the rotating components, while the second derivatives, $\ddot{\theta}_{in}$ and $\ddot{\theta}_{out}$, correspond to their angular accelerations. These time-varying parameters serve as inputs to the dynamic equations, enabling the real-time evaluation of CMG behavior under various loading and input conditions.

The simulation model, shown in **Fig. 3.38**, presents a Matlab Simulink-based dynamic simulation of a coaxial magnetic gear (CMG) system. It captures the interactions among the inner rotor, ferromagnetic modulator, and outer rotor. The model incorporates the torque inputs and rotational inertias of each component and computes their angular velocities and positions over time. Magnetic coupling between the components is represented through nonlinear functions derived from their relative angular positions. This simulation framework enables real-time analysis of torque transmission dynamics, load responses, and system stability under various operating conditions.

3.4 Coaxial Magnetic Gear Maximum Transmit Torque Line

In the previous two sections on Coaxial Magnetic Gear (CMG) transmission torque analysis, we presented both a computational method to calculate the magnetic flux within the CMG system and a numerical method using Finite Element Method (FEM) to determine the torque on the inner and outer rotors. By combining insights from these approaches, we developed general static and dynamic equations capable of predicting the transmitted torque response in CMG transmissions.

$$J_{in} \cdot \frac{d^2\theta_{in}}{dt^2} = (\pm)T_{m_{in}} * \sin\left(p_{in} * \theta_{in} + p_{out} * \theta_{out} - N_m * \theta_m + \varphi\right)$$

(Equ. 3.4.4)

$$J_m \cdot \frac{d^2\theta_m}{dt^2} = (\pm)T_{m_{in}} * \sin(p_{in} * \theta_{in} + p_{out} * \theta_{out} - N_m * \theta_m + \varphi) - T_{m_{out}} * \sin\left(p_{in} * \theta_{in} + p_{out} * \theta_{out} - N_m * \theta_m + \varphi\right) + T_{input,m}$$

(Equ. 3.4.5)

$$J_{out} \cdot \frac{d^2\theta_{out}}{dt^2} = T_{output} - T_{m_{out}} * \sin\left(p_{in} * \theta_{in} + p_{out} * \theta_{out} - N_m * \theta_m + \varphi\right)$$

(Equ. 3.4.6)

By examining Equations 3.3.4 to 3.3.6 in detail, we identify that the parameters J_{in}, J_m and J_{out} represent the inner rotor, ferro modulator, and outer rotor's rotational inertias, respectively—each of which can be determined from the geometric dimensions of the components. The terms θ_{in}, θ_{out} and θ_m is the angular positions of the inner rotor, ferro modulator, and outer rotor. Since the time derivative of angular position yields rotating velocity, the angular position of the input component is treated as a known input. Additionally, p_{in}, p_m and p_{out} denote the number of pole pairs (or ferromagnetic pieces) of the inner rotor, ferro modulator, and outer rotor. With this understanding, all parameters in the dynamic model are known except for $T_{m_{in}}$ and $T_{m_{out}}$, which represent the maximum transmitted torque of the CMG on the inner and outer rotors, separately. Based on this understanding, we aim to establish a more streamlined approach for rapid CMG transmission design. Rather than relying solely on iterative FEM simulations, we propose using a maximum torque line-based calculation model [49] to approximate the transmitted torque behavior efficiently. This method leverages the analytical relationship between the torque and the angular position, allowing us to quickly estimate the peak transmission capabilities of the CMG system under different configurations. By incorporating key design parameters—such as pole pair numbers, magnetic loading, and rotor dimensions—this model provides a practical tool for early-stage design evaluation and optimization.

To generate a maximum torque line for CMG transmission, the CMG system is divided into several key components, as shown in **Fig. 3.39**. This figure presents the geometric parameterization of a typical Coaxial Magnetic Gear (CMG) cross-sectional structure, serving as the foundation for evaluating transmission torque characteristics using the maximum torque line approach. The diagram clearly defines all critical radial dimensions and material thicknesses necessary for both structural analysis and electromagnetic modeling.

In this Figure illustration:

- r_i and r_o The diagram also denotes the inner and outer boundary radii of the CMG structure, which includes the respective boundaries of the inner and outer yokes, serving as key constraints for structural integration and magnetic flux confinement.
- t_{pmi} and t_{pmo} represent the radial thicknesses of the inner and outer permanent magnets, which generate the magnetic fields responsible for torque transmission.
- t_{fm} is the thickness of the ferromagnetic modulator, which is composed of high-permeability iron segments and modulates the magnetic field spatially.
- $t_{yi}$and t_{yo} are the yoke thicknesses for the inner and outer rotors, respectively, providing magnetic flux paths and mechanical support.
- An airgap is defined between the magnet-modulator and modulator-magnet interfaces, normalized to a unit value (airgap = 1) to simplify flux density scaling in analytical modeling.

This parametric model allows for scalable and systematic analysis of geometric influence on maximum torque. By adjusting these thickness and radius parameters, we can evaluate how each substructure—magnets, yokes, modulator, and airgap—contributes to the peak torque capacity. The maximum torque line is thus generated as a function of both geometry and magnetic loading, providing a practical and computationally efficient tool for rapid CMG transmission design.

To generate a maximum torque line for CMG transmission, we begin by analyzing the effect of the permanent magnets (PMs), as torque generation relies on magnetic flux interaction between rotating components. The PM thickness significantly influences the magnetic loading and thus the peak torque. Increasing the thickness of the permanent magnets can improve the magnetic flux density within the air gap, however, this effect diminishes once magnetic saturation is reached, limiting further improvement. Proper PM sizing is essential to balance torque performance, weight, and magnetic efficiency, while also reducing flux leakage and ensuring strong coupling through the modulator.

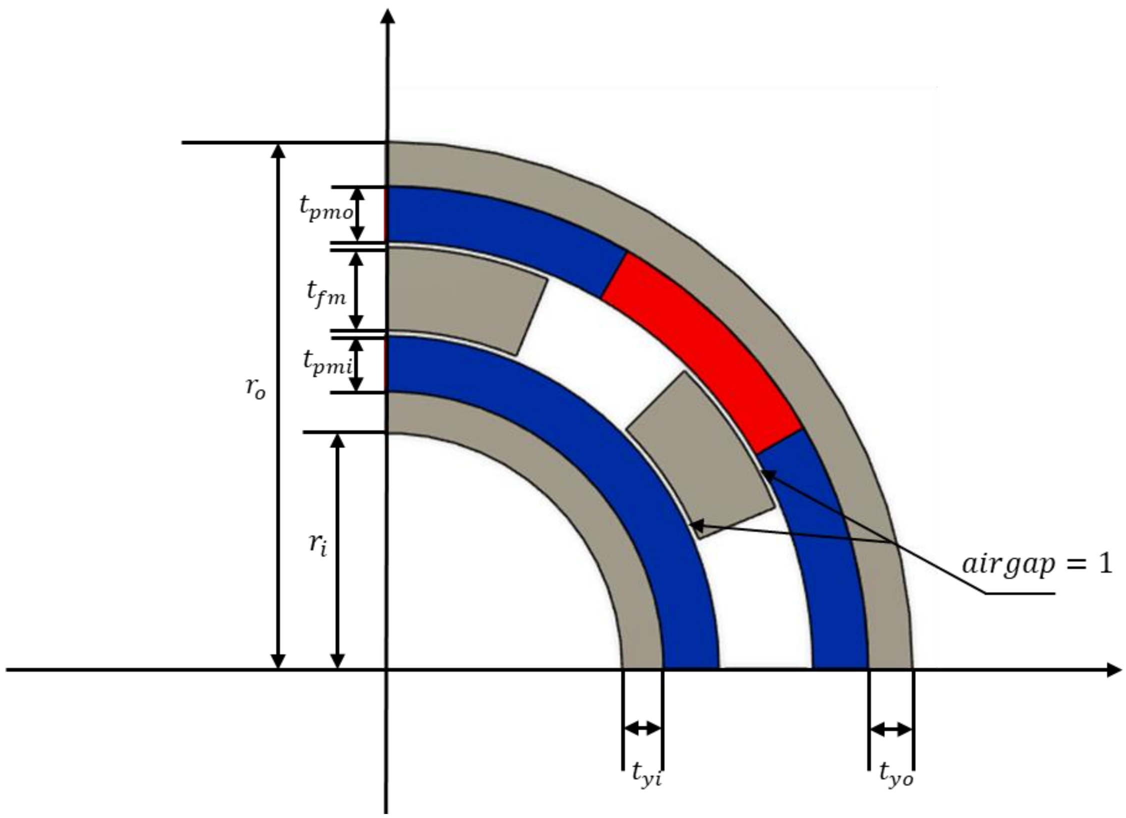

Fig. 3.18. Parameters of surface type of Coaxial Magnetic Gear.

1. Thickness Effect of Permanent Magnets

To analyze the thickness effect of the permanent magnets, it is important to first understand the characteristics of magnetic transmission in CMG systems. Magnetic flux symmetry and balance are essential for efficient torque transfer. When the inner and outer permanent magnets have equal thickness, the magnetic flux couples evenly through the ferromagnetic modulators, forming a closed and balanced magnetic circuit. This symmetry minimizes flux leakage, avoids local saturation, and prevents magnetic force imbalance, resulting in stable and efficient torque output.

Therefore, we assume equal thickness for the inner and outer permanent magnets and fix the dimensions of the other magnetic transmission components in the structure. This approach allows us to isolate and determine the optimal PM thickness required to achieve maximum torque transmission.

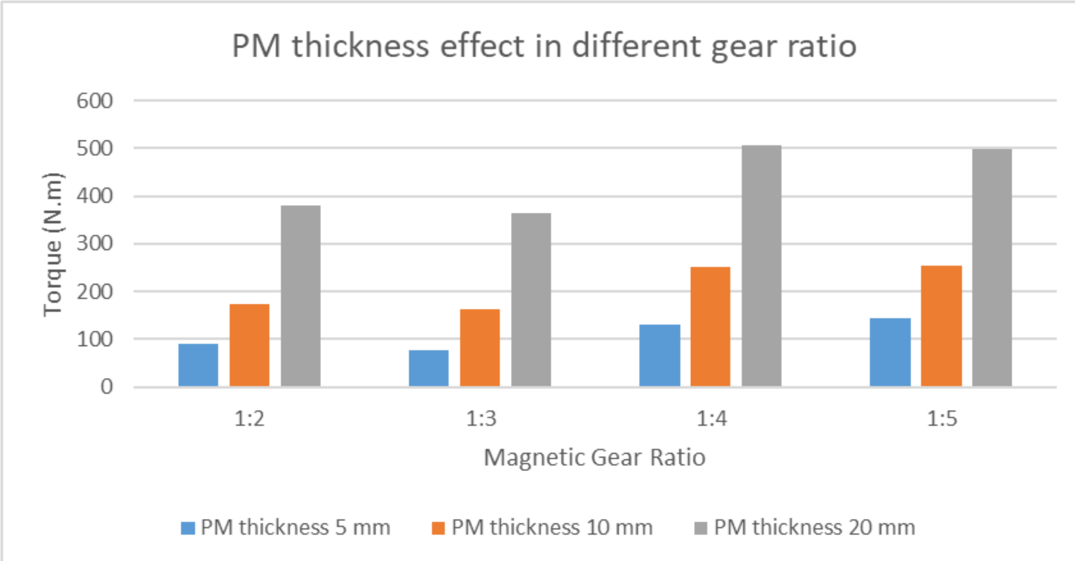

Fig. 3.19. Effect of permanent magnet thickness on transmitted torque across different gear ratios.

As shown in **Table. 3.11**, the geometric dimensions of each CMG component are defined and kept constant. Using this consistent CMG structure, we perform repeated torque calculations across different gear ratios. This enables us to establish the relationship between PM thickness and transmission torque, particularly in the high-torque, low-speed rotor side of the CMG system.

Fig. 3.40 illustrates the effect of permanent magnet (PM) thickness on the transmitted torque in CMG systems across various magnetic gear ratios (1:2, 1:3, 1:4, and 1:5). The analysis compares three PM thicknesses: 5 mm, 10 mm, and 20 mm, under the same geometric constraints defined in **Table 3.11**.

The results show a clear trend: increasing PM thickness leads to significantly higher torque output across all gear ratios. This is due to the enhanced magnetic flux density provided by thicker magnets, which strengthens the magnetic coupling between components. The torque improvement is especially noticeable when increasing PM thickness from 10 mm to 20 mm, indicating that magnetic saturation has not yet been reached within this range.

Table 3.7. 5mm PM thickness with various ferro thickness ratio.

5 mm PM thickness with different Ferro thickness ratio								
Thickness Ratio	outer pm_o	outer pm_i	ferro_o	ferro_i	inner pm_o	inner pm_i	inner yoke_i	outer R
0.5	97.5	92.5	92	88.5	88	83	70	107.5
1	99	94	93.5	88.5	88	83	70	109
1.5	101.5	96.5	96	88.5	88	83	70	111.5
2	104	99	98.5	88.5	88	83	70	114
2.5	106.5	101.5	101	88.5	88	83	70	116.5
3	109	104	103.5	88.5	88	83	70	119
3.5	111.5	106.5	106	88.5	88	83	70	121.5
4	114	109	108.5	88.5	88	83	70	124
4.5	116.5	111.5	111	88.5	88	83	70	126.5
5	119	114	113.5	88.5	88	83	70	129

Additionally, higher gear ratios (e.g., 1:4 and 1:5) result in greater torque transmission, particularly when paired with thicker PMs. This suggests that torque amplification benefits from both a favorable gear ratio and adequate magnetic material volume. However, designers must balance this with space and weight constraints in practical applications.

This thickness effect of permanent magnet's analysis confirms that permanent magnet thickness plays a crucial role in enhancing torque transmission in CMG systems, especially under higher gear ratios. By maintaining structural consistency and isolating PM thickness as a variable, the study demonstrates that increasing magnet thickness significantly improves magnetic coupling and torque output, without reaching saturation within the tested range. These insights provide a practical reference for balancing torque performance with design constraints such as size and weight in CMG applications.

2. Thickness Effect of Ferromagnetic Modulator

After understanding the effect of permanent magnet (PM) thickness, where an increase in thickness generally leads to higher transmission torque, we turn to the role of the ferromagnetic modulators, which are another critical component in coaxial magnetic gear (CMG) systems. Ferromagnetic materials contribute to improved magnetic coupling between the inner and outer magnets due to their high permeability before reaching

Table 3.8. 10 mm PM thickness with various ferro thickness ratio.

10 mm PM thickness with different Ferro thickness ratio								
Thickness Ratio	outer pm_o	outer pm_i	ferro_o	ferro_i	inner pm_o	inner pm_i	inner yoke_i	outer R
0.5	101	91	90.5	85.5	85	75	60	107.5
1	106	96	95.5	85.5	85	75	60	109
1.5	111	101	100.5	85.5	85	75	60	111.5
2	116	106	105.5	85.5	85	75	60	114
2.5	121	111	110.5	85.5	85	75	60	116.5
3	126	116	115.5	85.5	85	75	60	119
3.5	131	121	120.5	85.5	85	75	60	121.5
4	136	126	125.5	85.5	85	75	60	124
4.5	141	131	130.5	85.5	85	75	60	126.5
5	146	136	135.5	85.5	85	75	60	129

saturation. However, increasing the air gap introduces higher magnetic reluctance, which in turn reduces the efficiency of flux linkage between the magnetic elements. Although increasing the thickness of the ferromagnetic material improves magnetic flux guidance and supports greater torque transmission, it also enlarges the air gap, which reduces flux linkage and limits the maximum transferable torque. Therefore, it is essential to optimize the balance between ferromagnetic material thickness and air gap distance to achieve efficient torque transmission without causing magnetic saturation or significant flux leakage.

To eliminate the independent influence of permanent magnet (PM) thickness, we normalize the PM thickness as a unit reference and define the thickness of the ferromagnetic modulators as a ratio relative to it. This approach allows us to vary both PM and modulator thickness while maintaining a consistent proportion between them. By applying this method, we can systematically examine the effect of ferromagnetic-modulator thickness across different gear ratios and draw conclusions regarding its impact on torque transmission performance.

Table 3.12 to 3.14 present the geometric parameters of the CMG, where the thickness ratio of the ferromagnetic modulators to the permanent magnets ranges from 0.5 to 5. To isolate the effect of the ferromagnetic modulators, we will use the same overall geometry to repeat the analysis across different gear ratios, thereby eliminating the influence of PM thickness and gear ratio on the results.After extensive FEM calculations, we obtained the

torque transmission results for the high-torque rotor. Rather than comparing torque values alone, we also evaluate the torque density relative to both the volume of the permanent magnets and the total volume of the CMG system. This approach enables us to identify the maximum torque line of the CMG transmission as a function of the system's volume. **Fig. 3.41** to **3.52** present the torque density outcomes in relation to the volume of the permanent magnets as well as the overall volume of the magnetic gear system. From these results, we can identify the optimal thickness ratio range for different gear ratios and ultimately determine a unified optimal configuration across various CMG designs, regardless of gear ratio and PM thickness. Based on the comparative analysis of **Fig. 3.41 – 3.52**, the influence of ferro-magnetic modulator thickness ratio on torque performance was evaluated across gear ratios from 1:2 to 1:5 and various permanent magnet (PM) thicknesses (5 mm, 10 mm, and 20 mm). For the 1:2 gear ratio, simulation results show that maximum torque occurs at a ferro-magnetic modulator thickness ratio of 2.0, while the total torque density—torque divided by total system volume—peaks at a slightly lower ratio, around 1.0 to 1.5. This suggests that at lower gear ratios, thinner ferro modulators enhance volume efficiency without significantly compromising torque.
For the 1:3 gear ratio, both maximum torque and total torque density peak around 2.0 to 2.5, with 2.0 offering a balanced design point.
In the 1:4 gear ratio case, maximum torque is again near 2.0, while total torque density favors 1.5 to 2.0, indicating that modest ferro reduction can improve compactness with minimal performance trade-off.
At the 1:5 gear ratio, maximum torque is achieved at 2.0, and total torque density peaks in the 1.5 to 2.0 range. Performance drops beyond this, showing that overly thick ferro layers are ineffective in high-ratio configurations.
In conclusion, a ferro thickness ratio of 2.0 consistently delivers the highest torque across all gear ratios and PM sizes. When torque per system volume is the priority—such as in weight- and space-limited applications—a thinner ferro layer around 1.5 is more fficient. Designers are advised to choose 2.0 for maximum torque and 1.5 for improved torque density and compactness.

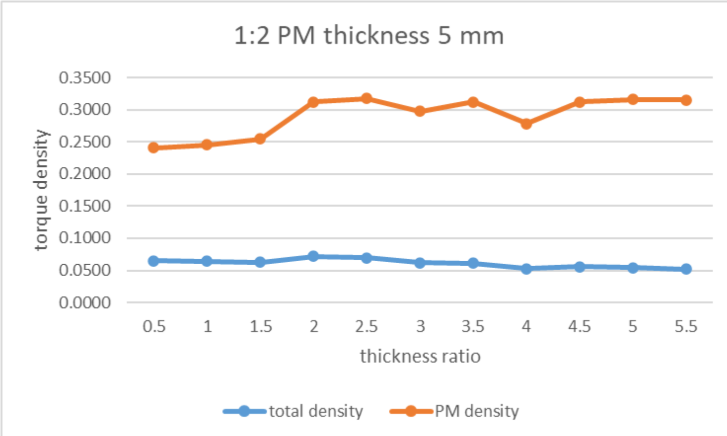

Fig. 3.41. Torque density as a function of Ferro thickness ratio for a 1:2 gear ratio and 5mm PM thickness.

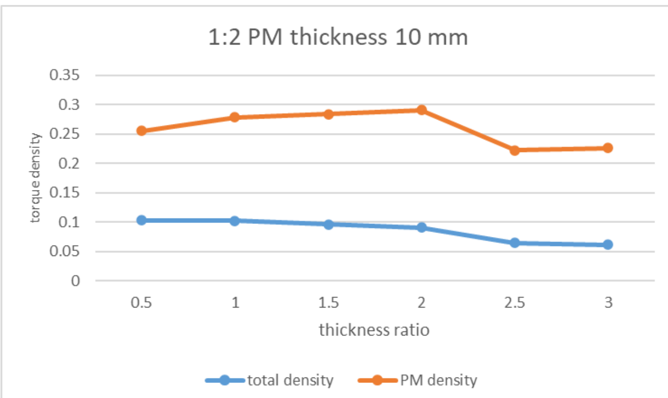

Fig. 3.42. Torque density as a function of Ferro thickness ratio for a 1:2 gear ratio and 10mm PM thickness.

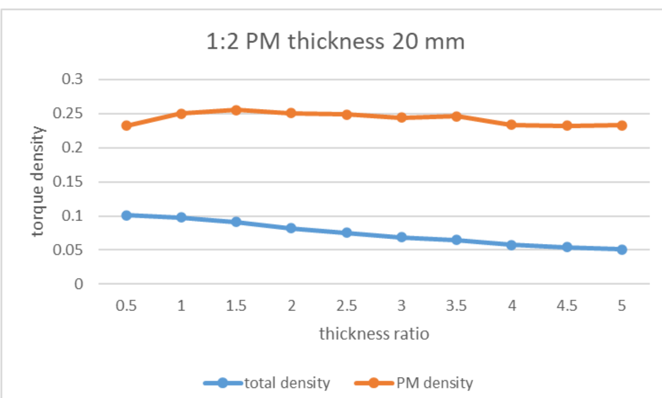

Fig. 3.43. Torque density as a function of Ferro thickness ratio for a 1:2 gear ratio and 20mm PM thickness.

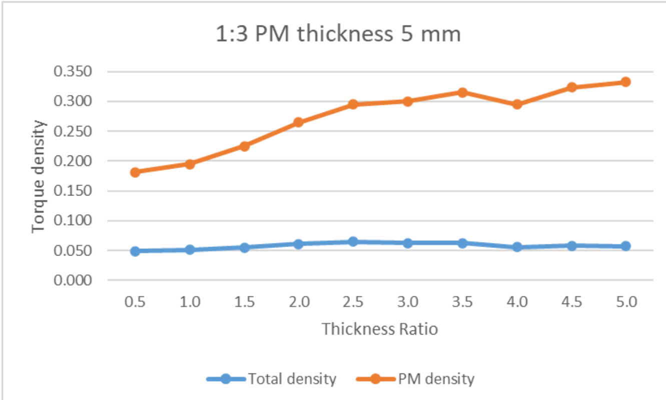

Fig. 3.44. Torque density as a function of Ferro thickness ratio for a 1:3 gear ratio and 5mm PM thickness.

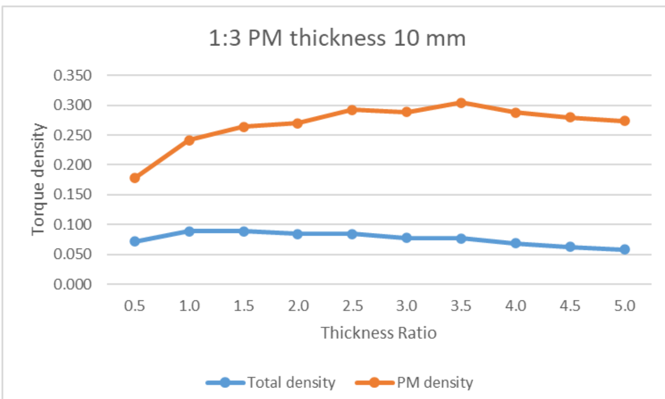

Fig. 3.45. Torque density as a function of Ferro thickness ratio for a 1:3 gear ratio and 10 mm PM thickness.

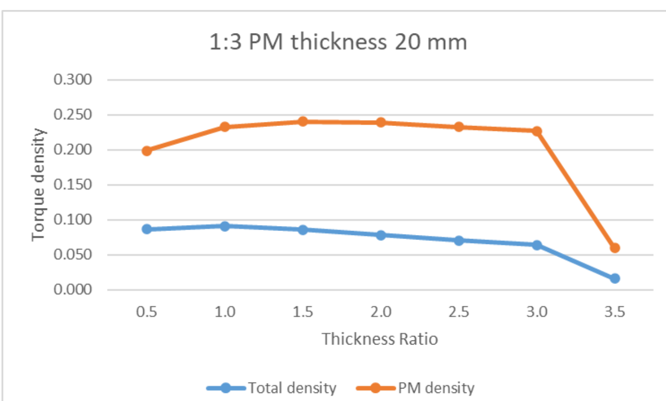

Fig. 3.46. Torque density as a function of Ferro thickness ratio for a 1:3 gear ratio and 20 mm PM thickness.

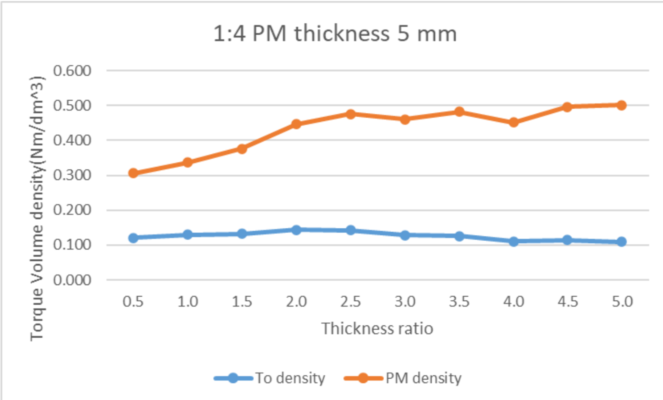

Fig. 3.47. Torque density as a function of Ferro thickness ratio for a 1:4 gear ratio and 5 mm PM thickness.

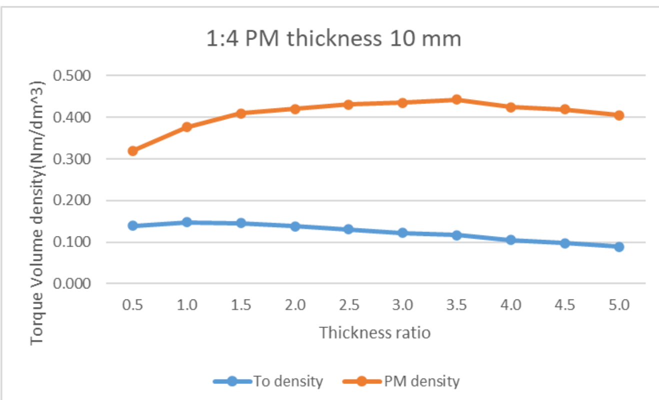

Fig. 3.48. Torque density as a function of Ferro thickness ratio for a 1:4 gear ratio and 10 mm PM thickness.

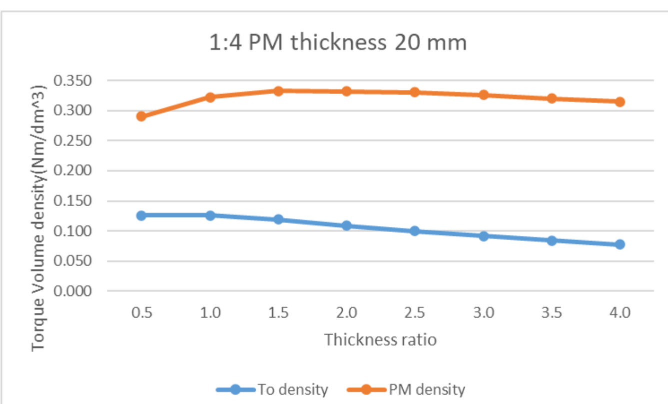

Fig. 3.49. Torque density as a function of Ferro thickness ratio for a 1:4 gear ratio and 20 mm PM thickness.

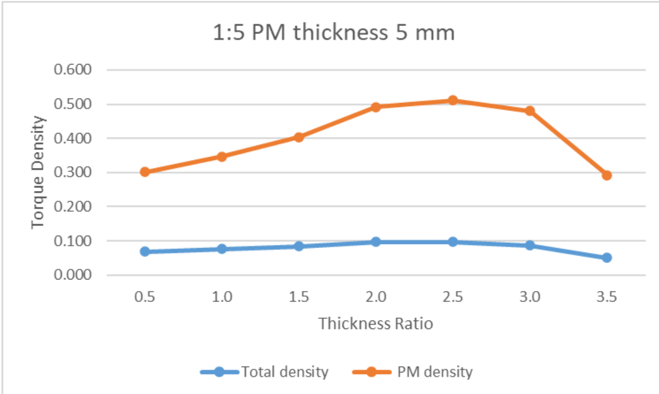

Fig. 3.50. Torque density as a function of Ferro thickness ratio for a 1:5 gear ratio and 5 mm PM thickness.

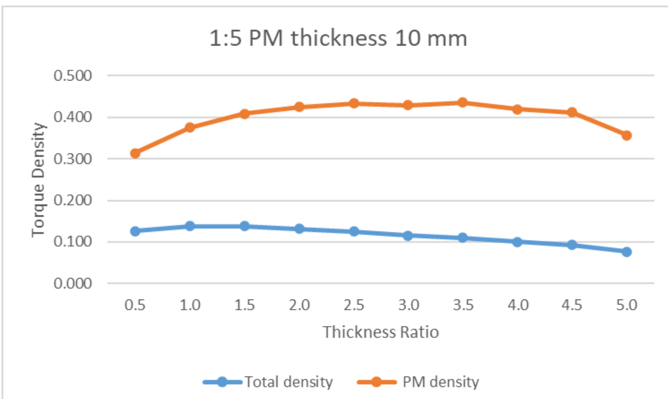

Fig. 3.51. Torque density as a function of Ferro thickness ratio for a 1:5 gear ratio and 10 mm PM thickness.

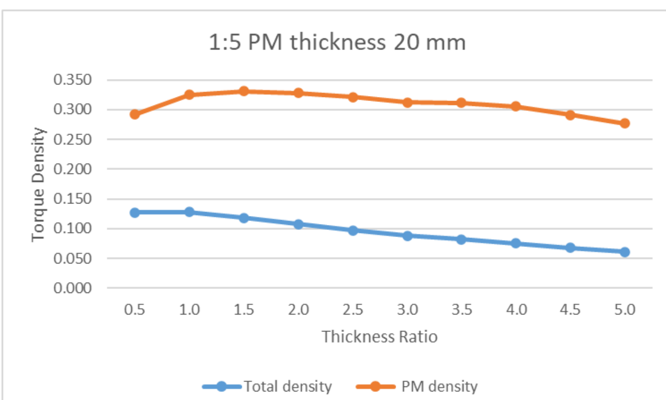

Fig. 3.20. Torque density as a function of Ferro thickness ratio for a 1:5 gear ratio and 20 mm PM thickness.

3. Thickness Effect of Inner and Outer Yokes

Following the investigation of the ferromagnetic modulator's impact, we now examine the role of the inner and outer yokes in the CMG system. The yokes, typically made of high-permeability ferromagnetic materials, serve as return paths for magnetic flux and provide mechanical support for the magnet assemblies. Their thickness directly influences the magnetic saturation margin, structural rigidity, and overall system volume. Thicker yokes can effectively prevent magnetic saturation, especially under high-torque conditions where strong magnetic fields are generated. A sufficient yoke thickness ensures the magnetic flux is fully contained within the core, minimizing leakage and maintaining efficient flux linkage between the inner and outer permanent magnets. However, excessively thick yokes not only increase the total volume and weight of the system but may also lead to underutilized magnetic material, adding mass without contributing significantly to torque transmission.

To quantify this trade-off, we define the yoke thickness as a proportion of the adjacent PM thickness, similar to the approach used for the ferro modulator. By varying this ratio systematically, we can isolate the effect of yoke dimensions while keeping other design parameters constant. FEM simulations are conducted to evaluate how yoke thickness influences both the peak torque transmission capability and the torque density relative to the system's volume. The analysis enables us to determine the minimum required yoke thickness that avoids magnetic saturation while also identifying the point beyond which additional material no longer contributes to performance gains. This provides practical guidelines for optimizing yoke dimensions in high-performance, volume-constrained CMG systems.

Tables 3.15 – 3.18 present the geometric dimensions of the CMG under different yoke thickness ratios. Unlike the previous two sections, where permanent magnet (PM) thickness was varied or normalized, in this section the PM size is held constant while only the inner and outer yoke thicknesses are adjusted. To better understand the yoke's effect under different magnetic loading conditions, we use multiple PM thicknesses as test cases.

Table 3.9. Geometric parameters of CMG for inner yoke thickness study (PM volume = 258 cm³).

Inner yoke Effect Permanent Magnet Volume 258 cm^3							
inner yoke ratio to PM	outer pm_o	outer pm_i	ferro_o	ferro_i	inner pm_o	inner pm_i	inner yoke_i
0	102	97.5	97	85.75	85.25	80.75	80.75
1	102	97.5	97	85.75	85.25	80.75	76.25
2	102	97.5	97	85.75	85.25	80.75	71.75
3	102	97.5	97	85.75	85.25	80.75	67.25
4	102	97.5	97	85.75	85.25	80.75	62.75
5	102	97.5	97	85.75	85.25	80.75	58.25
6	102	97.5	97	85.75	85.25	80.75	53.75

Table 3.16. Geometric parameters of CMG for inner yoke thickness study (PM volume = 155 cm³).

Inner yoke Effect Permanent Magnet Volume 155 cm^3							
inner yoke ratio to PM	outer pm_o	outer pm_i	ferro_o	ferro_i	inner pm_o	inner pm_i	inner yoke_i
0	102	97.5	97	85.75	85.25	80.75	80.75
1	102	97.5	97	85.75	85.25	80.75	76.25
2	102	97.5	97	85.75	85.25	80.75	71.75
3	102	97.5	97	85.75	85.25	80.75	67.25
4	102	97.5	97	85.75	85.25	80.75	62.75
5	102	97.5	97	85.75	85.25	80.75	58.25
6	102	97.5	97	85.75	85.25	80.75	53.75

Table 3.10. Geometric parameters of CMG for inner yoke thickness study (PM volume = 170 cm³).

Outer Yoke Effect Permanent Magnet Volume 170 cm^3							
outer yoke ratio to PM	outer pm_o	outer pm_i	ferro_o	ferro_i	inner pm_o	inner pm_i	inner yoke_i
0	120	115.5	115	103.75	103.25	98.75	76.25
1	115.5	111	110.5	99.25	98.75	94.25	71.75
2	111	106.5	106	94.75	94.25	89.75	67.25
3	106.5	102	101.5	90.25	89.75	85.25	62.75
4	102	97.5	97	85.75	85.25	80.75	58.25
5	97.5	93	92.5	81.25	80.75	76.25	53.75

This approach allows us to isolate the influence of yoke thickness and draw more accurate and generalizable conclusions about its impact on torque transmission and torque density.

Fig. 3.53 and **3.54** show the torque variation with respect to yoke thickness ratio for both inner and outer yokes under a 2:3 gear ratio configuration. Two different permanent magnet volume conditions (denoted as size_1 and size_2) are considered for comparison. For the inner yoke, torque increases significantly as the thickness ratio increases from 0 to 1, then plateaus from ratio 1 to 5, and slightly declines at ratio 6. This indicates that a thickness ratio of 2.0 is sufficient to prevent magnetic saturation, as further increases do not provide noticeable performance improvement. The torque trend is consistent across both magnet sizes, with size_1 generating higher absolute torque due to increased magnetic loading.

Contrary to the inner yoke case, the outer yoke shows a clear peak torque at a thickness ratio of 1.0, beyond which torque output gradually declines for both magnet sizes. This suggests that thicker outer yokes do not contribute to better flux conduction and instead introduce unnecessary magnetic reluctance or leakage paths that reduce effective torque transmission. The behavior is consistent across both magnet volume configurations, highlighting that an outer yoke thickness ratio of 1.0 is sufficient, and thicker designs not only fail to improve performance but may degrade it.

Overall, the results demonstrate that inner yoke thickness should reach at least a ratio of 1.0 to ensure magnetic saturation and stable torque output, while outer yoke thickness performs best at a ratio of 1.0. Further increases in outer yoke thickness reduce torque, indicating a clear trade-off between structural bulk and magnetic efficiency. These findings highlight the importance of differentiated optimization strategies for inner and outer yoke design in CMG systems.

4. Geometry Size Calculation of Coaxial Magnetic Gear

Building upon the previous analyses of component thickness effects—including the permanent magnets, inner and outer yokes, and ferromagnetic modulators—we can now derive the optimal geometric configuration for coaxial magnetic gears (CMGs). By

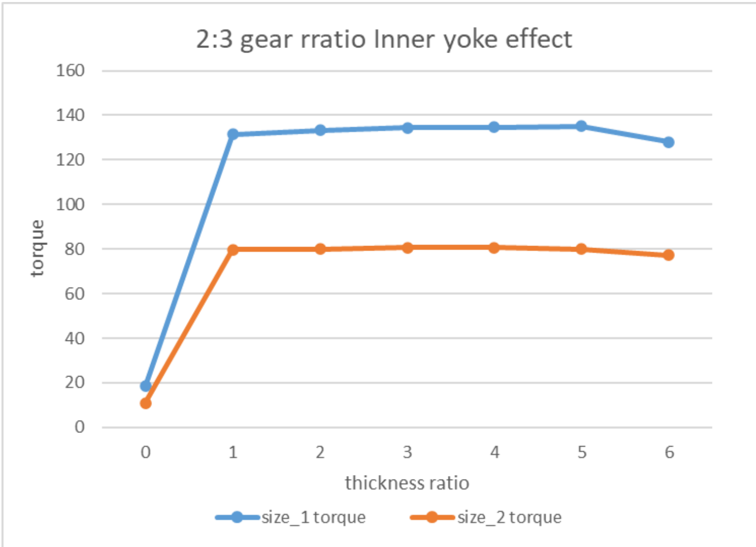

Fig. 3.53. Torque vs. inner yoke thickness ratio for 2:3 gear ratio.

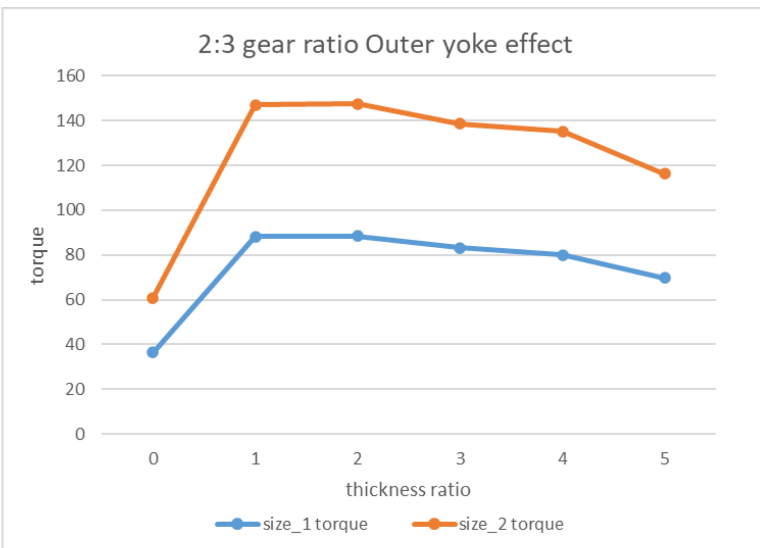

Fig. 3.54. Torque vs. outer yoke thickness ratio for 2:3 gear ratio.

evaluating how the transmission torque responds to variations in these thicknesses, we identify the most effective thickness ratios for maximizing performance. These relationships serve as the basis for determining the optimal geometry size of each component in the CMG structure to achieve high torque transmission efficiency. The final relationship between PMs' thickness and component dimensions is expressed as follows:

$$t_{pm_{in}} = t_{pm_{out}} = t_{pm}$$

$$t_i = t_o = t_{pm}$$

$$t_f = 1.5 * t_{pm}$$

After we define the outer radius of CMGs $r_o$and axial length of l, we could get a relationship between volume of CMGs or volume of permanent magnet of CMG. As shown following:

After defining the outer radius of the CMG as r_o and the axial length as l, we can derive the geometric relationships that link the torque performance to the structural volumes. Specifically, we can express the volume of the entire CMG system V_{total}, as well as the volume of the permanent magnets V_{pm}, as functions of these parameters and the corresponding thicknesses. These relationships are formulated as follows:

1. t_{pm} to V_{pm}

$$V_{pm} = \pi l(4r_o t_{pm} - 11t_{pm}^2 - 4t_{pm}) \qquad \text{(Equ. 3.4.1)}$$

$$t_{pm} = \frac{4-4r_o+\sqrt{(4r_o-4)^2-\frac{44V_{pm}}{\pi l}}}{22} \qquad \text{(Equ. 3.4.2)}$$

2. t_{pm} to V_{total}

$$V_{pm} = \pi l(9.5r_o t_{pm} - 26.125t_{pm}^2 - 9.5t_{pm}) \qquad \text{(Equ. 3.4.3)}$$

$$t_{pm} = \frac{9-9.5r_o+\sqrt{(9.5r_o-9.5)^2-\frac{104.5V_{pm}}{\pi l}}}{52.25} \qquad \text{(Equ. 3.4.4)}$$

Summary Validation of Maximum Torque Line

With the preceding analysis of size effects on CMG torque transmission, the calculation of maximum transmission torque can be simplified to a one-time computation based on system volume. Since all geometric parameters of the CMG can be derived from the defined size equations, the torque output becomes a function of the overall volume configuration. For a given gear ratio—which determines the number of permanent magnet pole pairs and ferromagnetic modulator pieces—we can efficiently compute the maximum transmission torque across a range of volume configurations using FEM or other computational methods. This approach significantly reduces the design complexity by linking performance directly to geometric scaling laws.

To validate the results of our maximum torque line analysis, we conducted 40 simulations using various CMG geometric configurations for each transmission gear ratio, as illustrated in **Fig. 3.55 – 3.58**. These figures include cases with 1:2 and 1:3 transmission ratios. In our analysis, four predefined configurations (nodes) were used to construct the maximum torque line, while the remaining 40 data points served to validate the accuracy and reliability of the predicted torque trend.

For the 1:2 gear ratio, the CMG consists of 2 pole pairs of permanent magnets on the inner rotor, 4 pole pairs on the outer rotor, and 6 ferromagnetic modulators. **Fig. 3.55** and **3.56** present the corresponding maximum torque lines with respect to the volume of permanent magnets and the total system volume, respectively.

For the 1:3 gear ratio, the CMG configuration includes 2 pole pairs on the inner rotor, 6 pole pairs on the outer rotor, and 8 ferromagnetic modulators. **Fig. 3.57** and **3.58** illustrate the maximum torque lines based on the volume of permanent magnets and total system volume, respectively.

Fig. 3.55 – 3.58 collectively validate the effectiveness of the maximum torque line estimation method across different CMG configurations. For both 1:2 and 1:3 gear ratios, the estimated maximum torque lines—constructed from only four predefined configurations—show strong agreement with the full set of simulation results (40 validation points per case). In **Fig. 3.55** and **3.57**, torque is plotted against the volume of permanent magnets, while **Fig. 3.56** and **3.58** use the total system volume as the reference. In both volume metrics, the estimated torque lines closely follow the upper envelope of the data points, accurately capturing the upper-bound torque capacity of the

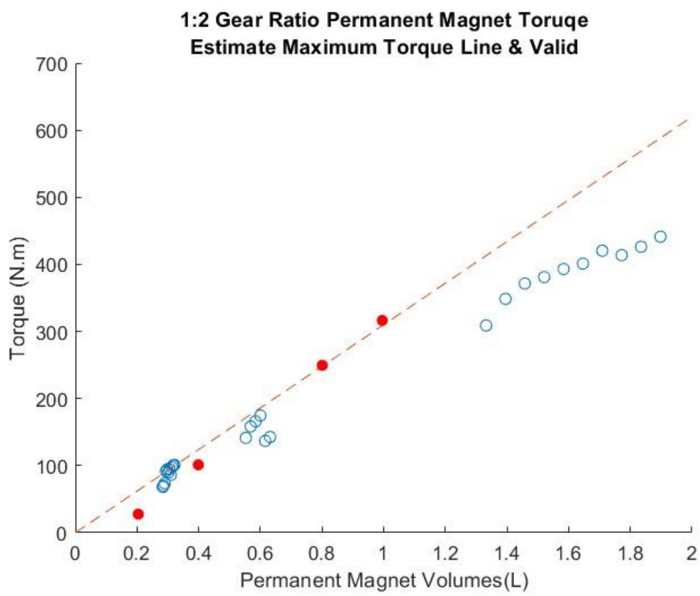

Fig. 3.55. 1:2 Gear ratio maximum torque line per PM volume estimation and validation.

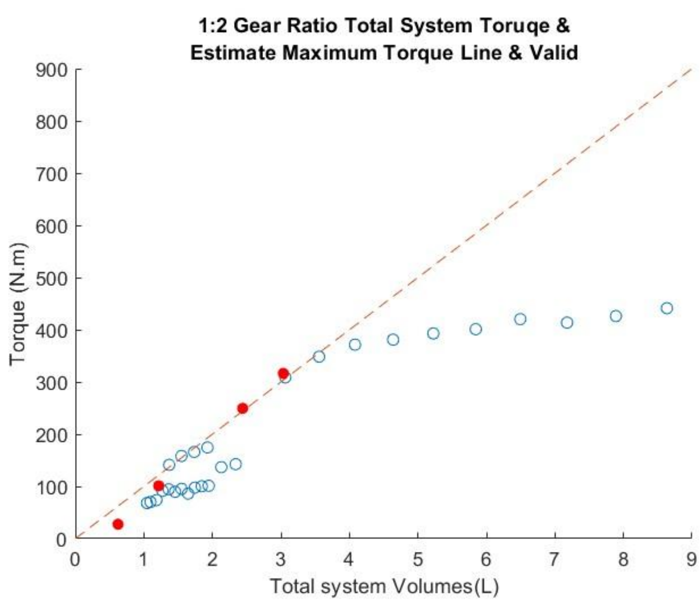

Fig. 3.56. 1:2 Gear ratio maximum torque line per total volume estimation and validation.

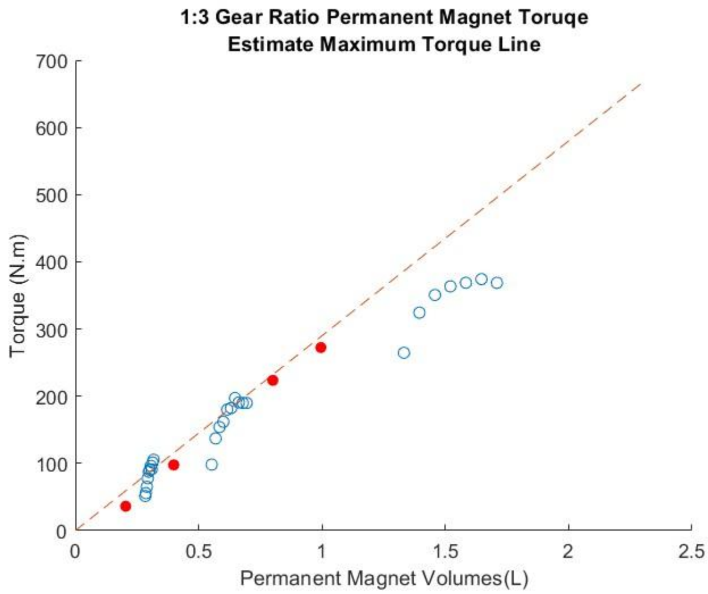

Fig. 3.57. 1:3 Gear ratio maximum torque line per PM volume estimation and validation.

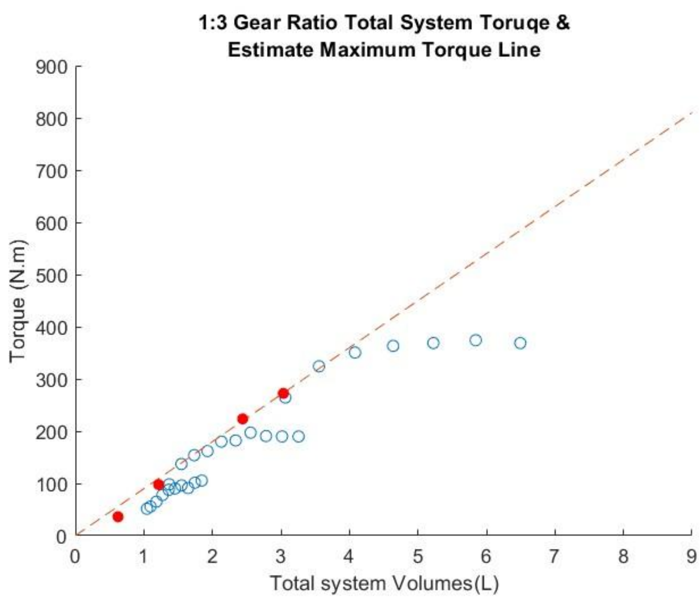

Fig. 3.58. 1:3 Gear ratio maximum torque line per total volume estimation and validation.

-system. This consistency across different gear ratios and volume types demonstrates the robustness of the maximum torque line approach. It confirms that torque potential can be effectively predicted based on system volume and key geometric parameters, significantly reducing the need for extensive simulation across the entire design space.

Design Process Based on the Maximum Torque Line

Shown in **Fig. 3.59**, the designer must define the required transmission torque and the overall size of the MG based on application-specific requirements firstly. The geometric size consists primarily of the outer radius r_o and the axial length l.

Second, the total volume of the permanent magnets V_{pm} is estimated to use the required torque T_l through the Maximum Torque Trend Line (MTTL), as FEM method generated and like shown in **Fig. 3.55 – 3.58**.

Third, the permanent magnet thickness t_{pm} is determined using Equation (3.42 or 3.4.4), by substituting the known values of r_o, l, and V_{pm}.

Finally, the remaining design parameters including the thickness of the outer yoke t_o, the pole piece t_f, and the inner yoke t_i—are calculated by substituting t_{pm} into relationship Equations, respectively.

With all geometric parameters obtained from this process, a complete and efficient MG design can be achieved. Notably, the maximum torque line serves as the key element that links performance requirements to design geometry, enabling a streamlined and scalable design methodology.

5. Optimization and further analysis of maximum torque line generation

Based on the maximum torque line generation methodology established in previous discussions, we identified both the angular position corresponding to the peak torque and the maximum torque density expressed per unit volume of permanent magnets and total CMG system volume across gear ratios ranging from 1:2 to 1:5, as illustrated in **Fig. 3.60** and **3.61**. This analysis is grounded in an additional assumption regarding the relationship between CMG geometric parameters and peak torque output. Specifically, we adopted an optimized configuration of permanent magnet pole pairs and ferromagnetic modulator pieces, along with their optimal thickness ratio, for each CMG design scenario.

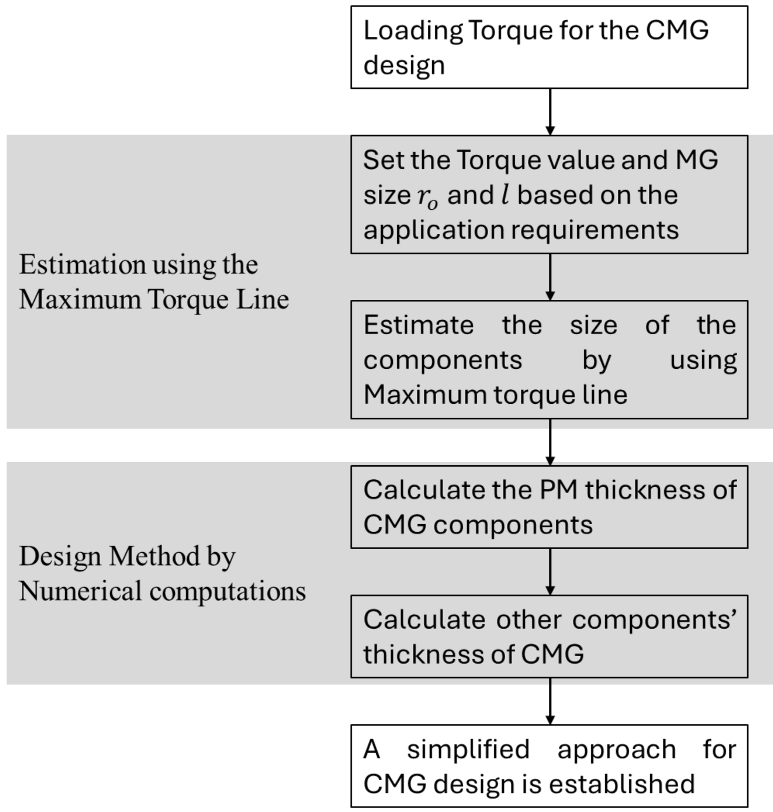

Fig. 3.59. Design process of a Coaxial Magnetic Gear by using maximum torque line method.

However, throughout the gear ratio variation analysis, we observed that the number of poles and modulator pieces changed concurrently. Given the dominant influence of permanent magnet count on torque transmission in CMG systems, we introduced a comparative analysis between double-pair and single-pair configurations while maintaining consistent geometric dimensions across models in **Table. 3.19**. This approach allows us to isolate and better understand the effect of pole count on torque performance, independent of size-related variables.

In this comparison of CMG geometries, design parameters were selected based on insights from the earlier analysis of thickness effects. The inner and outer permanent magnets were assigned to equal thickness, the ferromagnetic modulator was set to 1.5 times that thickness, and the yokes on both sides were given the same thickness as the permanent magnets. With such a geometric setup we could find the maximum torque estimation in such a way that of the volume. We then compare the static torque variation between the single-pair and double-pair CMG configurations and further evaluate these results against the estimated maximum torque line to validate our assumption regarding the influence of pole and piece numbers on maximum torque transmission.

The static torque variation of single and double pair CMG is shown in **Fig. 3.62**. This figure presents a comparison of static torque-angle characteristics between single-pair and double-pair coaxial magnetic gear (CMG) configurations under identical geometric conditions. The results clearly show that the double-pair configuration achieves significantly higher torque output on both the inner and outer rotors, confirming the strong influence of magnetic pole and modulator piece count on torque transmission performance. While the angular positions of peak torque remain largely unchanged, the torque amplitude increases noticeably with the double-pair setup, and the waveform appears more sinusoidal and symmetric. These findings support our earlier assumptions regarding optimal thickness ratios and confirm the significant role of pole count in enhancing magnetic coupling efficiency. The single-pair configuration exhibits a strong alignment with the predicted maximum torque line, indicating that its magnetic structure effectively leverages the optimal flux interaction path.

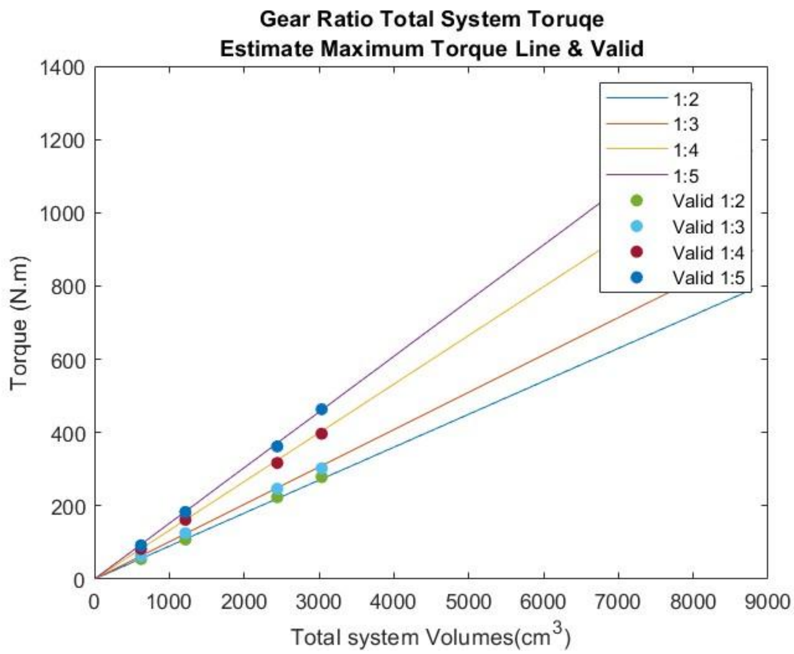

Fig. 3.60. 1:2 to 1:5 Gear ratio maximum torque line per system volume estimation and validation.

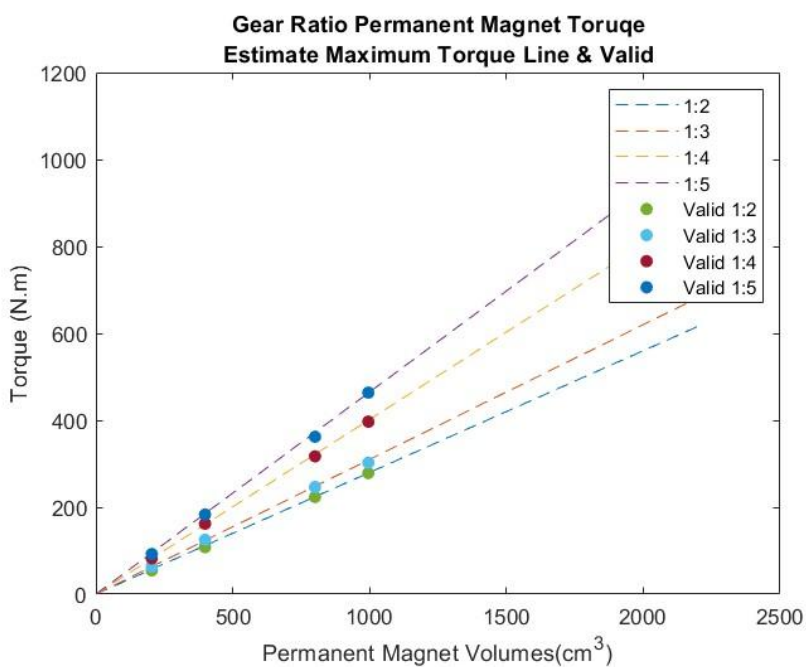

Fig. 3.61. 1:2 to 1:5 Gear ratio maximum torque line per PM volume estimation and validation.

Table. 3.19. Geometry size of CMG single and double pairs comparison.

Geometry Size of CMG Single vs Double Pairs			
inner yoke_i	inner pm_i	inner pm_o	ferro_i
59	69	79	80
ferro_o	outer pm_i	outer pm_o	outer yoke_o
95	96	106	116

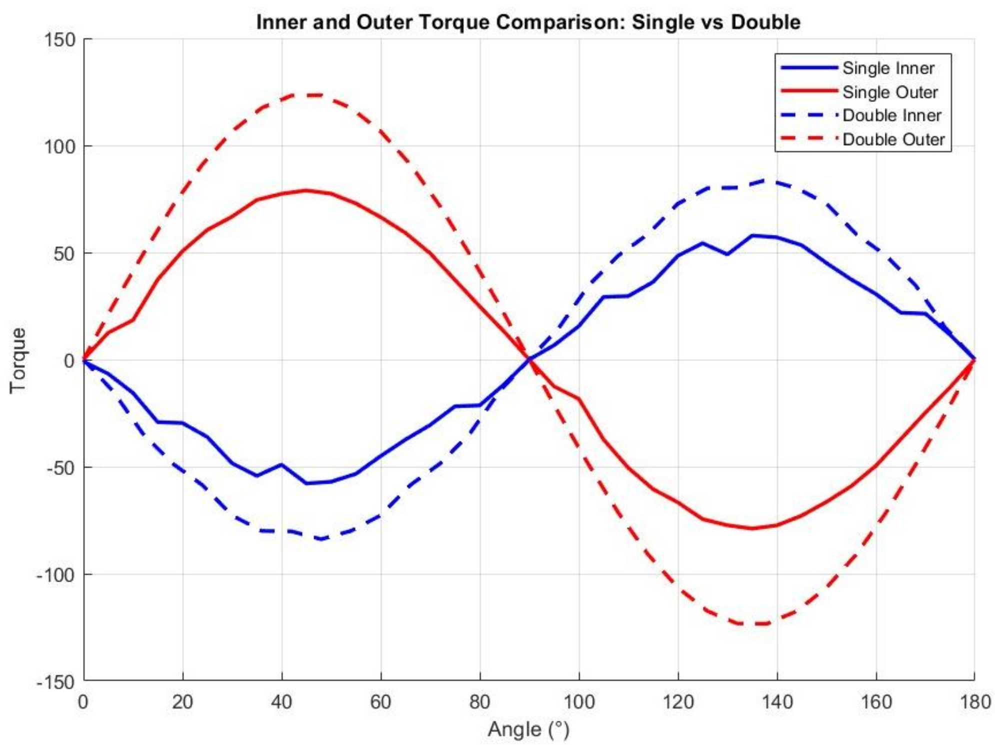

Fig. 3.62. Static torque-angle comparison of single-pair and double-pair CMG configurations.

This agreement validates the accuracy of the maximum torque line model and highlights its value in guiding CMG design. It enables the strategic selection of pole pair numbers and ferro modulator counts to optimize torque transmission.

In contrast, the double-pair configuration achieves higher torque capacity but deviates from the predicted maximum torque line. This discrepancy suggests that it enhances performance through an alternative magnetic coupling mechanism, reinforcing its potential in high-performance CMG applications where torque output is prioritized over structural alignment. Interestingly, the torque achieved by the double-pair configuration closely matches the torque density of a 1:4 CMG transmission. Given that both systems share similar structural characteristics, this resemblance is noteworthy.

Another key similarity lies in their use of the same pair number of outer poles. This observation leads to a hypothesis: the maximum output torque in CMG systems may be primarily governed by the outer pole count. Further investigation is warranted to examine whether the outer rotor pole number imposes a dominant constraint on torque transmission capacity, especially in configurations aiming for high gear ratios and torque density.

Building on this observation, we introduce a new hypothesis: by fixing the outer rotor pole pair number while allowing the gear ratio to vary, we can observe how changes in the inner rotor and ferromagnetic modulator—both of which adjust according to the gear ratio—affect the maximum torque output, under a constant geometric size. Since the gear ratio in CMG systems is determined by the relationship between the pole pair numbers of the inner and outer rotors and the number of ferromagnetic pieces, fixing the outer pole pair number while varying the ratio inherently alters the inner magnetic structure. This approach allows us to investigate how different magnetic configurations, under constrained volume and fixed outer geometry, influence the torque performance, and helps refine our understanding of the design trade-offs in achieving high-efficiency torque transmission.

To validate our assumptions regarding the influence of pole number on torque transmission across different gear ratios, we designed a comparative study using consistent CMG geometry. By holding the structural parameters constant, we aim to isolate the effect of varying outer pole numbers associated with different gear ratios. This ensures that any observed changes in torque output can be attributed primarily to the magnetic coupling mechanism, rather than dimensional or material variations. The geometric configuration used in this analysis is detailed in **Table 3.20**, which outlines the fixed dimensions applied across all cases for a fair and controlled comparison.

Fig. 3.63 illustrates the relationship between gear ratio and maximum torque for both the inner and outer rotors in a CMG system, under varying outer pole numbers. The CMG geometry is held constant across all configurations to isolate the effect of gear ratio and corresponding pole number variation.

As the gear ratio increases from 1:1 to 1:10, the inner torque (blue bars) shows a progressive decline, which is consistent with the inverse relationship between torque and speed in magnetic gear systems—higher gear ratios typically mean higher speed reduction but lower input torque.

In contrast, the outer torque (orange bars) shows a monotonic increase and appears to approach a saturation level around a gear ratio of 1:6 and above. This trend suggests that the outer torque becomes less sensitive to further increases in gear ratio or pole number beyond a certain threshold. This saturation behavior may be attributed to magnetic saturation in the materials or diminishing improvements in flux coupling efficiency at high pole counts. Interestingly, the curve implies that outer torque is highly correlated with the outer pole number, reinforcing the hypothesis that the outer rotor's pole count plays a dominant role in determining maximum output torque.

This insight aligns with earlier observations from the double-pair CMG configuration, which exhibited high output torque while sharing the same outer pole count as a 1:4 gear ratio case.

This observation may have significant implications for CMG design, suggesting that optimizing outer pole number could be a more effective strategy for improving output torque than simply adjusting inner rotor configuration or gear ratio alone. To further investigate the influence of magnetic pole distribution on maximum torque transmission,

Table 3.20. Geometry size of CMG for different gear ratio and outer pole number comparison.

size	inner yoke	IR inner PM	OR inner PM	IR Ferro	OR Ferro
mm	65	75	85	86	101
IR Outer PM	OR Outer PM	Outer Yoke	L_axial	weight	Volume
102	112	122	100	21.41	2.79

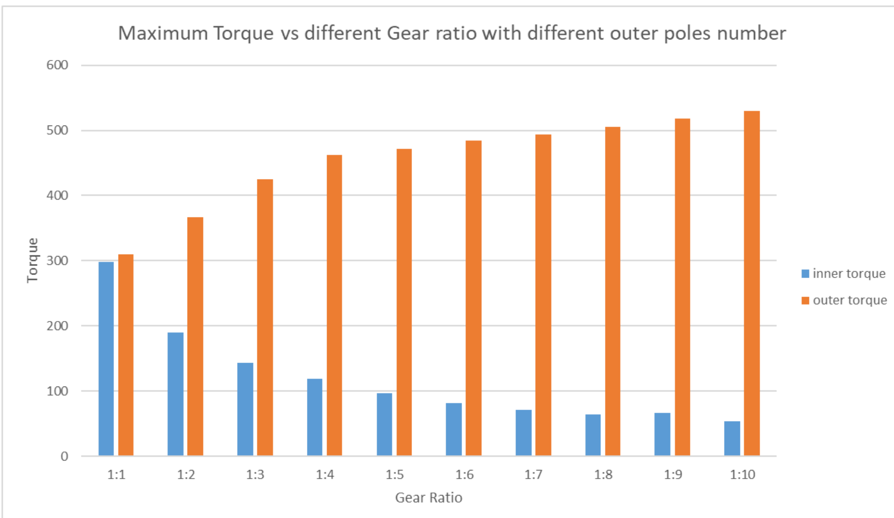

Fig. 3.63. Maximum torque variation across gear ratios with different outer pole numbers.

We extend our analysis by shifting the design focus. While the previous setup fixed the inner rotor's pole pair number and varied the outer pole count across gear ratios, in this phase we approximately fix the outer rotor's pole pair number within a narrow range and vary the inner pole count to explore its effect on torque performance. This strategy allows us to assess how inner-side magnetic structures contribute to torque transmission when the outer magnetic boundary condition remains relatively consistent. Although the outer pole number is not exactly constant across all configurations, it remains within a limited range to minimize its influence. Under this assumption, we hypothesize that an increase in the outer pole pair number will generally lead to higher maximum outer torque, due to enhanced magnetic coupling and flux density on the outer rotor side.

As with the previous analysis, the geometric parameters of the CMG system remain identical to those listed in **Table 3.20**, ensuring that any observed differences in torque output are primarily attributable to magnetic pole arrangement rather than variations in size or material properties.

A series of gear ratios ranging from 1:1 to 1:10 is analyzed in this study. For each gear ratio, the corresponding number of inner and outer pole pairs is selected to reflect realistic CMG configurations. These pole pair combinations are summarized in **Table 3.21**, presented in the form of ratios. Each ratio directly represents the actual number of pole pairs assigned to the inner and outer rotors during the analysis process.

The results presented will include the inner and outer torque values for each gear ratio, as well as the corresponding torque density per total system volume and torque density per unit weight. These metrics provide a comprehensive view of the system's mechanical efficiency and compactness across different pole configurations.

In addition to comparing absolute torque values, we will also analyze the maximum torque density under two conditions: across configurations with varying outer permanent magnet (PM) pole pair numbers, and across those with identical outer pole counts.

Table 3.21. Gear ratio with inner and outer pole pair number.

1:1		1:2		1:3		1:4		1:5	
Inner pole pairs	Outer pole pairs	Inner pole pairs	Outer pole pairs	Inner pole pairs	Outer pole pairs	Inner pole pairs	Outer pole pairs	Inner pole pairs	Outer pole pairs
8	8	6	12	5	15	4	16	4	20
1:6		1:7		1:8		1:9		1:10	
Inner pole pairs	Outer pole pairs	Inner pole pairs	Outer pole pairs	Inner pole pairs	Outer pole pairs	Inner pole pairs	Outer pole pairs	Inner pole pairs	Outer pole pairs
3	18	3	21	2	16	2	18	2	20

This dual comparison allows us to isolate Influence of the outer rotor pole pair number on torque transmission performance and assess whether higher outer PM pole numbers consistently result in improved performance.

Furthermore, we will evaluate the effect of multiple pole pair numbers on the torque ratio between the inner and outer rotors. Specifically, we aim to validate whether the resulting torque ratio approximates the inverse of the gear ratio, as predicted by magnetic gear theory. This validation will help confirm the theoretical torque scaling behavior in practical CMG configurations.

Fig. 3.59 shows that the torque density per unit volume (Nm/L) steadily increases from 1:1 to 1:5, driven by the increase in outer pole pair number. However, from 1:5 to 1:10—where the outer pole pair number is held constant at 20—the torque density values remain relatively close to one another, varying only slightly. This indicates that, under fixed outer magnetic conditions, further increases in gear ratio (i.e., changes in inner pole and modulator configuration) contribute less significantly to volume-based torque density.

Fig. 3.60 presents a similar trend in torque density per unit weight (Nm/kg). The values rise consistently up to 1:5, aligning with the rising outer pole count in **Table 3.21**. From 1:5 to 1:10, the torque density per weight stabilizes, with only marginal differences among the gear ratios. This reinforces the idea that the outer magnetic structure plays a dominant role in determining overall torque efficiency per mass, and that once saturated, the performance gain from internal variation is minimal.

Fig. 3.61 provides the clearest evidence of this effect. The outer rotor torque increases with gear ratio up to 1:5, but from 1:5 to 1:10—where the outer pole pair number is constant—the outer torque values remain nearly identical (ranging from approximately 564 Nm to 583 Nm). Despite variations in the inner rotor torque and gear ratio, the outer

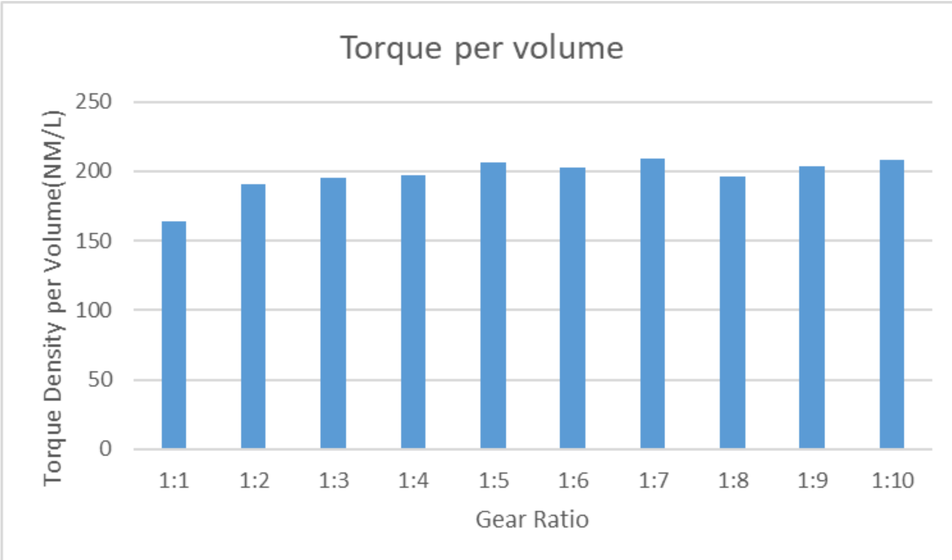

Fig. 3.60. Torque density per unit volume (Nm/L) across gear ratios based on configurations in Table 3.21.

rotor torque remains stable, confirming that the outer pole pair number is the key limiting factor for torque amplification. This consistency across gear ratios with the same outer pole count highlights a performance plateau dictated by outer magnetic geometry.

In summary, the analysis confirms that the outer pole pair number serves as a dominant factor in determining the maximum torque capability of a coaxial magnetic gear (CMG). When combined with the gear ratio and the established internal thickness ratio configuration of permanent magnets, ferromagnetic modulators, and yokes, a predictive model—termed the maximum torque line—can be constructed. This method enables rapid estimation of the maximum achievable torque without the need for repeated finite element simulations or detailed structural recalculations. Consequently, designers can efficiently generate and scale CMG configurations based on target torque requirements, significantly accelerating the design process while maintaining reliable performance predictions.

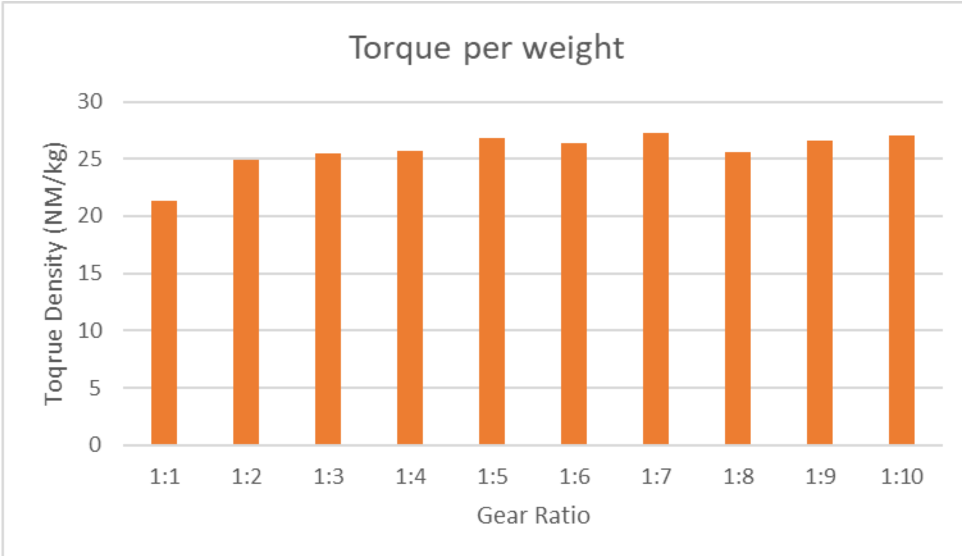

Fig. 3.61. Torque density per unit weight (Nm/kg) across gear ratios based on configurations in Table 3.21.

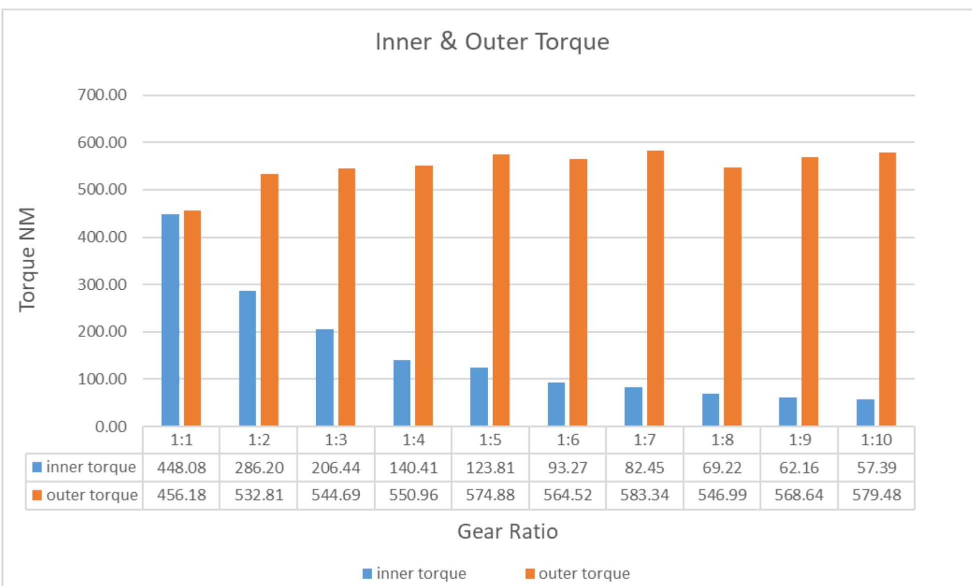

Fig. 3.62. Inner and outer torque (Nm) across gear ratios based on configurations in Table 3.21.

3.5 Magnetic Gear Transmission Efficiency

Magnetic gear transmissions have emerged as a promising alternative to conventional mechanical gear systems due to their contactless torque transfer, inherent overload protection, and reduced maintenance requirements. Despite these advantages, the overall efficiency of MGTs remains a critical concern, particularly in high-performance applications where power density and thermal management are paramount. The efficiency of magnetic gear systems is primarily affected by electromagnetic losses, including eddy current loss, hysteresis loss, and magnetic flux leakage, as well as parasitic mechanical losses such as bearing drag and windage. This section provides a comprehensive analysis of the major loss mechanisms in MGTs and discusses their impact on transmission efficiency under various operating conditions.

3.5.1. Key Determinants of Magnetic Gear Efficiency

The efficiency of a magnetic gear is governed by a combination of magnetic design, material properties, mechanical integration, and operating conditions. Unlike mechanical gears, which primarily lose energy through friction, lubrication, and wear, magnetic gears experience a distinct set of loss mechanisms:

1. Effects of Geometry on Magnetic Gear Performance

The geometry and topology of magnetic gears, including the number of pole pairs, air gap size, and magnet alignment, have a direct impact on the efficiency of magnetic flux transfer between the input and output rotors. Among these factors, the size and spatial configuration of magnetic components exert the most significant influence on gear performance. These design features commonly give rise to the following challenges:

- Flux leakage: Magnetic flux that does not complete its intended path, reducing torque transfer.
- Saturation: Occurs when the ferromagnetic materials (like the flux modulator or yokes) carry more flux than their saturation limits, causing nonlinear behavior and reduced efficiency.
- Unbalanced magnetic forces: Resulting in vibration and energy loss.

2. Effects of Material Properties on Magnetic Gear Performance

The selection of magnetic materials used in the construction of permanent magnets, flux modulators, and yokes plays a critical role in determining both the overall performance and the efficiency of magnetic gears. Material properties such as remanence, coercivity, magnetic permeability, and electrical resistivity directly affect the transmission capability and loss characteristics of the system. An appropriate material choice is essential not only for maximizing torque density and maintaining magnetic field strength, but also for minimizing energy losses during operation.

Permanent magnets, such as neodymium-iron-boron (NdFeB), should exhibit high remanence and coercivity to sustain strong and stable magnetic fields. Ferromagnetic materials, including silicon steel or soft magnetic composites, are preferred for modulators and yokes due to their high magnetic permeability and low core losses. Inappropriate material selection can lead to substantial energy losses, including:

- Hysteresis loss: Energy dissipated during repeated magnetization and demagnetization cycles in ferromagnetic materials.
- Eddy current loss: Heat generated by induced circulating currents within conductive components when exposed to changing magnetic fields.

3. Effects of Operation Condition on Magnetic Gear Performance

The operating conditions of magnetic gears have a profound impact on their performance, efficiency, and long-term reliability. Key variables such as rotational speed, load torque, and ambient temperature dynamically influence the behavior of magnetic fields, material properties, and loss mechanisms within the system. Understanding these dependencies is essential for accurate performance prediction and for ensuring robust operation under varying conditions.

- Load torque: Operating near or beyond the rated torque can push materials into saturation, increasing hysteresis and decreasing flux linkage.
- Temperature: Elevated temperatures can degrade magnet strength and increase core losses in ferromagnetic materials.

- Torque ripple: Periodic torque fluctuations during operation, often caused by geometric or magnetic irregularities. It can lead to vibration, noise, and energy loss, especially in high-speed or precision systems where stable torque is essential.

3.5.2 Magnetic Gear Efficiency Model

Expanding on the earlier analysis of factors affecting magnetic gear transmission efficiency—and drawing parallels with magnetically coupled mechanical systems such as electromagnetic machines—this section examines three major loss mechanisms: hysteresis loss, eddy current loss, and torque ripple. These components significantly impact the overall performance and energy efficiency of magnetic gear systems.

The torque ripple effect represents a distinct loss mechanism in magnetic gear systems, originating from periodic torque fluctuations caused by non-uniform magnetic coupling. These fluctuations result from magnetic field distortion, air gap variation, and modulator geometry. Although not an electrical loss, torque ripple contributes to mechanical vibration, increased control effort, and wear, leading to measurable energy dissipation. It is particularly relevant in high-speed and precision applications.

1. Hysteresis Loss

The Hysteresis Loss is a kind of energy dissipated during repeated magnetization and demagnetization cycles in ferromagnetic materials. Hence, we will only consider the loss happening in inner/outer yoke and Ferro Modulators:

$$P_{hin} = k_h * f_{in} * {B_{in}}^2 * V_{yi} \quad \text{(Equ. 3.5.1)}$$

$$P_{hout} = k_h * f_{out} * {B_{out}}^2 * V_{yo} \quad \text{(Equ. 3.5.2)}$$

$$P_{hm} = k_h * f_m * {B_m}^2 * V_m \quad \text{(Equ. 3.5.3)}$$

2. Eddy Current Loss

Eddy current loss arises from circulating currents induced within conductive components exposed to time-varying magnetic fields, resulting in heat generation. In magnetic gear systems, these losses are concentrated in regions with high magnetic flux variation, namely the inner yoke, outer yoke, and ferromagnetic modulators. Contributions from other areas are minimal and thus omitted from the analysis.

$$P_{eddin} = k_{edd} * f_{in} * {B_{in}}^2 * V_{yi} \quad \text{(Equ. 3.5.4)}$$

$$P_{eddout} = k_{edd} * f_{out} * {B_{out}}^2 * V_{yo} \quad \text{(Equ. 3.5.5)}$$

$$P_{eddm} = k_{edd} * f_m * {B_m}^2 * V_m \quad \text{(Equ. 3.5.6)}$$

3. Torque Ripple Induce Loss

Torque ripple induced loss represents a distinct loss mechanism in magnetic gear systems, originating from periodic torque fluctuations caused by non-uniform magnetic coupling. In our model, we assume that one of the three components in the concentric magnetic gear (CMG) is fixed, with the other two serving as input and output. Alternatively, a two-input one-output configuration is considered. Accordingly, torque ripple loss is evaluated only on the output rotor, where its impact on performance and energy dissipation is most critical:

$$P_{eddm} = \frac{{T_{output}}^2}{2 \cdot J \cdot \omega} \quad \text{(Equ. 3.5.7)}$$

In (Equ. 3.5.1) to (Equ. 3.5.7), the k_h denotes the empirical hysteresis loss coefficient and k_{edd} denotes the empirical eddy current loss coefficient and, f_{in} is the frequency of magentic field variation and V_{yi} is the volume of the inner/outer yoke or Ferro modulators, respectivley.

Using the same 1:3 gear ratio CMG example and applying the geometric dimensions provided in Table 1, we evaluate the gear transmission efficiency under an input torque of 500 Nm. This analysis yields the overall efficiency, the loss distribution across individual components, and the breakdown of loss magnitudes at varying rotor speeds shown in **Fig. 3.62 – 3.65**. As shown in **Fig. 3.67**, the gear transmission efficiency of a CMG system with a 1:3 gear ratio is evaluated under two configurations: one with standard pole pair numbers and another with doubled pole pair numbers. The efficiency decreases as input rotor speed increases from 500 to 5000 RPM due to rising dynamic and iron losses.

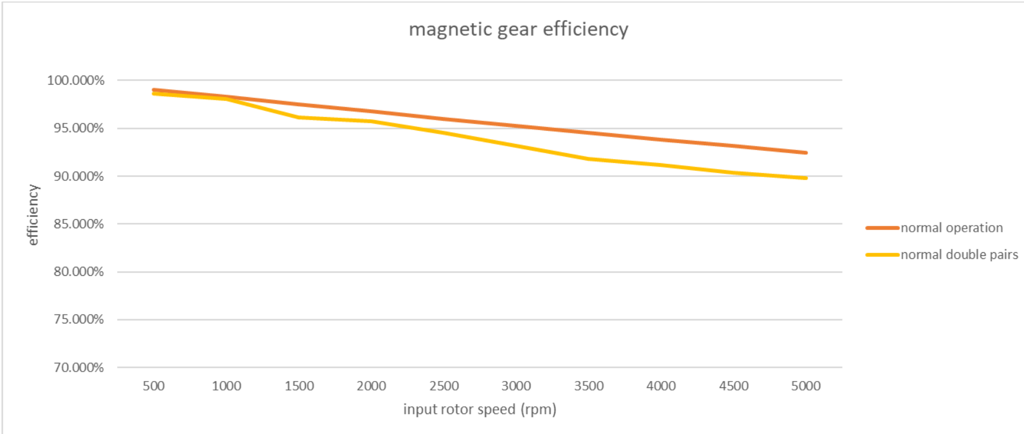

Fig. 3.67. Gear efficiency comparsion with same gear ratio different poles number.

However, the double-pair configuration consistently exhibits slightly higher efficiency, particularly at lower speeds. This improvement is attributed to enhanced magnetic coupling and reduced torque ripple provided by the higher pole pair count.

Fig. 3.68 presents the total loss in magnetic gear operation under the standard configuration, broken down into eddy current loss, hysteresis loss, and torque ripple across different speeds. The results show that total loss increases significantly with rotor speed. Eddy current loss is the dominant component, followed by hysteresis loss, while torque ripple remains relatively minor. The steep growth in eddy current loss with speed-confirms its dependence on frequency, making it the primary limiting factor in high-speed performance. The relative composition of losses is further detailed in **Fig. 3.69** and **Fig. 3.70**, which illustrate the percentage breakdown of iron losses at 500 RPM and 5000 RPM, respectively. **In Fig. 3.69**, at 500 RPM, eddy current loss accounts for approximately 84 percent of total loss, hysteresis loss contributes about 13 percent, and torque ripple is minimal. In contrast, **Fig. 3.70** shows that at 5000 RPM, eddy current loss becomes overwhelmingly dominant, while the contributions from hysteresis loss and torque ripple are nearly negligible. These figures emphasize that efficiency degradation at high speed is primarily driven by eddy losses, and further improvements require the use of low-conductivity materials and laminated structures.

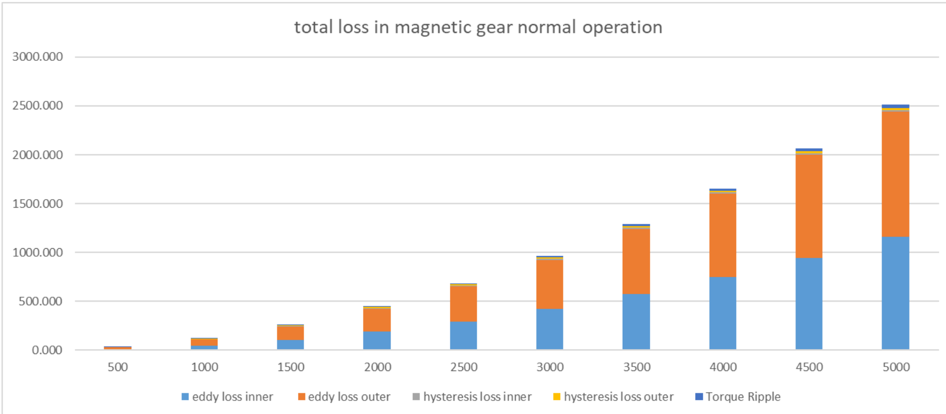

Fig. 3.68. Gear breakdown loss across individual components.

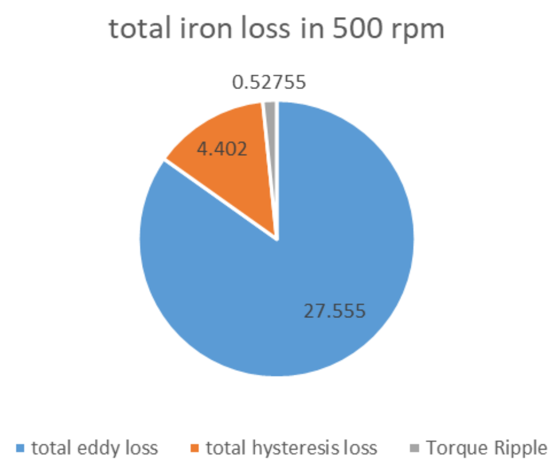

Fig. 3.69. Gear breakdown loss with input speed 500 RPM.

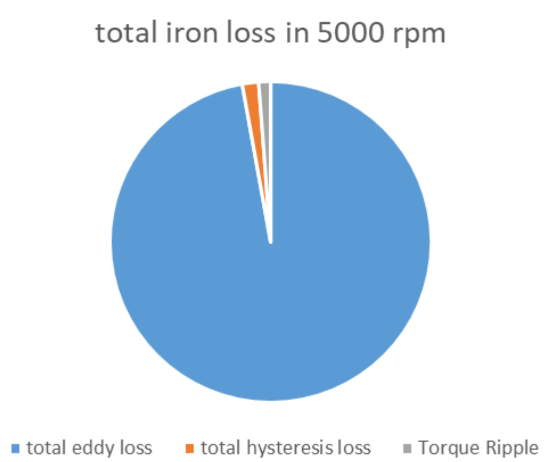

Fig. 3.70. Gear breakdown loss with input speed 5000 RPM.

3.6 Chapter Three Summary

This chapter provides a comprehensive theoretical and simulation-based exploration of coaxial magnetic gear (CMG) systems, focusing on their design methodology, torque transmission characteristics, and efficiency behavior under static and dynamic conditions. Starting from the basic operating principles of magnetic gears, this chapter introduces the concept of magnetic flux modulation and formulates a torque generation model based on the interaction between the permanent magnets mounted on the inner and outer rotors and the intermediate ferromagnetic modulator. Through a combination of analytical derivation and numerical simulation, a generalized torque expression is established, capturing the sinusoidal dependence of torque output on angular displacement, influenced by the configuration of pole pairs and the magnetic properties of the materials involved.

A key contribution of this chapter is the derivation of the maximum torque line, which provides a predictive tool for estimating the upper bound of torque transmission based on the CMG's outer pole pair number, gear ratio, and internal thickness ratios. This method significantly reduces the need for repetitive finite element simulations during the design phase. Parametric studies are conducted to examine how variations in inner and outer permanent magnet thickness, as well as ferromagnetic modulator geometry, influence torque amplitude, transmission stability, and torque density metrics (per volume and per weight). Results indicate that configurations with higher outer pole pair count consistently exhibit better torque density performance, particularly when geometric size is fixed.

Furthermore, both single-pair and double-pair magnetic configurations are compared using static torque simulations, revealing that torque output and waveform stability improve with increased pole count. When the outer pole pair number is held constant and only the gear ratio is varied, the torque performance converges across configurations, suggesting a saturation point for torque density dictated by outer rotor design.

The chapter also extends into dynamic simulation using MATLAB-based finite element modeling. Two dynamic engagement scenarios—partial engagement and full steady-state operation—are investigated to capture the transient and steady torque response under realistic loading. These simulations confirm that the general torque equation aligns well with FEM results, particularly for the outer rotor where torque response is smoother and more predictable.

In the final section, the chapter shifts focus to efficiency and loss analysis, breaking down magnetic loss components including eddy current loss, hysteresis loss, and torque ripple. Simulation results show that eddy current loss dominates, especially at high rotor speeds, whereas the benefit of increasing pole pairs is most evident at lower speeds. Pie charts and trend plots across multiple speeds (500 to 5000 RPM) provide quantitative insights into how loss composition evolves with speed, reinforcing the need for advanced magnetic materials and lamination strategies for high-speed CMG applications.

Overall, this chapter establishes a robust framework for CMG design and optimization. It integrates theoretical modeling, geometric sizing, dynamic response validation, and loss prediction to support high-torque-density magnetic gear development. The presented models and methods are applicable to aerospace, electric vehicle, and robotic drivetrains, where compactness, non-contact operation, and high efficiency are critical design requirements.

CHAPTER FOUR
RESULTS AND DISCUSSION

In the previous chapter, we presented a detailed analysis of both planetary and magnetic gear transmission systems, including their fundamental operating principles and analytical modeling approaches. Specifically, we introduced the mechanical transmission mechanism of planetary gear sets and their associated size modeling methods. For magnetic gears, we focused on the Concentric Magnetic Gear (CMG) system, which mimics the architecture of planetary gear trains but utilizes magnetic coupling instead of physical contact between components.

To construct an accurate CMG transmission model, we introduced both analytical and numerical methods for calculating magnetic field distribution and magnetic flux linkage between the rotating components. In particular, we implemented a Finite Element Method (FEM) model to simulate the magnetic field behavior and to evaluate torque transmission under varying structural and magnetic configurations.

Through this analysis, we established the relationship between the magnetic torque and the relative angular position of the inner rotor, outer rotor, and ferromagnetic modulator. This relationship was further extended to angular velocity, enabling dynamic modeling of CMG components. To streamline the design process, we also proposed a size modeling approach for CMGs based on the thickness ratios of the inner/outer permanent magnets, ferromagnetic modulators, and yokes. By optimizing these ratios, we identified configurations that maximize torque density per unit volume across a range of magnetic gear ratios.

Moreover, we developed an optimization framework to define the maximum torque line for CMG systems, based on the best-performing geometric ratios and the number of pole pairs on the outer rotor. A key conclusion is that CMGs with the same number of outer pole pairs tend to exhibit similar maximum torque characteristics regardless of gear ratio. This is due to the outer rotor’s dominant role in determining the overall magnetic field intensity and torque capability.

This insight enables a more efficient and systematic design approach for CMG systems, where the geometric structure and pole pair numbers can be tailored to meet specific torque and size requirements. In the following sections, we will extend this foundational model by integrating the CMG system into a hybrid Magnetic-Electric Continuously Variable Transmission (MECVT) drivetrain architecture and investigate its application to advanced rotorcraft powertrains.

In this chapter, we will consolidate the previous findings and integrate CMG and planetary gear transmissions with electric motor/generator components to design a Magnetic Electric Continuously Variable Transmission (MECVT) system. A dynamic simulation model will be employed to analyze and evaluate the MECVT's performance under realistic operational conditions.

4.1 Electric Motor Geometric Model Using a Four-Rule Parametric Approach

To simplify the design of a high-performance outer-rotor Permanent Magnet Synchronous Motor (PMSM), a four-rule parametric sizing framework has been developed. This method enables systematic prediction of the motor's key geometric parameters, mass distribution, and structural stress behavior under a fixed torque requirement. By establishing clear relationships between electromagnetic loading, mechanical constraints, and dimensional variables, the model supports rapid early-stage evaluation and iterative optimization.

Moreover, this rule-based approach facilitates seamless integration with magnetic gear systems, making it especially suitable for use in hybrid electromechanical drivetrains such as Magnetic Electric Continuously Variable Transmissions (MECVTs) [50]. The design process follows a structured flow, as illustrated in **Fig. 4.1**, which outlines each phase of motor development from torque input to full geometry and stress verification. The key parameters and their assumed or calculated values used in this model are summarized in **Table 4.1**, including target torque, linear current density, air gap flux density, material properties, and layer thicknesses for each structural component.

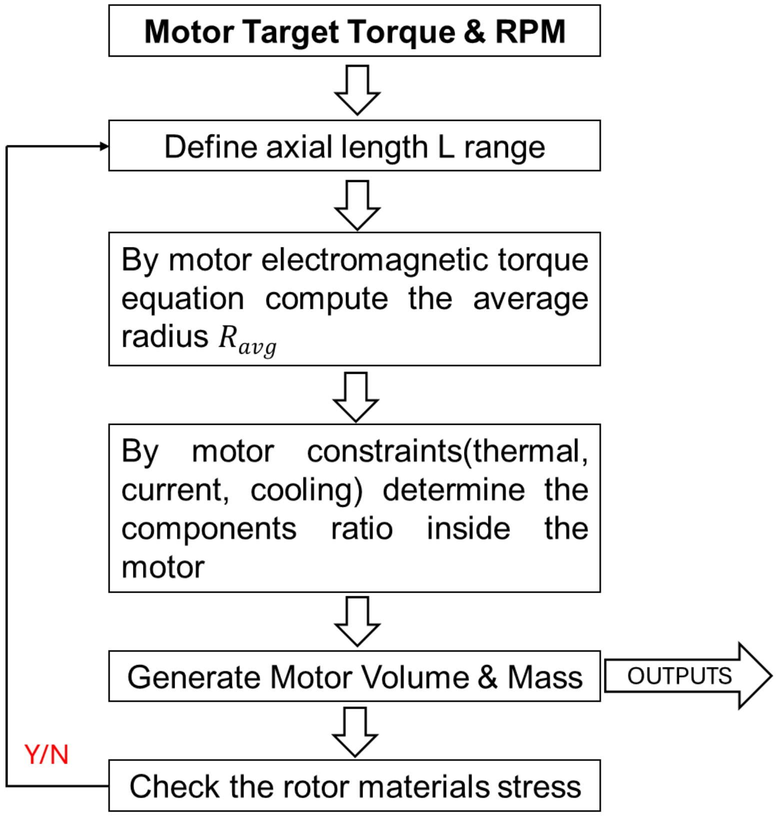

Fig. 4.1. Electric motor design and optimization flow chart.

According to this principle, the electromagnetic torque T generated by the motor is directly related to the product of the shear stress in the air gap and the effective volume where this stress is applied. The torque can be expressed as:

$$T = 2\pi\, {R_{avg}}^2\, B_{gap}\, A_{linear}\, L \qquad \text{(Equation 4.1)}$$

$$R_{avg} = \sqrt{\frac{T}{2\pi\, R_{avg}\, B_{gap}\, A_{linear}\, L}} \qquad \text{(Equation 4.2)}$$

Here, B_{gap} is the air gap flux density, and A_{linear} is the linear current density—two key electromagnetic loading parameters in high-performance motor design [51]. In this model, we assume $B_{gap} = 1.0\, T$ and A_{linear} is range from $30 - 80(kA/m,)$ for the air cooling system, $80 - 150(kA/m)$ for the water cooling system and $150 - 200(kA/m)$ for the water Air-Hydrogen Cooling system[55]-[56], based on values reported for high-speed aerospace PMSMs [52]. This torque-based sizing rule ensures that the machine can generate the required torque without exceeding practical limits on magnetic loading and thermal capacity. It serves as the foundation for determining the motor's radial dimensions and is especially useful in early-stage analytical design before proceeding to finite element refinement [59]-[60]. The second rule defines the stator layer distribution, dividing the stator radially into three regions: the inner radius (around 50% of R_{avg}), the slot region (around 15% R_{avg}), and the stator yoke (around 10% of R_{avg}). The thicknesses of these layers are assigned in proportion to the average stator radius to ensure balanced electrical, magnetic, and mechanical performance. Specifically, the slot region must be thick enough to accommodate the required conductor area for a target linear current density without exceeding thermal limits. The stator yoke thickness is constrained by the magnetic saturation level of the core material which usually typically around 1.5–1.8 T for electrical steel to prevent excessive core losses and magnetic inefficiency. The inner radius is often dictated by shaft size, insulation clearance, or structural support. This proportional dimensional strategy provides a simplified yet effective framework for early-stage sizing, consistent with established practices in lamination stack optimization for radial-flux machines [53],[57]-[58].

Table 4.1. Computation parameters in electric motor design.

Parameter	Unit
Inner radius of stator (R_i)	m
Outer radius of stator (R_o)	m
Length of motor (L)	m
Density of steel (rho_steel)	kg/m^3
Density of copper (rho_copper)	kg/m^3
Density of permanent magnets (rho_magnet)	kg/m^3
Density of modulator material (rho_modulator)	kg/m^3
Number of slots (N_slots)	-
Area of copper in slot (A_cu)	m^2
Number of turns per slot (N_turns)	-
Breakdown field strength of insulation (E_bd)	V/m
Insulation thickness (d_ins)	m
Maximum current density (J_max)	A/m^2
Resistance at reference temperature (R_0)	Ohm
Temperature coefficient of resistance (alpha)	1/K
Ambient temperature (T_amb)	K
Maximum allowable temperature (T_max)	K
Heat transfer coefficient (h)	W/m^2*K
Cooling surface area (A_cool)	m^2
Inner rotor pole pairs (p_i)	-
Outer rotor pole pairs (p_o)	-
Permeability of free space (mu_0)	H/m
Relative permeability of core material (mu_r)	-
Magnetic path length (l_mag)	m
Magnetic saturation limit (B_sat)	T
Air gap flux density (B_g)	Wb/m^2
Supply voltage (V_supply)	V

The third rule establishes the geometry of the rotor and its outer structural layers, which define the motor's outer radius. This radius is composed of a series of fixed thicknesses: a 1 mm air gap to maintain electromagnetic decoupling, a 10 mm permanent magnet layer for torque generation, an 8 mm rotor yoke to complete the magnetic circuit, and a 2 mm carbon fiber shell for mechanical reinforcement. These values are selected based on a combination of electromagnetic design needs and mechanical integrity under high-speed operation [54], [61].

At high rotational speeds, centrifugal forces induce significant hoop stresses in the rotor components, particularly in the permanent magnets and carbon fiber shell. Permanent magnets, typically made of brittle materials such as NdFeB, are vulnerable to mechanical failure if not properly constrained [62]. Therefore, a pre-tensioned carbon fiber sleeve is applied to enhance the rotor’s mechanical strength and mitigate tensile failure [63].

Hoop stresses in each cylindrical layer are calculated using standard analytical models for rotating cylinders [61], [63]. For isotropic materials, the hoop stress σ_θ at a given radius r can be expressed as:

$$\sigma_\theta(r) = \rho \cdot \omega^2 \cdot (\frac{3+v}{8} \cdot ({r_o}^2 + {r_i}^2) + \frac{1-3v}{8} \cdot \frac{{r_o}^2 {r_i}^2}{r^2} - \frac{1+v}{4} \cdot r^2) \qquad \text{(Equation 4.3)}$$

Where the ρ is the material density, ω is the angular velocity, r_o and r_i are the inner and outer radius of the rotating ring, v is the Poisson’s ratio. For composite materials like carbon fiber more advanced anisotropic models may be used to capture the directional dependence of the modulus and strength. This layered structure enables the rotor to remain structurally stable during operation at speeds up to 9000 rpm or higher, as commonly seen in aerospace and high-performance traction applications [64].

Finally, the fourth rule computes volume and mass of each component (stator iron, copper, PMs, rotor yoke, shell) based on their geometry and material density. Copper volume is capped at 60% of the slot space, following conventional winding fill factor limits [65], and constrained by a maximum current density is decided by the cooling system applied in the electric system under $20 \times 10^6 \ A/m^2$.

Together, these four rules form a modular and analytically tractable framework for evaluating PMSM designs across a range of axial lengths. This rule-based approach enables parametric exploration of how variations in axial geometry affect key performance indicators such as torque density, rotor and stator mass distribution, thermal behavior, and structural stress limits. In addition, the framework supports design modularity, making it compatible with other electromechanical subsystems. Specifically, it can be seamlessly linked with the Coaxial Magnetic Gear (CMG) model, allowing for co-design and integration of the motor and magnetic gear components into a unified Magnetic Electric Continuously Variable Transmission (MECVT) architecture. This combined design methodology enables system-level trade studies, where electromagnetic performance, mechanical robustness, and torque conversion flexibility can be jointly optimized for advanced hybrid drivetrain applications.

4.2 Magnetic Electric Variable speed transmission system architecture

In industrial applications, approximately 90% of electric motors require large gearboxes to deliver low-speed, high-torque output. However, incorporating such gearboxes significantly increases the overall volume and weight of the transmission system, potentially leading to excessive infrastructure costs. Moreover, traditional gear-based systems are often associated with drawbacks such as elevated acoustic noise, reduced efficiency, limited transmission precision, and slower dynamic response [65]-[66].

In this section, we present a Magnetic Electric Variable-Speed Transmission system, which integrates a coaxial magnetic gear with an electric motor to achieve variable-speed operation by adjusting the motor’s rotational speed.

Fig. 4.2 shows a 2D cross-sectional view of a Coaxial Magnetic Gear (CMG) system that integrates an inner electric motor with an outer magnetic gear into a single compact unit. In this configuration, the electric motor drives one set of magnetic rings composed of alternating north and south permanent magnets. The magnetic field generated by the motor's rotor interacts with the outer magnetic gear through a set of ferromagnetic modulators. This interaction enables torque transmission to the outer rotor of the magnetic gear without physical contact [67]-[68]. By varying the motor’s output speed,

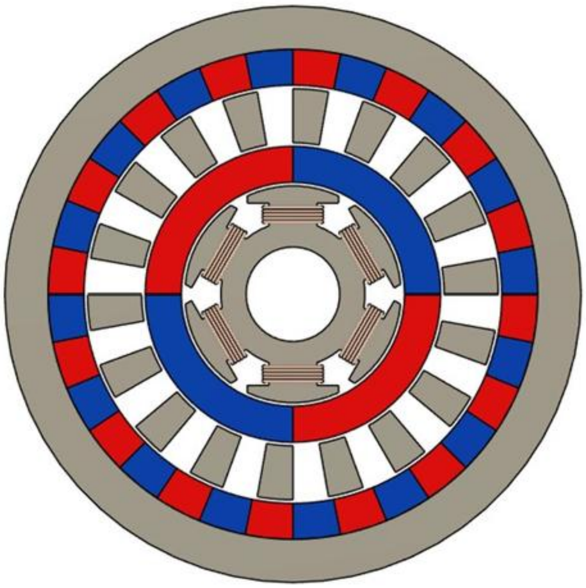

Fig. 4.2. 2D cross-sectional view of a Coaxial Magnetic Gear (CMG) with inner motor system.

torque density, reduced noise, improved efficiency, and potential weight savings compared to traditional mechanical gear couplings between electric motors and downstream stages[69]-[70].

In this figure, the system is composed of several concentric layers. At the center there is an opening that serves either for airflow or for housing an air-hydrogen cooling system within the electric motor section. Encircling the central channel is the motor stator, which houses the windings responsible for producing a rotating magnetic field that drives the rotor. Positioned just beyond the stator is a circular array of permanent magnets arranged in alternating north and south polarities. This structure functions both as the motor's rotor and as the inner rotor of the magnetic gear stage.

Following this, the outer section transitions into the magnetic gear component. Since the rotor magnets of the electric motor are shared with the inner magnetic gear rotor, there is no need for a separate inner rotor for the magnetic gear stage. Instead, a ring of ferromagnetic modulators is positioned directly around the shared rotor. These modulators facilitate magnetic field interaction between the inner and outer rotors, enabling torque transmission through the magnetic gear mechanism.

Finally, the outermost layer consists of the outer rotor and magnetic yoke of the CMG system. The magnetic flux passing through the ferromagnetic modulators and interacting with the outer PM rotor guided and strengthened by this outer yoke, resulting in efficient, non-contact torque transmission. The combination of these layers enables compact integration, enhanced torque density, and improved mechanical performance.

Fig. 4.3 presents a 2D cross-sectional view of a Coaxial Magnetic Gear (CMG) system that integrates an outer rotor electric motor. At the center is the stator core with evenly distributed windings (depicted in copper color), which are fixed and generate a rotating magnetic field. Surrounding the stator is a ring of alternating north and south permanent magnets (colored red and blue), which act as the outer rotor of the electric motor. This outer rotor is mechanically connected to the inner rotor of the magnetic gear system.

Just inside the outer permanent magnets, a ring of ferromagnetic modulators is placed to enable magnetic interaction between the motor's outer rotor and the inner PM ring of the CMG system. These modulators bridge the flux paths between the magnetic gear components, enabling torque transmission without physical contact. The inner ring of red/blue alternating magnets serves dual purposes: it operates as the inner PM rotor of the CMG and is magnetically coupled to the outer electric motor rotor via the ferromagnetic modulators. Finally, the central shaft remains stationary or connected to downstream components depending on application needs.

This outer-rotor motor configuration allows the magnetic gear's mechanical structure to envelop the electric motor components, offering a compact design, high torque density, and enhanced cooling potential. With the integration of a coaxial magnetic gear and an electric motor, this structure enables continuously variable speed transmission by adjusting the motor's output speed. However, the goal of our Electric Continuously Variable Transmission (ECVT) system is not just to achieve speed variability but to embed this functionality within a fixed-ratio drivetrain—such as those used in helicopters.

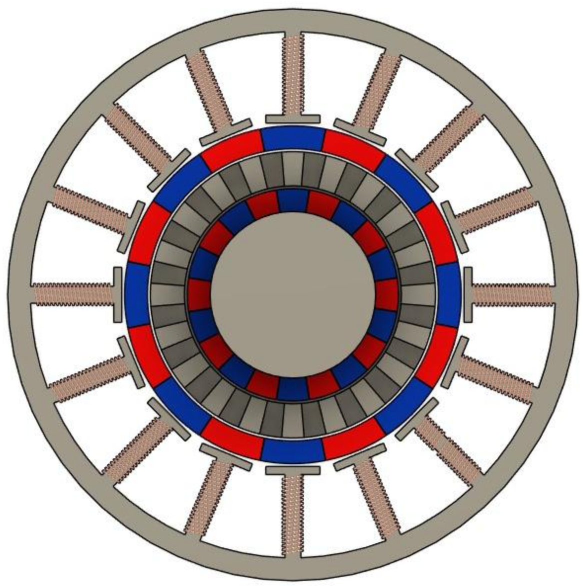

Fig. 4.3. 2D cross-sectional view of a Coaxial Magnetic Gear (CMG) with outer motor system.

Helicopter engines typically operate within a narrow and stable speed range due to their design constraints and efficiency requirements. As a result, varying engine speed to achieve transmission flexibility is not practical. To overcome this, we propose incorporating an additional electric motor at an intermediate stage in the drivetrain. This motor adjusts the rotational speed at that stage, enabling a wide range of speed variability at the final output, while allowing the main engine to operate at its optimal fixed speed. This approach achieves continuous speed modulation and torque control without compromising engine performance.

Therefore, when establishing an ECVT system for a fixed-ratio drivetrain, the design process begins by identifying the input-torque and speed provided by the main drivetrain. Once these input parameters are determined, a complete system model can be developed by combining the planetary gear or coaxial magnetic gear sizing methods introduced in Chapter 3 with the electric motor sizing model discussed in the previous section.

Both planetary and magnetic gear systems are composed of several rotating components. In a planetary gearbox, these include the sun gear, planet gears, carrier, and ring gear. In a coaxial magnetic gear (CMG), the key components consist of the inner permanent magnet (PM) rotor, outer PM rotor, and the ferromagnetic modulators. Each of these rotating elements can function either as the input from the main drivetrain or as the output to the subsequent transmission stage. The remaining component is connected to the electric motor. This flexibility is the basis for designing two configurations of magnetic gear systems—one integrated with an inner-rotor electric motor and the other with an outer-rotor electric motor.

In the case of the planetary gear transmission, the combined rotation of the carrier and planet gears plays a role similar to that of the ferromagnetic modulators in the CMG system. These elements enable the modulation and transfer of torque and speed, allowing for various structural arrangements depending on the connection between the power source, electric motor, and transmission stages.

Based on the input torque and speed values, we can optimize how the planetary and magnetic gear systems are connected within the overall transmission architecture. As shown in Figures 4.4 to 4.6, three different types of planetary gear configurations are illustrated, where the electric motor is connected to the carrier, sun gear, and ring gear, separately. In helicopter drivetrain systems, which are characterized by high torque and high rotational speed, the sizing and performance of the electric motor are significantly influenced by the torque transmission path. Therefore, the target output torque becomes a critical factor in determining the most suitable connection type between the motor and the planetary gear components. Selecting the optimal configuration ensures that the system can meet performance requirements while maintaining manageable motor dimensions and improving overall drivetrain efficiency.

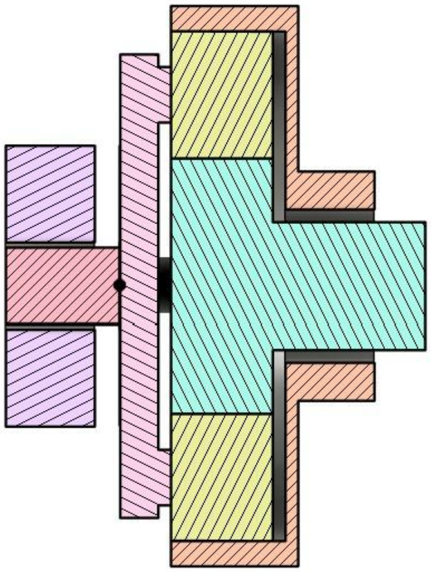

Fig. 4.4. Planetary gear configuration with motor connected to the carrier.

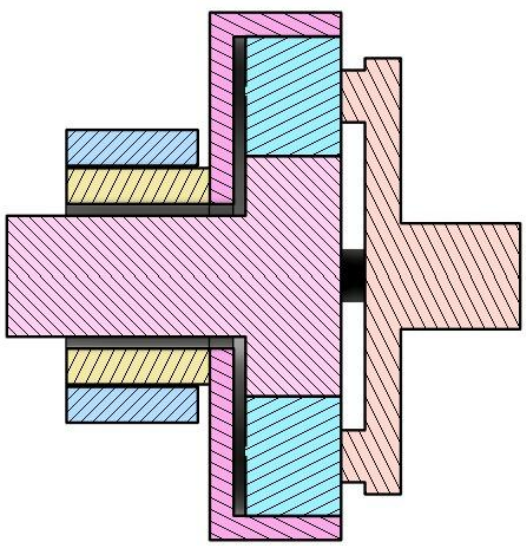

Fig. 4.5. Planetary gear configuration with motor connected to the ring gear.

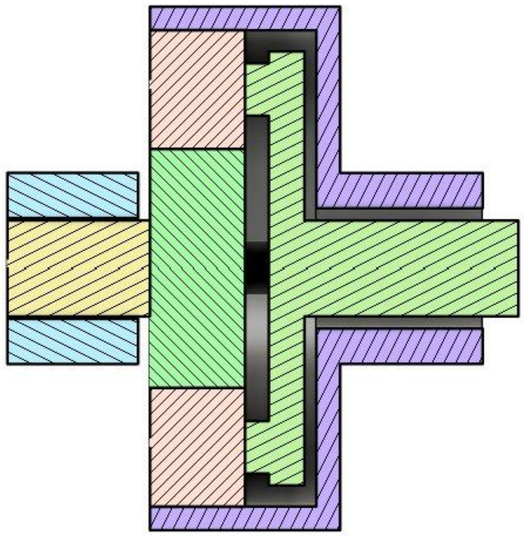

Fig. 4.6. Planetary gear configuration with motor connected to the sun gear.

PGT Type 1. Planetary gear with motor connected to the carrier

As shown in **Fig. 4.4**, the purple region represents the electric motor, which is mechanically connected to the carrier, shown in pink. The carrier supports and drives the planetary gears, illustrated in yellow, which in turn mesh with the ring gear (in orange), serving as the output of the transmission. The sun gear remains fixed to the main drivetrain, which is powered by the engine. In this configuration, the system allows for a fixed torque ratio between the input and output, while the output speed can be varied by adjusting the motor's rotational speed. This setup is well-suited for applications where torque consistency is critical, and variable-speed control is desired without modifying the engine's operating point.

Their speed and torque ratio in the planetary gear and connection is shown follow:

$$\omega_r = \omega_c \frac{N_s + N_r}{N_r} - \omega_s \frac{N_s}{N_r}$$

Engine Torque: T_s

Motor Target Torque: $T_c = -T_s \frac{N_s + N_r}{N_s}$

Loading Torque: $T_r = T_s \frac{N_r}{N_s}$

Where the torque ratio from motor to engine is $r_{m/e} = \frac{N_s+N_r}{N_s}$ is always larger than one, that means a speed reduction stage but torque increases prototype.

PGT Type 2. Planetary gear with motor connected to the ring

As illustrated in **Fig. 4.5**, the dark pink region denotes the ring gear, which is directly actuated by the electric motor. The light blue elements represent the planetary gears, mounted on a carrier that is mechanically linked to the output shaft. Positioned at the center, the sun gear is rigidly coupled to the primary drivetrain driven by the engine.

In this configuration, the electric motor drives the ring gear, while the torque is transferred through the planetary gears to the carrier, resulting in rotational output. The sun gear remains connected to the fixed-speed input, and the motor enables variable-speed control. This layout provides a compact and efficient structure for implementing continuously variable transmission behavior, allowing for flexible speed adjustment at the output while maintaining stable input torque from the engine.

Their speed and torque ratio in the planetary gear and connection is shown follow:

$$\omega_c = \omega_s \frac{N_s}{N_s + N_r} + \omega_r \frac{N_r}{N_r + N_s}$$

Engine Torque: T_s

Motor Target Torque: $T_r = T_s \frac{N_r}{N_s}$

Loading Torque: $T_c = -T_s \frac{N_s+N_r}{N_s}$

Where the torque ratio from motor to engine is $r_{m/e} = \frac{N_r}{N_s}$ is larger than one too, that means another speed reduction stage but torque increases prototype.

PGT Type 3. Planetary gear with motor connected to the ring

As shown in **Fig. 4.6**, the green section represents the sun gear, which is directly connected to the electric motor. The orange components are the planetary gears, mounted on the light green carrier, which act as the output of the transmission. The ring gear, shown in purple, is connected to the main drivetrain and remains fixed during operation.

In this configuration, the electric motor drives the sun gear, while the ring gear provides a grounded reference point. The planet gears transfer torque to the rotating carrier, enabling speed modulation at the output. This setup is commonly used when the motor is intended to operate at high speed with relatively lower torque. It allows for effective torque multiplication and smooth speed variation at the output, making it a suitable candidate for integration into high-speed rotorcraft drivetrains where precision and power delivery are essential.

Their speed and torque ratio in the planetary gear and connection is shown follow:

$$\omega_r = \omega_c \frac{N_s + N_r}{N_r} - \omega_s \frac{N_s}{N_r}$$

Engine Torque: T_c

Motor Target Torque: $T_s = -T_c \frac{N_s}{N_s+N_r}$

Loading Torque: $T_r = -T_c \frac{N_r}{N_s+N_r}$

Where the torque ratio from motor to engine is $r_{m/e} = \frac{N_s}{N_r+N_s}$ is less than one, that means another speed increase stage but torque decreases prototype. Therefore, an additional speed reduction stage is required for this third configuration in order to achieve the same output speed as the previous two transmission prototypes.

CMG Type 1. Magnetic gear with motor connected to Inner & Engine to Modulator

In the CMG (Coaxial Magnetic Gear) transmission system, torque transmission is the primary design consideration. If the electric motor is placed outside the CMG, the required motor torque becomes significantly large, which would lead to an oversized and inefficient motor design. To avoid this, only the two configurations are shown in Figures 4.7 and 4.8, A configuration in which the electric motor is coupled to the inner rotor of the CMG is incorporated into our design. As shown in **Fig. 4.7**, this coaxial magnetic gear (CMG) setup connects the motor or generator to the inner shaft, which also functions as the inner rotor of the gear.

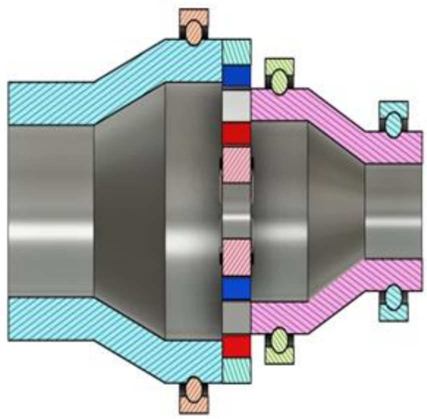

Fig. 4.7. Magnetic gear configuration with motor connected to the inner rotor output & Engine to Modulator.

The engine is linked to the central modulator shaft, positioned between the inner and outer permanent magnet (PM) rotors. Torque is transmitted via magnetic flux modulation between the engine-driven modulator and the rotating fields generated by the motor. The outer shaft, connected to the outer PM rotor, serves as the system's output. And its torque and speed ratio are shown:

$$\omega_{out} = \frac{p_{in} * \omega_{in} - (p_{in} + p_{out}) * \omega_{mod}}{p_{out}}$$

Engine Torque: T_{mod}

Motor Target Torque: $T_{in} = -T_{mod} \frac{p_{in}}{N_{mod}}$

Loading Torque: $T_{out} = -T_{mod} \frac{p_{out}}{N_{mod}}$

Where the relationship between ferro modulators piece is equal to the sum of inner and outer poles pair numbers, the torque from motor to engine is $r_{m/e} = \frac{p_{in}}{N_{mod}}$ always less than one. This characteristic allows the motor/generator to operate with relatively low torque demand while enabling variable-speed control at the output. The modulator in the middle ensures efficient magnetic coupling between the inner and outer rotors, allowing non-contact torque transmission with high reliability and reduced mechanical complexity. This layout is well-suited for hybrid drivetrain systems, such as in helicopters, where the engine runs at a nearly constant speed, and the motor adjusts intermediate speed stages for fine-tuned output control.

CMG Type 2. Magnetic gear with motor connected to Inner & Engine to outer rotor

Fig. 4.8 presents a Coaxial Magnetic Gear (CMG) transmission configuration that shares many similarities with CMG Type 1, with the primary difference being the reversed connection of the ferromagnetic modulator and outer rotor to the engine. In this design, the electric motor or generator is connected to the inner rotor (inner shaft), while the engine drives the outer rotor (outer shaft). The ferromagnetic modulator is positioned between the two permanent magnet rotors and facilitates magnetic flux coupling between them.

In this configuration, the engine supplies high-speed, high-torque input through the outer PM rotor, while the motor operates on the inner PM rotor to adjust or fine-tune the output speed. The modulator plays a critical role in enabling non-contact torque transfer by synchronizing the magnetic interaction between the two rotors. And its torque and speed ratio are shown:

$$\omega_{mod} = \frac{p_{out} * \omega_{out} - p_{in} * \omega_{in}}{p_{in} + p_{out}}$$

Engine Torque: T_{out}

Motor Target Torque: $T_{in} = -T_{out}\frac{p_{in}}{p_{out}}$

Loading Torque: $T_{mod} = -T_{out}\frac{N_{mod}}{p_{out}}$

Where the relationship between ferro modulators piece is equal to the sum of inner and outer poles pair numbers, the torque from motor to engine is $r_{m/e} = \frac{p_{in}}{p_{out}}$ always less than one but compare to the Type 1 the ratio is larger because the outer rotor pole pairs number are always less than ferro modulators piece number. This architecture is particularly advantageous for hybrid drivetrain applications, especially in aerospace or rotorcraft systems where the engine must operate at a fixed speed.

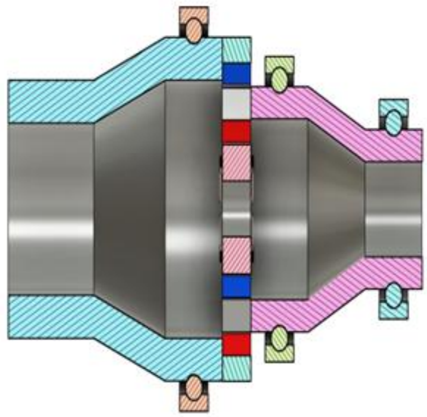

Fig. 4.8. Magnetic gear configuration with motor connected to the inner rotor output & Engine to Modulator.

The electric motor, by influencing the magnetic interaction, enables output speed variability without altering the engine's mechanical behavior. This allows for efficient speed blending and precise torque control in high-performance powertrains.

4.3 Magnetic & Planetary Electric Variable speed transmission system

In the Magnetic and Planetary ECVT sizing models, torque transmission is the primary design consideration, as the transmitted torque directly determines the required size and weight of the electric motor or generator. The connection between the rotating components and the power sources, including the fixed-speed turbine engine and the variable-speed electric motor, is a key factor in system optimization. Therefore, careful evaluation and comparison of different connection configurations are essential for achieving an efficient and lightweight ECVT design.

Therefore, the connection configuration is integrated into the electric motor design model, where the target motor torque is determined based on the engine torque and how both the motor and engine are connected to the rotating components. As shown in **Fig. 4.9**, the design flow chart outlines the overall process of determining the motor torque requirement by considering the drivetrain architecture, torque transmission paths, and

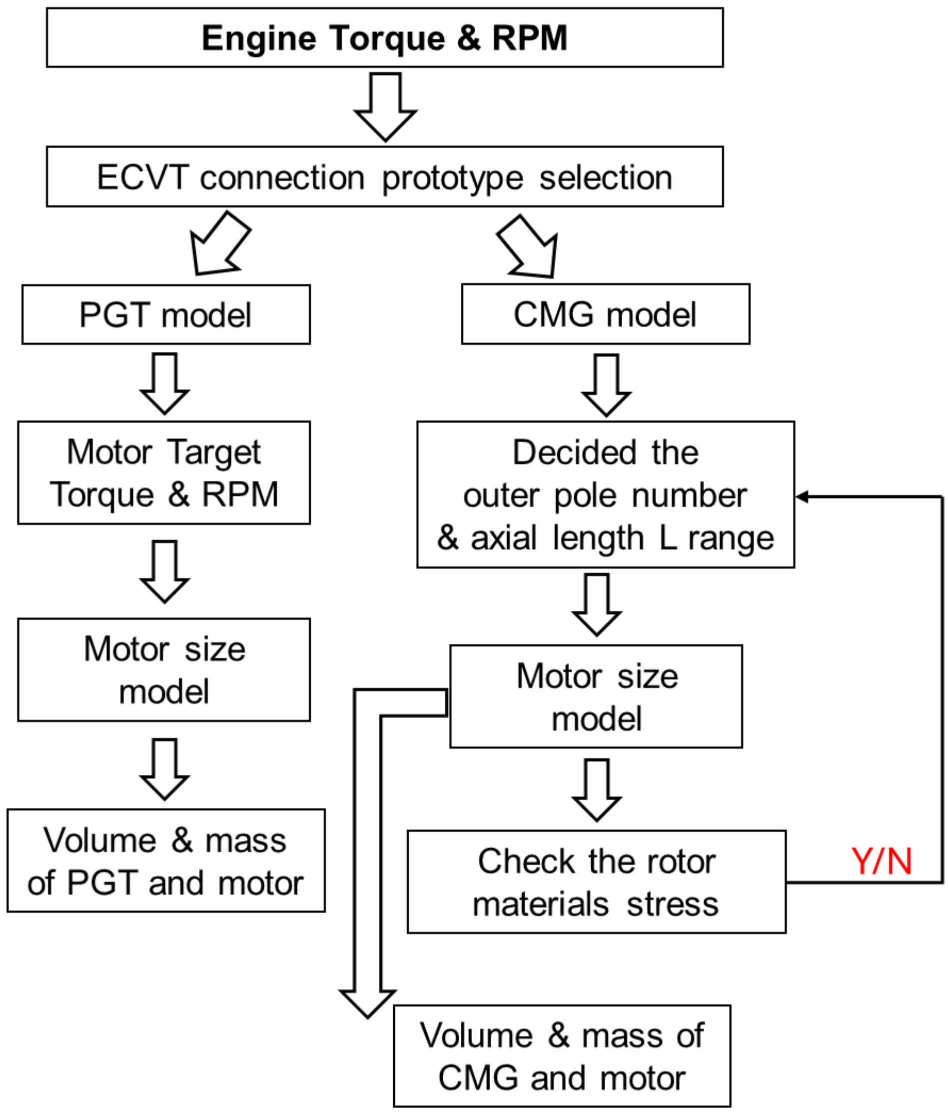

Fig. 4.9. Motor and gear design flow considering engine input and system architecture.

configuration selection. This framework ensures that the sizing of the electric motor aligns with the torque demands of the system while optimizing weight, efficiency, and integration with the ECVT structure.

4.3.1 Magnetic electric motor size model analysis

After establishing the electric motor size model using a four-rule parametric approach, we can proceed with the geometric optimization of the motor. In this design phase, our goal is to integrate the Electric Continuously Variable Transmission (ECVT) into a helicopter transmission drivetrain. To achieve this, we utilize a helicopter turbine engine configuration to estimate and optimize the motor's size and performance.

In this section, we use a helicopter drivetrain turbine engine rated at 1280 HP and 20,000 rpm as the fixed input power source. By varying the gear ratio connected to the electric motor, we can obtain different target torque ranges for the motor to generate. This means that when the ECVT system is integrated into a low-torque stage, the rotor speed must increase accordingly to maintain the constant power input. Based on the turbine engine parameters, the engine generates a minimum torque of approximately 420 Nm. As the helicopter drivetrain is designed as a sequential speed reduction system, it converts this high-speed, low-torque input into the high-torque, low-speed output required to drive the rotor blades.

First, we integrate the electric motor directly into the drivetrain system without using a CMG or PGT gearbox, but with a conventional speed reduction gearbox, to validate whether the speed and torque requirements can be met by the motor design. The target operating conditions are 9,000 rpm and 1000 Nm of torque. As shown in the design flowchart of the electric motor, the axial length has minimal impact on the rotor stress. Therefore, axial length will be treated as a variable parameter for optimizing the motor geometry.

As shown in **Fig. 4.10**, the variation of motor dimensions with respect to axial length under a fixed torque constraint of 1000 Nm. As the axial length increases from 100 mm to 400 mm, the stator inner radius, stator outer radius, and motor outer radius all decrease. This trend highlights a key design trade-off: increasing axial length allows the

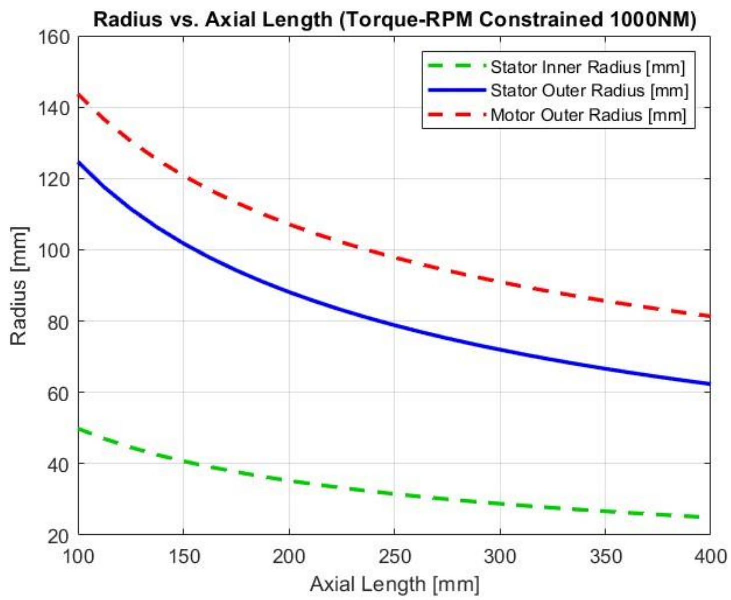

Fig. 4.10. Radius Variation with Axial Length under Torque-RPM Constraint (1000 Nm).

motor to maintain the required torque while reducing its radial size. This relationship is particularly important for optimizing motor size, as the weight of each component varies with the radius, as shown in **Fig. 4.11**. This figure illustrates how the mass of major motor components changes with axial length under a fixed torque output of 1000 Nm. As the axial length increases from 100 mm to 400 mm, the total motor mass (black dashed line) shows a gradual increase. This rise is primarily driven by the increase in permanent magnet (PM) mass (magenta line), while the masses of the stator iron (blue line) and copper windings (red line) remain relatively constant. The increase in PM mass occurs because as the axial length grows, the motor's radial dimensions, particularly the average air gap radius, tend to decrease. To maintain the same torque output with a smaller radius, the magnetic flux density must be preserved by increasing the volume or thickness of the magnets. Since the PM volume scales with axial length and the required magnetic flux, this results in a steady increase in PM mass while the other components remain largely unaffected.

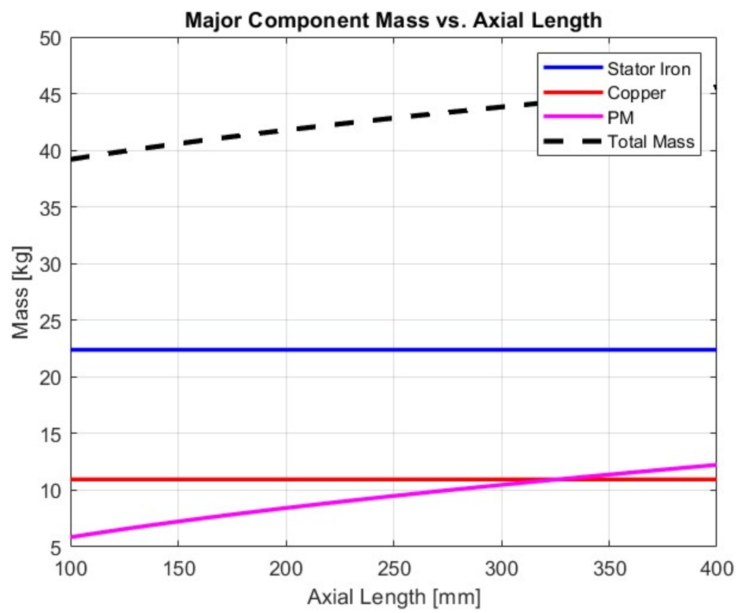

Fig. 4.11. Mass Breakdown of Major Motor Components vs. Axial Length.

As the axial length increases, the electric motor's rotor radius decreases, resulting in a more compact rotor structure. Conversely, when the axial length decreases, the motor radius must increase to maintain the required torque, which leads to higher hoop stress and circumferential force on the rotor. This places greater demands on the rotor material. Since this motor adopts an outer rotor permanent magnet (PM) structure, and the density of permanent magnets is lower than that of high-strength metals, the structural strength of the rotor becomes a critical design concern. To address this issue, we introduce an alternative solution by reinforcing the PM structure with a carbon fiber sleeve, as illustrated in **Fig. 4.12**.

This figure shows the variation of rotor hoop stress with axial length for both permanent magnet (PM) material and carbon fiber (CF) reinforcement under fixed torque-speed conditions. As axial length increases from 100 mm to 400 mm, PM hoop stress (red line) decreases significantly due to the reduced rotor radius, while CF hoop stress (blue line) remains consistently lower. The dashed red line indicates the 80 MPa yield limit of

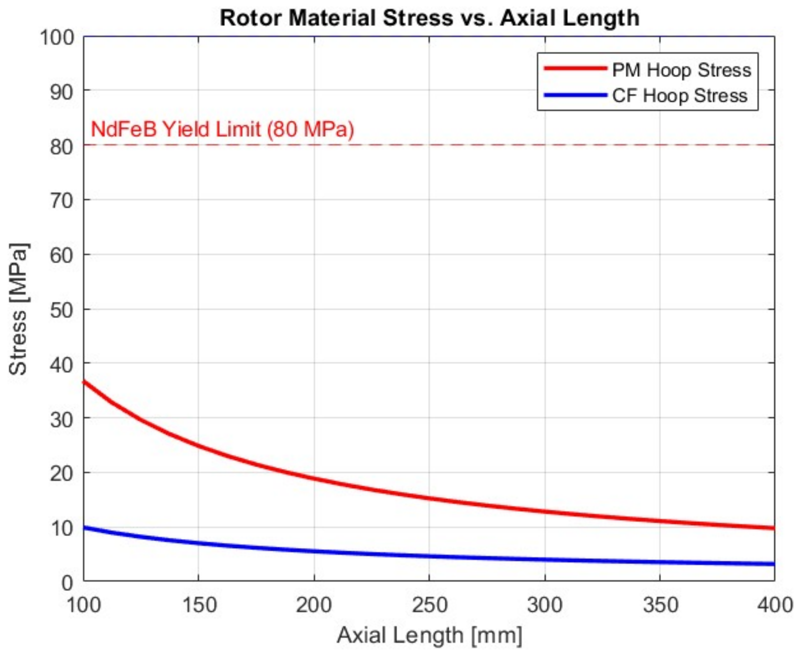

Fig. 4.12. Rotor Hoop Stress vs. Axial Length for PM and Carbon Fiber Reinforcement.

NdFeB magnets. Both stress levels stay well below this limit, confirming the structural safety of the outer rotor design. The use of carbon fiber further enhances mechanical -integrity, particularly at shorter lengths where stress is higher.

Since both the Coaxial Magnetic Gear (CMG) transmission and the electric motor operate based on electromagnetic interactions, they rely on magnetic field and flux coupling to generate and transmit torque. In particular, the Permanent Magnet Synchronous Motor (PMSM) features a ring of permanent magnets to establish its magnetic field. This shared principle leads to the idea of integrating the PM rotor between the PMSM and the CMG. This principle underlies the inner-motor and outer-motor CMG configurations discussed earlier. In the inner-motor design, the outer rotor of the permanent magnet synchronous motor (PMSM) functions concurrently as the inner rotor of the CMG. This integration enables the development of a unified sizing model, anchored on the geometric parameters of the motor’s outer rotor. To ensure effective torque transmission between the CMG’s inner and outer rotors, both the motor and gear components are required to maintain a consistent axial length. The resulting volume and mass estimations for this integrated structure are presented in **Fig. 4.13** and **Fig. 4.14**.

Fig. 4.13 shows the variation in magnetic gear volume as a function of axial length, where the CMG dimensions are derived from the outer rotor geometry of the PMSM. The green line indicates the total CMG volume from 100 mm to 400 mm axial length. The dashed line represents the maximum torque boundary calculated based on a torque density around 180 Nm/L, corresponding to a target of 1000 Nm. Designs above the dashed line satisfy the torque requirement, but excessive volume may lead to overdesign and unnecessary bulk. Therefore, selecting an axial length just above the boundary is essential for balancing performance and compactness.

Fig. 4.14 illustrates the magnetic gear mass as a function of axial length. The magenta curve represents the total mass derived from the PMSM outer rotor size, while the dashed line indicates the calculated minimum mass required for transmitting 1000 Nm torque around 25 Nm/kg. Only the designs above this threshold meet the CMG torque requirement. However, significantly larger masses imply overdesign, which can negatively impact weight-sensitive systems such as aerospace drivetrains. An optimal axial length must balance performance with structural and weight efficiency. With the defined sizes of the CMG and PMSM, we can evaluate the overall weight of the integrated Magnetic ECVT system, as shown in **Fig. 4.15**. This figure presents the mass breakdown of the combined PMSM and CMG across different axial lengths. The blue line represents the motor mass, while the magenta line shows the total mass of the magnetic gear. The green dashed line indicates the shared permanent magnet (PM) mass used in both components, and the black line reflects the total combined mass after accounting for this shared portion. As the axial length increases, the motor mass grows gradually, whereas the gear mass increases more significantly. This accelerated rise in gear mass is partially attributed to overdesign—beyond a certain axial length, the CMG exceeds the torque requirement, resulting in excessive structural volume and weight. However, the shared PM portion between the motor and gear, highlighted by the green

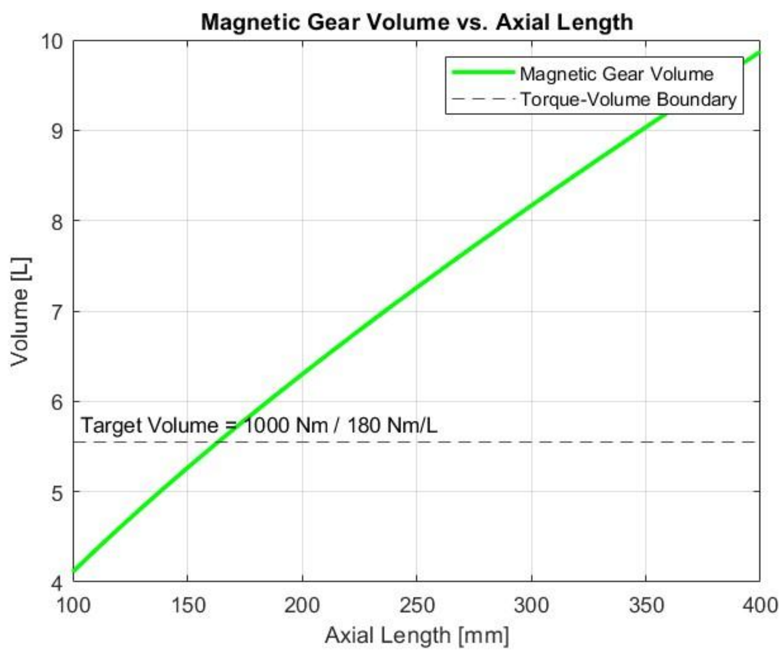

Fig. 4.13. Coaxial Magnetic Gear volume based on PMSM outer rotor dimensions.

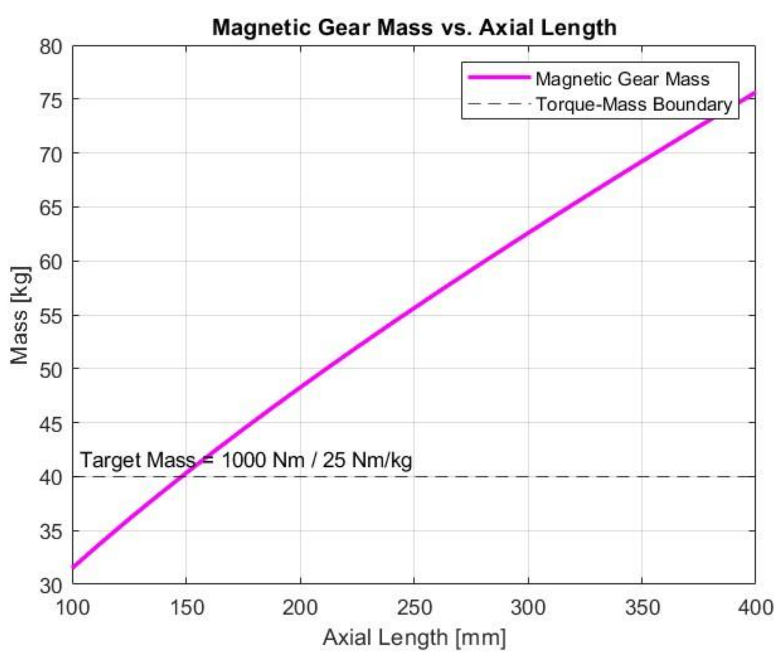

Fig. 4.14. Coaxial Magnetic Gear mass based on PMSM outer rotor dimensions.

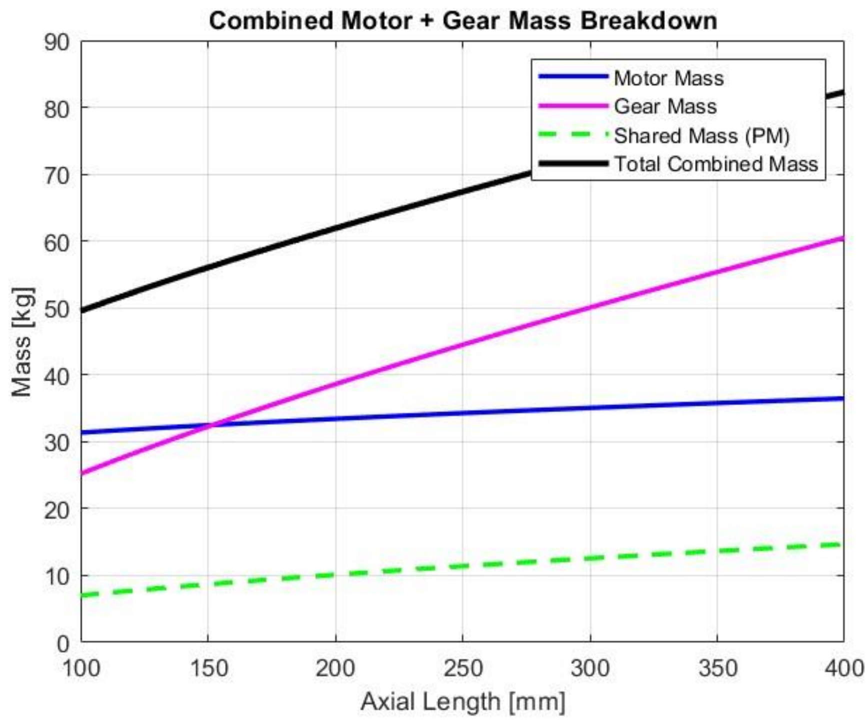

Fig. 4.15. Total Mass Evaluation of Integrated Magnetic ECVT System

dashed line, contributes meaningfully to reducing total system mass. This shared component accounts for approximately 10–15% of the combined motor and gear mass at typical axial lengths, making it a highly attractive design feature for Magnetic ECVT integration. Therefore, axial length optimization, together with shared-component utilization, is essential to achieve a balance between performance and mass efficiency in the integrated system.

4.3.2 Planetary and Magnetic ECVT size comparison and analysis

In the previous section, we discussed the size model of the electric motor, the maximum torque boundary for the CMG transmission, the dimensional design of the CMG under maximum torque, and the planetary gearbox configuration. An additional critical aspect is the connection prototype between the PGT and CMG within the ECVT transmission system, which significantly influences both motor and gearbox design. As shown in the motor and gear design flowchart in **Fig. 4.9**, this approach adopts a reverse design logic

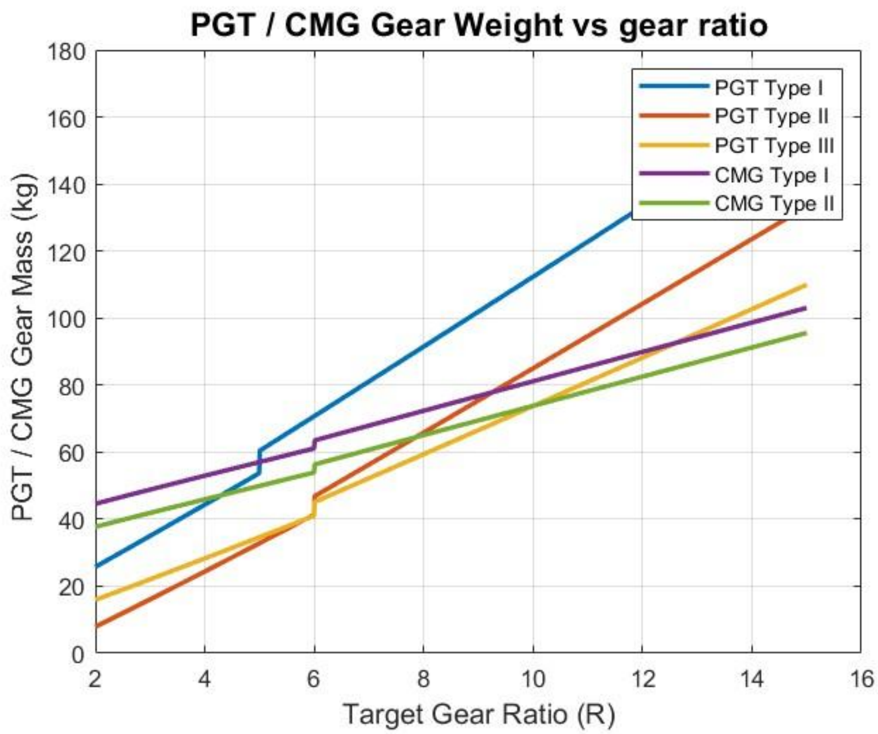

Fig. 4.16. PGT and CMG Gear Mass Comparison over engine-to-output Gear Ratios.

compared to the previous section—starting with the motor first, followed by the CMG sizing, which can lead to overdesign of the CMG. Therefore, the most effective strategy for designing a CMG or PGT ECVT system is to begin with the gear design and then size the motor accordingly. Firstly, the **Fig. 4.16** shows the weight comparison of different connect type of PGT and CMG.

To eliminate the influence of gear connection topology, the x-axis uses the engine-to-output torque ratio to represent the effective gear ratio. In PGT systems, this may correspond to configurations like ring-to-sun or carrier-to-sun, while in CMG systems it refers to the outer to inner rotor torque ratio. Note that this torque ratio reflects the final transmission requirement rather than a specific physical connection. For instance, although PGT Type I and II are both speed-reducing stages, their internal configurations differ, requiring additional reduction stages to achieve higher torque outputs. In contrast, PGT Type III and CMG Type II begin with torque-reducing stages and must employ larger secondary stages to meet the same output torque ratio. In **Fig. 4.16**, the transmission ratio of PGT systems is constrained by geometric limitations of the sun and planetary gears, typically capped at around 1:5 to 1:6. Beyond this range, a secondary PGT stage is required to achieve further speed reduction, which aligns with conventional helicopter drivetrain architectures. Among the configurations evaluated, PGT Type II exhibits the lowest weight for single-stage reduction, making it the preferred choice for secondary reduction across all methods. The observed step increases in mass correspond to points where the required transmission ratio exceeds the capability of a single stage—thus necessitating two or even three combined stages. This multi-stage design inherently reduces torque density, contributing to the observed mass escalation in PGT systems at higher ratios.

As a result, PGT systems exhibit sharp mass increases, particularly beyond gear ratios of ~6, due to the need for multi-stage configurations when surpassing the single-stage transmission limit (typically around 1:5 or 1:6). Among them, PGT Type II consistently shows the lowest mass in lower gear ratio ranges, making it a suitable choice for secondary-stage reduction. However, as gear ratio increases, even PGT II's mass begins to rise steeply due to cascading stages and reduced torque density.

In CMG systems, on the other hand, show more gradual and smoother mass increases because of the weight increase of the secondary stage transmission. Both CMG Type I and CMG Type II maintain relatively stable torque densities over a broader range of gear ratios, avoiding the sharp jumps seen in PGT. This highlights the advantage of CMGs in high-ratio, lightweight applications, especially when avoiding complex multi-stage mechanical assemblies.

Shown in **Fig. 4.17** and **4.18** is the motor weight and total ECVT weight comparison for different PGT and CMG connections. **Fig. 4.17** illustrates the variation in motor mass across different ECVT configurations as the target gear ratio increases. The PGT-based systems show a steep rise in motor weight, particularly for Type I and Type II, because their mechanical configurations place the motor on high-torque transmission paths. This leads to torque amplification, where the motor-to-engine torque ratio is greater than one,

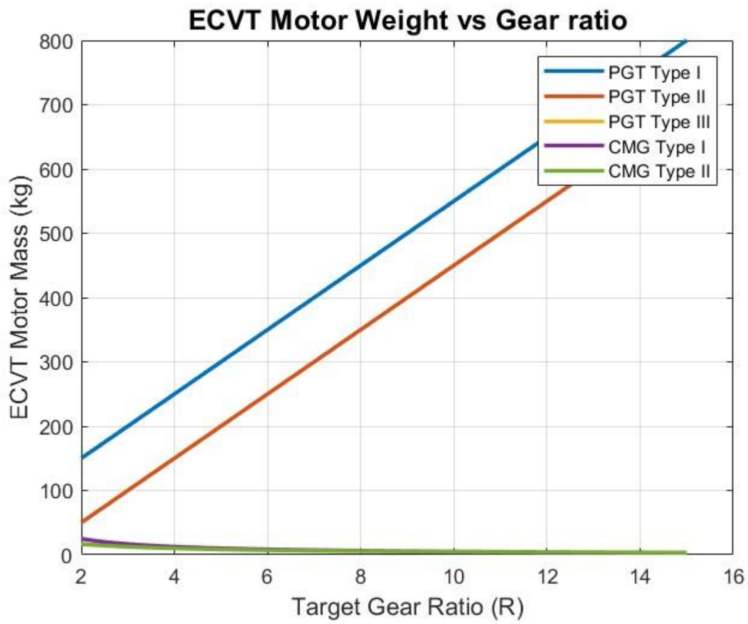

Fig. 4.17. ECVT system motor mass vs. target gear ratio for different PGT and CMG configurations.

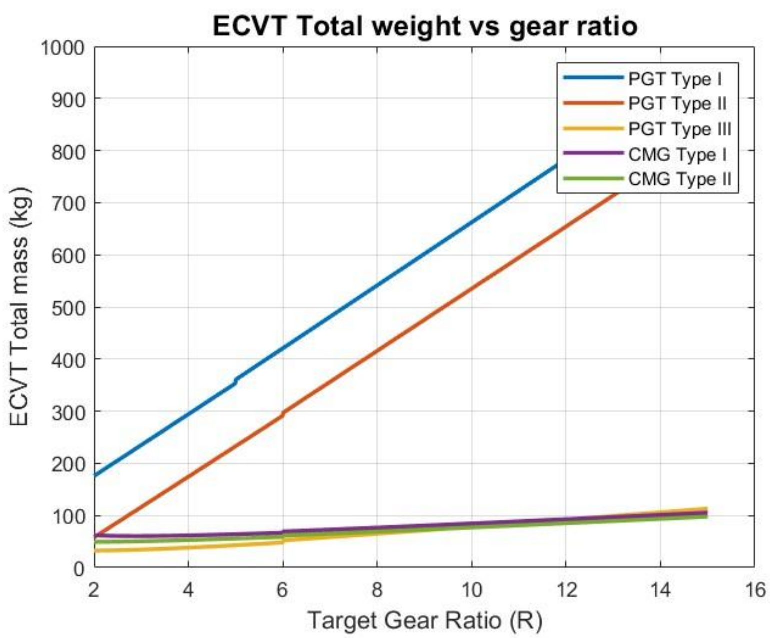

Fig. 4.18. ECVT system total mass vs. target gear ratio for different PGT and CMG configurations.

requiring significantly heavier motors. In contrast, PGT Type III places the motor on a low torque path and engine connect to a higher torque component, resulting in much lower motor mass. Both CMG Type I and Type II maintain nearly constant motor weight across the entire gear ratio range, taking advantage of the high torque density of magnetic coupling, which allows for lightweight motor designs even under high torque conditions. For ECVT total weight in **Fig. 4.18**, this figure shows the total mass of the ECVT system as a function of target gear ratio for different configurations. The PGT-based systems, especially Type I and Type II, exhibit a sharp increase in total weight as the gear ratio increases. This is primarily due to the significant growth in motor mass when the motor is placed on high-torque transmission paths. PGT Type III, which places the motor on a low-torque path, maintains much lower system weight. In contrast, both CMG Type I and Type II demonstrate minimal weight growth across the entire range of gear ratios. Their use of magnetic coupling allows the system to achieve high transmission ratios while keeping both motor and gear mass low, making them more efficient and lightweight solutions for high-ratio applications.

Therefore, we conclude that PGT Type III, CMG Type I, and CMG Type II are better choices for ECVT structures, offering a significant advantage in mass efficiency compared to the other two PGT configurations. To illustrate this comparison, we provide detailed analyses in Figs. 4.16–4.18 for PGT Type I and CMG Types I and II, and present comparative results in Figs. 4.19–4.21. These three figures provide a detailed comparison between PGT Type III and two CMG configurations (Type I and Type II), showing how gear mass, motor mass, and overall ECVT system mass evolve with increasing target gear ratio. In **Fig. 4.19**, PGT Type III exhibits a stepwise increase in gear mass due to its multistage architecture beyond certain ratio thresholds (e.g., 6:1 and 12:1). In contrast, both CMG Type I and II show smoother, linear-like growth, benefiting from their high gear ratio capability in a single-stage magnetic structure. Below a gear ratio of 10, CMGs are heavier than PGT Type III, but this reverses at higher ratios due to the rapid mass accumulation in PGT multistage designs. As a result, the CMGs are more weight-efficient in high-ratio applications and PGT Type III is lighter for low-to-moderate ratios.

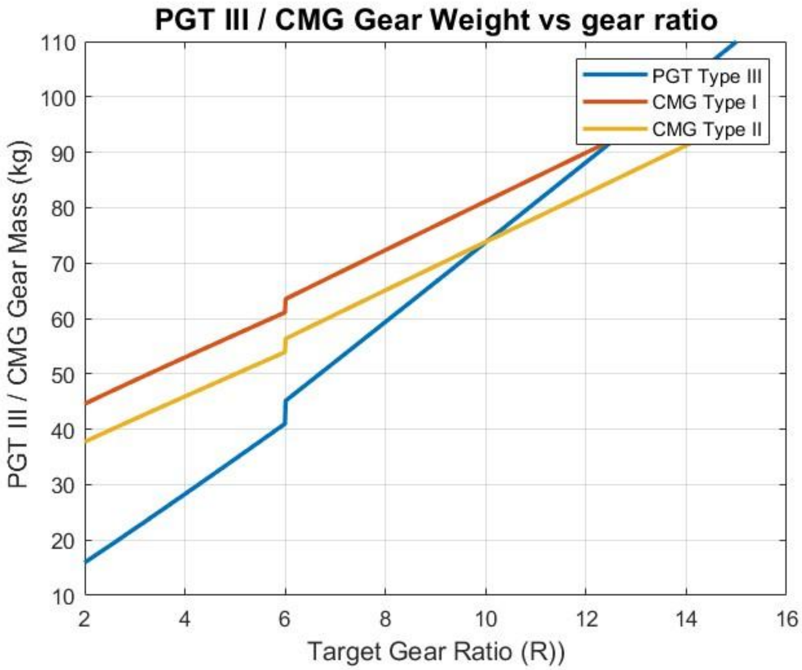

Fig. 4.19. Detail PGT and CMG Gear mass comparison over engine-to-output gear ratios.

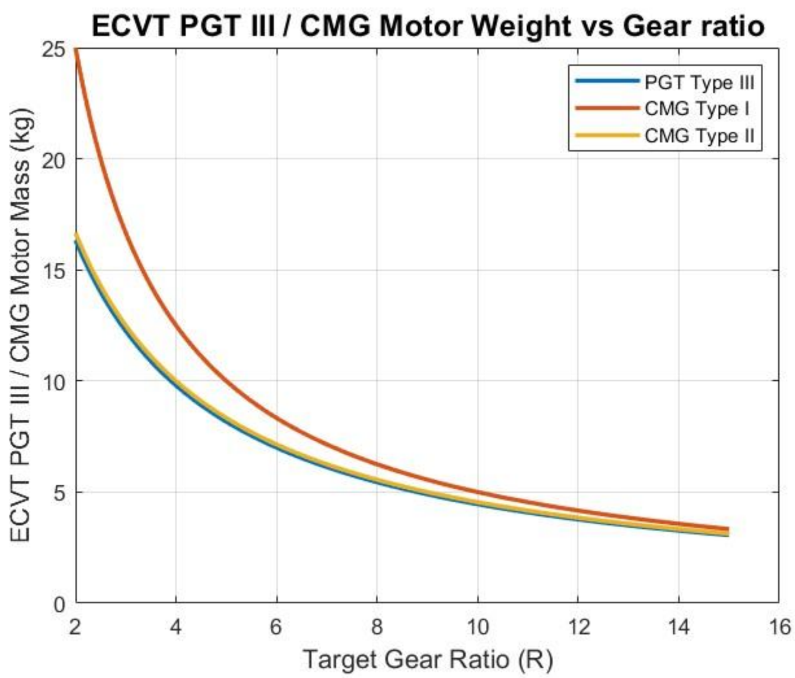

Fig. 4.20. Detail PGT and CMG motor mass comparison over engine-to-output gear ratios.

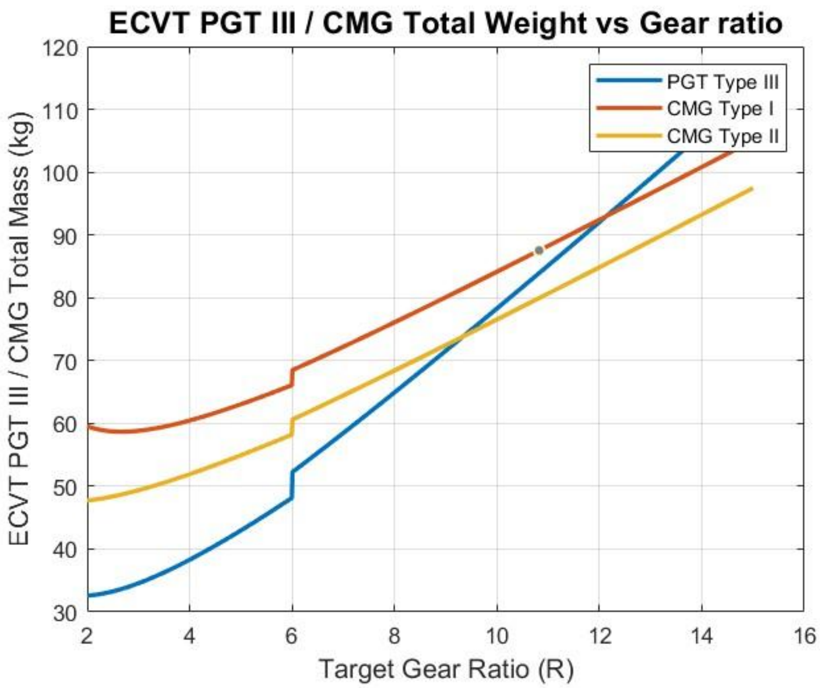

Fig. 4.21. Detail PGT and CMG total mass comparison over engine-to-output gear ratios.

In **Fig. 4.20**, All three configurations show a declining motor mass trend as the gear ratio increases. This is expected, as a higher gear ratio allows the motor to provide less torque for the same output. CMG Type I has slightly higher motor mass at lower ratios due to its lower torque split efficiency ($\tau_{m/e} \gg 1$). PGT Type III and CMG Type II benefit from lower required motor torque, especially in the mid-to-high gear ratio range.

Fig. 4.21 presents the total mass of ECVT systems using PGT Type III and CMG Types I and II as a function of target gear ratio. For all configurations, total mass increases with gear ratio due to either growing gear complexity or increased magnetic material usage. PGT Type III starts with the lowest total mass at low gear ratios and gradually increases due to the need for additional gear stages. In contrast, CMG Type I and II show smoother mass growth, benefiting from their ability to achieve high gear ratios within a compact structure. A crossover point is observed where the total mass of CMG-based systems becomes lower than that of PGT Type III as the gear ratio increases.

While the gear mass comparison in the first figure shows that CMG gears only become lighter than PGT Type III gears around gear ratios of 1:10 (CMG Type II) and 1:13 (CMG Type I), this total weight figure reveals a key advantage of CMG systems: the total ECVT mass becomes lower than that of PGT Type III much earlier, approximately between gear ratios of 1:8 and 1:11.

This earlier advantage is due to the shared use of permanent magnets (PMs) between the motor and magnetic gear in CMG architectures, which reduces redundant material and structural mass. In contrast, PGT-based ECVTs rely on separate mechanical gear stages and motor assemblies, each contributing independently to the overall weight. As a result, even though CMG gears alone may not be lighter at moderate ratios, their integrated motor-gear structure yields a lower system-level mass sooner.

Despite the clear advantage of CMG-based ECVT systems in terms of total mass, especially at high gear ratios, efficiency remains one of the main limitations of magnetic gear architectures. In CMG systems, torque is transmitted through magnetic coupling across multiple air gaps and ferromagnetic modulation regions. This indirect transmission introduces losses due to eddy currents, magnetic hysteresis, and flux leakage, particularly at high rotational speeds or under varying load conditions. In contrast, conventional PGT systems transmit torque through direct mechanical contact, which allows them to achieve higher mechanical efficiency shown in **Fig. 4.22**.

Fig. 4.22 illustrates the transmission efficiency of three configurations: PGT, CMG, and a hybrid CMG combined with PGT, across various gear ratios at a constant operating speed of 10000 rpm. The blue curve shows that the traditional planetary gear transmission (PGT) maintains the highest efficiency, gradually declining from 0.98 to 0.94 as the gear ratio increases. In contrast, the orange curve representing the CMG system begins near 0.93 but experiences a sharper drop in efficiency due to magnetic losses, primarily from eddy currents and hysteresis. The yellow curve depicts the hybrid CMG and PGT configuration, which exhibits the lowest efficiency overall, falling below 0.88 at high gear ratios as a result of compounded losses from both magnetic and mechanical transmission stages.

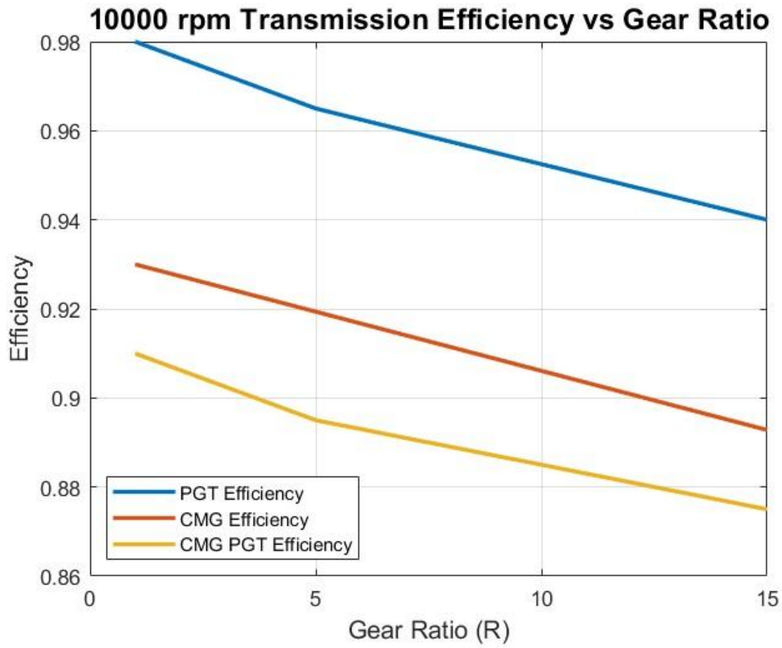

Fig. 4.22. Transmission efficiency comparison of PGT, CMG, and CMG-PGT systems at 10000 rpm.

Although CMG-based systems offer significant mass advantages as previously discussed, this plot clearly reveals their efficiency disadvantage, particularly as the gear ratio increases. The CMG transmission exhibits a stronger efficiency decline than PGT because magnetic gears suffer from frequency-dependent losses that intensify with increasing rotational speed and gear complexity. In contrast, PGT systems retain better efficiency at higher ratios because mechanical contact losses scale more linearly. The CMG–PGT hybrid configuration performs the worst in terms of efficiency, as it accumulates losses from both mechanisms. While it may offer structural or integration benefits in certain applications, its efficiency penalty becomes critical in energy-sensitive environments.

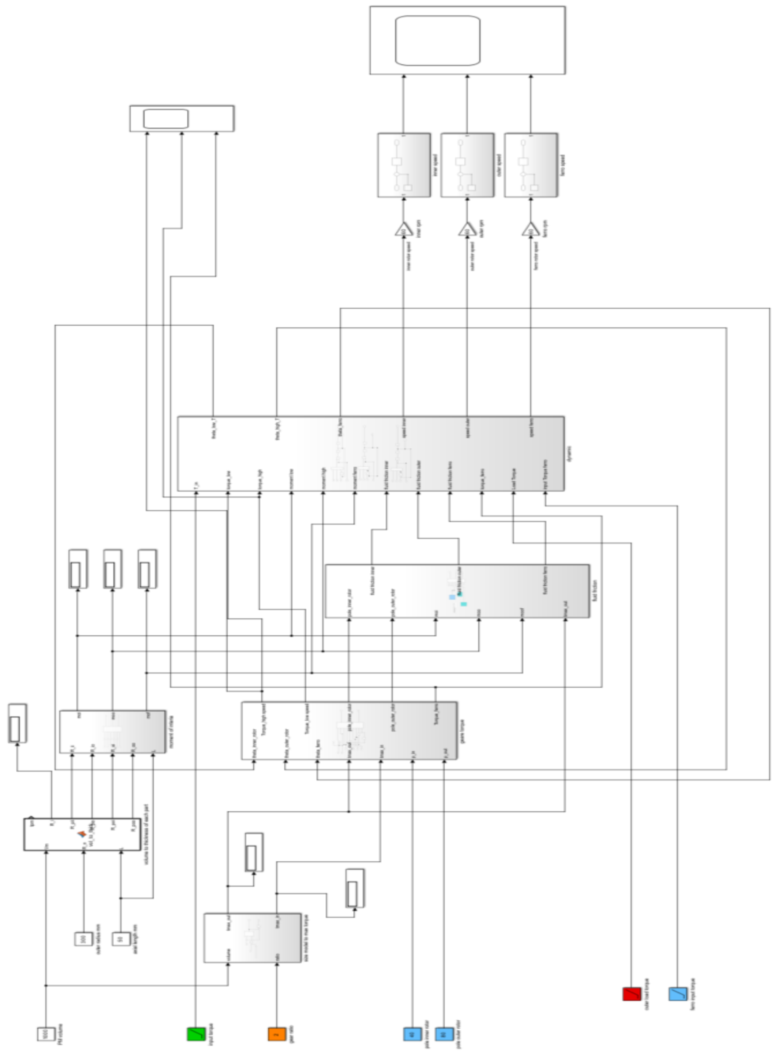

Fig. 4.23. Comprehensive simulation model of CMG ECVT with size model

4.3.3 ECVT Dynamic Simulation Model

Using the CMG and PGT-based ECVT size models, we can determine the appropriate dimensions of the CMG by specifying the torque output from the engine, which serves as the primary power source, along with the electric motor that functions as a supplementary speed control mechanism. Depending on the specific connection architecture within the ECVT system, the torque distribution, motor size, and target torque requirements will vary. Given a fixed maximum torque value from the engine, we can derive a corresponding CMG size model and define its internal structural dimensions.
Furthermore, by integrating the size model with a dynamic simulation framework, we can establish a comprehensive simulation environment for the CMG-based ECVT system, as illustrated in **Fig. 4.23**. This simulation includes the dynamic module, size module, input parameters, and the resulting torque and speed responses.
As shown in Equations 3.4.1 to 3.4.3, we can derive the complete and detailed dynamic equations governing each component of the CMG system.

$$J_{in} \cdot \frac{d^2\theta_{in}}{dt^2} = (\pm)T_{m_{in}} * \sin\left(p_{in} * \theta_{in} + p_{out} * \theta_{out} - N_m * \theta_m + \varphi\right)$$

$$J_m \cdot \frac{d^2\theta_m}{dt^2} = (\pm)T_{m_{in}} * \sin(p_{in} * \theta_{in} + p_{out} * \theta_{out} - N_m * \theta_m + \varphi) -$$
$$T_{m_{out}} * \sin\left(p_{in} * \theta_{in} + p_{out} * \theta_{out} - N_m * \theta_m + \varphi\right) + T_{input,m}$$

$$J_{out} \cdot \frac{d^2\theta_{out}}{dt^2} = T_{output} - T_{m_{out}} * \sin\left(p_{in} * \theta_{in} + p_{out} * \theta_{out} - N_m * \theta_m + \varphi\right)$$

Such a model for magnetic gear transmission constitutes an ideal dynamic transmission model that represents the torque induced by the dynamic acceleration of the input rotors, as well as the relationship between this mechanical input and the electromagnetic torque internally generated through magnetic interactions between permanent magnets and ferromagnetic materials. By applying the dynamic torque balance principle, the model formulates governing equations that enable the estimation of torque transmission and speed variation from the input rotors to the output components. By implementing these equations in a MATLAB Simulink model, the simulation results indicate that the angular speed continues to increase indefinitely without reaching a steady state.

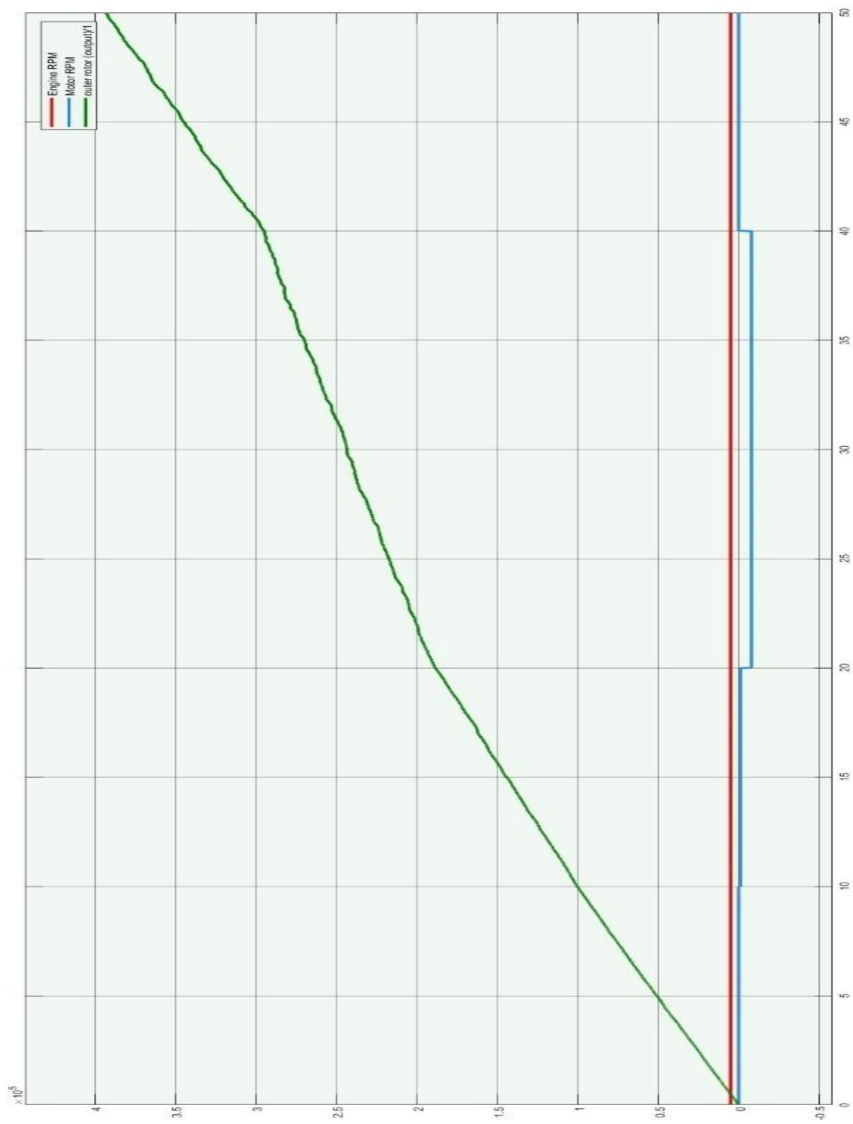

Fig. 4.24 Ideal dynamic simulation model speed result

As shown in **Fig. 4.24**, when the motor speed is varied as an alternative speed control input, the resulting output speed exhibits different rates of increase across various phases, though the overall trend remains increasing. However, the acceleration ratio varies over time. This type of speed variation does not align with the expected behavior of a magnetic ECVT system, which aims to provide a smooth and controlled speed transition. To further investigate this issue, we revisited the dynamic equations governing the magnetic ECVT system. Under the condition of constant input torque, constant load torque, and a fixed input speed from the turbine engine, the terms on the right-hand side of the equations become constant. These terms represent the magnetic coupling torque, which corresponds to the electromagnetic torque generated between the input permanent magnets and the flux modulator due to the phase difference in their magnetic fields. Because the rotor inertias are also constant, a constant net torque on the right-hand side leads to a theoretically unbounded increase in angular acceleration $\frac{d^2\theta}{dt^2}$, which explains the continuously increasing rotor speed observed in the simulation of the magnetic ECVT system. However, in realistic magnetic ECVT dynamic simulations, dampers play a critical role in stabilizing the system and ensuring realistic behavior. Due to the inherently oscillatory nature of magnetic torque—often modeled as a sinusoidal function of rotor positions—energy can accumulate rapidly in the system if no dissipation mechanism is present. Without damping, the simulated rotor speeds may increase uncontrollably, leading to non-physical results such as infinite acceleration.

By introducing linear damping elements (i.e., torque terms proportional to angular velocity), the simulation accounts for real-world energy losses caused by factors such as bearing friction, air resistance, magnetic core losses, and induced eddy currents. These damping torques act to counterbalance driving torques, preventing runaway acceleration and allowing the system to reach a steady-state or stable oscillatory response.

Therefore, the dynamic equations of the magnetic ECVT system are revised to incorporate a damping factor, which accounts for bearing friction and magnetic eddy current losses within the transmission. The modified equations are shown below:

$$J_{in} \cdot \frac{d^2\theta_{in}}{dt^2} = (\pm)T_{m_{in}} * \sin(p_{in} * \theta_{in} + p_{out} * \theta_{out} - N_m * \theta_m + \varphi) - b_{in}\frac{d\theta_{in}}{dt}$$

$$J_m \cdot \frac{d^2\theta_m}{dt^2} = (\pm)T_{m_{in}} * \sin(p_{in} * \theta_{in} + p_{out} * \theta_{out} - N_m * \theta_m + \varphi) -$$

$$T_{m_{out}} * \sin\,(p_{in} * \theta_{in} + p_{out} * \theta_{out} - N_m * \theta_m + \varphi) + T_{input,m} - b_{mod}\frac{d\theta_{mod}}{dt}$$

$$J_{out} \cdot \frac{d^2\theta_{out}}{dt^2} = T_{output} - T_{m_{out}} * \sin\,(p_{in} * \theta_{in} + p_{out} * \theta_{out} - N_m * \theta_m + \varphi) - b_{out}\frac{d\theta_{out}}{dt}$$

Where the J_{in}, J_m and $J_{out}$is the moment of inertia of the inner outer and ferro rotor but the difference is the b_{in}, b_{out} and b_{mod} which is adding to represent a linear damping coefficient of the bearing friction and eddy current loss. In this project, prior to integrating the dynamic simulation of the ECVT system with the magnetic gear transmission, we investigated and analyzed the factors affecting the transmission efficiency of the magnetic gear. Our analysis revealed that the efficiency is primarily influenced by eddy current losses in the yokes and ferromagnetic pole pieces. Based on this finding, the damping coefficient can be derived from the eddy current losses obtained in the magnetic gear efficiency analysis. By analyzing the distribution of eddy current losses across the inner rotor, outer rotor, and modulation ring, we established a proportional relationship between the damping coefficients and the corresponding eddy current losses in each rotor. Accordingly, the damping coefficients were estimated as $b_{in} = 0.18$, $b_{out} = 0.2$ and $b_{mod} = 0.3$ which align with the relative magnitude of eddy current losses observed in each component.

And the result is shown in **Fig. 4.25**, with both response torque and the speed. The torque plot illustrates the torque response of each rotating component over time, including the outer rotor, inner rotor, and system load. The outer rotor torque, representing the engine input, increases in steps, remains constant during mid-phase operation, and then gradually decreases. In contrast, the inner rotor torque shows a negative trend, indicating the electric motor or generator is operating in a power-absorbing mode to assist with speed modulation. A magnified insect highlights periodic torque ripples in the inner rotor, which likely result from magnetic coupling effects or control-related fluctuations within the system.

The speed figure shows the rotational speed response of the CMG output. Initially, the speed exhibits high-frequency oscillations before stabilizing. As the system progresses through different torque phases, the speed decreases slightly and then rise again, corresponding to the load demand and motor compensation. The enlarged view reveals fine-scale speed ripples, indicating transient dynamic effects that arise from system inertia and magnetic interaction. Together, these two plots demonstrate the coordinated operation of the ECVT size and dynamic model, capturing the complex torque-speed behavior under time-varying load and control conditions.

Noticeable torque ripple and speed ripple occur during the transient phase, primarily due to magnetic coupling effects and dynamic load variations. In the coupled condition, the ripple magnitude remains within 0.8–2%, which does not significantly impact the efficiency or safety of CMG operation. These ripples gradually diminish as the system reaches steady state, indicating effective speed stabilization. However, under an uncoupled condition, the ripple may increase to 3–8%, which poses a significant challenge for transmission stability and performance. Compared to **Fig. 4.25**, **Fig. 4.26** illustrates the output speed variation under ECVT speed control and demonstrates the dynamic response of a magnetic Electric Continuously Variable Transmission (ECVT) system to step changes in motor input speed. The red curve indicates the engine RPM, which remains constant throughout the simulation, representing a steady power source such as a turbine engine. The blue curve shows the motor RPM, which undergoes discrete step changes at approximately 10 s, 20 s, and 40 s—simulating transitions in control strategies or driving conditions. The green curve represents the output rotor speed (typically the outer rotor of the magnetic gear), which exhibits a dynamic response corresponding to the variations in motor speed.

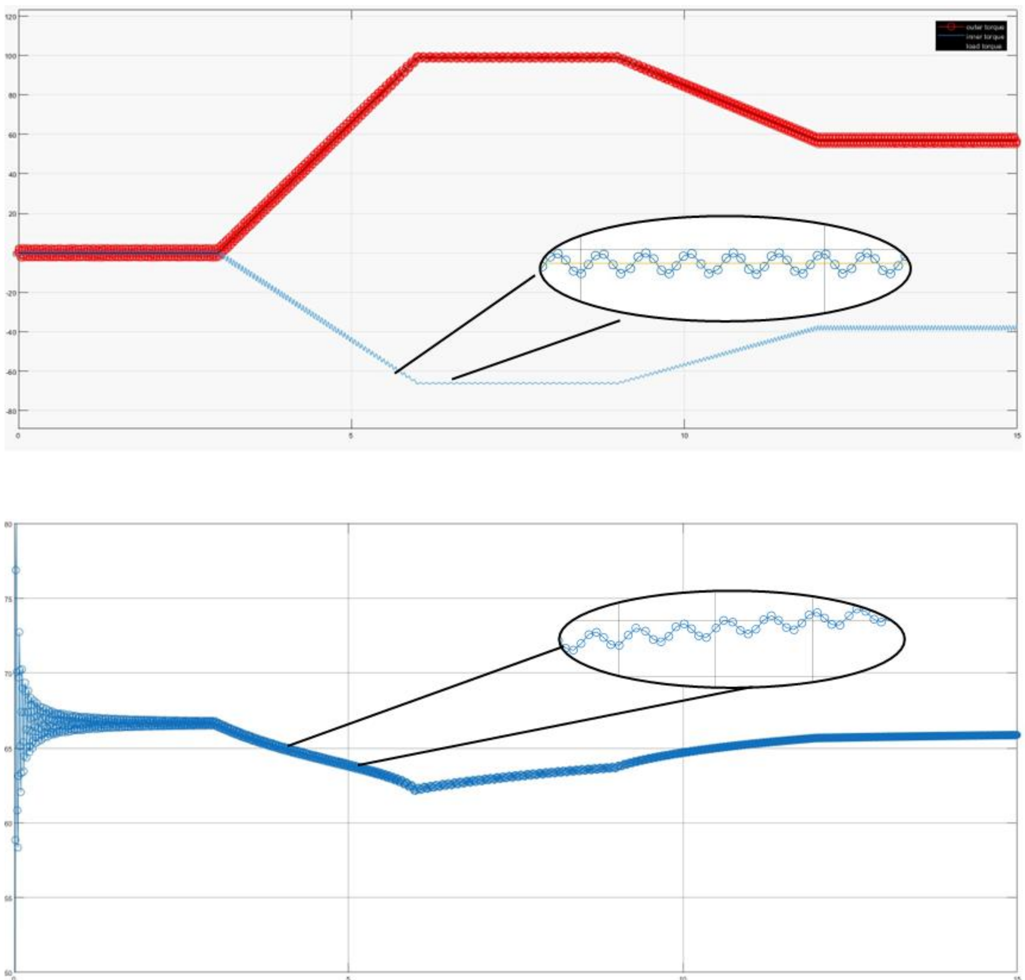

Fig. 4.25 Dynamic simulation model torque and speed result

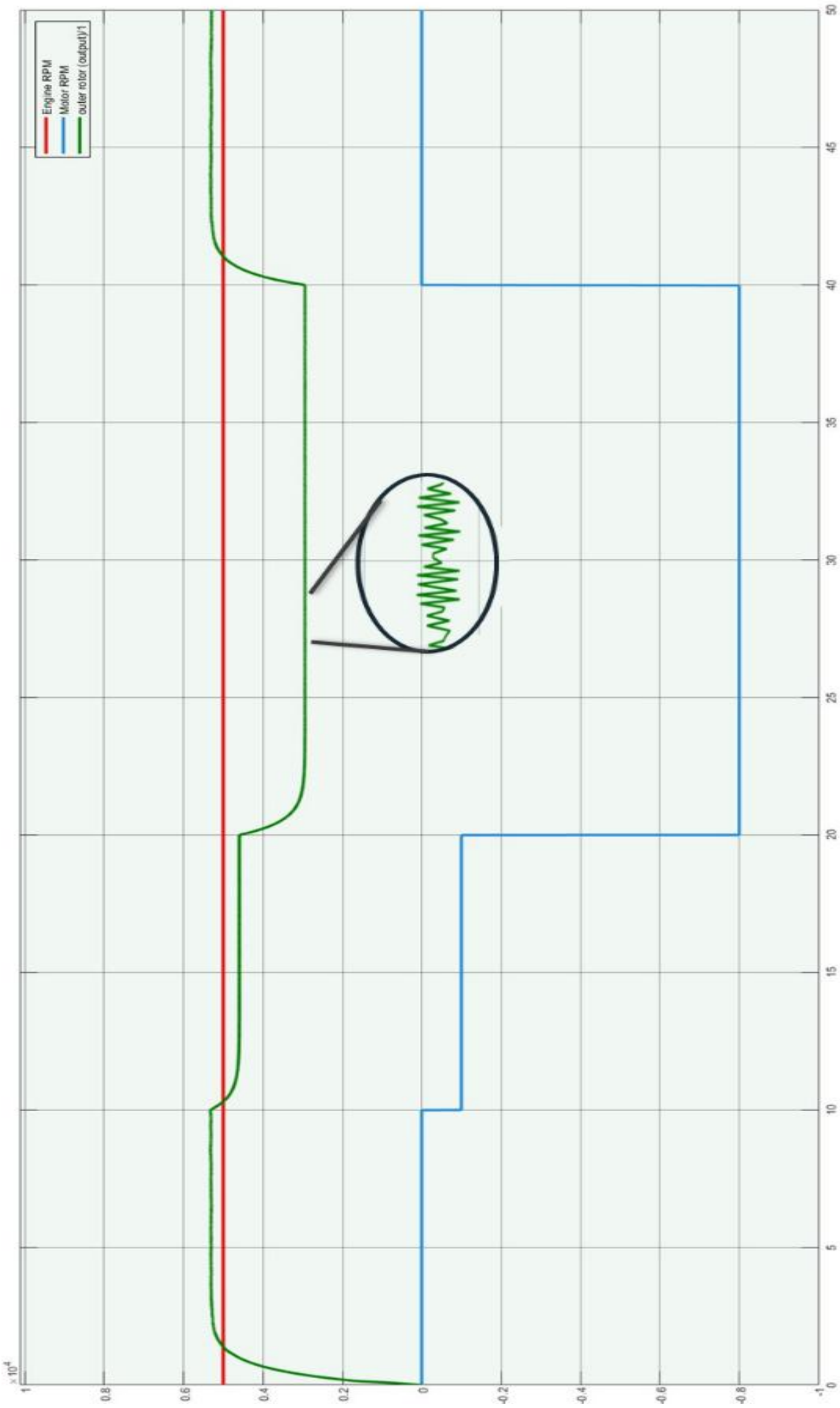

Fig. 4.26 Dynamic simulation model speed result with speed control

At each step change in motor speed, the output speed transitions accordingly, demonstrating the gear ratio adaptability of the magnetic ECVT. However, during the lowest motor speed phas, the output speed exhibits clear high-frequency oscillations. A zoomed-in section highlights these oscillations, which likely result from insufficient damping, rotor-mode resonance, or abrupt changes in electromagnetic coupling torque. This behavior underscores the critical role of damping—whether mechanical, electromagnetic, or control-based—in suppressing instability and ensuring smooth power transmission in practical systems. Overall, the figure validates the system's ability to modulate output speed under a fixed engine input, while also revealing the need for optimized damping and control strategies to mitigate transient oscillations and maintain system stability.

4.4 Chapter Four Summary

This chapter presented a comprehensive evaluation of Magnetic Electric Continuously Variable Transmission (MECVT) architectures integrating electric motors with either planetary gear transmissions (PGTs) or coaxial magnetic gears (CMGs). A parametric sizing framework was developed for motor design, followed by integrated system modeling to compare gear mass, motor mass, total system weight, and transmission efficiency across various configurations.

Quantitative results indicate that CMG systems achieve substantial mass savings in high-ratio applications. For example, at a target gear ratio of 12, the total ECVT mass of CMG Type II is approximately 17% lower than that of PGT Type III, primarily due to the elimination of multi-stage gearing and the use of permanent shared magnets between the motor and gear. This shared PM structure alone contributes to a 10–15% weight reduction in the integrated system compared to a non-shared design.

Even though CMG gear mass alone only becomes lighter than that of PGT Type III beyond gear ratios of 10–13, the total system mass becomes lighter at much lower ratios, around 1:8–1:9, because of the shared electromagnetic components and more favorable torque distribution.

However, these weight advantages come at a cost. As shown in the transmission efficiency analysis at 5000 rpm, PGT systems maintain over 97% efficiency across most gear ratios, while CMG systems drop from 98% to below 92%, representing a 5–7% absolute efficiency loss. The hybrid CMG–PGT system performs worst, with efficiency declining below 90% at high gear ratios due to compounding magnetic and mechanical losses.

In conclusion, PGT Type III remains favorable for low-to-moderate gear ratios ($R < 8$) where both mass and efficiency are balanced. In contrast, CMG-based systems excel in high-ratio, mass-sensitive applications, especially where integration and compactness are prioritized. The choice of architecture depends heavily on the system-level trade-offs between weight and efficiency, both of which are quantified and visualized in this chapter’s results. This data-driven comparison supports informed decision-making for future hybrid drivetrain applications in aerospace and electric propulsion systems.

CHAPTER FIVE

CONCLUSIONS AND RECOMMENDATIONS

The advancement of Motor Generator Integrated Permanent Magnet Gear (MIPMG) technology represents a transformative development in meeting the increasing demands for high efficiency, compactness, and high torque density in modern propulsion systems [71], [72]. By integrating high-performance permanent magnet motors with magnetic gear transmissions, particularly in axial and coaxial configurations, these systems enable smooth and contactless power delivery, offering reduced maintenance, increased mechanical reliability, and enhanced protection against overload. Demonstrated across a wide range of applications such as wind energy [73]-[75], space robotics, traction drives, and electric vehicles, MIPMG systems have achieved torque density levels that match or surpass those of traditional mechanical gear systems.

Despite existing challenges including thermal limitations, design complexity, and manufacturing constraints [76], ongoing advancements in gear topology, magnetic field modulation, and motor-gear integration continue to push performance boundaries. These innovations are especially critical for emerging variable-speed and multi-speed propulsion systems in aerospace and electric mobility platforms, where lightweight construction and efficient power transmission are essential [77]. Within this context, MIPMG systems present a scalable and efficient solution that aligns with the evolving needs of advanced drivetrain architectures.

A detailed theoretical and simulation-based investigation was conducted to explore coaxial magnetic gear (CMG) systems in terms of their design methodology, torque transmission behavior, and operational efficiency under both static and dynamic conditions [78]. Beginning with the fundamental principles of magnetic gear operation, the study introduces the concept of magnetic flux modulation and develops a torque model based on the interaction between permanent magnets on the inner and outer rotors and the intermediate ferromagnetic modulator. This model, supported by both analytical and numerical methods, defines a sinusoidal relationship between torque output and angular displacement, governed by pole pair combinations and material properties.

A significant outcome of the modeling process is the derivation of a maximum torque line that predicts the upper limit of torque transmission based on outer pole pair count, gear ratio, and internal thickness distribution [79]. This model provides a practical alternative to repeated finite element simulations in early-stage design. Parametric studies demonstrate that increasing the thickness of the outer permanent magnets and optimizing the geometry of the ferromagnetic modulator can significantly improve torque amplitude, waveform smoothness, and torque density, measured both by volume and weight [81]. Across fixed size envelopes, configurations with higher outer pole counts consistently show better torque density, making them favorable for applications with stringent space constraints.

Static simulations comparing single-pair and double-pair magnetic configurations reveal that increased pole count enhances torque magnitude and waveform stability. When the outer pole pair number is fixed and only the gear ratio is varied, torque performance shows convergence across configurations. This indicates a saturation point where outer rotor design becomes the limiting factor for further torque density improvements [82]. The study is extended through dynamic simulations using a MATLAB-based finite element model to capture transient and steady-state torque behavior under realistic load conditions. Two scenarios are evaluated, one representing partial engagement and the other representing full engagement under steady operation. Results confirm that the analytical torque model closely matches dynamic simulation data, especially in the outer rotor where torque response is more stable and predictable. These findings validate the accuracy and applicability of the proposed model under dynamic operating conditions [83], [84].

Efficiency and magnetic loss mechanisms are then examined in detail. The analysis separates the sources of loss into eddy current loss, hysteresis loss, and torque ripple. Results show that eddy current loss becomes dominant at higher rotational speeds, while the advantages of increasing pole pair count are most evident at lower speeds. Pie charts and trend plots over the speed range from 500 to 5000 revolutions per minute provide insight into how loss composition evolves, highlighting the importance of advanced magnetic materials and lamination strategies for high-speed applications.

To evaluate the broader applicability of magnetic gear integration, a full system-level comparison was conducted for Magnetic Electric Continuously Variable Transmission (MECVT) architectures, integrating electric motors with either planetary gear transmissions or CMG systems. A parametric motor sizing model was developed to quantify motor mass, gear mass, total system mass, and transmission efficiency across different gear ratios[85].

Quantitative results show that CMG-based systems offer substantial mass savings in high gear ratio applications. At a gear ratio of 12, the total MECVT mass for CMG Type II is approximately 17 percent lower than that of the planetary gear transmission Type III. This advantage is primarily due to the elimination of multi-stage mechanical gearing and the use of a shared permanent magnet structure between the motor and gear. The shared structure alone contributes to a 10 to 15 percent reduction in system weight compared to non-integrated designs. Although CMG gear mass only becomes lower than that of the planetary gear system beyond gear ratios of 10 to 13, the total system mass is already lighter at ratios around 8 to 9, due to more efficient electromagnetic integration and improved torque distribution.

However, these mass advantages come with efficiency trade-offs. At 9000 revolutions per minute, planetary gear systems maintain transmission efficiencies above 97 percent across all gear ratios. In contrast, CMG systems experience a gradual drop in efficiency from 98 percent to below 92 percent, primarily due to magnetic losses, particularly eddy currents. Hybrid systems combining CMG and planetary gears perform the worst, with efficiency dropping below 90 percent at high gear ratios due to the cumulative effects of both magnetic and mechanical losses [87]-[89].

These findings highlight a clear trade-off between mass and efficiency. Planetary gear systems remain favorable for low to moderate gear ratios where a balance of performance and weight is required. On the other hand, CMG-based designs are more advantageous in high-ratio, mass-sensitive scenarios where compact integration and low component count are prioritized. The selection of the optimal architecture should be guided by system-level priorities and constraints.

In summary, this integrated exploration of CMG-based magnetic transmission systems brings together theoretical modeling, geometric design, dynamic simulation, and loss analysis to support the development of high-performance, high-torque-density gear systems. The modeling framework and comparative data provided here offer valuable tools for the design and optimization of future aerospace, electric vehicle, and robotic powertrains where compactness, efficiency, and reliability are essential.

Recommendation and Future Work

1. Improved Magnetic Loss Mitigation at High Rotational Speeds

The analysis indicates that coaxial magnetic gear (CMG) systems experience a significant drop in efficiency at high speeds, primarily due to eddy current losses in the yoke and rotor structures. Future work should explore the use of low-loss magnetic materials such as amorphous or nanocrystalline alloys, along with laminated core designs, to reduce eddy current effects. Additionally, adaptive magnetic path structures optimized for different speed regimes could further improve performance.

2. Thermal Modeling and Multiphysics Simulation

While this work focuses on torque transmission and mass characteristics, thermal buildup remains a key limitation in integrated motor–gear systems. Future research should incorporate thermal–magnetic–mechanical Multiphysics simulations to predict temperature rise under continuous operation. These models would also aid in optimizing cooling strategies, including airflow channels or embedded heat pipes.

3. Dynamic Response under Non-ideal and Transient Conditions

The current dynamic simulations assume idealized loading conditions. Future studies should examine system performance under transient events such as sudden torque changes, acceleration or deceleration cycles, and external disturbances typical in aerospace or electric vehicle operations. This would provide deeper insights into control stability, torque ripple behavior, and mechanical resilience.

4. Prototype Development and Experimental Validation

To validate the simulation models and theoretical predictions, the construction of a physical prototype is essential. A low-to-medium power MIPMG system could be developed for laboratory testing. Experimental results on torque output, loss breakdown, and thermal behavior under various loads would help verify the analytical torque model and support further refinement of efficiency estimations.

5. Control Strategy Design for CMG–PGT Hybrid Architectures

Although the hybrid CMG–PGT architecture demonstrated lower efficiency in simulation, its performance could be enhanced through intelligent control strategies. For instance, torque routing could be adjusted based on load demand, using CMG for low-load high-speed conditions and PGT for high-torque scenarios. Real-time energy flow control could help minimize losses and improve operational adaptability.

6. System-level Impact Assessment and Lifecycle Evaluation

Future work should extend component-level findings to the system level by evaluating how integrated MIPMG or CMG–PGT architectures influence overall vehicle performance. This includes studying impacts on range, endurance, fuel economy, and thermal budget in aircraft, electric vehicles, or robotic platforms. Lifecycle analysis could also assess long-term reliability and maintenance costs, supporting broader industrial adoption.

LIST OF REFERENCES

[1] Han, Dong, Vasileios Pastrikakis, and George N. Barakos. "Helicopter performance improvement by variable rotor speed and variable blade twist." *Aerospace Science and Technology* 54 (2016): 164-173.

[2] Stevens, Mark A., Robert F. Handschuh, and David G. Lewicki. *Variable/multispeed rotorcraft drive system concepts*. No. NASA/TM-2009-215456. 2009.

[3] Johnson, W.; Yamauchi, G.K.; and Watts, M.E.: NASA Heavy Lift Study. NASA/TP‒2005-213467, 2005.

[4] Kluger, M.A., et al., "An Overview of Current CVT Mechanisms, Forces and Efficiencies," SAE Technical Paper Series, 970687, 1997.

[5] Davis, K., J. Frisk, and G. Jewett, "Pericyclic Differential," Univ. of Connecticut, Dept. of Mechanical Eng., Sr. Design Project, April 2004.

[6] Lemanski A.J, Monahan, T.J.," Non-Traction Pericyclic CVT's," 2004 International Continuously Variable and Hybrid Transmission Conference University of California, Davis, September 23-25, 2004.

[7] Parker, Richard J., Loewenthal, Stuart H., Fischer, George K., National Aeronautics and Space Administration, Lewis Research Center, "Design Studies of Continuously Variable Transmissions for Electric Vehicles," Society of Automotive Engineers Congress, Detroit, Michigan, DOE/NASA/1044-12, NASA TM-81642, February 23-27, 1981.

[8] Sauer, Georg, Institute of Agricultural Machinery, Technical University of Munich, Germany, "Continuously Variable Transmissions for Tractor Drive Line," Report No 94-D-020, AGENG, Milano 1994.

[9] DeSmidt, Hans A., et al. Comprehensive modeling and analysis of rotorcraft variable speed propulsion system with coupled engine/transmission/rotor dynamics. No. E-18646. 2013.

[10] Stevens, Mark A., Robert F. Handschuh, and David G. Lewicki. "Offset Compound Gear Inline Two-Speed Drive." (2014).

[11] Zaretsky, Erwin V. "NASA helicopter transmission system technology program." *Advanced Power Transmission Technol.* (1983).

[12] Kachel, Stanisław, Robert Rogólski, and Jakub Kocjan. "Review of modern helicopter constructions and an outline of rotorcraft design parameters." *Problems of Mechatronics. Armament, Aviation, Safety Engineering* 12, no. 3 (2021): 27-52.

[13] Aoyama Takashi, Jeiji Kawachi, Shigeru Saito. 1995. "Effect of Blade-Tip Planform on Shock Wave of Advancing Helicopter Blade". Journal of Aircraft 32 (5) : 955-961.

[14] Brocklehurst A., George N. Barakos. 2013. "A Review of Helicopter Rotor Blade Tip Shapes". Progress in Aerospace Sciences 56 : 35-74.

[15] Johnson, Timothy, and Ameya Joshi. "Review of vehicle engine efficiency and emissions." *SAE International Journal of Engines* 11, no. 6 (2018): 1307-1330.

[16] Khonsari, Michael M., and E. Richard Booser. *Applied tribology: bearing design and lubrication*. John Wiley & Sons, 2017.

[17] Coulomb, J-L., and G. Meunier. "Finite element implementation of virtual work principle for magnetic or electric force and torque computation." *IEEE Transactions on magnetics* 20, no. 5 (1984): 1894-1896.

[18] Johnson, W.; Yamauchi, G.K.; and Watts, M.E.: NASA Heavy Lift Study. NASA/TP‒2005-213467,2005.

[19] Kish. J.: Vertical Lift Drive System Concept Studies Variable Speed/Two-Speed Transmissions. NASA/CR‒2002-211564 (ARL−CR−495), 2002.

[20] Bossler, R.B., Jr.: Vertical Lift Drive System Concepts Studies. NASA/CR‒2002-211563, 2002.

[21] Wei, Yuan, Renliang Chen, Ye Yuan, and Luofeng Wang. "Influence of Engine Dynamic Characteristics on Helicopter Handling Quality in Hover and Low-Speed Forward Flight." *Aerospace* 11, no. 1 (2023): 34.

[22] Oh, Jiwon J., Jinsung Kim, and Seibum B. Choi. "Design of self-energizing clutch actuator for dual-clutch transmission." IEEE/ASME Transactions on Mechatronics 21, no. 2 (2015): 795-805.

[23] Wang, Yu, Enli Lü, Huazhong Lu, Nong Zhang, and Xingxing Zhou. "Comprehensive design and optimization of an electric vehicle powertrain equipped with a two-speed dual-clutch transmission." Advances in Mechanical Engineering 9, no. 1 (2017): 1687814016683144.

[24] Dolcini, Pietro J., Carlos Canudas-de-Wit, and Hubert Béchart. Dry clutch control for automotive applications. Springer Science & Business Media, 2010.

[25] Galvagno, Enrico, Mauro Velardocchia, and Alessandro Vigliani. "Dynamic and kinematic model of a dual clutch transmission." Mechanism and machine theory 46, no. 6 (2011): 794-805.

[26] Glielmo, Luigi, and Francesco Vasca. "Optimal control of dry clutch engagement." SAE transactions (2000): 1233-1239.

[27] Serrarens, Alex, Marc Dassen, and Maarten Steinbuch. "Simulation and control of an automotive dry clutch." In Proceedings of the 2004 American Control Conference, vol. 5, pp. 4078-4083. IEEE, 2004.

[28] Galvagno, Enrico, Mauro Velardocchia, and Alessandro Vigliani. "Dynamic and kinematic model of a dual clutch transmission." Mechanism and machine theory 46, no. 6 (2011): 794-805.

[29] C. G. Armstrong, “Power transmitting device,” US Pat. 687 292, 1901.

[30] S. Rand, “Magnetic transmission system,” US Pat. 3 523 204, 1970.

[31] M. Hetzel, “Low friction miniature gear drive for transmitting small forces, and method of making same,” US Pat. 3 792 578, 1974.

[32] K. Ikuta et al., “Non-contact magnetic gear for micro transmission mechanism,” in Micro Electro Mechanical Systems, Proc. An Investigation of Micro Structures, Sensors, Actuators, Machines & Robots. IEEE, 1991, pp. 125–130.

[33] Y. Yao et al., “Magnetic coupling studies between radial magnetic gears,” IEEE T-MAG, 33(5):4236-4238, 1997.

[34] “Simulation study of the magnetic coupling between radial magnetic gears,” IEEE T-MAG, 33(2):2203-2206, 1997.

[35] McGilton, Ben, Richard Crozier, Alasdair McDonald, and Markus Mueller. "Review of magnetic gear technologies and their applications in marine energy." *IET Renewable Power Generation* 12, no. 2 (2018): 174-181.

[36] Tlali, P. M., Rong-Jie Wang, and Stiaan Gerber. "Magnetic gear technologies: A review." In *2014 International Conference on Electrical Machines (ICEM)*, pp. 544-550. IEEE, 2014.

[37] K. Davey, L. McDonald, and T. Hutson, "Axial flux cycloidal magnetic gears," IEEE Transactions on Magnetics, vol. 50, no. 4, pp. 1-7, 2014.

[38] Johnson, Matthew, Alireza Shapoury, Pedram Boghrat, Mike Post, and Hamid A. Toliyat. "Analysis and development of an axial flux magnetic gear." In *2014 IEEE Energy Conversion Congress and Exposition (ECCE)*, pp. 5893-5900. IEEE, 2014.

[39] Holehouse, Robert C., Kais Atallah, and Jiabin Wang. "A linear magnetic gear." In *2012 XXth International Conference on Electrical Machines*, pp. 563-569. IEEE, 2012.

[40] Li, Wenlong, K. T. Chau, and J. Z. Jiang. "Application of linear magnetic gears for pseudo-direct-drive oceanic wave energy harvesting." *IEEE Transactions on Magnetics* 47, no. 10 (2011): 2624-2627.

[41] Holehouse, Robert C., Kais Atallah, and Jiabin Wang. "Design and realization of a linear magnetic gear." *IEEE transactions on magnetics* 47, no. 10 (2011): 4171-4174.

[42] Venturini, M., and F. Leonardi. "High torque, low speed joint actuator based on PM brushless motor and magnetic gearing." In *Conference Record of the 1993 IEEE Industry Applications Conference Twenty-Eighth IAS Annual Meeting*, pp. 37-42. IEEE, 1993.

[43] Atallah, Kais, Stuart Calverley, Richard Clark, Jan Rens, and David Howe. "A new PM machine topology for low-speed, high-torque drives." In *2008 18th International Conference on Electrical Machines*, pp. 1-4. IEEE, 2008.

[44] Rasmussen, Peter Omand, H. H. Mortensen, T. N. Matzen, T. M. Jahns, and H. A. Toliyat. "Motor integrated permanent magnet gear with a wide torque-speed range."

In *2009 IEEE Energy Conversion Congress and Exposition*, pp. 1510-1518. IEEE, 2009.

[45] Chau, K. T., Dong Zhang, J. Z. Jiang, Chunhua Liu, and Yuejin Zhang. "Design of a magnetic-geared outer-rotor permanent-magnet brushless motor for electric vehicles." *IEEE transactions on magnetics* 43, no. 6 (2007): 2504-2506.

[46] Jian, Linni, K. T. Chau, and J. Z. Jiang. "A magnetic-geared outer-rotor permanent-magnet brushless machine for wind power generation." *IEEE Transactions on Industry Applications* 45, no. 3 (2009): 954-962.

[47] Rasmussen, Peter Omand, H. H. Mortensen, T. N. Matzen, T. M. Jahns, and H. A. Toliyat. "Motor integrated permanent magnet gear with a wide torque-speed range." In *2009 IEEE Energy Conversion Congress and Exposition*, pp. 1510-1518. IEEE, 2009.

[48] R. Qu, D. Li, "High Torque Density Machines," Tutorial in ICEM 2018

[49] Misron, Norhisam, Luqman Mohd Saini, Ishak Aris, Chockalingam Aravind Vaithilingam, and Hanamoto Tsuyoshi. "Simplified design of magnetic gear by considering the maximum transmission torque line." *Applied Sciences* 10, no. 23 (2020): 8581.

[50] Zhu, Zi-Qiang, and David Howe. "Electrical machines and drives for electric, hybrid, and fuel cell vehicles." *Proceedings of the IEEE* 95, no. 4 (2007): 746-765.

[51] P. Krein, Elements of Power Electronics, (The Oxford Series in Electrical and Computer Engineering), 2nd ed. London, U.K.: Oxford Univ. Press, Dec. 2014

[52] Hofmann, Heath, and Seth R. Sanders. "High-speed synchronous reluctance machine with minimized rotor losses." *IEEE Transactions on Industry Applications* 36, no. 2 (2002): 531-539.

[53] Cupertino, Francesco, Riccardo Leuzzi, Vito Giuseppe Monopoli, and Giuseppe Leonardo Cascella. "Design procedure for high-speed pm motors aided by optimization algorithms." *Machines* 6, no. 1 (2018): 5.

[54] Fitzgerald, Arthur Eugene, Charles Kingsley, and Stephen D. Umans. "Electric machinery." (2003).

[55] Pyrhonen, Juha, Tapani Jokinen, and Valeria Hrabovcova. *Design of rotating electrical machines*. John Wiley & Sons, 2013.

[56] Pyrhonen J., Jokinen T., Hrabovcova V. Design of Rotating Electrical Machines, The Atrium, Southern Gate, Chichester, West Sussex, PO19 8SQ, United Kingdom: John Wiley and Sons; 2008.

[57] S. D. Sudhoff and Y. Lee, “Energy systems analysis consortium (ESAC) genetic optimization system engineering tool (GOSET) version manual,” School Electr. Comput. Eng., Purdue Univ., West Lafayette, IN, 2003.

[58] B. N. Cassimere, “Modeling and evolutionary design of permanent magnet synchronous machines,” Ph.D. dissertation, School Electr. Comput. Eng., Purdue Univ., West Lafayette, IN, May 2008.

[59] Cheng, Yuan, Fuyi Duan, and Shumei Cui. "The design principle of electric motors and drive systems for electric vehicles." In *2005 International Conference on Electrical Machines and Systems*, vol. 1, pp. 802-805. IEEE, 2005.

[60] Toliyat, Hamid A., and Gerald B. Kliman. *Handbook of electric motors*. CRC press, 2018.

[61] T. Lubin et al., "Design Strategies for High-Speed Permanent Magnet Machines," *IEEE Trans. Ind. Electron.*, vol. 63, no. 1, pp. 125–135, Jan. 2016.

[62] K. Atallah and D. Howe, "A novel high-performance magnetic gear," *IEEE Trans. Magn.*, vol. 37, no. 4, pp. 2844–2846, 2001.

[63] A. Mebarki et al., "Study of Rotor Sleeve Materials for High-Speed PM Machines," *IEEE Trans. Ind. Appl.*, vol. 48, no. 3, pp. 952–960, May-Jun 2012.

[64] S. Ruoho et al., "High-Speed PM Machine Design for Aerospace Applications," *Proc. EPE-PEMC*, 2012.

[65] P. D. Nguyen and S. H. Lee, "A High Torque Density Motor Integrated with Magnetic Gear," *IEEE Transactions on Industrial Electronics*, vol. 65, no. 7, pp. 5854–5863, Jul. 2018.

[66] K. Atallah and D. Howe, "A novel high-performance magnetic gear," *IEEE Transactions on Magnetics*, vol. 37, no. 4, pp. 2844–2846, Jul. 2001.

[67] K. T. Chau, D. Zhang, J. Z. Jiang, C. Liu, and Y. Zhang, “Design of a magnetic-geared outer-rotor permanent-magnet brushless motor for electric vehicles,” IEEE Trans. Magn., vol. 43, no. 6, pp. 2504–2506, Jun. 2007.

[68] Y. Tang, F. Chai, Y. Xie, and W. Cai, “Design of a modular inwheel motor with high fault-tolerant performance and low MMF space harmonic,” IEEE Trans. Ind. Electron., vol. 70, no. 7, pp. 6574–6584, Jul. 2023.

[69] C. V. Pop and D. Fodorean, “In-wheel motor with integrated magnetic gear for extended speed applications,” in Proc. Int. Symp. Power Electron., Electr. Drives, Autom. Motion (SPEEDAM), Jun. 2016, pp. 413–418.

[70] H. Goto, Y. Suzuki, K. Nakamura, T. Watanabe, H. J. Guo, and O. Ichinokura, “A multipolar SR motor and its application in EV,” J. Magn. Magn. Mater., vol. 290, pp. 1338–1342, Apr. 2005.

[71] Gerber, Stiaan. "Evaluation and design aspects of magnetic gears and magnetically geared electrical machines." PhD diss., Stellenbosch: Stellenbosch University, 2015.

[72] Akuru, Udochukwu B., and Maarten J. Kamper. "Design and investigation of low-cost PM flux switching machine for geared medium-speed wind energy applications." *Electric Power Components and Systems* 46, no. 9 (2018): 1084-1092.

[73] Lampola, Petri. Directly driven, low-speed permanent-magnet generators for wind power applications. Helsinki University of Technology, 2000.

[74] Jian, Linni, K. T. Chau, and J. Z. Jiang. "A magnetic-geared outer-rotor permanent-magnet brushless machine for wind power generation." *IEEE Transactions on Industry Applications* 45, no. 3 (2009): 954-962.

[75] Gerber, Stiaan, and Rong-Jie Wang. "Design and evaluation of a magnetically geared PM machine." *IEEE transactions on magnetics* 51, no. 8 (2015): 1-10.

[76] Li, Hui, and Zhe Chen. "Design optimization and site matching of direct-drive permanent magnet wind power generator systems." *Renewable Energy* 34, no. 4 (2009): 1175-1184.

[77] Ubadigha, Chinweze U., and Mi-Ching Tsai. "Analysis of integrated magnetic gear motor with dual mechanical output port: A block diagram approach." *IEEE Transactions on Energy Conversion* 35, no. 3 (2020): 1301-1308.

[78] Heikkilä, Tanja. "Permanent magnet synchronous motor for industrial inverter applications-analysis and design." (2002).

[79] Jian, Linni, and K. T. Chau. "A coaxial magnetic gear with Halbach permanent-magnet arrays." *IEEE Transactions on Energy conversion* 25, no. 2 (2010): 319-328.

[80] Filippini, Mattia, and Piergiorgio Alotto. "Coaxial magnetic gear design and optimization." *IEEE Transactions on Industrial Electronics* 64, no. 12 (2017): 9934-9942.

[81] Liu, Yulong, Siu Lau Ho, and W. N. Fu. "A novel magnetic gear with intersecting axes." *IEEE Transactions on Magnetics* 50, no. 11 (2014): 1-4.

[82] Li, Xianglin, K. T. Chau, Ming Cheng, Wei Hua, and Yi Du. "An improved coaxial magnetic gear using flux focusing." In *2011 International Conference on electrical machines and systems*, pp. 1-4. IEEE, 2011.

[83] K. T. Chau, C. C. Chan, and C. Liu, "Overview of permanent-magnet brushless drives for electric and hybrid electric vehicles," *IEEE Transactions on Industrial Electronics*, vol. 55, no. 6, pp. 2246–2257, June 2008.

[84] J. A. Tapia and T. A. Meynard, "Multiphysics design tools for high-performance electromechanical energy conversion systems," *IEEE Transactions on Energy Conversion*, vol. 36, no. 1, pp. 153–165, Mar. 2021.

[85] C. Y. Wu, C. T. Liu, and M. C. Tsai, "Development of a PM motor with magnetic gear for electric vehicle drive," *IEEE Transactions on Magnetics*, vol. 53, no. 11, pp. 1–4, Nov. 2017.

[86] M. T. Wolff, M. Bruckner, and H. Grotstollen, "Thermal modeling of magnetic gears for high-torque applications," *IEEE Transactions on Industrial Electronics*, vol. 58, no. 6, pp. 2424–2431, June 2011.

[87] Mateev, Valentin, and Iliana Marinova. "Loss estimation of magnetic gears." *Electrical Engineering* 102, no. 1 (2020): 387-399.

[88] Filippini, Mattia, Piergiorgio Alotto, Vincenzo Cirimele, Maurizio Repetto, Carlo Ragusa, Luca Dimauro, and Elvio Bonisoli. "Magnetic loss analysis in coaxial magnetic gears." *Electronics* 8, no. 11 (2019): 1320.

[89] Rasmussen, Peter Omand, Tommy V. Frandsen, Kasper K. Jensen, and Kenneth Jessen. "Experimental evaluation of a motor-integrated permanent-magnet gear." *IEEE Transactions on Industry applications* 49, no. 2 (2013): 850-859.

[90] T. Yamamura, K. Kakihana, Y. Kanai, and M. Takemoto, "Development of magnetic gear using permanent magnets," *IEEE Transactions on Magnetics*, vol. 41, no. 10, pp. 3961–3963, Oct. 2005.

[91] J. Wang, W. N. Fu, S. L. Ho, and G. H. Liu, "Design and analysis of high-performance magnetic gears using finite element method," *IEEE Transactions on Magnetics*, vol. 49, no. 7, pp. 3941–3944, Jul. 2013.

[92] K. Atallah, S. D. Calverley, and D. Howe, "Design and operation of a magnetic gear," *IEEE Transactions on Industry Applications*, vol. 41, no. 3, pp. 764–770, May-Jun. 2005.

[93] J. J. Hwang, K. T. Chau, and C. Liu, "Design and analysis of a novel axial-flux magnetic gear," *IEEE Transactions on Magnetics*, vol. 50, no. 11, pp. 1–4, Nov. 2014.

[94] T. A. Costin, "Offset compound gear arrangements and their application in dual-speed transmissions," *SAE Technical Paper*, no. 2011-01-0796, Apr. 2011.

[95] G. F. Smith and K. N. Anderson, "Design of a lightweight two-speed inline transmission for aerospace applications," *NASA Technical Memorandum*, NASA TM-106958, 1994.

[96] R. B. Anand and K. G. Muralidharan, "Design and performance analysis of two-speed automatic transmission system for electric vehicle application," *International Journal of Automotive Technology*, vol. 19, no. 2, pp. 329–337, Apr. 2018.

[97] H. Hirata and M. Kawamura, “A novel electric actuator using permanent magnet gear,” in Proceedings of the 27th Annual Conference of the IEEE Industrial Electronics Society (IECON), Denver, CO, USA, 2001, pp. 1443–1448. doi: 10.1109/IECON.2001.963407.

[98] S. I. Kim, J. H. Lee, and S. K. Sul, “New high-torque-density motor integrated with magnetic gear,” *IEEE Transactions on Magnetics*, vol. 46, no. 6, pp. 2680–2683, Jun. 2010. doi: 10.1109/TMAG.2010.2040421.

[99] J. E. Shigley, R. G. Budynas, and K. J. Nisbett, *Shigley’s Mechanical Engineering Design*, 10th ed., New York, NY, USA: McGraw-Hill, 2015, pp. 622–647.

[100] J. H. B. Smith and T. L. Schmitz, *Mechanical Engineering Design*, 9th ed., New York, NY, USA: McGraw-Hill, 2011, ch. 14, pp. 701–750.

[101] N. T. Nguyen, H. T. Nguyen, and S. C. Lee, “Analysis and comparison of coaxial magnetic gear with different ferromagnetic pole-piece configurations,” *IEEE Transactions on Magnetics*, vol. 55, no. 6, pp. 1–5, Jun. 2019. doi: 10.1109/TMAG.2019.2904509.

[102] Du, Qingfa, Jiafei Hu, Kun Sun, Dixiang Chen, Long Pan, Yulu Che, Xinmiao Zhang et al. "High efficiency magnetic flux modulation structure for magnetoresistance sensor." *IEEE Electron Device Letters* 40, no. 11 (2019): 1824-1827.

[103] N. Niguchi, Y. Amara, and L. Vido, "Harmonic modeling of coaxial magnetic gears," *IEEE Transactions on Magnetics*, vol. 49, no. 7, pp. 3961–3964, July 2013.

[104] P. T. Krein, "Magnetic gearing: Fundamentals, modeling, and design," *IEEE Power Electronics Magazine*, vol. 3, no. 4, pp. 24–32, Dec. 2016.

APPENDIX

Table 3.2. Dimension for 1:3 Gear Ratio CMG in Fig. 3.4.

Symbol	Dimensions for models		
	Description	Size	Units
Ryi	Inner yoke inner Radius	65	mm
Rii	Inner Rotor inner Radius	75	mm
Rio	Inner Rotor outer Radius	85	mm
g_air	Air gap thickness	1	mm
Rfi	Ferro Modulator inner Radius	86	mm
Rfo	Ferro Modulator outer Radius	101	mm
Roi	Outer Rotor inner Radius	102	mm
Roo	Outer Rotor outer Radius	112	mm
Ryo	Outer yoke outer Radius	122	mm
Robc	Outer Boundary Condition	135	mm
L	Length/height of CMG	50	mm
p_in	Inner PMs Pole pairs number	2	/
p_out	Outer PMs Pole pairs number	6	/
N_m	Ferro Modulator poles number	8	/
Br	Remanence flux density	1.2	T
μ_0	Permeability of Vacuum	1.24E-06	H/m
μ	Absolut Permeability of Magnets	1.32E-07	H/m
μ_r	Relative Permeability of Magnets	1.05	/

Table 3.8. Condition II: Inner/outer angular position and torque variation.

IR angular position	Inner Rotor Torque	OR angular position	Outer rotor Torque
0.00	-1.35	0.00	0.04
5.00	-6.33	0.00	12.38
10.00	-14.80	0.00	18.22
15.00	-29.48	0.00	37.33
20.00	-29.46	0.00	50.56
29.00	-35.01	6.00	50.99
38.00	-30.79	12.00	51.45
47.00	-35.01	18.00	51.00
56.00	-30.79	24.00	51.45
65.00	-35.02	30.00	51.00
74.00	-30.79	36.00	51.45
83.00	-35.04	42.00	50.98
92.00	-30.77	48.00	51.45
101.00	-35.04	54.00	50.99
110.00	-30.78	60.00	51.45
119.00	-35.04	66.00	50.98
128.00	-30.78	72.00	51.45
137.00	-35.03	78.00	50.99
146.00	-30.78	84.00	51.44
155.00	-35.01	90.00	50.98
164.00	-30.78	96.00	51.45
173.00	-35.03	102.00	50.98
182.00	-30.78	108.00	51.44
191.00	-35.03	114.00	50.99
200.00	-30.77	120.00	51.45

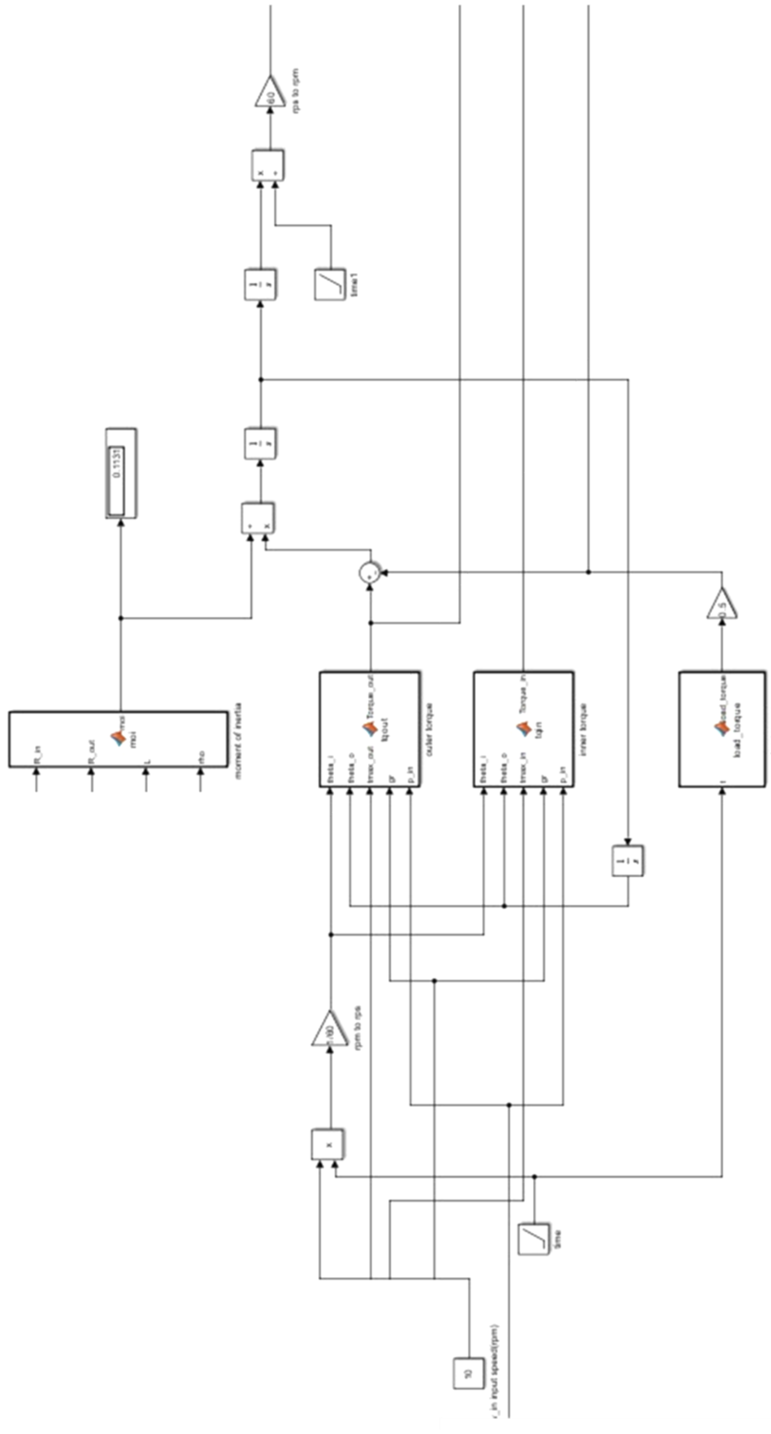

Fig. 3.27. Dynamic simulation model of Coaxial Magnetic Gear transmission.

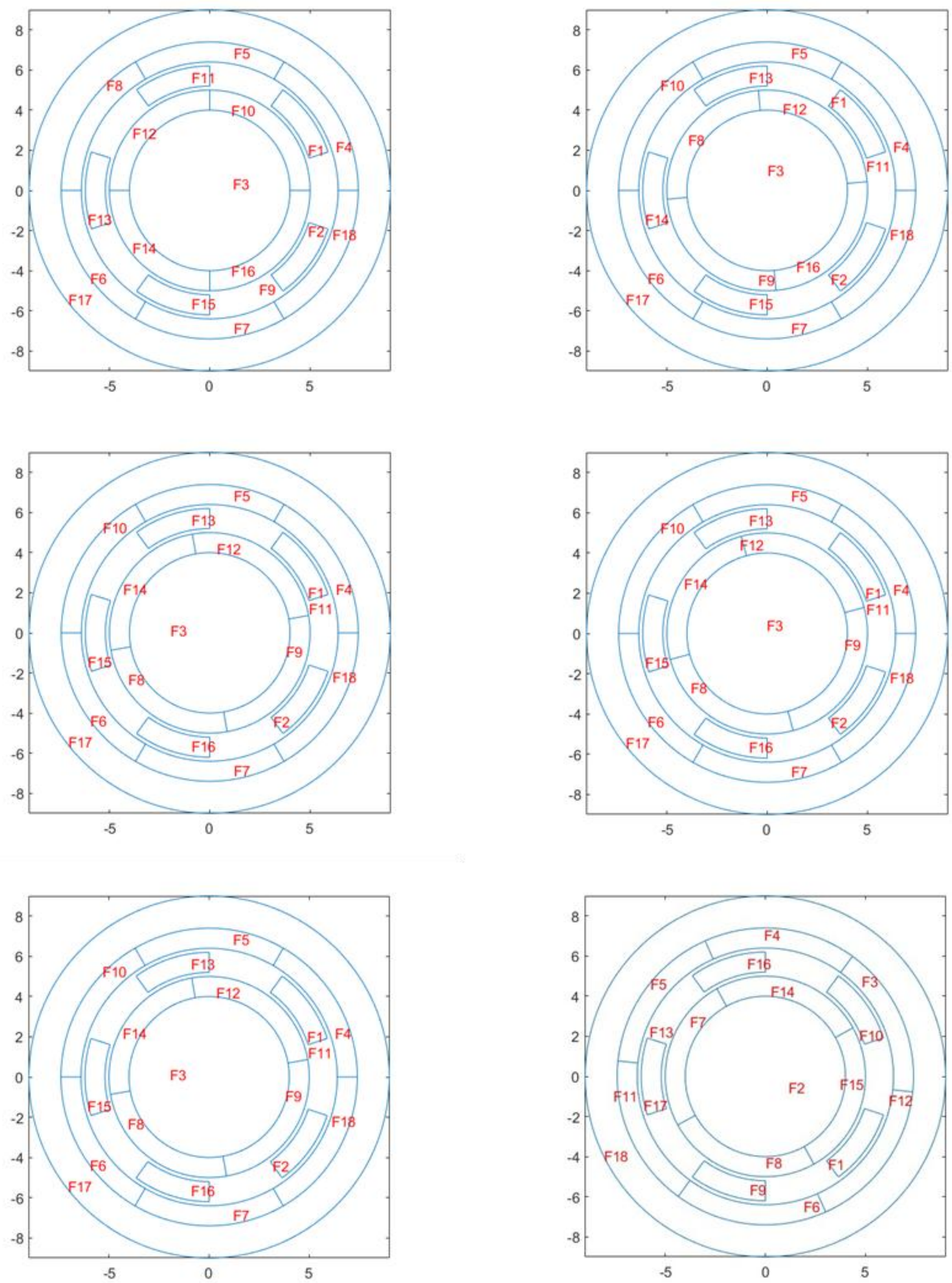

Fig. 3.34 1) - 14) Condition II: 70% steady-state operation.

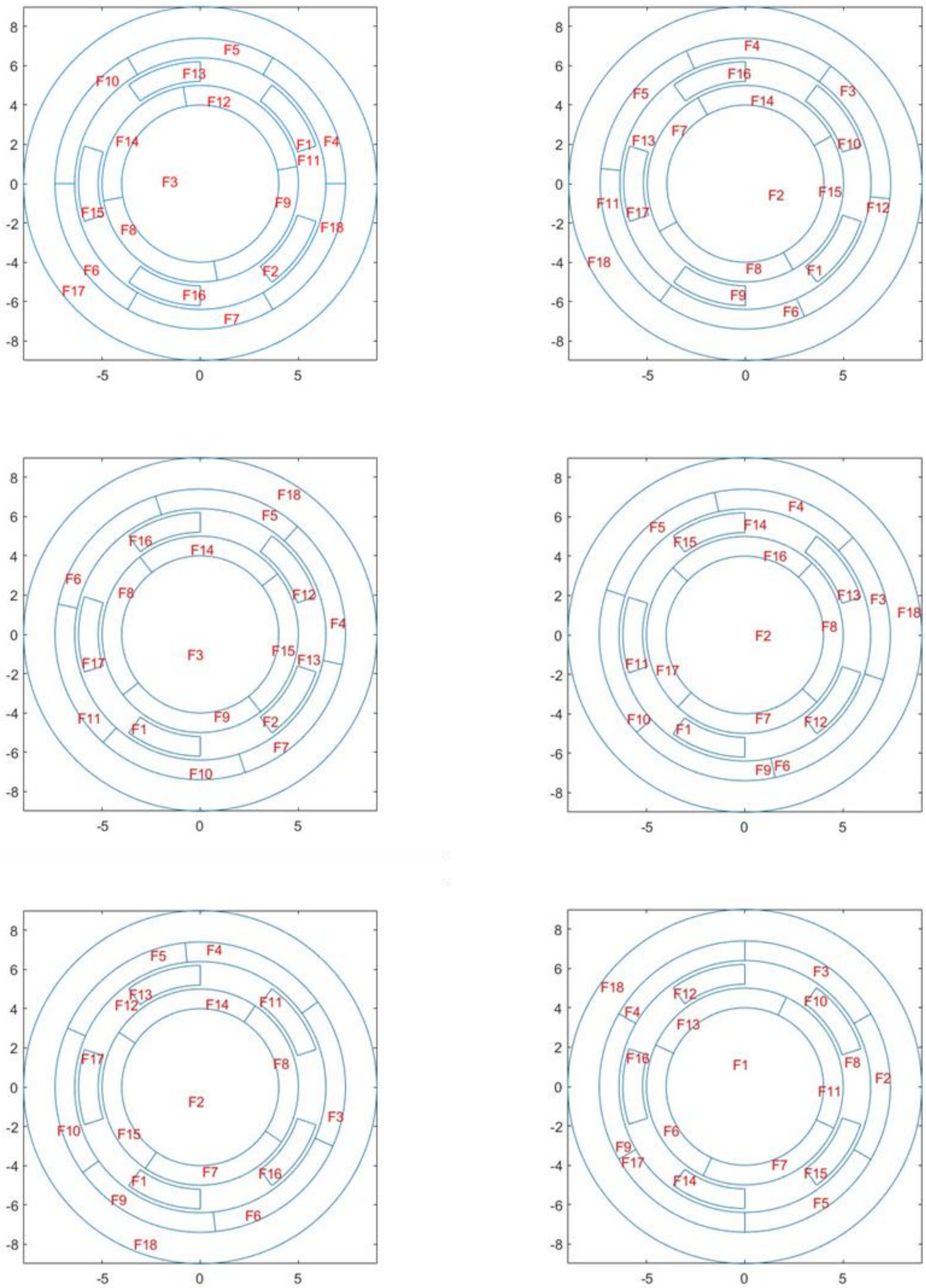

Fig. 3.34 1) - 14) (Continued) Condition II: 70% steady-state operation.

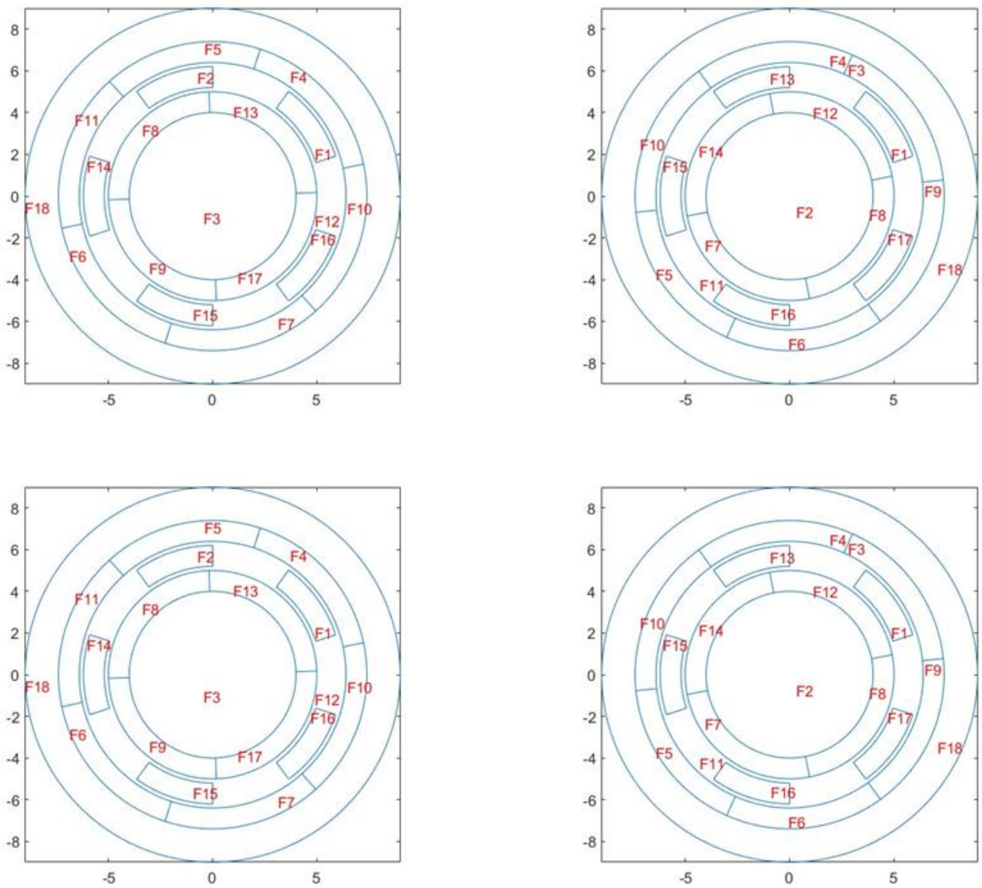

Fig. 3.34. 1) - 14) (Continued) Condition II: 70% steady-state operation.

Table 3.9. Condition III: Inner/outer angular position and torque variation.

Inner angular	Inner rotor torque	Outer angular	Outer rotor torque
0	-47.62027	0	82.143746
9	-55.354756	6	86.721314
18	-47.618548	12	82.140302
27	-55.348934	18	86.728366
36	-47.619286	24	82.132512
45	-55.34877	30	86.743782
54	-47.6215	36	82.126936
63	-55.350082	42	86.706062
72	-47.618548	48	82.140302
81	-55.348934	54	86.728366
90	-47.619286	60	82.132512
99	-55.34877	66	86.743782
108	-47.6215	72	82.126936
117	-55.350082	78	86.706062
126	-47.618548	84	82.140302
135	-55.348934	90	86.728366
144	-47.619286	96	82.132512
153	-55.34877	102	86.743782
162	-47.6215	108	82.126936
171	-55.350082	114	86.706062
180	-47.61781	120	82.143746

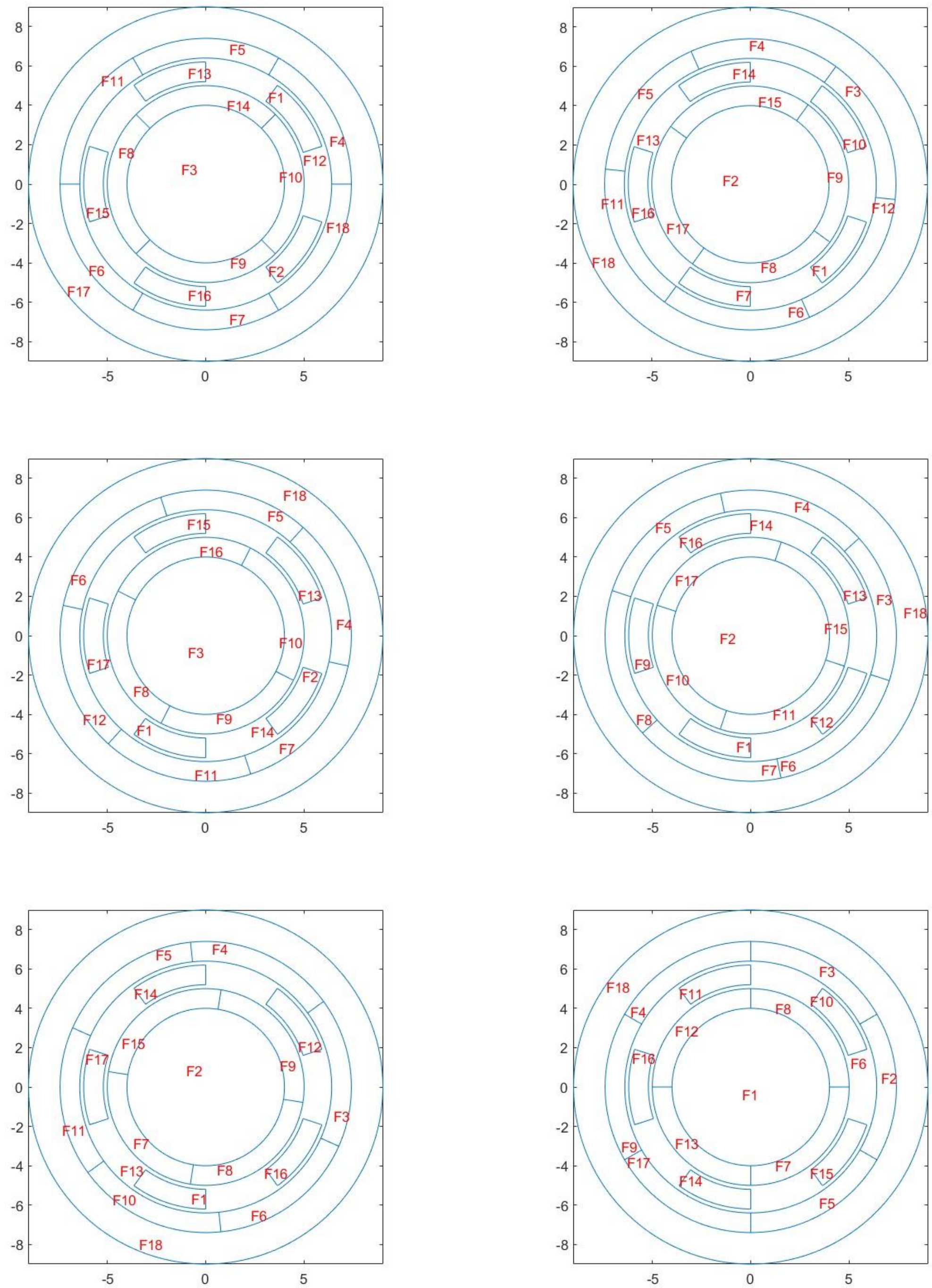

Fig. 3.35. 1) - 10) Condition III: Initial full steady-state operation.

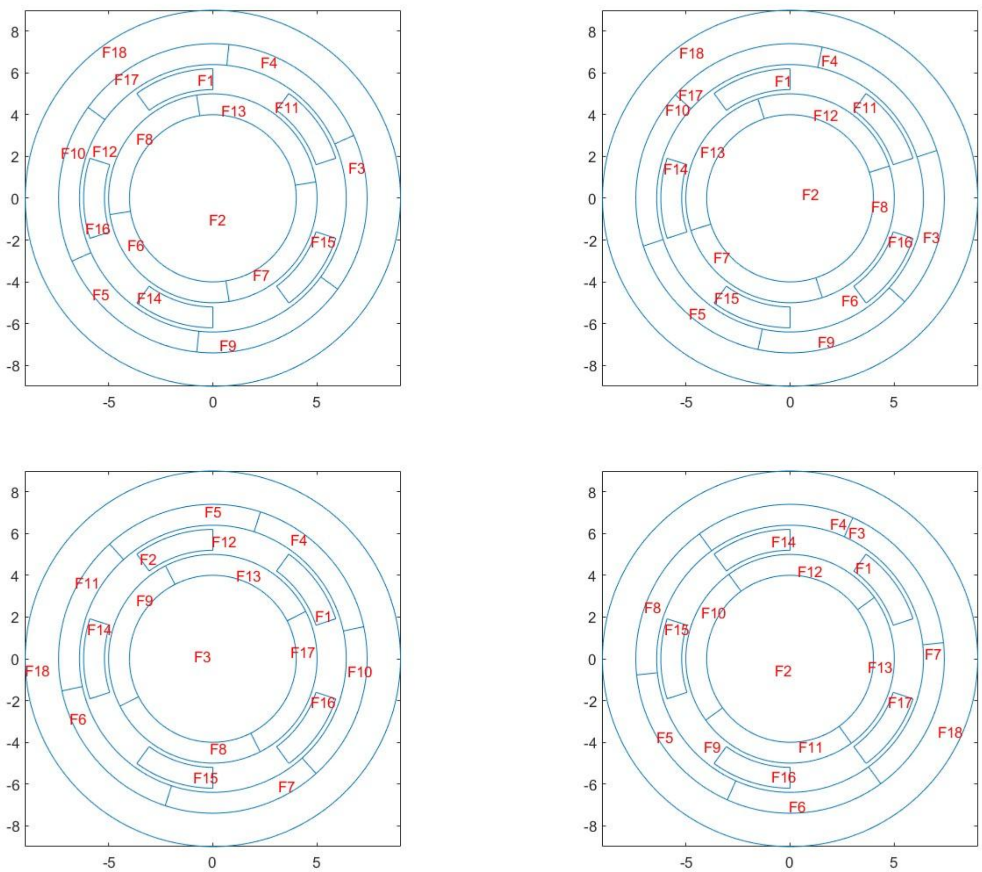

Fig. 35. 1) - 10) (Continued) Condition III: Initial full steady-state operation.

Table 3.11. Geometric parameters of CMG structure for torque analysis.

	outer pm_o	outer pm_i	ferro_o	ferro_i	inner pm_o	inner pm_i	inner yoke_i	outer R
PM thickness 5 mm	94	89	88.5	78.5	78	73	60	104
PM thickness 10 mm	116	106	105.5	85.5	85	75	60	126
PM thickness 20 mm	162	142	141	101	100	80	60	182

Table 3.14. 20 mm PM thickness with various ferro thickness ratio.

20 mm PM thickness with different Ferro thickness ratio								
Thickness Ratio	outer pm_o	outer pm_i	ferro_o	ferro_i	inner pm_o	inner pm_i	inner yoke_i	outer R
0.5	132	112	111	101	100	80	60	152
1	142	122	121	101	100	80	60	162
1.5	152	132	131	101	100	80	60	172
2	162	142	141	101	100	80	60	182
2.5	172	152	151	101	100	80	60	192
3	182	162	161	101	100	80	60	202
3.5	192	172	171	101	100	80	60	212
4	202	182	181	101	100	80	60	222
4.5	212	192	191	101	100	80	60	232
5	222	202	201	101	100	80	60	242

Table 3.17. Geometric parameters of CMG for inner yoke thickness study (PM volume = 300 cm³).

Outer Yoke Effect Permanent Magnet Volume 300 cm^3							
outer yoke ratio to PM	outer pm_o	outer pm_i	ferro_o	ferro_i	inner pm_o	inner pm_i	inner yoke_i
0	120	115.5	115	103.75	103.25	98.75	76.25
1	115.5	111	110.5	99.25	98.75	94.25	71.75
2	111	106.5	106	94.75	94.25	89.75	67.25
3	106.5	102	101.5	90.25	89.75	85.25	62.75
4	102	97.5	97	85.75	85.25	80.75	58.25
5	97.5	93	92.5	81.25	80.75	76.25	53.75

Table 3.18. Geometric parameters of CMG for inner yoke thickness study (PM volume = 300 cm³).

Outer Yoke Effect Permanent Magnet Volume 300 cm^3							
outer yoke ratio to PM	outer pm_o	outer pm_i	ferro_o	ferro_i	inner pm_o	inner pm_i	inner yoke_i
0	120	115.5	115	103.75	103.25	98.75	76.25
1	115.5	111	110.5	99.25	98.75	94.25	71.75
2	111	106.5	106	94.75	94.25	89.75	67.25
3	106.5	102	101.5	90.25	89.75	85.25	62.75
4	102	97.5	97	85.75	85.25	80.75	58.25
5	97.5	93	92.5	81.25	80.75	76.25	53.75

VITA

Zhisheng (Jason) Ai is a Ph.D. candidate in Mechanical and Aerospace Engineering at the University of Tennessee, Knoxville, where he also pursued a minor in Computational Science. His research focuses on the design and optimization of rotorcraft drivetrains and electronic continuously variable transmissions (E-CVT), with particular expertise in magnetic and planetary gear transmission systems. Jason has extensive experience in permanent magnet synchronous motor (PMSM) and brushless DC motor (BLDC) integration with gear systems, as well as system-level dynamic simulations and structural and thermal finite element analysis. He earned his Bachelor of Science in Energy and Power Engineering from Hohai University in 2017. His work has been recognized with multiple publications and presentations, including receiving the Alfred Gessow Best Paper Award at the 2024 Vertical Flight Society Forum.